TENDON STRUCTURE-FUNCTION RELATIONSHIP IN HEALTH, AGEING AND INJURY

EDITED BY: Huub Maas, Toni Arndt and Jason Franz
PUBLISHED IN: Frontiers in Sports and Active Living and
Frontiers in Bioengineering and Biotechnology

frontiers Research Topics

frontiers

ISSN 1664-8714
ISBN 978-2-88971-163-5
DOI 10.3389/978-2-88971-163-5

About Frontiers

Frontiers is more than just an open-access publisher of scholarly articles: it is a pioneering approach to the world of academia, radically improving the way scholarly research is managed. The grand vision of Frontiers is a world where all people have an equal opportunity to seek, share and generate knowledge. Frontiers provides immediate and permanent online open access to all its publications, but this alone is not enough to realize our grand goals.

Frontiers Journal Series

The Frontiers Journal Series is a multi-tier and interdisciplinary set of open-access, online journals, promising a paradigm shift from the current review, selection and dissemination processes in academic publishing. All Frontiers journals are driven by researchers for researchers; therefore, they constitute a service to the scholarly community. At the same time, the Frontiers Journal Series operates on a revolutionary invention, the tiered publishing system, initially addressing specific communities of scholars, and gradually climbing up to broader public understanding, thus serving the interests of the lay society, too.

Dedication to Quality

Each Frontiers article is a landmark of the highest quality, thanks to genuinely collaborative interactions between authors and review editors, who include some of the world's best academicians. Research must be certified by peers before entering a stream of knowledge that may eventually reach the public - and shape society; therefore, Frontiers only applies the most rigorous and unbiased reviews.
Frontiers revolutionizes research publishing by freely delivering the most outstanding research, evaluated with no bias from both the academic and social point of view. By applying the most advanced information technologies, Frontiers is catapulting scholarly publishing into a new generation.

What are Frontiers Research Topics?

Frontiers Research Topics are very popular trademarks of the Frontiers Journals Series: they are collections of at least ten articles, all centered on a particular subject. With their unique mix of varied contributions from Original Research to Review Articles, Frontiers Research Topics unify the most influential researchers, the latest key findings and historical advances in a hot research area! Find out more on how to host your own Frontiers Research Topic or contribute to one as an author by contacting the Frontiers Editorial Office: frontiersin.org/about/contact

TENDON STRUCTURE-FUNCTION RELATIONSHIP IN HEALTH, AGEING AND INJURY

Topic Editors:
Huub Maas, Vrije Universiteit Amsterdam, Netherlands
Toni Arndt, Swedish School of Sport and Health Sciences, Sweden
Jason Franz, University of North Carolina at Chapel Hill, United States

Citation: Maas, H., Arndt, T., Franz, J., eds. (2021). Tendon Structure-Function Relationship in Health, Ageing and Injury. Lausanne: Frontiers Media SA.
doi: 10.3389/978-2-88971-163-5

Table of Contents

frontiers in Sports and Active Living

EDITORIAL
published: 18 June 2021
doi: 10.3389/fspor.2021.701815

Editorial: Tendon Structure-Function Relationship in Health, Ageing, and Injury

Huub Maas[1]*, *Toni Arndt*[2] *and Jason R. Franz*[3]

[1] Department of Human Movement Sciences, Faculty of Behavioural and Movement Sciences, Vrije University Amsterdam, Amsterdam Movement Sciences, Amsterdam, Netherlands, [2] Swedish School of Sport and Health Sciences, Stockholm, Sweden, [3] University of North Carolina at Chapel Hill and North Carolina State University, Chapel Hill, NC, United States

Keywords: subtendon, non-uniform deformation, Achilles tendon, ultrasound, aging, skeletal muscle

Editorial on the Research Topic

Tendon Structure-Function Relationship in Health, Ageing, and Injury

OPEN ACCESS

Edited by:
Jaap Van Dieen,
Vrije Universiteit Amsterdam, Netherlands

Reviewed by:
Taija Finni,
University of Jyväskylä, Finland
Falk Mersmann,
Humboldt University of Berlin, Germany
Gaspar Epro,
London South Bank University, United Kingdom

***Correspondence:**
Huub Maas
h.maas@vu.nl

Specialty section:
This article was submitted to Biomechanics and Control of Human Movement, a section of the journal Frontiers in Sports and Active Living

Received: *28 April 2021*
Accepted: *25 May 2021*
Published: *18 June 2021*

Citation:
Maas H, Arndt T and Franz JR (2021) Editorial: Tendon Structure-Function Relationship in Health, Ageing, and Injury. Front. Sports Act. Living 3:701815. doi: 10.3389/fspor.2021.701815

Tendons connect muscle fibers to the skeleton and, thereby, serve as transmitters of muscle force. Through their viscoelastic properties, tendons can store and release energy during movement contributing to the performance of motor tasks including locomotion. In contrast to the representation of tendons in textbooks and models of the musculoskeletal system, tendons are not simple viscoelastic bands, but are intricate multi-stranded structures. The objective of this Research Topic was to bring together studies aimed at improving our understanding of the tendon structure-(dys)function relationship in health and disease, with a particular interest in tendons linked to multiple muscles. All but one (Audenaert et al.) of the contributions investigated the Achilles tendon (AT), which is contiguous with the soleus and lateral and medial gastrocnemius muscles. Several other tendons arise from multiple muscles, such as the patellar tendon, and would be equally interesting to investigate.

Using a simulation approach, enhanced lengthening of the M. Psoas major tendon was found to be related to a rotational variant in human femoral morphology (Audenaert et al.). The influence of the skeletal system on AT mechanical properties was also indicated as a factor explaining the lack of tendon adaptation to mechanical loading during growth in a guinea fowl model (Katugam et al.). These studies exemplify the importance of assessing tendon behavior and adaptation within an integrated framework, such as described by Pizzolato et al.. Ultrasound imaging has been frequently used to study the differences in displacement of the deep and superficial portions of the AT (e.g., Arndt et al., 2012; Slane and Thelen, 2014). Internal tendon tissue displacements were more uniform when an ankle foot orthosis was applied and when the range of motion was reduced (Froberg et al.). A simulation study also reported that the amount of sliding between subtendons was task specific (Handsfield et al.). They further found effects of subtendon twisting and connectivity between subtendons. Tendon tissue displacements were found to be less uniform when subtendons were substantially twisted (Knaus and Blemker). Important for the ultrasound-based assessment of non-uniform displacements, a twisted morphology of the AT was also found to result in errors when estimating local strains. Regarding the connectivity between subtendons, clear evidence of force transmission via the inter-subtendon matrix was provided for rat AT (Gains et al.). Previous studies have demonstrated effects of aging on the mechanical properties of tendon (Sprague et al., 2020), its matrix (Thorpe et al., 2015) and non-uniformity of tendon tissue displacements (Franz and Thelen, 2015). In this Research Topic, it was shown that the structure-function relationship between the AT and the triceps surae muscles is disrupted in older adults (Knaus et al.). Using shear wave tensiometry to assess AT forces, differential effects of age on work

performed by the soleus and gastrocnemius were observed (Ebrahimi et al.). While this method does not allow assessment of forces of each of the subtendons, such effects of age may also be related to the changes in mechanical independence between subtendons.

It is evident from the articles in this topic that the notion of subtendons in the human Achilles tendon, as introduced recently (Handsfield et al., 2016), has become relatively accepted terminology in the field of biomechanics, including some of the editors' own work. Nevertheless, the editors of this topic feel called to provide a note of caution concerning any definitive determination about the division of the human AT into subtendons and their relative independence. Studies on subtendons in the rat AT convincingly demonstrate that these are at least not purely independent structures (e.g., Finni et al., 2018). Previous studies and those presented in this Research Topic are providing solid evidence that behavior, in particular internal tendon tissue displacements, differs across separate regions of the tendon and that this correlates in anatomically consistent ways with individual muscle length changes. An important question raised is whether the relatively clear identification of inter-subtendon regions in rat and rabbit AT (Gains et al.; Handsfield et al.) can also be applied to human AT. Although our interpretations often consider the possibility, it is not yet clear that these regions can be specifically attributed to individual muscles—a prerequisite to the premise upon which subtendons are based. Anatomic human cadaver analysis shows that the collagenous material of the distal AT cannot be easily dissected into subtendons (Arndt et al., 1997) without considerable force. Recent evidence from ultrasound speckle tracking studies shows that adjacent fascicles within the tendon can slide relative to each other (e.g., Arndt et al., 2012; Slane and Thelen, 2014). However, such sliding appears to be a phenomenon occurring throughout the tendon's cross-sectional area. More sophisticated imaging or analysis routines (see for example Handsfield et al.) are warranted to investigate the extent to which boundary regions exist within longitudinal tendon tissue displacement fields that could signal the presence or refute the premise of individual subtendons, *per se*. We therefore suggest that caution be exercised and the state of the science be acknowledged when using the term subtendon to investigate and/or describe internal human AT tissue function.

Sliding within the AT may be necessary to allow muscles crossing one (soleus) or two joints (gastrocnemius) with distinct activation patterns (Moritani et al., 1991) to function normally, and lack of sliding may be a sign of malfunction (Franz and Thelen, 2015; Froberg et al., 2017). For rat AT, it was described that while the elastic interfascicular matrix allows relative sliding of the tendon fascicles (Finni et al., 2018), it can also bear considerable loads (see also Gains et al.). Non-uniform fascicle sliding may facilitate protective mechanisms for tendon sections subjected to greater strain, thus preventing excessive forces in the relevant fascicles. Consequently, tendon organization may provide an inbuilt protective mechanism against tendon injuries (Maas and Finni, 2018) and lack of sliding may be a risk factor for injury or disease (Franz and Thelen, 2015; Froberg et al., 2017). Ultimately, research on tendons arising from multiple muscles should continue to elucidate the role of maintaining non-uniform tendon tissue displacements and its implications for injury, pathology, aging, and rehabilitation.

AUTHOR CONTRIBUTIONS

All authors listed have made a substantial, direct and intellectual contribution to the work, and approved it for publication.

REFERENCES

Arndt, A., Bengtsson, A. S., Peolsson, M., Thorstensson, A., and Movin, T. (2012). Non-uniform displacement within the Achilles tendon during passive ankle joint motion. *Knee Surg. Sports Traumatol. Arthrosc.* 20, 1868–1874. doi: 10.1007/s00167-011-1801-9

Arndt, A., Notermans, H.-P., Koebke, J., and Bruggemann, G. P. (1997). Mazeration der menschlichen Achillessehne zur Betrachtung der kollagenen Fasern. *Der. Präparator.* 43, 63–70.

Finni, T., Bernabei, M., Baan, G. C., Noort, W., Tijs, C., and Maas, H. (2018). Non-uniform displacement and strain between the soleus and gastrocnemius subtendons of rat Achilles tendon. *Scand. J. Med. Sci. Sports* 28, 1009–1017. doi: 10.1111/sms.13001

Franz, J. R., and Thelen, D. G. (2015). Depth-dependent variations in Achilles tendon deformations with age are associated with reduced plantarflexor performance during walking. *J. Appl. Physiol.* 119, 242–249. doi: 10.1152/japplphysiol.00114.2015

Froberg, A., Cisse, A. S., Larsson, M., Martensson, M., Peolsson, M., Movin, T., et al. (2017). Altered patterns of displacement within the Achilles tendon following surgical repair. *Knee Surg. Sports Traumatol. Arthrosc.* 25, 1857–1865. doi: 10.1007/s00167-016-4394-5

Handsfield, G. G., Slane, L. C., and Screen, H. R. (2016). Nomenclature of the tendon hierarchy: an overview of inconsistent terminology and a proposed size-based naming scheme with terminology for multi-muscle tendons. *J. Biomech.* 49, 3122–3124. doi: 10.1016/j.jbiomech.2016.06.028

Maas, H., and Finni, T. (2018). Mechanical coupling between muscle-tendon units reduces peak stresses. *Exerc. Sport Sci. Rev.* 46, 26–33. doi: 10.1249/JES.0000000000000132

Moritani, T., Oddsson, L., and Thorstensson, A. (1991). Phase-dependent preferential activation of the soleus and gastrocnemius muscles during hopping in humans. *J. Electromyogr. Kinesiol.* 1, 34–40. doi: 10.1016/1050-6411(91)90024-Y

Slane, L. C., and Thelen, D. G. (2014). Non-uniform displacements within the Achilles tendon observed during passive and eccentric loading. *J. Biomech.* 47, 2831–2835. doi: 10.1016/j.jbiomech.2014.07.032

Sprague, A. L., Awokuse, D., Pohlig, R. T., Cortes, D. H., and Silbernagel, K. G. (2020). Relationship between mechanical properties (shear modulus and viscosity), age, and sex in uninjured Achilles tendons. *Transl. Sports Med.* 3, 321–327. doi: 10.1002/tsm2.148

Thorpe, C. T., Godinho, M. S., Riley, G. P., Birch, H. L., Clegg, P. D., and Screen, H. R. (2015). The interfascicular matrix enables fascicle sliding and recovery in tendon, and behaves more elastically in energy storing tendons. *J. Mech. Behav. Biomed. Mater.* 52, 85–94. doi: 10.1016/j.jmbbm.2015.04.009

Conflict of Interest: The authors declare that the research was conducted in the absence of any commercial or financial relationships that could be construed as a potential conflict of interest.

frontiers in Sports and Active Living

ORIGINAL RESEARCH
published: 17 March 2020
doi: 10.3389/fspor.2020.00016

The Effect of Ankle Foot Orthosis' Design and Degree of Dorsiflexion on Achilles Tendon Biomechanics—Tendon Displacement, Lower Leg Muscle Activation, and Plantar Pressure During Walking

Åsa Fröberg[1]*, *Mattias Mårtensson*[2] and *Anton Arndt*[1,3]

[1] Division of Orthopaedics and Biotechnology, Department of Clinical Sciences, Intervention and Technology (Clintec), Karolinska Institute, Stockholm, Sweden, [2] KTH, Biomedical Engineering and Health Systems, Stockholm, Sweden, [3] The Swedish School of Sport and Health Sciences (GIH), Stockholm, Sweden

OPEN ACCESS

Edited by:
Kiros Karamanidis,
London South Bank University,
United Kingdom

Reviewed by:
Falk Mersmann,
Humboldt University of Berlin, Germany
Jim Richards,
University of Central Lancashire,
United Kingdom

***Correspondence:**
Åsa Fröberg
asa.froberg@ki.se

Specialty section:
This article was submitted to Biomechanics and Control of Human Movement, a section of the journal Frontiers in Sports and Active Living

Received: 26 September 2019
Accepted: 14 February 2020
Published: 17 March 2020

Citation:
Fröberg Å, Mårtensson M and Arndt A (2020) The Effect of Ankle Foot Orthosis' Design and Degree of Dorsiflexion on Achilles Tendon Biomechanics—Tendon Displacement, Lower Leg Muscle Activation, and Plantar Pressure During Walking. Front. Sports Act. Living 2:16. doi: 10.3389/fspor.2020.00016

Background: Following an Achilles tendon rupture, ankle foot orthoses (AFO) of different designs are used to protect the healing tendon. They are generally designed to protect against re-rupture by preventing undesired dorsiflexion and to prevent elongation by achieving plantarflexion in the ankle. There is limited knowledge of the biomechanical effects of different AFO designs and ankle angles on the tendon and lower leg muscles.

Hypothesis: The hypothesis was that non-uniform displacement in the Achilles tendon, lower leg muscle activity, and plantar pressure distribution would be affected differently in different designs of AFO and by varying the degree of dorsiflexion limitation.

Study Design: Controlled laboratory study.

Methods: Ultrasound of the Achilles tendon, EMG of the lower leg muscles and plantar pressure distribution were recorded in 16 healthy subjects during walking on a treadmill unbraced and wearing three designs of AFO. Ultrasound speckle tracking was used to estimate motion within the tendon. The tested AFO designs were a rigid AFO and a dorsal brace used together with wedges and an AFO with an adjustable ankle angle restricting dorsiflexion to various degrees.

Results: There were no significant differences in non-uniform tendon displacement or muscle activity between the different designs of AFO. For the rigid AFO and the adjustable AFO there was a significant reduction in non-uniform displacement within the tendon and soleus muscle activity as restriction in dorsiflexion increased.

Conclusion: The degree of dorsiflexion allowed within an AFO had greater effects on Achilles tendon displacement patterns and muscle activity in the calf than differences in AFO design. AFO settings that allowed ankle dorsiflexion to neutral resulted in displacement patterns in the Achilles tendon and muscle activity in the lower leg which were close to those observed during unbraced walking.

Keywords: Achilles tendon, ankle foot orthoses, brace, speckle tracking, deformation, EMG, plantar pressure

INTRODUCTION

In previous studies of Achilles tendon rupture, short leg casts and ankle foot orthoses (AFO) were used during rehabilitation to protect the healing tendon (Mortensen et al., 1999; Maffulli et al., 2003; Kangas et al., 2007; Nilsson-Helander et al., 2010; Willits et al., 2010; Silbernagel et al., 2012; Schepull and Aspenberg, 2013). In these studies casts and different designs of AFO were used in various combinations, which makes it difficult to get a clear idea about whether some AFO designs are more suitable than others. Different types of AFO used in clinical practice are generally designed to protect against re-rupture by preventing undesired dorsiflexion and to prevent elongation by achieving plantarflexion (Kearney et al., 2011). One design has a rigid outer shell which restricts both dorsiflexion and plantarflexion and the desired ankle angle is achieved by adding heel wedges (Willits et al., 2010; Olsson et al., 2013). Another design has an adjustable foot plate which can be set at different angles allowing a limited range of motion (Nilsson-Helander et al., 2010; Twaddle and Poon, 2013). Thirdly, dorsal braces are used to restrict undesired dorsiflexion while plantarflexion is allowed (Maffulli et al., 2003; Kangas et al., 2007). Previous studies have shown differences in muscle activity in the gastrocnemius and the soleus during walking with a rigid AFO design (Akizuki et al., 2001; Kadel et al., 2004) compared to an adjustable AFO design (Fröberg et al., 2009). Ankle moments as calculated from plantar pressure measurements have been shown to decrease when walking in a rigid AFO (Sandberg et al., 2015), whereas force in the Achilles tendon has been shown to increase when using an adjustable AFO with increasing restriction of dorsiflexion (Fröberg et al., 2009). In these studies no imaging of the Achilles tendon was used.

The Achilles tendon transmits forces from the medial and lateral gastrocnemius and soleus which can be individually activated (Bojsen-Moller and Magnusson, 2015). Ultrasound speckle tracking studies of the Achilles tendon have shown that displacement within the Achilles tendon is non-uniform during walking and that non-uniformity increases with increasing walking speed (Franz et al., 2015). The non-uniform displacement pattern observed in the Achilles tendon is thought to reflect gliding between tendon fascicles (Haraldsson et al., 2008; Arndt et al., 2012; Slane and Thelen, 2014; Franz et al., 2015) and it has been shown to be disturbed in previously ruptured tendons (Fröberg et al., 2017). Fascicle gliding is thought to be important in optimizing force transmission during motion, as the level of gastrocnemius and soleus activity and the angles of the knee and ankle varies (Arndt et al., 2012; Bojsen-Moller and Magnusson, 2015).

The aim was to investigate how non-uniform displacement patterns within the Achilles tendon, muscle activity in the lower leg, and plantar pressure distribution in healthy subjects is affected by the use of three different designs of AFO and by allowing varying degrees of dorsiflexion during walking. The hypothesis was that non-uniform displacement in the Achilles tendon, lower leg muscle activity, and plantar pressure distribution would be affected differently in different designs of AFO and by varying the degree of dorsiflexion limitation. It was hypothesized that non-uniform displacement would be (1) lower in the AFO conditions compared to unbraced walking and (2) lower in AFO settings restricting dorsiflexion.

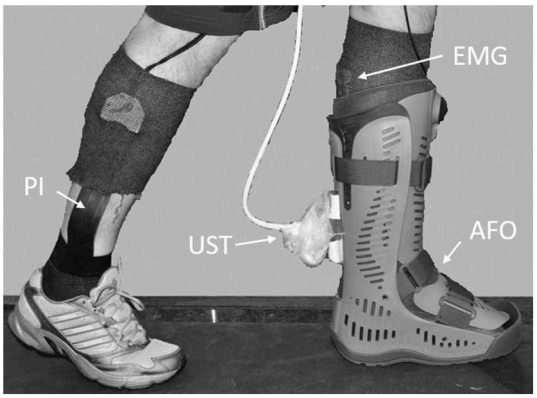

FIGURE 1 | Experimental set up. EMG, emg electrodes; UST, ultrasound transducer; PI, pressure insole; AFO, rigid ankle foot orthosis.

METHODS

Ultrasound of the Achilles tendon, EMG of the lower leg muscles and plantar pressure distribution were recorded in 16 healthy subjects during walking on a treadmill without an AFO and wearing three designs of AFO (**Figure 1**). Subjects were eight males (mean ± standard deviation (SD) age: 45 ± 3 years, height: 183 ± 7 cm, body mass: 82 ± 13 kg) and eight females (mean ± SD age: 44 ± 3 years, height: 170 ± 5 cm, body mass: 66 ± 10 kg). The Regional Ethics Committee approved the study (2016/1970-31) and subjects gave written informed consent.

AFO Conditions

Three different designs of AFO were tested during walking on a treadmill at 2 km/h (**Figure 2**). The first design was an AFO with a rigid outer shell and a rocker bottom sole (Rebound Air Walker, Össur, Reykjavik, Iceland) which restricted both dorsiflexion and plantarflexion. It was tested using zero, two or three 10 mm heel wedges. The second design was an AFO with an adjustable rocker bottom foot plate (ROM Walker, DJO Global, Vista, USA) which was tested using three different settings with dorsiflexion limited to 10° dorsiflexion, 10° plantarflexion or 30° plantarflexion respectively, while plantarflexion was unrestricted. Thirdly, a dorsal brace was made for each subject using 10 layers of casting tape (Scotchcast Plus, 3M Health Care, St Paul, USA) with the ankle in neutral position. The brace was fixed to the leg using cohesive bandage (Mollelast haft, Lohmann & Rauscher International GmbH & Co, Rengsdorf, Germany) and thus restricted dorsiflexion to neutral. It was used together with regular running shoes and was tested with no heel wedge and with a 10 mm wedge in the shoe. As the brace was worn inside the shoes, there was a soft resistance to plantarflexion. All subjects also walked and ran in stocking feet (unbraced) at 2 and 10 km/h, respectively. A slow walking speed (2 km/h) was chosen to facilitate a relaxed walking pattern at all AFO conditions.

FIGURE 2 | The three different designs of ankle foot orthoses that were tested. **(A)** rigid AFO, **(B)** adjustable AFO, and **(C)** dorsal brace.

The test order was randomized. The right foot was tested in all subjects. For the AFO conditions subjects wore a running shoe with a 10 mm wedge on the opposite foot to compensate for leg length difference. After change of condition, subjects were allowed to get accustomed to the new AFO before recordings started. The AFO were adjusted so that the ultrasound probe could be placed on the Achilles tendon. For the rigid AFO a 17 $\times$ 5.5 cm opening was cut in the plastic shell over the Achilles tendon, but the compressive air bladders were left intact. For the adjustable AFO, an opening was cut in the soft material covering the Achilles tendon and the distal Velcro strap was moved a few cm proximally.

Synchronization and Electromyography

In order to synchronize EMG data collection, plantar pressure measurement and ultrasound acquisition, a data collection configuration was created using Spike2 software (7.09a $\times$86, Cambridge Electronic Design, Cambridge, UK). At start of data collection the data acquisition unit (Micro 1401, Cambridge Electronic Design) generated a square wave signal that was fed into the ultrasound machine and a trigger signal that was sent to the plantar pressure measurement software (25.3.6, Pedar-x online, Novel GmbH, Munich, Germany). EMG activity was measured in the medial and lateral gastrocnemius, the soleus and in the tibialis anterior using adhesive bipolar surface electrodes (BlueSensorN, Ambu, Ballerup, Denmark) with an inter-electrode distance of 20 mm. The electrodes and cables were further fixed using compressive stockings before the AFO were fitted (**Figure 1**). Data was collected at 3,000 Hz and sent by wireless transmission to a receiver box (TeleMyo 2400R G, Noraxon, Scottsdale, USA), then converted to digital in the data acquisition unit and saved on a PC. Three 15 s recordings were made for each walking condition. EMG data was exported as text files and imported into MATLAB (R2014a, MathWorks Inc., Natick, USA). EMG raw data and corresponding ultrasound images were visually inspected and ten strides with good quality EMG and ultrasound were chosen for each walking condition and subject, respectively. A stride was defined as heelstrike to heelstrike and the time for heelstrike for the chosen strides were identified in the plantar pressure data. EMG raw data was moved to zero, rectified, smoothed using 200 point adjacent averaging and normalized to mean peak EMG of unbraced running at 10 km/h. Peak EMG values were identified on the resulting curves and mean and SD of the peak values were calculated. Mean EMG curves for all strides and all subjects were calculated for each muscle and walking condition.

Plantar Pressure

Each subject was fitted with a pair of pressure measurement insoles (Pedar-xf-16/R system, Novel GmbH) of appropriate size which were held in place by compressive stockings inside the AFO. For the unbraced conditions an extra pair of compressive stockings was worn. Between each change in walking condition the insoles were calibrated so that the unloaded foot resembled zero pressure. Three 15 s recordings at a sampling frequency of 100 Hz were made for each walking condition. Data were saved and then exported as asc-files into MATLAB for further analysis. The time for heelstrikes for the right foot were identified from the plantar pressure data. For further analysis of plantar pressure the foot was divided into three regions according to recommendations (Barnett, 1998), where the forefoot equaled the distal 40% of the total length, midfoot equaled the middle 30% and rearfoot equaled the proximal 30%. Forefoot and rearfoot pressure were then calculated as a mean of the pressure sensors in each region, respectively. To allow for comparisons between subjects, pressure data was normalized and expressed as a percentage of mean peak pressure during unbraced walking at 2 km/h. Peak forefoot and rearfoot pressures for the ten strides previously chosen for each subject and walking condition were identified and averaged. Strides with data artifacts were removed. Mean forefoot pressure curves were calculated for all subjects and walking conditions and then used to identify toe off time for each walking condition.

Ultrasound

Ultrasound speckle tracking is a method developed for measuring deformation in tissue. Speckle tracking algorithms use the speckle pattern present in all ultrasound images to track deformation

between frames in ultrasound sequences (Arndt et al., 2012; Slane and Thelen, 2014; Franz et al., 2015; Fröberg et al., 2017). For ultrasound imaging, a 9L linear array transducer (GE Healthcare, Horten, Norway) connected to a Vivid-q ultrasound machine (GE Healthcare) was fixed over the Achilles tendon using a fixation device that supported the probe to prevent it from swaying. The transducer was placed so that the posterior process of the distal tibia was visible in the distal end of all images and it remained fixed in the same position for all walking conditions. For each walking condition, three 15 s B-mode ultrasound acquisitions (10 MHz, 40 FPS, depth 3 cm) were made using a standoff pad. The time of the synchronization signal visible in the ultrasound image was noted for each recording using EchoPAC (110.1.2, GE Healthcare). Motion files were converted to HDF format and imported into MATLAB. Two dimensional motion estimation was performed with a MATLAB speckle tracking algorithm which has previously been validated (Fröberg et al., 2017), using a kernel size of 52λ (laterally) × 25λ (axially), 80% kernel overlap and normalizes cross correlation as similarity measure. For each subject the same 10 strides that were previously chosen for EMG and plantar pressure evaluation were analyzed. A 25 mm region of interest (ROI) was placed in the middle of the visible tendon portion and adjusted so that it covered the full thickness of the tendon. Average displacement within the superficial and deep thirds of the ROI was computed. All resulting displacement curves were interpolated to obtain data sets of equal length and then mean curves for superficial and deep displacement for all subjects were computed using MATLAB. Peak displacement during stance phase was defined as displacement during the time from the beginning of dorsiflexion to maximum dorsiflexion as determined from the displacement curves. Minimum and maximum displacement values were identified on all superficial and deep displacement curves for all evaluated strides, and peak displacement was calculated as the difference between the minimum and maximum values. Differential displacement was calculated as the difference in deep and superficial peak displacement. Mean and SD of peak values were calculated for all subjects.

Statistical Analysis

A two-tailed paired *t*-test was performed for pairwise comparison of displacement in the superficial and deep layers of the tendon for all walking conditions using SPSS (Statistics 24, IBM, Armonk, USA). A repeated measures analysis of variance was performed in SPSS to establish if there were any differences in superficial displacement, deep displacement, differential displacement, EMG activity, forefoot pressure, and rearfoot pressure between walking conditions. Two comparisons were made between the different designs of AFO and unbraced walking. Firstly the conditions with least restriction in dorsiflexion (rigid AFO 0 wedges, adjustable AFO 10° dorsiflexion and dorsal brace 0 wedges) were compared amongst themselves and with unbraced walking. Secondly the conditions restricting dorsiflexion most (rigid AFO 3 wedges and adjustable

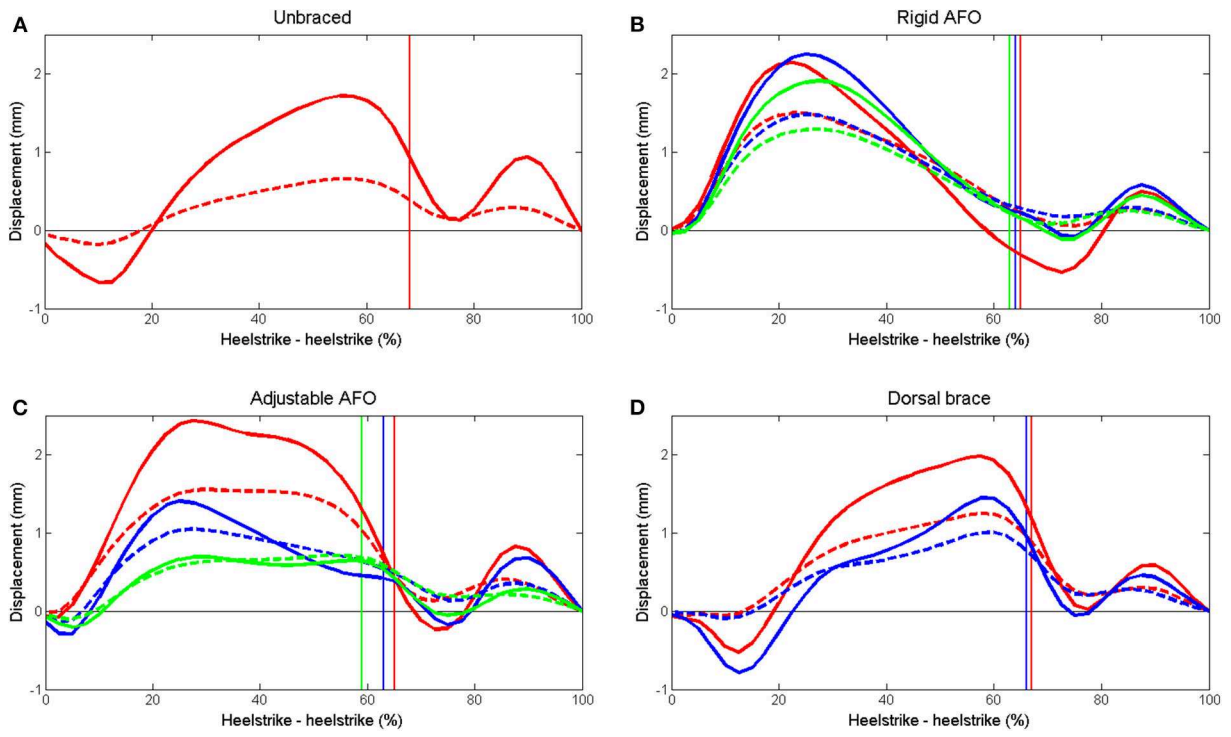

FIGURE 3 | Mean displacement in the superficial (dashed) and deep (solid) layers of the Achilles tendon during walking. **(A)** unbraced walking, **(B)** rigid AFO with 0 wedges (red), 2 wedges (blue) and 3 wedges (green), **(C)** adjustable AFO with ankle dorsiflexion limited to 10° dorsiflexion (red), 10° plantarflexion (blue) and 30° plantarflexion (green), and **(D)** dorsal brace with 0 wedges (red) and 1 wedge (blue). Toe off time is indicated for each setting by a vertical line in the corresponding color.

AFO 30° plantarflexion) were compared amongst themselves and with unbraced walking. The dorsal brace was not included in the second comparison as it did not place the ankle in the same degree of plantarflexion. To test the influence of dorsiflexion range of motion within each AFO design, the different settings within each AFO were compared to each other and to unbraced walking. Mauchly's test of Sphericity was used to test the assumption of sphericity. When the assumption of sphericity was violated the Greenhouse-Geisser correction was used. The Bonferroni correction was used to make pairwise comparisons between condition means for superficial displacement, deep displacement, differential displacement, and EMG activity. Forefoot pressure and rearfoot pressure for all AFO conditions were normalized against mean pressure during unbraced walking, which was set to 100%. Mean forefoot and rearfoot pressure and 95% confidence intervals (CI) were then calculated for all AFO conditions and compared to unbraced walking. If the CI did not include 100%, the difference was considered to be significant.

RESULTS

Mean curves for superficial and deep displacement in the Achilles tendon, EMG for soleus, medial gastrocnemius and tibialis anterior and forefoot pressure for all subjects are shown in **Figures 3–5**. Mean and SD of peak displacement in the Achilles tendon, peak EMG activity of the lower leg muscles and peak plantar pressure are shown in **Table 1**. Mean peak displacement in the deep parts of the tendon was significantly larger than superficial displacement for all walking conditions ($p < 0.001$). There were no significant differences in differential displacement or muscle activity between the rigid AFO 0 wedges, the adjustable AFO 10°dorsiflexion or the dorsal brace 0 wedges or between the rigid AFO 3 wedges and the adjustable AFO 30° plantarflexion.

Rigid AFO

Differential displacement was significantly reduced ($p = 0.03$) from condition rigid AFO 0 wedges to rigid AFO 3 wedges. EMG activity was significantly reduced in the medial ($p = 0.006$) and lateral ($p = 0.042$) gastrocnemius and soleus ($p = 0.006$) from condition rigid AFO 0 wedges to rigid AFO 3 wedges. Forefoot pressure showed a progressive reduction with each extra wedge ($p < 0.014$).

Adjustable AFO

Differential displacement was significantly reduced as range of motion decreased from adjustable AFO set at 10° dorsiflexion to 30° plantarflexion ($p < 0.001$). EMG activity in the soleus showed

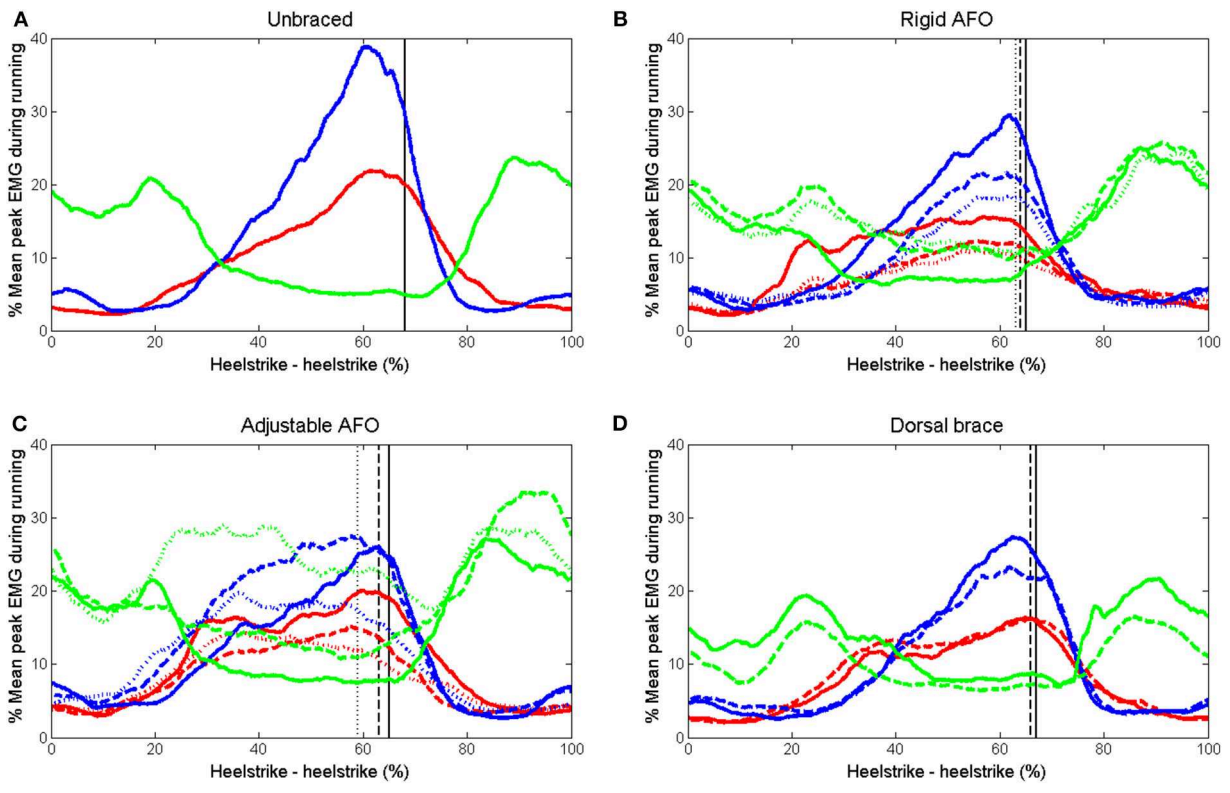

FIGURE 4 | Mean EMG curves for medial gastrocnemius (blue), soleus (red), and tibialis anterior (green) during walking. **(A)** unbraced walking **(B)** rigid AFO with 0 wedges (solid), 2 wedges (dashed), and 3 wedges (dotted). **(C)** adjustable AFO with ankle dorsiflexion limited to 10° dorsiflexion (solid), 10° plantarflexion (dashed), and 30° plantarflexion (dotted) **(D)** dorsal brace with 0 wedges (solid) and 1 wedge (dashed). Toe off time is indicated for each setting by a vertical line with the corresponding line format.

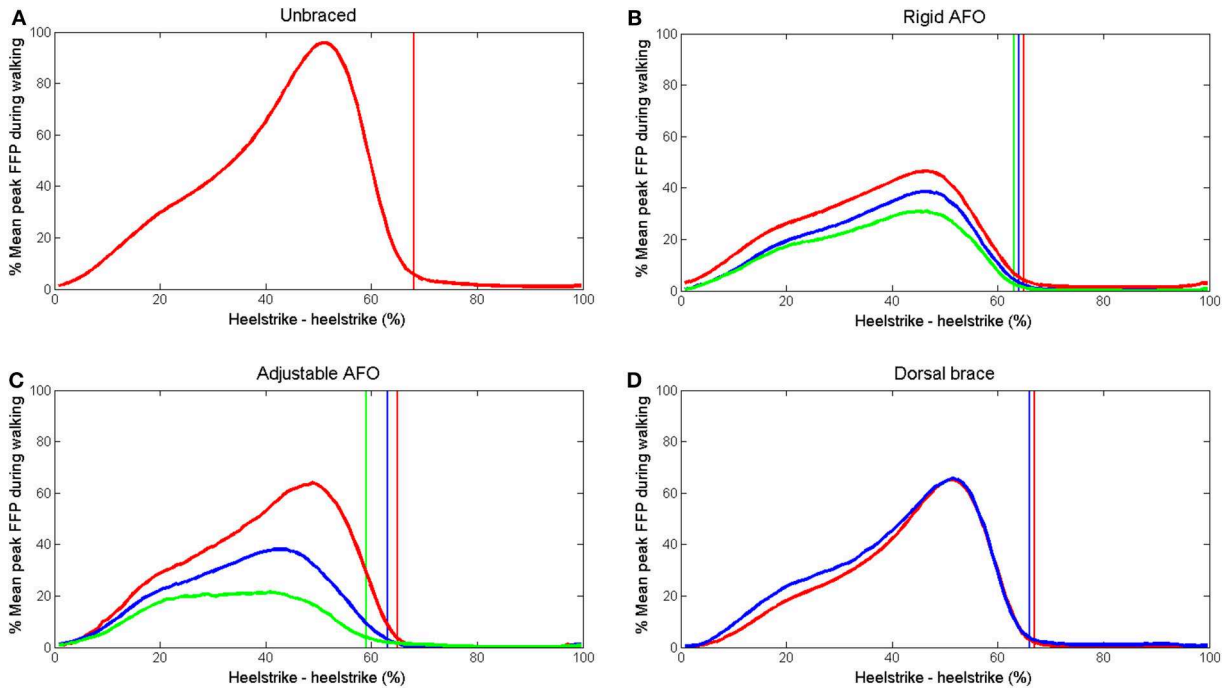

FIGURE 5 | Mean forefoot pressure during walking. **(A)** unbraced walking **(B)** rigid AFO with 0 wedges (red), 2 wedges (blue) and 3 wedges (green). **(C)** adjustable AFO with ankle dorsiflexion limited to 10° dorsiflexion (red), 10° plantarflexion (blue), and 30° plantarflexion (green) **(D)** dorsal brace with 0 wedges (red) and 1 wedge (blue). Toe off time is indicated for each setting by a vertical line in the corresponding color.

a trend to decrease as dorsiflexion limitation increased and there was a significant reduction from condition unbraced walking to adjustable AFO setting 30° plantarflexion ($p = 0.024$). Medial gastrocnemius activity varied between settings. Tibialis anterior activity significantly increased from condition unbraced walking to adjustable AFO set at 10° plantarflexion ($p = 0.03$) or 30° plantarflexion ($p = 0.008$).

Dorsal Brace

During walking with the dorsal brace with or without wedge, differential displacement did not differ significantly compared to unbraced walking. Medial gastrocnemius and soleus EMG activity significantly decreased when the dorsal brace was used compared to unbraced walking ($p < 0.027$).

DISCUSSION

A non-uniform displacement pattern with greater displacement in deep compared to superficial parts of the Achilles tendon was present for all walking conditions (**Figure 3**). When the rigid and the adjustable AFO were used, tendon displacement became more uniform, EMG activity in the soleus decreased and forefoot pressure decreased as the ankle was placed in gradually increasing plantarflexion and less dorsiflexion was permitted (**Table 1**). No significant differences in differential displacement or lower leg muscle activity were found between the different designs of AFO for either of the compared conditions (**Table 1**).

Peak superficial Achilles tendon displacement was significantly larger for all AFO conditions compared to unbraced walking, except for the adjustable walker set to 30° plantarflexion (**Table 1**). The same tendency was observed for deep displacement although this was not significant. As the AFO are designed to limit ankle range of motion, this was unexpected. It was subjectively observed that participants altered their walking patterns between the different walking conditions, but no motion analysis was performed to verify this. For the rigid and the adjustable AFO, displacement appeared to increase more rapidly from ∼5–25% of stride with an earlier peak displacement compared to unbraced walking and the dorsal brace condition (**Figure 3**). The initial negative displacement seen in the unbraced and dorsal brace conditions (**Figure 3**) did not occur in these AFO which may indicate that no initial plantarflexion occured directly after heelstrike. The rigid and the adjustable AFO both have a rocker bottom sole which may affect this phase of stance. Such gait modifications are at present not fully understood and their effect upon tendon displacement remains to be investigated.

Despite differences in their design, no differences in the non-uniform displacement pattern of the Achilles tendon were found between the AFO designs for either of the compared conditions (**Table 1**). AFO are thought to protect the Achilles tendon by reducing passive tension by restricting dorsiflexion and by reducing active loading by decreasing muscle activity (Akizuki et al., 2001; Kearney et al., 2011). For a rigid AFO, ankle plantarflexion torque during walking estimated from EMG

TABLE 1 | Mean and SD of peak displacement in the Achilles tendon, peak EMG activity in the soleus, medial, and lateral gastrocnemius and tibialis anterior and peak plantar pressure.

Condition	Superficial disp*	Deep disp*	Δ disp	EMG med gast	EMG lat gast	EMG sol	EMG tib ant	Forefoot P		Rearfoot P	
	Mean ± SD (mm)	Mean ± SD (mm)	Mean ± SD (mm)	Mean ± SD (%)	Mean ± SD (%)	Mean ± SD (%)	Mean ± SD (%)	Mean ± SD (%)	95% CI	Mean ± SD (%)	95% CI
Unbraced	1.1 ± 0.4 *rAFO 0,2 & 3 wdg, aAFO 10df & 10pf, db 0 & 1wdg*	3.2 ± 0.8 *aAFO 30 pf*	2.2 ± 0.7 *aAFO 30pf*	58 ± 24 *rAFO 0,2 & 3wdg, aAFO 10pf & 30pf, db*	27 ± 12 *rAFO 0,2 & 3wdg*	31 ± 7 *rAFO 2 & 3wdg, aAFO 30pf, db 0wdg*	38 ± 18 *aAFO 10pf, aAFO 30pf*	100	–	100	–
rAFO 0 wdg	1.9 ± 0.7 *ub*	3.7 ± 0.7	1.7 ± 0.7 *rAFO 3wdg*	43 ± 18 *ub, rAFO 2wdg, rAFO 3wdg*	18 ± 11 *ub, rAFO 3wdg*	29 ± 13 *rAFO 2wdg, rAFO 3wdg*	41 ± 24	48 ± 17 *rAFO 2wdg, rAFO 3wdg*	39–58	76 ± 15 *rAFO 2wdg, rAFO 3wdg*	68–84
rAFO 2 wdg	1.7 ± 0.6 *ub*	3.3 ± 0.9	1.5 ± 0.8	34 ± 14 *ub, rAFO 0wdg*	14 ± 9 *ub*	19 ± 5 *ub, rAFO 0wdg*	43 ± 23	42 ± 19 *rAFO 0 wdg, rAFO 3wdg*	31–52	99 ± 21 *rAFO 0wgd*	88–110
rAFO 3 wdg	1.7 ± 0.6 *ub*	3.1 ± 0.7	1.4 ± 0.7 *rAFO 0wdg*	31 ± 14 *ub, rAFO 0wdg*	14 ± 8 *ub, rAFO 0wdg*	18 ± 7 *ub, rAFO 0wdg*	45 ± 28	34 ± 18 *rAFO 0wdg, rAFO 2wdg*	24–43	103 ± 21 *rAFO 0wgd*	92–114
aAFO 10°df	2.1 ± 0.7 *ub, aAFO 10pf & 30pf*	4.1 ± 0.6 *aAFO 10pf, aAFO 30pf*	2.0 ± 0.7 *aAFO 30pf*	41 ± 16 *ub*	23 ± 13	31 ± 15	46 ± 27	69 ± 22 *aAFO 10pf, aAFO 30pf*	57–82	73 ± 15	65–82
aAFO 10°pf	1.6 ± 0.7 *ub,aAFO 10df*	3.1 ± 0.8 *aAFO 10df, aAFO 30pf*	1.6 ± 0.7	47 ± 17 *aAFO 30pf*	26 ± 16	24 ± 9	52 ± 28 *ub*	45 ± 21 *aAFO 10df, aAFO 30pf*	33–57	82 ± 26	68–96
aAFO 30°pf	1.2 ± 0.5 *aAFO 10df*	2.2 ± 0.5 *ub, aAFO 10df, aAFO 10pf*	1.1 ± 0.5 *ub,aAFO 10df*	31 ± 16 *ub, aAFO 10pf*	23 ± 13	23 ± 10 *ub*	55 ± 28 *ub*	27 ± 18 *aAFO 10df, aAFO 10pf*	17–36	85 ± 27	70–100
DB 0 wdg	1.7 ± 0.7 *ub*	3.7 ± 0.8	2.0 ± 0.6	42 ± 20 *ub*	21 ± 16	24 ± 10 *ub*	44 ± 45	65 ± 23 *DB 1wdg*	53–77	77 ± 23 *DB 1wdg*	65–89
DB 1wdg	1.5 ± 0.6 *ub*	3.4 ± 0.8	1.9 ± 0.5	37 ± 17 *ub*	19 ± 14	24 ± 12	32 ± 16	72 ± 26 *DB 0wdg*	58–86	88 ± 30 *DB 0wdg*	72–104

*EMG is normalized to mean peak EMG during unbraced running at 10 km/h. Statistical differences between conditions are shown in italics ($p < 0.05$). disp, displacement; Δ disp, differential displacement; P, pressure, normalized to pressure during unbraced walking at 2 km/h. ub, unbraced; rAFO, rigid AFO; aAFO, adjustable AFO; db, dorsal brace; wdg, wedges; df, dorsiflexion; pf, plantarflexion. *Mean peak displacement in the deep parts of the tendon was significantly larger than in superficial parts for all walking conditions ($p < 0.001$).*

has previously been shown to decrease with the addition of heel wedges (Akizuki et al., 2001). In the adjustable AFO dorsiflexion was limited by setting the foot plate in different ankle angles and when it was set in plantarflexion there was no support under the heel. For the most plantarflexed positions it was difficult to achieve a relaxed walking pattern and participants needed to support their weight entirely on the forefoot. Force in the Achilles tendon during walking has previously been shown to increase compared to unbraced walking in the most plantarflexed postions for this AFO design (Fröberg et al., 2009). Therefore, some difference in tendon displacement patterns was expected between these AFO designs. Instead the degree of dorsiflexion limitation within each AFO design seemed to affect tendon displacement patterns more. For the rigid and the adjustable AFO differential displacement was significantly reduced as limitation in dorsiflexion increased (**Table 1**). The dorsal brace was tested with or without a single 10 mm wedge and the difference between the two conditions was perhaps too small for this effect to be seen.

There were no significant differences in gastrocnemius, soleus, or tibialis anterior activity between the different AFO designs, but differences were observed between different degrees of dorsiflexion limitation. EMG activity in the medial and lateral gastrocnemius and soleus was reduced compared to unbraced walking when the rigid AFO was used, and the reduction was more pronounced as dorsiflexion was limited with added wedges (**Table 1**). This finding is similar to previous results shown for this AFO design (Akizuki et al., 2001; Kadel et al., 2004). When the adjustable AFO was used, EMG activity in soleus showed a tendency to decrease as dorsiflexion limitation gradually increased (**Table 1**). In contrast, gastrocnemius activity was higher when the ankle was placed in 10° plantarflexion than for 10° dorsiflexion (**Table 1**). This has been shown previously for this AFO design (Fröberg et al., 2009). As mentioned above, when this AFO is set in 30° plantarflexion participants had to support on their toes and bend their knees to avoid limping. Muscle activity in the soleus and the gastrocnemius during isometric plantarflexion has previously been shown to vary depending on the knee angle (Arndt et al., 1998). Differences in muscle activity in the soleus and the gastrocnemius between the different AFO designs might be explained by differences in the walking patterns. Muscle activity in the tibialis anterior increased compared to unbraced walking when the adjustable AFO was set to 10° plantarflexion or beyond. This may have been due to the AFO design with the plantarflexed foot plate and an increased effort to dorsiflex the foot during swing phase to avoid stumbling.

During walking the Achilles tendon produces plantarflexion moment around the ankle and the forefoot is used for push-off against the ground. Therefore the amount of forefoot pressure produced during walking has been suggested as an important parameter to evaluate regarding Achilles tendon loading (Kearney et al., 2011). During barefoot walking, differential displacement has previously been shown to increase with higher walking speeds (Franz et al., 2015) where push-off is expected to be more forceful. Forefoot pressure was reduced compared to unbraced walking for all AFO conditions. For the rigid AFO and the adjustable AFO the reduction in forefoot pressure became more pronounced as the ankle was placed in successively more plantarflexion and less dorsiflexion was allowed in conjunction with reduced non-uniform displacement. This result is similar to the results reported in a previous study, where forefoot pressure was also shown to correlate to the degree of dorsiflexion allowed within an AFO (Kearney et al., 2011).

In rat studies of Achilles tendon ruptures it has been shown that, weight bearing on the injured limb and exercise on a treadmill resulted in earlier formation of mature repair tissue with thicker and longitudinally organized collagen (Bring et al., 2007) and tendons with higher peak force and stiffness (Andersson et al., 2009; Eliasson et al., 2012), than if the limbs were unloaded or immobilized in a cast. Continuous activity without immobilization also seemed to be more effective than immobilization and intermittent training in stimulating healing (Andersson et al., 2009). It is not known how these findings translate into humans, but it indicates that loading which mimics unbraced walking may be a good stimulus for healing. The AFO settings with least restriction of dorsiflexion resulted in non-uniform tendon deformation patterns that most resembled those during unbraced walking. Neuromuscular electrical stimulation or exercise has been shown to partly counteract reduction in muscle mass and strength which result from limb immobilization (Alkner and Tesch, 2004; Dirks et al., 2018). Further it has been demonstrated in animal models that calf muscles undergo more atrophy if they are immobilized in shortened positions compared to lengthened positions (Sjostrom et al., 1979; Rantanen et al., 1999). AFO designs and settings which permitted more dorsiflexion resulted in less reduction in muscle activity and less calf muscle shortening which may be beneficial in preventing muscle atrophy.

Following an Achilles tendon rupture it has been common practice to place the ankle in plantarflexion in a cast or AFO to adapt the tendon ends and protect the healing tendon from elongation (Nilsson-Helander et al., 2010; Willits et al., 2010; Schepull et al., 2012; Olsson et al., 2013). There are a few studies of surgical treatment of Achilles tendon ruptures where dorsiflexion to neutral was allowed early. A dorsal brace limiting dorsiflexion to neutral applied either the day after surgery or after 2 weeks and with full weight bearing after 2–3 weeks was compared to cast immobilization and no increase in re-ruptures (Kangas et al., 2003; Maffulli et al., 2003) or tendon elongation (Kangas et al., 2003) were found. The adjustable AFO design set to limit dorsiflexion to neutral 2 weeks postoperatively was compared to cast treatment and no difference in re-rupture rate or tendon elongation were found (Mortensen et al., 1999). These studies suggest that mobilizing the ankle to neutral within 2 weeks following surgical treatment of an Achilles tendon rupture is safe, while evidence regarding non-surgical treatment is lacking.

There are limitations to this study. Validation of Speckle tracking on tendon tissue has previously been done *in vitro* on porcine tendon samples (Chernak and Thelen, 2012; Fröberg et al., 2017) and *in vivo* validation is lacking. It has been reported that speckle tracking has a tendency to systematically underestimate displacement in tendon tissue (Chernak and Thelen, 2012; Fröberg et al., 2017). Peak superficial and deep displacement during stance phase were defined as

displacement during the time from the beginning of dorsiflexion to maximum dorsiflexion as determined from the displacement curves. Differential displacement was calculated as the difference between peak superficial and deep displacement. Although this potentially introduces a risk of error due to a time shift between superficial and deep displacement, no major time shifts were observed.

Pressure in-sole systems are limited to measuring force vectors that are perpendicular to the sensors and therefore there is a risk for underestimation of forces if the insoles are placed on sloping surfaces (Spooner et al., 2010). In this study AFO conditions with different plantar surface slopes were compared and therefore there might be measurement errors present. Tendon deformation patterns were observed in healthy participants who were not limited by pain or caution and were able to fully load their braced leg. This may not be the case following an Achilles tendon rupture. It was observed that participants changed walking patterns with the use of the different types of AFO, but as motion analysis was not used this could not be analyzed further. The rigid AFO had to be adjusted to fit the ultrasound probe over the Achilles tendon. The opening may have affected the biomechanical properties of the AFO, but no apparent instabilities were observed.

In conclusion, the degree of dorsiflexion allowed within an AFO had greater effects on Achilles tendon displacement patterns and muscle activity in the calf than differences in AFO design. AFO settings that allowed ankle dorsiflexion to neutral resulted in displacement patterns in the Achilles tendon and muscle activity in the lower leg which were close to those observed during unbraced walking. Further research is needed to establish if these effects are related to clinical benefits.

DATA AVAILABILITY STATEMENT

The datasets generated for this study are available on request to the corresponding author.

ETHICS STATEMENT

The studies involving human participants were reviewed and approved by the Stockholm Regional Ethics Committe (2016/1970-31). The patients/participants provided their written informed consent to participate in this study.

AUTHOR CONTRIBUTIONS

ÅF contributed to conception, design and data collection of the study, performed data analysis, and wrote the manuscript. MM contributed to conception, design and data collection of the study, performed data analysis, and assisted in writing the manuscript. AA contributed to conception, design and data collection of the study, assisted in data analysis, and assisted in writing the manuscript.

FUNDING

This study was supported by grants from the Karolinska Institute, the Stockholm County Council and the Swedish National Centre for Research in Sports (CIF). All funding was used for practical performance of the experiments and travel to present the research at international scientific conferences. Karolinska Institute and Stockholm County Council funding also financed time for ÅF to conduct the study. The Swedish School of Sport and Health Sciences provides funding for open access publication fees.

REFERENCES

Akizuki, K. H., Gartman, E. J., Nisonson, B., Ben-Avi, S., and McHugh, M. P. (2001). The relative stress on the Achilles tendon during ambulation in an ankle immobiliser: implications for rehabilitation after Achilles tendon repair. *Br. J. Sports Med.* 35, 329–333; discussion 333–334. doi: 10.1136/bjsm.35.5.329

Alkner, B. A., and Tesch, P. A. (2004). Efficacy of a gravity-independent resistance exercise device as a countermeasure to muscle atrophy during 29-day bed rest. *Acta Physiol. Scand.* 181, 345–357. doi: 10.1111/j.1365-201X.2004.01293.x

Andersson, T., Eliasson, P., and Aspenberg, P. (2009). Tissue memory in healing tendons: short loading episodes stimulate healing. *J. Appl. Physiol.* 107, 417–421. doi: 10.1152/japplphysiol.00414.2009

Arndt, A., Bengtsson, A. S., Peolsson, M., Thorstensson, A., and Movin, T. (2012). Non-uniform displacement within the Achilles tendon during passive ankle joint motion. *Knee Surg. Sports Traumatol. Arthrosc.* 20, 1868–1874. doi: 10.1007/s00167-011-1801-9

Arndt, A. N., Komi, P. V., Bruggemann, G. P., and Lukkariniemi, J. (1998). Individual muscle contributions to the *in vivo* Achilles tendon force. *Clin. Biomech.* 13, 532–541. doi: 10.1016/S0268-0033(98)00032-1

Barnett, S. (1998). International protocol guidelines for plantar pressure measurement. *Diabetic Foot.* 1, 137–140.

Bojsen-Moller, J., and Magnusson, S. P. (2015). Heterogeneous loading of the human Achilles tendon *in vivo*. *Exerc. Sport Sci. Rev.* 43, 190–197. doi: 10.1249/JES.0000000000000062

Bring, D. K., Kreicbergs, A., Renstrom, P. A., and Ackermann, P. W. (2007). Physical activity modulates nerve plasticity and stimulates repair after Achilles tendon rupture. *J. Orthop. Res.* 25, 164–172. doi: 10.1002/jor.20257

Chernak, L. A., and Thelen, D. G. (2012). Tendon motion and strain patterns evaluated with two-dimensional ultrasound elastography. *J. Biomech.* 45, 2618–2623. doi: 10.1016/j.jbiomech.2012.08.001

Dirks, M. L., Wall, B. T., and van Loon, L. J. C. (2018). Interventional strategies to combat muscle disuse atrophy in humans: focus on neuromuscular electrical stimulation and dietary protein. *J. Appl. Physiol.* 125, 850–861. doi: 10.1152/japplphysiol.00985.2016

Eliasson, P., Andersson, T., and Aspenberg, P. (2012). Achilles tendon healing in rats is improved by intermittent mechanical loading during the inflammatory phase. *J. Orthop. Res.* 30, 274–279. doi: 10.1002/jor.21511

Franz, J. R., Slane, L. C., Rasske, K., and Thelen, D. G. (2015). Non-uniform *in vivo* deformations of the human Achilles tendon during walking. *Gait Posture.* 41, 192–197. doi: 10.1016/j.gaitpost.2014.10.001

Fröberg, A., Cisse, A. S, Larsson, M., Martensson, M., Peolsson, M., Movin, T., et al. (2017). Altered patterns of displacement within the Achilles tendon following surgical repair. *Knee. Surg. Sports Traumatol. Arthrosc.* 25, 1857–65. doi: 10.1007/s00167-016-4394-5

Fröberg, A., Komi, P., Ishikawa, M., Movin, T., and Arndt, A. (2009). Force in the achilles tendon during walking with ankle foot orthosis. *Am. J. Sports Med.* 37, 1200–1207. doi: 10.1177/0363546508330126

Haraldsson, B. T., Aagaard, P., Qvortrup, K., Bojsen-Moller, J., Krogsgaard, M., Koskinen, S., et al. (2008). Lateral force transmission between human tendon fascicles. *Matrix Biol.* 27, 86–95. doi: 10.1016/j.matbio.2007.09.001

Kadel, N. J., Segal, A., Orendurff, M., Shofer, J., and Sangeorzan, B. (2004). The efficacy of two methods of ankle immobilization in reducing gastrocnemius, soleus, and peroneal muscle activity during stance phase of gait. *Foot Ankle Int.* 25, 406–409. doi: 10.1177/107110070402500607

Kangas, J., Pajala, A., Ohtonen, P., and Leppilahti J. (2007). Achilles tendon elongation after rupture repair: a randomized comparison of 2 postoperative regimens. *Am. J. Sports Med.* 35, 59–64. doi: 10.1177/0363546506293255

Kangas, J., Pajala, A., Siira, P., Hamalainen, M., and Leppilahti J. (2003). Early functional treatment versus early immobilization in tension of the musculotendinous unit after Achilles rupture repair: a prospective, randomized, clinical study. *J. Trauma.* 54, 1171–1180; discussion 80–81. doi: 10.1097/01.TA.0000047945.20863.A2

Kearney, R. S., Lamb, S. E., Achten, J., Parsons, N. R., and Costa, M. L. (2011). In-shoe plantar pressures within ankle-foot orthoses: implications for the management of achilles tendon ruptures. *Am. J. Sports Med.* 39, 2679–2685. doi: 10.1177/0363546511420809

Maffulli, N., Tallon, C., Wong J., Lim, K. P., and Bleakney, R. (2003). Early weightbearing and ankle mobilization after open repair of acute midsubstance tears of the achilles tendon. *Am. J. Sports Med.* 31, 692–700. doi: 10.1177/03635465030310051001

Mortensen, H. M., Skov, O., and Jensen, P. E. (1999). Early motion of the ankle after operative treatment of a rupture of the Achilles tendon. A prospective, randomized clinical and radiographic study. *J. Bone Joint Surg. Am.* 81, 983–990. doi: 10.2106/00004623-199907000-00011

Nilsson-Helander, K., Silbernagel, K. G, Thomee, R., Faxen, E., Olsson, N., Eriksson, B. I., et al. (2010). Acute achilles tendon rupture: a randomized, controlled study comparing surgical and nonsurgical treatments using validated outcome measures. *Am. J. Sports Med.* 38, 2186–2193. doi: 10.1177/0363546510376052

Olsson, N., Silbernagel, K. G., Eriksson, B. I., Sansone, M., Brorsson, A., Nilsson-Helander, K., et al. (2013). Stable surgical repair with accelerated rehabilitation versus nonsurgical treatment for acute Achilles tendon ruptures: a randomized controlled study. *Am. J. Sports Med.* 41, 2867–76. doi: 10.1177/0363546513503282

Rantanen, J., Hurme, T., and Kalimo, H. (1999). Calf muscle atrophy and Achilles tendon healing following experimental tendon division and surgery in rats. Comparison of postoperative immobilization of the muscle-tendon complex in relaxed and tensioned positions. *Scand. J. Med. Sci. Sports.* 9, 57–61. doi: 10.1111/j.1600-0838.1999.tb00208.x

Sandberg, O. H., Danmark, I., Eliasson, P., and Aspenberg, P. (2015). Influence of a lower leg brace on traction force in healthy and ruptured Achilles tendons. *Muscles Ligaments Tendons J.* 5, 63–67. doi: 10.32098/mltj.02.2015.03

Schepull, T., and Aspenberg, P. (2013). Early controlled tension improves the material properties of healing human achilles tendons after ruptures: a randomized trial. *Am. J. Sports Med.* 41, 2550–2557. doi: 10.1177/0363546513501785

Schepull, T., Kvist, J., and Aspenberg, P. (2012). Early E-modulus of healing Achilles tendons correlates with late function: similar results with or without surgery. *Scand. J. Med. Sci. Sports.* 22, 18–23. doi: 10.1111/j.1600-0838.2010.01154.x

Silbernagel, K. G., Steele, R., and Manal, K. (2012). Deficits in heel-rise height and achilles tendon elongation occur in patients recovering from an Achilles tendon rupture. *Am. J. Sports Med.* 40, 1564–1571. doi: 10.1177/0363546512447926

Sjostrom, M., Wahlby, L., and Fugl-Meyer, A. (1979). Achilles tendon injury. 3. Structure of rabbit soleus muscles after immobilization at different positions. *Acta Chir. Scand.* 145, 509–521.

Slane, L. C., and Thelen, D. G. (2014). Non-uniform displacements within the Achilles tendon observed during passive and eccentric loading. *J. Biomech.* 47, 2831–2835. doi: 10.1016/j.jbiomech.2014.07.032

Spooner, S. K., Smith, D. K., and Kirby, K. A. (2010). In-shoe pressure measurement and foot orthosis research: a giant leap forward or a step too far? *J. Am. Podiatr. Med. Assoc.* 100, 518–529. doi: 10.7547/1000518

Twaddle, B. C., and Poon, P. (2013). Early motion for Achilles tendon ruptures: is surgery important? *A randomized, prospective study. Am. J. Sports Med.* 35, 2033–2038. doi: 10.1177/0363546507307503

Willits, K., Amendola, A., Bryant, D., Mohtadi, N. G., Giffin, J. R., Fowler, P., et al. (2010). Operative versus nonoperative treatment of acute Achilles tendon ruptures: a multicenter randomized trial using accelerated functional rehabilitation. *J. Bone Joint Surg. Am.* 92, 2767–2775. doi: 10.2106/JBJS.I.01401

Conflict of Interest: The authors declare that the research was conducted in the absence of any commercial or financial relationships that could be construed as a potential conflict of interest.

frontiers in Bioengineering and Biotechnology

ORIGINAL RESEARCH
published: 27 March 2020
doi: 10.3389/fbioe.2020.00264

Mechanics of Psoas Tendon Snapping. A Virtual Population Study

Emmanuel A. Audenaert[1,2,3,4], Vikas Khanduja[2], Peter Claes[5,6,7,8], Ajay Malviya[9,10] and Gunther Steenackers[3]*

[1] Department of Orthopedic Surgery and Traumatology, Ghent University Hospital, Ghent, Belgium, [2] Department of Trauma and Orthopedics, Addenbrooke's Hospital, Cambridge University Hospitals National Health Service Foundation Trust, Cambridge, United Kingdom, [3] Op3Mech Research Group, Department of Electromechanics, University of Antwerp, Antwerp, Belgium, [4] Department of Human Structure and Repair, Ghent University, Ghent, Belgium, [5] Medical Imaging Research Center (MIRC), University Hospitals Leuven, Leuven, Belgium, [6] Department of Electrical Engineering/Processing Speech and Images, KU Leuven, Leuven, Belgium, [7] Department of Human Genetics, KU Leuven, Leuven, Belgium, [8] Murdoch Children's Research Institute, Royal Children's Hospital, Melbourne, VIC, Australia, [9] Department of Orthopedic Surgery and Traumatology, Northumbria National Health Service Foundation Trust, Newcastle upon Tyne, United Kingdom, [10] Department of Regenerative Medicine, Institute of Cellular Medicine, Newcastle University, Newcastle upon Tyne, United Kingdom

Internal snapping of the psoas tendon is a frequently reported condition, especially in young adolescents involved in sports. It is defined as an increased tendon excursion over bony or soft tissue prominence causing local irritation and inflammation of the tendon leading to groin pain and often is accompanied by an audible snap. Due to the lack of detailed dynamic visualization means, the exact mechanism of the condition remains poorly understood and different theories have been postulated related to the etiology and its location about the hip. In the present study we simulated psoas tendon behavior in a virtual population of 40,000 anatomies and compared tendon movement during combined abduction, flexion and external rotation and back to neutral extension and adduction. At risk phenotypes for tendon snapping were defined as the morphologies presenting with excess tendon movement. There were little differences in tendon movement between the male and female models. In both populations, abnormal tendon excursion correlated with changes in mainly the femoral anatomy (male $r = 0.72$, $p < 0.001$, female $r = 0.66$, $p < 0.001$): increased anteversion and valgus as well as a decreasing femoral offset and ischiofemoral distance. The observed combination of shape components correlating with excess tendon movement in essence presented with a medial positioning of the minor trochanter. This finding suggest that psoas snapping and ischiofemoral impingement are possibly two presentations of a similar underlying rotational dysplasia of the femur.

Keywords: tendon mechanics, ischiofemoral impingement, muscle wrapping, geometric morphoinetric analysis, virtual population

OPEN ACCESS

Edited by:
Jason Franz, University of North Carolina at Chapel Hill, United States

Reviewed by:
Takashi Sakai, Yamaguchi University School of Medicine, Japan
Cara Lewis, Boston University, United States

****Correspondence:***
Emmanuel A. Audenaert
emmanuel.audenaert@ugent.be

Specialty section:
This article was submitted to Biomechanics, a section of the journal Frontiers in Bioengineering and Biotechnology

Received: *22 January 2020*
Accepted: *13 March 2020*
Published: *27 March 2020*

Citation:
Audenaert EA, Khanduja V, Claes P, Malviya A and Steenackers G (2020) Mechanics of Psoas Tendon Snapping. A Virtual Population Study. Front. Bioeng. Biotechnol. 8:264. doi: 10.3389/fbioe.2020.00264

INTRODUCTION

Internal snapping hip, also referred to as coxa saltans or "dancer's hip," is a relatively common and potentially debilitating disorder produced by the iliopsoas tendon slipping over soft tissue and bony prominences during hip movement, causing an audible clicking that is typically accompanied by pain. The condition was originally described by Nunziata and Blumenfeld (1951) and garnered growing interest in the last decade, coinciding with the increasing

use of hip arthroscopy. The pioneering authors described the snapping as a consequence of the proximal portion of the iliopsoas tendon gliding over the iliopectineal eminence (Lyons and Peterson, 1984). Howse (1972), however, believed that a "clicking hip" in ballet dancers was caused by the iliofemoral ligaments sliding over the femoral head. These historical suppositions were mainly speculative, with little supporting scientific evidence.

Jacobson and Allen (1990) were among the first to perform anatomical and radiographic studies, associating the iliopsoas tendon snap with its movement across the femoral head from lateral to medial with the hip brought to extension. The exact pattern of psoas tendon movement, however, remains debated and unresolved to date, with most authors claiming snapping to occur either over the iliopectineal eminence or the anterior part of the caput femoris (Taher and Power, 2003; Verhelst et al., 2012; Lee et al., 2013; Philippon et al., 2014; Ilizaliturri et al., 2015; Yen et al., 2015). Furthermore, several anatomical variations and focal pathological conditions, e.g., labral cysts, have been reported to increase the likelihood of occasional snapping to become recurrent and therefore clinically symptomatic.

While the location of tendon movement remains debated, literature does agree on the hip positions which can provoke coxa saltans. In all descriptions of the condition it occurs predominantly when the hip is moved from combined flexion, abduction, and external rotation (FABER) back to neutral adduction and internal rotation (Winston et al., 2007; Yen et al., 2015). This explains why snapping hip can be provoked when climbing stairs or when one gets out of a car or gets up from a chair. This also explains its higher incidence in athletes who walk, dance, lift weight and play football (Lee et al., 2013). For competitive ballet dancers it is reported that symptoms mount up to 90% and bilateral involvement as high as 80% (Nolton and Ambegaonkar, 2018). Winston et al. (2007) reported snapping in ballet dancers to occur almost exclusively during abduction-external rotation activities: grande battement à la seconde (a high kick to the side with a straight leg) in 41.8%, grand plié (a deep knee bend) in 25.3%, and développé à la second (a slow extension of the leg from the FABER position) in 22.8%. In the general population the prevalence of audible snapping is estimated at 5–10%, with a higher frequency in females as compared with males (Taher and Power, 2003; Lee et al., 2013; Yen et al., 2015).

Despite the condition being relatively common, little is known about the exact mechanism or origin of psoas tendon snapping. Notwithstanding the numerous theories proposed on the topic, in depth analysis of psoas mechanics during movement has not been carried out previously. This is mainly due to its difficult dynamic visualization and the condition therefore largely remains unsubstantiated.

RELATED WORK

Tendon-Muscle Path Prediction: Muscle Wrapping Algorithms

The shortest path problem of tendon-muscle path predictions is one of the oldest biomechanical challenge. The earliest techniques to represent and predict a tendon-muscle path adopted "via" points connecting straight line segments (Delp and Loan, 1995; Kruidhof and Pandy, 2006). Later authors improved upon this approach by the use of passive geometric constraints -e.g., cylinders, spheres, and ellipsoids- over which these line segments are wrapped (Arnold et al., 2000; Garner and Pandy, 2000; Charlton and Johnson, 2001; Audenaert and Audenaert, 2008). These so -called "obstacle-set" methods have been successfully applied in upper and lower limb models and resulting estimates for muscle location, lengths, and moments have been shown comparable to experimental measurements (Vasavada et al., 2008). Probably the most important property of this approximate method is speed of calculation, allowing for real time visualization of tendon-muscle paths during motion. In addition, these predictions can be used as "seeding" position for more complex volumetric wrapping techniques (Kohout et al., 2013) or full 3D finite element (FE) models of muscle (Reynolds et al., 2004; Blemker and Delp, 2005). In parallel with this evolution, research has focused on more anatomical descriptions of the 3D geometry of adjacent bony and soft tissue structures as limiting constraints, adding to the complexity of an already challenging problem (Gao et al., 2002; Marai et al., 2004; Desailly et al., 2010; Liu et al., 2012; Kohout et al., 2013; Hammer et al., 2019).

In spite of the obvious advancement in anatomical authenticity, these techniques have, however, been facing the challenges of increased complexity and associated computational requirements, restricting their usage in real time or population size applications as compared to the traditional obstacle-set methods. A valid and computational efficient alternative over personalized anatomical FE models, however, was recently proposed by Audenaert et al. (2019a) using rigid body spring models. This discrete element (DE) model provides an anatomical truthful description of tendon-muscle paths as they wrap over any anatomical, geometric or combined sets of surface structures, while allowing for fast processing of large simulations series (Audenaert et al., 2019a). The present work makes use of this recent technique to investigate the problem of psoas tendon movement in a population scale model.

Articulated Shape Models and Virtual Population Models

While simulation of tendon-muscle positions using finite or discrete element analysis has been shown to be reliable on a patient specific basis, replication of such analyses across large populations introduces an additional ethical, logistical, and computational challenge in order to obtain the required data set (Audenaert et al., 2019b,c, 2020). In that respect, population-based modeling has been applied to meaningful effect in biomechanics by capturing the effect of anatomical variation in many body regions (Rao et al., 2013; Bischoff et al., 2014; Campbell and Petrella, 2016). The description of shape variation at the population level a challenge, necessitating considerable training samples to reach acceptable generalization properties of the models. The number of training samples required for covering population variance of anatomical structures is scarce

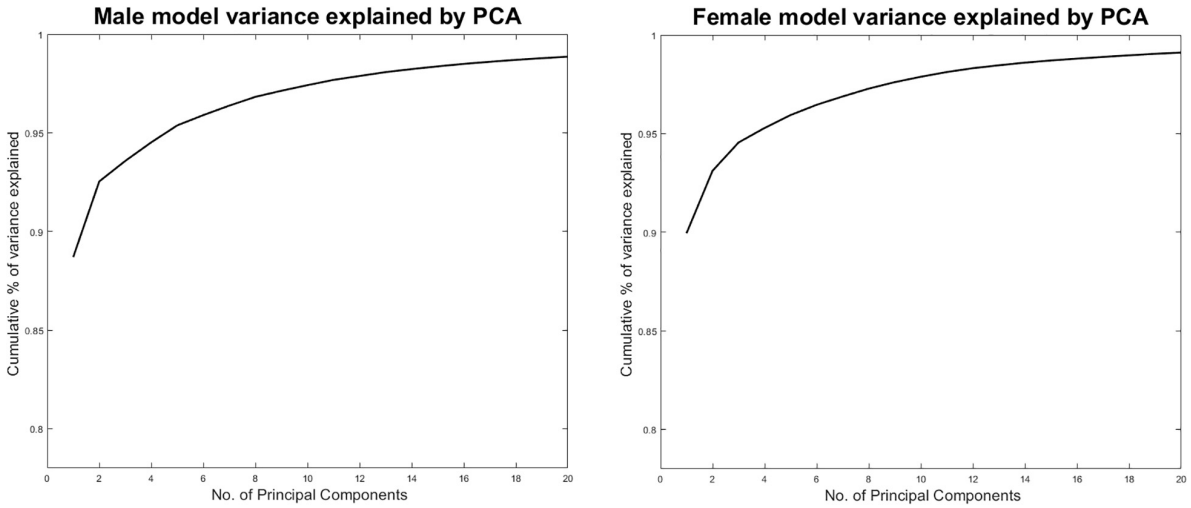

FIGURE 1 | Cumulative male and female variance explained by PCA.

in the literature. In the area of face recognition, it has been documented that in order to representatively achieve population coverage, at least 250 samples are required (Claes, 2007). Similar numbers of training samples have recently been described to be required in osteological models (Audenaert, 2019). In order to apply statistical shape modeling in the evaluation of joint mechanics, one must consider the multiple structures comprising the joint, their interdependencies and their relative alignment (Rao et al., 2013). Differences in pose among scanned subjects at the time of the image acquisition, however, adds undesirable intersubject variability that does not describe variance in patient anatomy. Because of this issue and for the purpose of modeling the lumbar spine, Rasoulian et al. (2013) previously argued that shape and pose should be deled with separately, as they are not correlated. Other authors have tried to handle the difference between alignment and pose either by defining statistical transformation models to capture differences in pose (Boisvert et al., 2008) or by explicitly modeling motion trough idealized joint models (e.g., a ball and socket joint with three degrees of freedom for the hip or hinged joint in case of the knee joint) (Kainmueller et al., 2008, 2009; Rao et al., 2013). We recently developed a novel method to decrease pose variance to increase compactness and thereby usability of multi-component shape models based on learning methodology and not enforcing idealized kinematic definitions on the joints (Audenaert et al., 2020). For the present study and with the aim to investigate the relationship between hip anatomy and psoas movement, the latter approach was implemented. In particular we hypothesized snapping would be associated with particular anatomical variation of pelvis and femur.

In summary, the objective of this manuscript is double. First, we propose to the best of our knowledge the first computational model of the lower limb to investigate psoas tendon behavior in a population sized approach. Secondly, we test the hypothesis that the variation in anatomy is correlated with abnormal tendon excursions during movement.

To this end, the following key technical challenges will be addressed: (1) We describe a representative virtual population of pelvifemoral models, within which psoas anatomy are derived. (2) We simulate psoas tendon behavior during provocative hip motions, which is a critical step in understanding why some anatomical configurations might be associated with abnormal psoas tendon excursion.

METHODS

Patient Population and Kinematic Protocol

The Ghent Lower Limb model was used to generate a virtual cohort of 20,000 male and an equal number of 20,000 female cases, representative for a western European population. The model was previously validated in terms of population coverage and model specificity, generalizability and accuracy. It is composed following principal component analysis of dens corresponding meshes obtained from 544 lower limb segmentations (362 male and 182 female training samples) (Styner et al., 2003; Audenaert, 2014, 2019, Almeida et al., 2016; Audenaert et al., 2019c). After segmentation and registration of the anatomical shape entries, male and female shape entries were separated and used for the construction of two distinct PCA models to describe shape variance Mathematically, each model was described using the following equation:

$$S = \overline{S} + Pb$$

where S is a vector of size 3n representing the shape in terms of n 3D landmark points. In the equation above $\overline{S}$ corresponds to the average shape of the model and P represents a t × 3n matrix encapsulating t eigenvectors describing the principal directions of variation of the model. Further, every unit vector is associated with an eigenvalue λ_i, i ∈ {1, ⋯, t} which describes

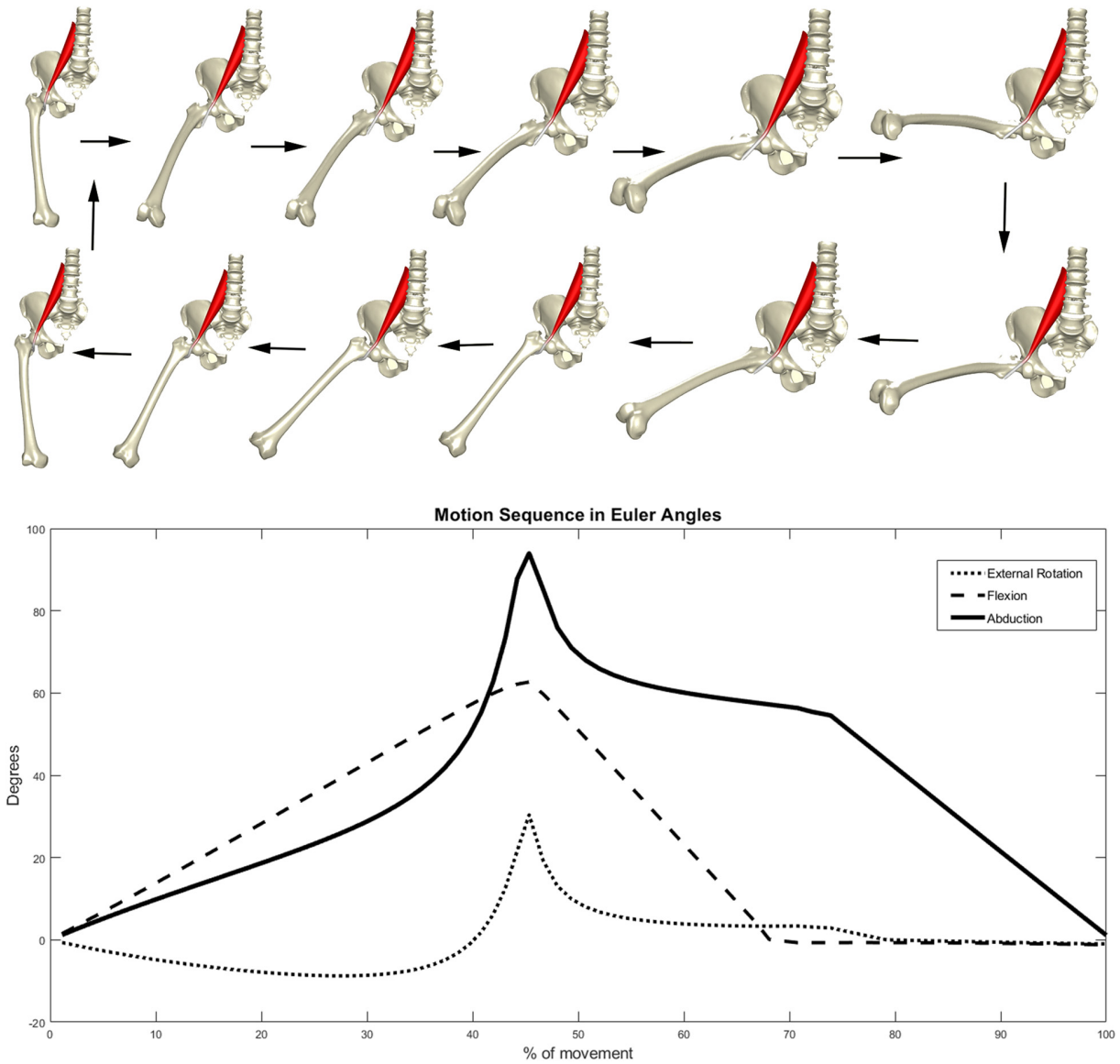

FIGURE 2 | Motion sequence enforced on the virtual models.

the magnitude of variation along each axis. Lastly, b = (b_1, $\cdots$,b_t) represents a vector containing the b_i weights that regulate the deviation of the shape S from the mean and follow a normal distribution.

For both sexes, it was determined that 20 shape modes were necessary to describe a sizable 99% of anatomical variance (**Figure 1**). We therefore retained t = 20 modes of variation to generate the virtual shapes, by randomly varying the normal distributed deviation weights b_i within the model. Doing so, a virtual population of 20,000 cases per sex class was generated and used to simulate psoas tendon movement, based on the same provoking kinematics of femoral abduction and rotation.

Psoas anatomy was predicted and the tendon path modeled according to a previously validated discrete element model of the psoas muscle and tendon (Audenaert et al., 2010, 2019a). Kinematics of circumduction, abduction up to 90 degrees with a concomitant 60 degrees of flexion and 30 degrees of external rotation and returning to the neutral position, were enforced on the virtual population and the position of the psoas tendon was evaluated during that motion performed at an angular velocity of 25 deg/s. Motions were enforced in a stepwise procedure with increasing and decreasing amount of rotation around the x, y, and z axis. The motion sequence that was implemented to describe a circumduction is demonstrated in **Figure 2**. Decomposition of the rotation matrices was performed to provide an approximative surrogate of clinical semantics in terms of amount of abduction, flexion, and rotation at each step of the motion sequence. The hip joint was modeled as a spherical joint with three degrees of

rotational freedom. Psoas tendon positions were evaluated and the angular velocity of tendon movement in relation to the center of the femur head were reported. Simulations were performed on a Dell EMC PowerEdge 940 server hosting 72 cores, processing in parallel at 2.9 GHz. The imposed kinematics were evaluated in 120 consecutive steps. Average simulation time, solving the starting position followed by 120 kinematics steps, was ˜3.5 min per case, mounting the required computational cost for 20,000 samples (males and females separately) at 18 h. An overview of the study workflow is presented in **Figure 3**.

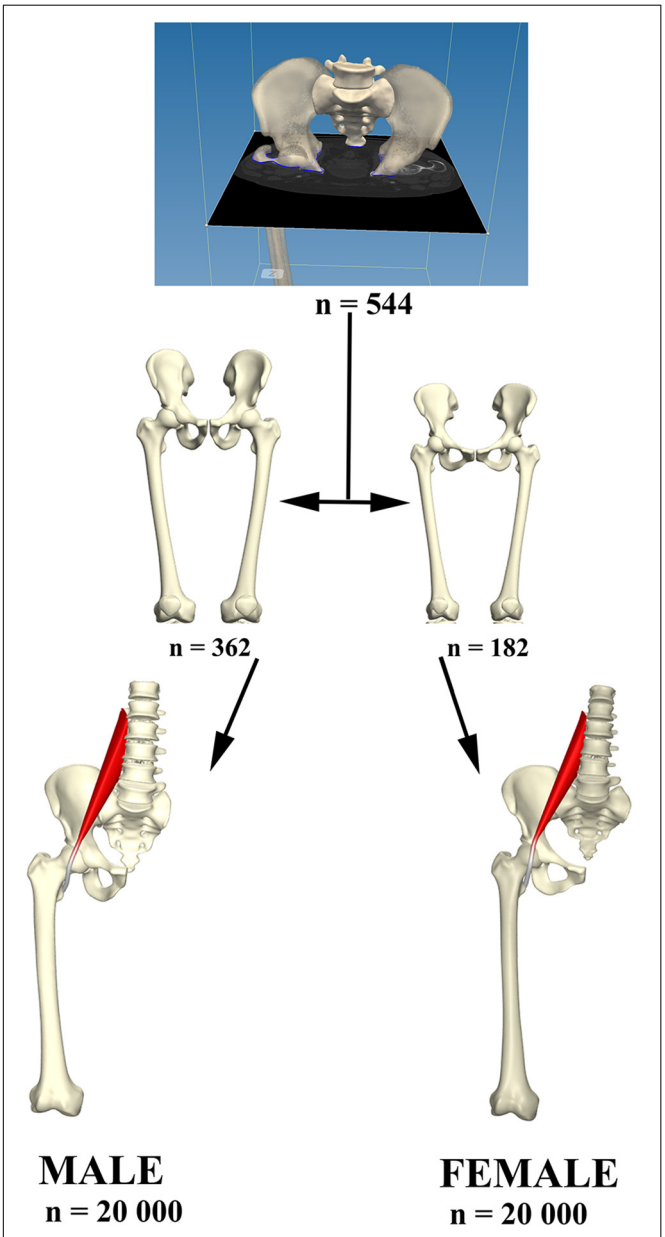

FIGURE 3 | Relevant osteological structures were segmented and use for the construct of a PCA model describing male and female anatomical variance. From each model 20,000 virtual anatomies were created to study psoas tendon behavior in the population created.

Statistical Analysis

Given the profound dominance of size in shape models of human anatomy in the Euclidian subspace (Audenaert, 2019), the tendon velocity-shape relationship was evaluated by means of canonical correlation analysis (CCA) in the Mahalanobis subspace. In particular, the PC values of the shape data, serving as predictor variables for the observed peak tendon-velocity measures, were used. Overall explained variance in the observed shape components by the factor peak tendon-velocity was evaluated using partial least squares regression (PLSR). PLSR regression and CCA are highly related to each other and essentially perform the same operation, maximizing the tendon-velocity feature onto the combined shape modes, however, the emphasis is slightly different. In CCA, the goal is to maximize correlation and allows for the statistical interpretation of this observed correlation. In contrast, PLSR maximizes the covariance instead of the correlation, and is typically performed for predictive purposes as a result and again in contrast to CCA. In conclusion, we used CCA to report on the statistical correlation, while PLSR was used to define the predictive value of the peak tendon-velocity feature.

PLSR was further used to describe the male and female consensus shape configurations correlating with low and excess tendon movements. Differences in male and female tendon excursions were further compared between both sexes using the common student t statistics.

RESULTS

Studying correlations within the virtual cohort based on isolated discrete measures, e.g., femoral anteversion, would obviously brake any important covariations of shape and result in noisy data describing small effects, hence the advantage of using PCA. Nevertheless, discrete measures are valid anatomical descriptions and usually well known by clinical researchers. To be able to translate our findings to the clinical field, a series of commonly used radiographical measures were therefore studied additional to the PCA in the cohort. Findings are described in detail in **Tables 1**, **2**.

PCA is a celebrated linear data compression technique. Although frequently performed, it is absolutely incorrect to interpret isolated PCs as if they were truly existing, independent anatomical variants. PCA can be used anatomically truthful, however, studying observed PC combinations instead of isolated

TABLE 1 | Table showing mean values and standard deviations of common used discrete measures to describe femur morphology and sex differences.

	Male (n = 20,000)	Female (n = 20,000)	P-value
Neck shaft angle (°)	125.23 ± 5.48	126.48 ± 5.49	<0.001
Femoral anteversion (°)	9.86 ± 7.02	10.72 ± 6.09	<0.001
Femoral offset (mm)	43.89 ± 6.54	39.11 ± 6.29	<0.001
Ischiofemoral distance (mm)	29.05 ± 4.18	22.23 ± 4.34	<0.001
Head radius (mm)	25.28 ± 1.10	22.37 ± 1.04	<0.001

TABLE 2 | List of the femur morphological parameters correlations with peak tendon velocity (SSM statistical shape model).

Correlations with peak tendon velocity	Correlation coefficient r Male (n = 20,000)	P-value	Correlation coefficient r Female (n = 20,000)	P-value
Neck shaft angle	0.48	<0.001	0.34	<0.001
Femoral anteversion	0.21	<0.001	0.31	<0.001
Femoral offset	−0.54	<0.001	−0.39	<0.001
Ischiofemoral distance	−0.38	<0.001	−0.32	<0.001
Head diameter	−0.14	<0.001	−0.17	<0.001
Femoral shape (SSM)	**0.72**	**<0.001**	**0.66**	**<0.001**

PC findings, with the use of use multivariable statistics. To this end, we firstly evaluated the correlation between the individual shape components and the peak angular velocity of tendon movement. Several contributing PC's were observed, conferring small to medium effects on peak tendon excursion. Because of the disproportionate size of the study cohort, p values were all small and even converged to zero for some of the variables. Based on the findings it was decided only the first 20 shape components were relevant to further include in the statistical analysis. Effect size and statistical significance of the correlation of these individual shape components are presented in a Manhattan-like plot in **Figure 4**.

In a second stage, the correlation between the composite of shape descriptors and peak tendon velocity was defined by CCA. The observed correlation was considerable in both males (r = 0.72, p < 1e-300) and females (r = 0.66, p < 1e-300). The consensus shape configurations relating to the variance in peak tendon velocity were defined using PLSR (**Figures 5**, **6**) images below at ±3 SD. In both populations, abnormal tendon excursion correlated with changes predominantly in the femoral anatomy: increasing femoral head anteversion, valgus, torsion and medial bowing. In essence a rotational variant in femoral shape configuration presenting with a medially located minor trochanter in respect to the pelvis. Interestingly, such shape configuration translates as a decreasing ischiofemoral distance.

A similar pattern of tendon movement was observed in all cases. With ongoing abduction and femoral external rotation, the psoas tendon gradually follows a smooth excursion from the medial portion of the anterior femoral head to lateral, reaching a lateralized position at the valley of the femoral head neck junction (**Figures 5**, **6**).

Upon return to the neutral position, however, the tendon tends to remain hooked in this valley – a stable local minimum in its shortest path position – before initiating its return back medially, causing a sudden increase in tendon velocity at the end of the movement when finding its new optimal medial position over the top of the femoral head. Differences in tendon velocity were observed nearly exclusively in the final stage of the movement, and it was decided to run further statistics against the peak velocity value at this point.

Females were slightly more prone to increased peak tendon movement as compared to males (p < 1e-60) The peak angular velocity was found to be slightly higher, 87.5 deg/s in females (range 27.5–247.5 deg/s) as compared to 82.5 deg/s in males (range 19.8–212.5 deg/s).

For the purpose of clinical translation of the findings, digitally reconstructed x-rays from the ±3 SD 3d shapes with low and high tendon velocity were generated and presented in **Figure 7**.

DISCUSSION

With larger datasets becoming available, in combinations with increased computational resources, statistical and probabilistic modeling presents an exciting and novel means for non-invasive testing and the evaluation of physiology and biomechanical variability across populations (Bischoff et al., 2014; Gosselin et al., 2014; Sims et al., 2018) In the context of musculoskeletal disease, pathology usually represents an extreme or outlier condition of function, shape, kinetics, or biomechanics at large. The unmet advantage of population numbers in virtual population models allows for the identification and study of these extremes, in cohort sizes beyond what is clinically achievable (Campbell and Petrella, 2016). Based on the current study on a virtual population of 40,000 cases, we were indeed able to describe variation in psoas movement and identify excessive psoas excursion in selected cases.

As mentioned earlier, opinions vary notably on the exact location of psoas tendon movement. Both the femoral head and iliopectineal eminence have been suggested at possible regions of involvement (Howse, 1972). In the present study, the tendon was found to move exclusively laterally and back to the tendon groove. The majority of tendon movement therefore occurred over the femoral head. This finding is in agreement with the sparse *in vivo* dynamic visualization data is available on the topic. Deslandes et al. (2008) observed a similar pattern of motion on dynamic ultrasonography and even claimed absolutely no involvement of the iliopectineal eminence at all. We can, however, based on the particular movement studied, not exclude snapping to occur over the ischiofemoral eminence. In particular during adduction a relative more medial positioning of the minor trochanter might result in such snapping mechanism. Further studies are definitely warranted.

Numerous associated factors, anatomical variants, and pathological conditions, have been reported to increase the risk of psoas movement to become symptomatic snapping. It can be anticipated, that any condition hampering a smooth medial return of the tendon during adduction will further trigger the snapping mechanics. Several clinical studies have indeed described a positive correlation between symptomatic

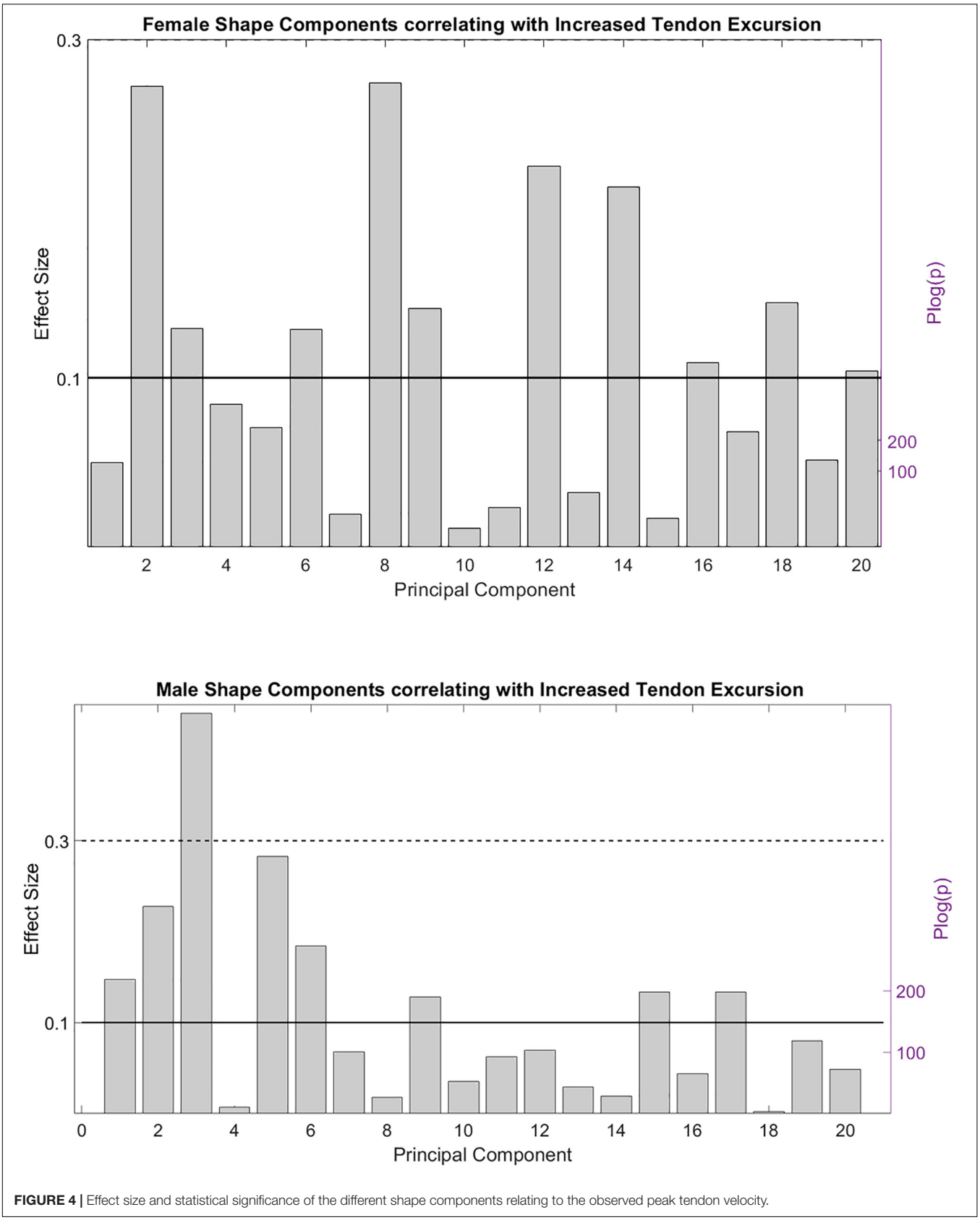

FIGURE 4 | Effect size and statistical significance of the different shape components relating to the observed peak tendon velocity.

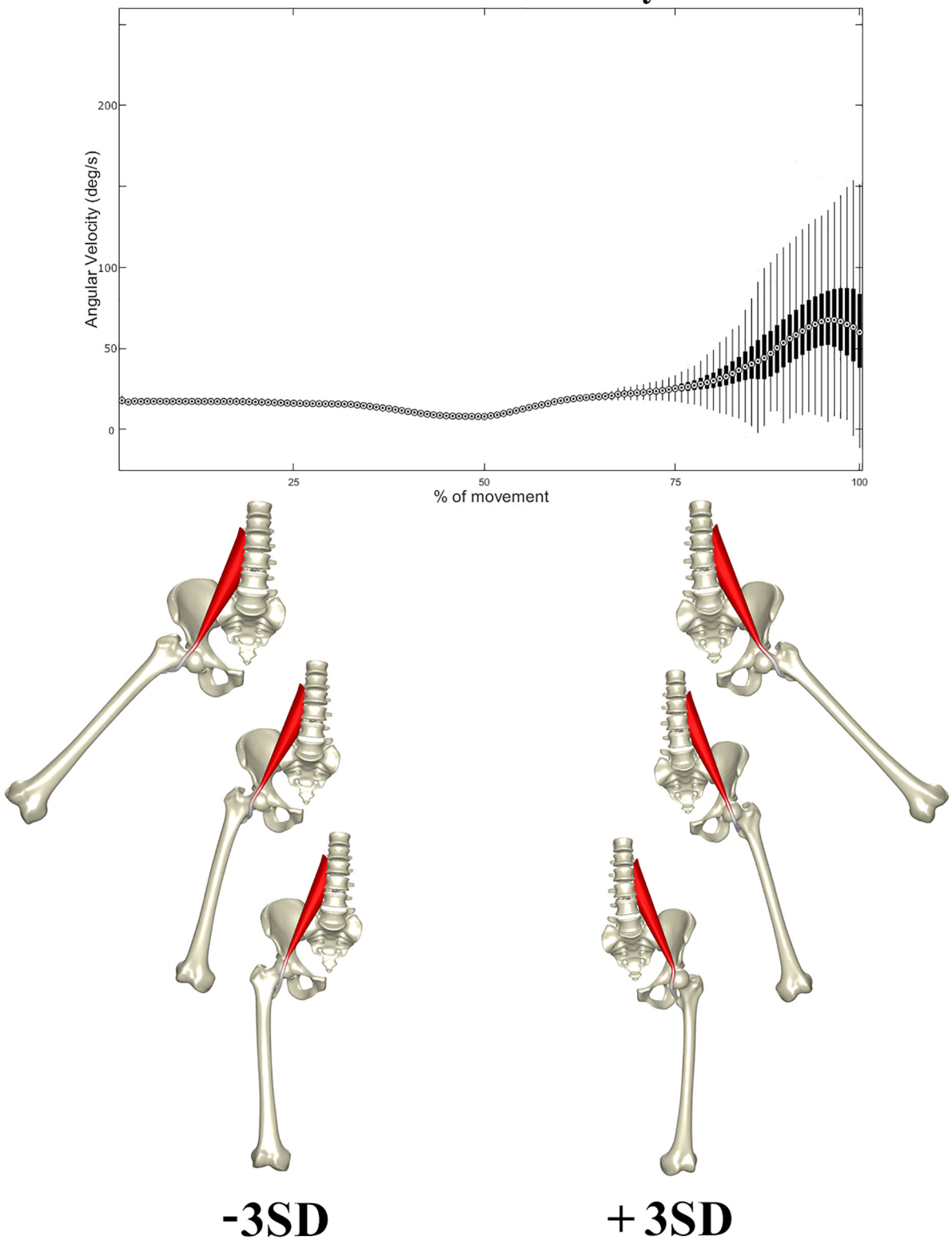

FIGURE 5 | Tendon velocity in the female population studied (Above). Reconstructed shapes correlating with decreased and increased tendon velocity upon return to the neutral position (Below).

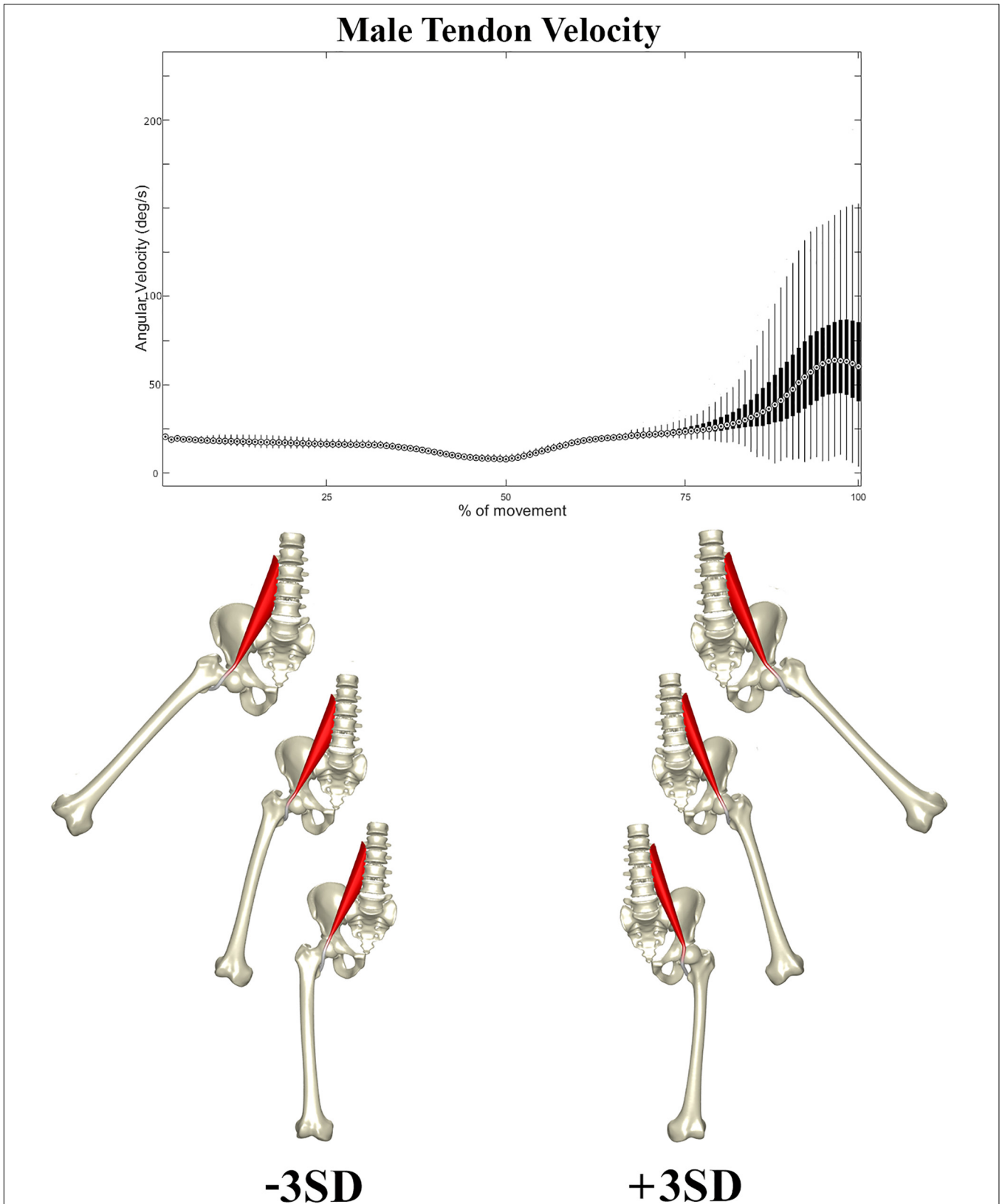

FIGURE 6 | Tendon velocity in the male population studied (Above). Reconstructed shapes correlating with decreased and increased tendon velocity upon return to the neutral position (Below).

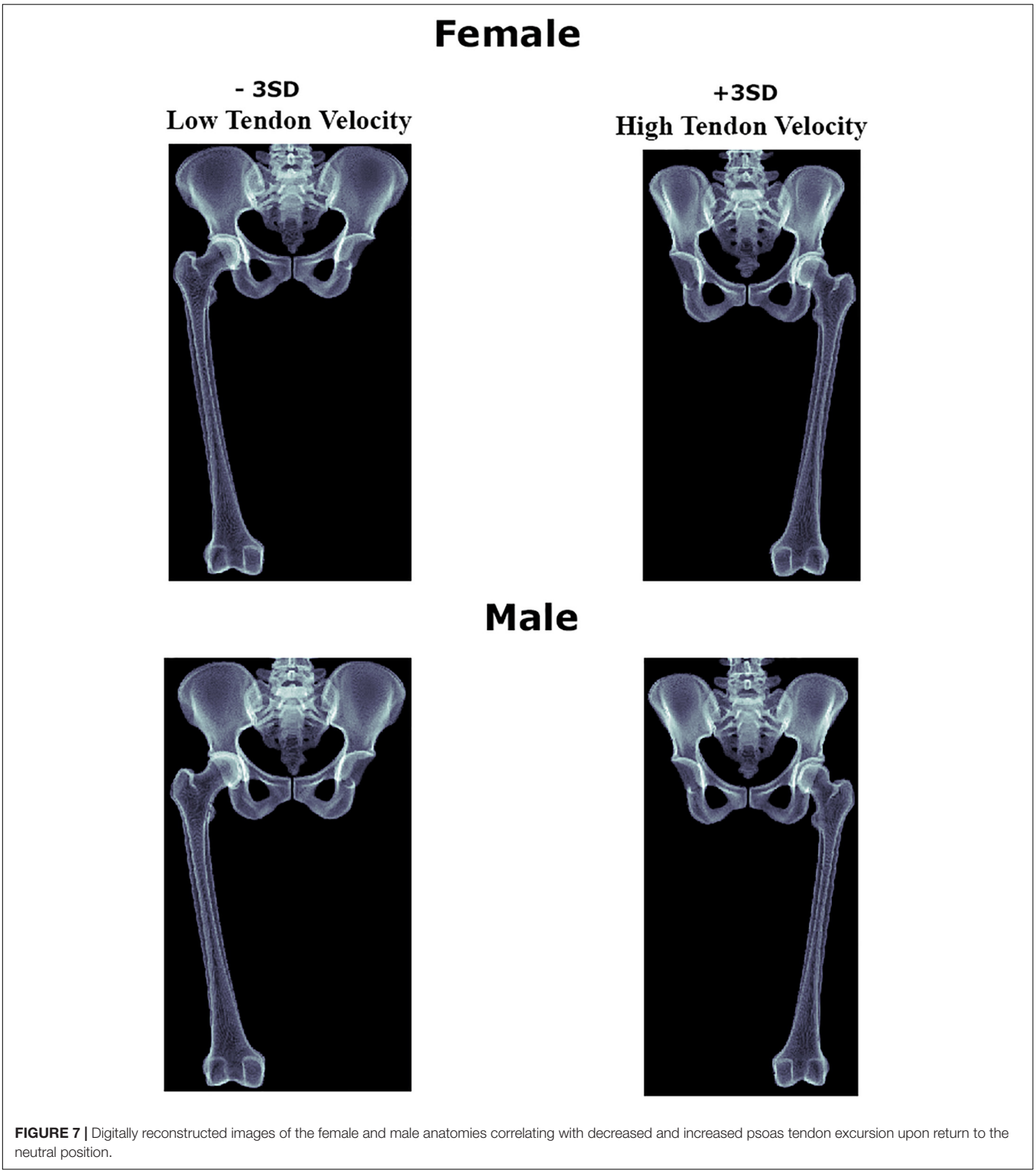

FIGURE 7 | Digitally reconstructed images of the female and male anatomies correlating with decreased and increased psoas tendon excursion upon return to the neutral position.

snapping and the presence of labral cysts. The observation of such relationship has not led to any solid etiological proof to date, nevertheless (Blankenbaker et al., 2012). Further dynamic studies are required to elucidate whether snapping becomes symptomatic in the presence of labral pathology or whether labral pathology can occur in case of increased and recurrent psoas tendon movement. Other conditions and structures have also been associated including the iliopsoas bursa, undoubling of the psoas tendon, the ligamentum iliofemoralis, labrum lacerations, paralabral cysts, ligamentum teres lacerations, and instability

of the joint (Verhelst et al., 2012; Lee et al., 2013; Philippon et al., 2014; Yen et al., 2015). Moreover, and likely ensuing a similar pathway, snapping has been reported following trauma and surgery of the hip joint (Taher and Power, 2003; Regev et al., 2011; Van Riet et al., 2011; Lee et al., 2013). Similarly, coxa saltans has been reported to occur after total hip prosthesis surgery due to the prosthesis protruding or incorrect positioning of the prosthetic components (Pattyn et al., 2011; Lee et al., 2013; Yen et al., 2015).

A particular interesting observation within this study is the increase in tendon excursion with a decreasing ischiofemoral distance. Ischiofemoral impingement is rather newly described condition with reports describing as well an audible snapping in a significant proportion of the patients reported (Stafford and Villar, 2011). The findings of the presents study seem to associate both snapping hip syndrome and ischiofemoral impingement with a similar underlying torsional femoral dysplasia. In the case of ischiofemoral impingement, excess femoral anteversion has indeed been documented in recent studies (Gomez-Hoyos et al., 2016). This observation might explain the disappointing outcome of psoas lengthening in anteverted femurs in the literature before ischiofemoral impingement was recognized as a distinct clinical condition (Fabricant et al., 2012). Further clinical studies are definitely warranted to elucidate this observed association as to define whether for distinct cases of snapping varisating derotational osteotomy is perhaps more in place than cutting the psoas tendon or removing the lesser trochanter.

The present work needs to be interpreted within is methodological limitations. Firstly, the study remains an *in silico* experiment which will require further *in vivo* confirmation and replication. Secondly, an important restriction of the presented work relates to the population model implemented, namely statistical model of shape obtained from Belgian people and the unknown extent of which findings can be extrapolated to other populations. The complex interaction between gens, environment, and culture, results in a population-based variation. Numerous studies have indeed demonstrated that the appropriate evaluation of this variation necessitates specific standards for each population (Rissech et al., 2013; San-Millan et al., 2017). Nonetheless, in general terms we expect our anatomical model results to be representative for a Western European population.

A second study limitation relates to the motion that was investigated. Snapping has been reported to occur during a broad spectrum of activities, ranging from simple walking to complex ballet exercises. In the present report a circumduction including abduction, flexion and external rotation back to neutral extension and adduction was investigated in order to cover a wide kinematic space. Even though an almost unphysiological 90 degrees of abduction was included in the analysis, increased tendon velocity was only observed in the final part of the motion sequence, close to the return to neutral position. This finding suggests researchers can restrict their analysis in future work in a smaller kinematic range as compared to what we have simulated. Further, this observation suggests more focused research is warranted to investigate common ADL activities in close range to a neutral hip position such as walking and stair climbing. While these activities have been reported to potentially evoke snapping, they mainly involve flexion-extension, with limited abduction and rotation. Considering we investigated a multiplanar hip motion, our findings in terms of the location and mechanism of the snapping can therefore not be generalized to ADL activities that are believed relevant but mainly involve pure flexion-extension. Clearly more work is needed.

In conclusion we found the psoas tendon to exclusively wrap around the anterior femoral head, not conflicting with the iliopectineal eminence. It was associated with female sex, femoral malrotation and a decreased ischiofemoral distance.

DATA AVAILABILITY STATEMENT

The datasets generated for this study are available on request to the corresponding author.

AUTHOR CONTRIBUTIONS

All authors contributed to the study design, data acquisition, and drafting.

FUNDING

EA was financially supported by a senior research fellowship from the Research Foundation Flanders.

REFERENCES

Almeida, D. F., Ruben, R. B., Folgado, J., Fernandes, P. R., Audenaert, E., Verhegghe, B., et al. (2016). Fully automatic segmentation of femurs with medullary canal definition in high and in low resolution CT scans. *Med. Eng. Phys.* 38, 1474–1480. doi: 10.1016/j.medengphy.2016.09.019

Arnold, A. S., Salinas, S., Asakawa, D. J., and Delp, S. L. (2000). Accuracy of muscle moment arms estimated from MRI-based musculoskeletal models of the lower extremity. *Comput. Aided. Surg.* 5, 108–119. doi: 10.3109/10929080009148877

Audenaert, A., and Audenaert, E. (2008). Global optimization method for combined spherical-cylindrical wrapping in musculoskeletal upper limb modelling. *Comput. Methods Programs* 92, 8–19. doi: 10.1016/j.cmpb.2008.05.005

Audenaert, E. (2014). "). Development of a multi-modal, multi-component, articulated model of the lower limb," in *A Laborious Work in Progress*, ed. G. Székely (Delémont: SICAS), 38.

Audenaert, E. (2019). Statistical shape modelling of skeletal anatomy for sex discrimination: their training size, sexual dimorphism and asymmetry journal. *Front. Bioeng. Biotechnol. Section Biomech.* 7:302. doi: 10.3389/fbioe.2019.00302

Audenaert, E. A., Khanduja, V., Bauwens, C., Van Hoof, T., Pattyn, C., and Steenackers, G. (2019a). A discrete element model to predict anatomy of the psoas muscle and path of the tendon: design implications for total hip

arthroplasty. *Clin. Biomech.* 70, 186–191. doi: 10.1016/j.clinbiomech.2019.09.004

Audenaert, E. A., Pattyn, C., Steenackers, G., De Roeck, J., Vandermeulen, D., and Claes, P. (2019b). Statistical shape modeling of skeletal anatomy for sex discrimination: their training size, sexual dimorphism, and asymmetry. *Front. Bioeng. Biotech.* 7:302.

Audenaert, E. A., Van Houcke, J., Almeida, D. F., Paelinck, L., Peiffer, M., Steenackers, G., et al. (2019c). Cascaded statistical shape model based segmentation of the full lower limb in CT. *Comput. Methods Biomech. Biomed. Engin.* 22, 644–657. doi: 10.1080/10255842.2019.1577828

Audenaert, E. A., Van den Eynde, J., de Almeida, D. F., Steenackers, G., Vandermeulen, D., and Claes, P. (2020). Separating positional noise from neutral alignment in multicomponent statistical shape models. *Bone Rep.* 12:100243. doi: 10.1016/j.bonr.2020.100243

Audenaert, E. A., Mahieu, P., van Hoof, T., and Pattyn, C. (2010). Soft tissue structure modelling for use in orthopaedic applications and musculoskeletal biomechanics. *Eurasip J. Adv. Sig. Pr.* 2010:389356.

Bischoff, J. E., Dai, Y., Goodlett, C., Davis, B., and Bandi, M. (2014). Incorporating population-level variability in orthopedic biomechanical analysis: a review. *J. Biomech. Eng.* 136:021004. doi: 10.1115/1.4026258

Blankenbaker, D. G., Tuite, M. J., Keene, J. S., and del Rio, A. M. (2012). Labral injuries due to iliopsoas impingement: can they be diagnosed on MR arthrography? *Am. J. Roentgenol.* 199, 894–900. doi: 10.2214/ajr.11.8211

Blemker, S. S., and Delp, S. L. (2005). Three-dimensional representation of complex muscle architectures and geometries. *Ann. Biomed. Eng.* 33, 661–673. doi: 10.1007/s10439-005-1433-7

Boisvert, J., Cheriet, F., Pennec, X., Labelle, H., and Ayache, N. (2008). Geometric variability of the scoliotic spine using statistics on articulated shape models. *IEEE Trans Med. Imaging* 27, 557–568. doi: 10.1109/TMI.2007.911474

Campbell, J. Q., and Petrella, A. J. (2016). Automated finite element modeling of the lumbar spine: using a statistical shape model to generate a virtual population of models. *J. Biomech.* 49, 2593–2599. doi: 10.1016/j.jbiomech.2016.05.013

Charlton, I. W., and Johnson, G. R. (2001). Application of spherical and cylindrical wrapping algorithms in a musculoskeletal model of the upper limb. *J. Biomech.* 34, 1209–1216. doi: 10.1016/s0021-9290(01)00074-4

Claes, P. (2007). *A robust Statistical Surface Registration Framework Using Implicit Function Representations: Application in Craniofacial Reconstruction*. Thesis, Katholieke Universiteit Leuven, Belgium.

Delp, S. L., and Loan, J. P. (1995). A graphics-based software system to develop and analyze models of musculoskeletal structures. *Comput. Biol. Med.* 25, 21–34. doi: 10.1016/0010-4825(95)98882-e

Desailly, E., Sardain, P., Khouri, N., Yepremian, D., and Lacouture, P. (2010). The convex wrapping algorithm: a method for identifying muscle paths using the underlying bone mesh. *J. Biomech.* 43, 2601–2607. doi: 10.1016/j.jbiomech.2010.05.005

Deslandes, M., Guillin, R., Cardinal, E., Hobden, R., and Bureau, N. J. (2008). The snapping iliopsoas tendon: new mechanisms using dynamic sonography. *Am. J. Roentgenol.* 190, 576–581. doi: 10.2214/AJR.07.2375

Fabricant, P. D., Bedi, A., De La Torre, K., and Kelly, B. T. (2012). Clinical outcomes after arthroscopic psoas lengthening: the effect of femoral version. *Arthroscopy* 28, 965–971. doi: 10.1016/j.arthro.2011.11.028

Gao, F., Damsgaard, M., Rasmussen, J., and Christensen, S. T. (2002). Computational method for muscle-path representation in musculoskeletal models. *Biol. Cybern.* 87, 199–210. doi: 10.1007/s00422-002-0326-1

Garner, B. A., and Pandy, M. G. (2000). The obstacle-set method for representing muscle paths in musculoskeletal models. *Comput. Methods Biomech. Biomed. Engin.* 3, 1–30. doi: 10.1080/10255840008915251

Gomez-Hoyos, J., Schroder, R., Reddy, M., Palmer, I. J., and Martin, H. D. (2016). Femoral neck anteversion and lesser trochanteric retroversion in patients with ischiofemoral impingement: a case-control magnetic resonance imaging study. *Arthroscopy* 32, 13–18. doi: 10.1016/j.arthro.2015.06.034

Gosselin, M. C., Neufeld, E., Moser, H., Huber, E., Farcito, S., Gerber, L., et al. (2014). Development of a new generation of high-resolution anatomical models for medical device evaluation: the virtual population 3.0. *Phys. Med. Biol.* 59, 5287–5303. doi: 10.1088/0031-9155/59/18/5287

Hammer, M., Gunther, M., Haeufle, D. F. B., and Schmitt, S. (2019). Tailoring anatomical muscle paths: a sheath-like solution for muscle routing in musculoskeletal computer models. *Math. Biosci.* 311, 68–81. doi: 10.1016/j.mbs.2019.02.004

Howse, A. J. G. (1972). Orthopedists aid ballet. *Clin. Orthop. Relat. R* 89, 52–63.

Ilizaliturri, V. M. Jr., Suarez-Ahedo, C., and Acuna, M. (2015). Internal snapping hip syndrome: incidence of multiple-tendon existence and outcome after endoscopic transcapsular Release. *Arthroscopy* 31, 1991–1995. doi: 10.1016/j.arthro.2015.04.083

Jacobson, T., and Allen, W. C. (1990). Surgical-correction of the snapping iliopsoas tendon. *Am. J. Sport Med.* 18, 470–474. doi: 10.1177/036354659001800504

Kainmueller, D., Lamecker, H., Zachow, S., and Hege, H. C. (2008). Coupling deformable models for multi-object segmentation. *Biomed. Simul., Proc.* 5104, 69–78. doi: 10.1007/978-3-540-70521-5_8

Kainmueller, D., Lamecker, H., Zachow, S., and Hege, H. C. (2009). An articulated statistical shape model for accurate hip joint segmentation. *IEEE Eng. Med. Bio.* 2009, 6345–6635.

Kohout, J., Clapworthy, G. J., Zhao, Y., Tao, Y., Gonzalez-Garcia, G., Dong, F., et al. (2013). Patient-specific fibre-based models of muscle wrapping. *Interface Focus* 3:20120062. doi: 10.1098/rsfs.2012.0062

Kruidhof, J., and Pandy, M. G. (2006). Effect of muscle wrapping on model estimates of neck muscle strength. *Comput. Methods Biomech. Biomed. Engin.* 9, 343–352. doi: 10.1080/10255840600924781

Lee, K. S., Rosas, H. G., and Phancao, J. P. (2013). Snapping hip: imaging and treatment. *Semin.Musculoskeletal Radiol.* 17, 286–294. doi: 10.1055/s-0033-1348095

Liu, J., Shi, J. F., Fitton, L. C., Phillips, R., O'Higgins, P., and Fagan, M. J. (2012). The application of muscle wrapping to voxel-based finite element models of skeletal structures. *Biomech. Model Mechan.* 11, 35–47. doi: 10.1007/s10237-011-0291-5

Lyons, J. C., and Peterson, L. F. A. (1984). The snapping iliopsoas tendon. *Mayo Clin. Proc.* 59, 327–329. doi: 10.1016/s0025-6196(12)61428-1

Marai, G. E., Laidlaw, D. H., Demiralp, C., Andrews, S., Grimm, C. M., and Crisco, J. J. (2004). Estimating joint contact areas and ligament lengths from bone kinematics and surfaces. *IEEE Trans. Biomed. Eng.* 51, 790–799. doi: 10.1109/tbme.2004.826606

Nolton, E. C., and Ambegaonkar, J. P. (2018). Recognizing and managing snapping hip syndrome in dancers. *Med. Probl. Perform. Ar.* 33, 286–291. doi: 10.21091/mppa.2018.4042

Nunziata, A., and Blumenfeld, I. (1951). Cadera a resorte; a proposito de una variedad. *Prensa Med. Argent.* 38, 1997–2001.

Pattyn, C., Verdonk, R., and Audenaert, E. (2011). Hip arthroscopy in patients with painful hip following resurfacing arthroplasty. *Knee Surg. Sports Traumatol. Arthroscopy* 19, 1514–1520. doi: 10.1007/s00167-011-1463-7

Philippon, M. J., Devitt, B. M., Campbell, K. J., Michalski, M. P., Espinoza, C., Wijdicks, C. A., et al. (2014). Anatomic variance of the iliopsoas tendon. *Am. J. Sports Med.* 42, 807–811. doi: 10.1177/0363546513518414

Rao, C., Fitzpatrick, C. K., Rullkoetter, P. J., Maletsky, L. P., Kim, R. H., and Laz, P. J. (2013). A statistical finite element model of the knee accounting for shape and alignment variability. *Med. Eng. Phys.* 35, 1450–1456. doi: 10.1016/j.medengphy.2013.03.021

Rasoulian, A., Rohling, R., and Abolmaesumi, P. (2013). Lumbar spine segmentation using a statistical multi-vertebrae anatomical shape plus pose model. *IEEE Trans. Med. Imaging* 32, 1890–1900. doi: 10.1109/tmi.2013.2268424

Regev, G. J., Kim, C. W., Tomiya, A., Lee, Y. P., Ghofrani, H., Garfin, S. R., et al. (2011). Psoas muscle architectural design, in vivo sarcomere length range, and passive tensile properties support its role as a lumbar spine stabilizer. *Spine* 36, E1666–E1674. doi: 10.1097/BRS.0b013e31821847b3

Reynolds, H., Smith, N., and Hunter, P. J. (2004). Construction of an anatomically accurate geometric model of the forearm and hand musculo-skeletal system. *Conf. Proc. IEEE Eng. Med. Biol. Soc.* 3, 1829–1832.

Rissech, C., Marquez-Grant, N., and Turbon, D. (2013). A collation of recently published Western European formulae for age estimation of subadult skeletal remains: recommendations for forensic anthropology and osteoarchaeology. *J. Forensic Sci.* 58(Suppl. 1), S163–S168. doi: 10.1111/1556-4029.12011

San-Millan, M., Rissech, C., and Turbon, D. (2017). Shape variability of the adult human acetabulum and acetabular fossa related to sex and age by geometric

morphometrics. Implications for adult age estimation. *Forensic Sci. Int.* 272, 50–63. doi: 10.1016/j.forsciint.2017.01.005

Sims, C. R., Delima, L. R., Calimaran, A., Hester, R., and Pruett, W. A. (2018). Validating the physiologic model hummod as a substitute for clinical trials involving acute normovolemic hemodilution. *Anesth. Analg.* 126, 93–101. doi: 10.1213/ANE.0000000000002430

Stafford, G. H., and Villar, R. N. (2011). Ischiofemoral impingement. *J. Bone Joint Surg.Br.* 93B, 1300–1302.

Styner, M. A., Rajamani, K. T., Nolte, L. P., Zsemlye, G., Szekely, G., Taylor, C. J., et al. (2003). Evaluation of 3D correspondence methods for model building. *Inform. Process. Med. Imaging Proc.* 2732, 63–75. doi: 10.1007/978-3-540-45087-0_6

Taher, R. T., and Power, R. A. (2003). Iliopsoas tendon dysfunction as a cause of pain after total hip arthroplasty relieved by surgical release. *J. Arthroplasty* 18, 387–388. doi: 10.1054/arth.2003.50047

Van Riet, A., De Schepper, J., and Delport, H. P. (2011). Arthroscopic psoas release for iliopsoas impingement after total hip replacement. *Acta Orthop. Belg.* 77, 41–46.

Vasavada, A. N., Lasher, R. A., Meyer, T. E., and Lin, D. C. (2008). Defining and evaluating wrapping surfaces for MRI-derived spinal muscle paths. *J. Biomech.* 41, 1450–1457. doi: 10.1016/j.jbiomech.2008.02.027

Verhelst, L., Guevara, V., De Schepper, J., Van Melkebeek, J., Pattyn, C., and Audenaert, E. A. (2012). Extra-articular hip endoscopy: a review of the literature. *Bone Joint Res.* 1, 324–332. doi: 10.1302/2046-3758.112.2000133

Winston, P., Awan, R., Cassidy, J. D., and Bleakney, R. K. (2007). Clinical examination and ultrasound of self-reported snapping hip syndrome in elite ballet dancers. *Am. J. Sport Med.* 35, 118–126. doi: 10.1177/0363546506293703

Yen, Y. M., Lewis, C. L., and Kim, Y. J. (2015). Understanding and treating the snapping hip. *Sports Med. Arthrosc.* 23, 194–199. doi: 10.1097/JSA.0000000000000095

Conflict of Interest: The authors declare that the research was conducted in the absence of any commercial or financial relationships that could be construed as a potential conflict of interest.

frontiers in Sports and Active Living

ORIGINAL RESEARCH
published: 19 June 2020
doi: 10.3389/fspor.2020.00069

Shear Wave Tensiometry Reveals an Age-Related Deficit in Triceps Surae Work at Slow and Fast Walking Speeds

Anahid Ebrahimi[1], *Jack A. Martin*[1,2], *Dylan G. Schmitz*[1] *and Darryl G. Thelen*[1,2,3]*

[1] Department of Mechanical Engineering, University of Wisconsin-Madison, Madison, WI, United States, [2] Department of Orthopedics and Rehabilitation, University of Wisconsin-Madison, Madison, WI, United States, [3] Department of Biomedical Engineering, University of Wisconsin-Madison, Madison, WI, United States

Prior studies have observed an age-related decline in net ankle power and work at faster walking speeds. However, the underlying changes in muscle-tendon behavior are not well-understood, and are challenging to infer from joint level analyses. This study used shear wave tensiometry to investigate the modulation of force and work done by the triceps surae across walking speeds. Fourteen healthy young (7F/7M, 26 ± 5 years) and older (7F/7M, 67 ± 5 years) adults were tested. Subjects walked on an instrumented treadmill at four walking speeds (0.75, 1.00, 1.25, and 1.50 m/s) while lower extremity kinematics and Achilles tendon shear wave speeds were collected. Subject-specific calibrations were used to compute Achilles tendon force from wave speed. Excursions of the soleus and gastrocnemius muscle-tendon units were computed from the kinematic data and subject-specific measures of the Achilles tendon moment arm. Work loop plots were then used to assess effective muscle-tendon stiffness during lengthening, and positive, negative, and net work production during stance. Two-way mixed ANOVAs were used to evaluate the effects of age group and walking speed on each outcome measure. Tendon loading during muscle-tendon lengthening (effective stiffness) did not differ between age groups, but did vary with speed. The soleus became effectively stiffer with increasing speed while the gastrocnemius became effectively more compliant. There was a marked age-related deficit in net soleus (−66% on average) and gastrocnemius (−36%) work across all walking speeds. We did not observe an age-speed interaction effect on net work production. These results suggest the age-related deficit in triceps surae output in walking is pervasive across speed, and hence seemingly not linked to absolute mechanical demands of the task.

Keywords: aging gait, Achilles tendon force, gastrocnemius, soleus, work loops, muscle-tendon unit

OPEN ACCESS

Edited by:
Huub Maas,
Vrije Universiteit
Amsterdam, Netherlands

Reviewed by:
Jonas Rubenson,
Pennsylvania State University (PSU),
United States
Janne Avela,
University of Jyvaskyla, Finland

***Correspondence:**
Darryl G. Thelen
dgthelen@wisc.edu

Specialty section:
This article was submitted to Biomechanics and Control of Human Movement, a section of the journal Frontiers in Sports and Active Living

Received: *01 March 2020*
Accepted: *18 May 2020*
Published: *19 June 2020*

Citation:
Ebrahimi A, Martin JA, Schmitz DG and Thelen DG (2020) Shear Wave Tensiometry Reveals an Age-Related Deficit in Triceps Surae Work at Slow and Fast Walking Speeds. Front. Sports Act. Living 2:69. doi: 10.3389/fspor.2020.00069

INTRODUCTION

Typical human walking relies heavily on power generation by the ankle plantar flexors (McGowan et al., 2008). For example, inverse dynamics analyses have found that the ankle accounts for 35–40% of the positive work generated at joints of the lower extremity during gait (Sawicki et al., 2009; Ebrahimi et al., 2017). Numerous studies have shown that ankle power (Winter et al., 1990; Cofré et al., 2011) and positive work (DeVita and Hortobagyi, 2000; Silder et al., 2008; Cofré et al., 2011;

Crenna and Frigo, 2011) are diminished with aging, even when accounting for differences in step length. The decline in ankle power generation becomes more apparent at faster walking speeds (Judge et al., 1996; Kerrigan et al., 1998; Silder et al., 2008; Cofré et al., 2011).

Age-related changes in musculoskeletal properties and neural control likely contribute to the decline in distal power production. For example, older adults exhibit greater Achilles tendon compliance (Onambele et al., 2006; Stenroth et al., 2012), which can affect power generation by altering the operating lengths and contraction velocities of the triceps surae (Conway and Franz, 2020). In addition, older adults exhibit evidence of greater co-contraction about the ankle during stance (Schmitz et al., 2009), which could increase ankle stiffness while diminishing net ankle torque production. The use of co-contraction to stiffen the ankle joint could be a compensation for increased Achilles tendon compliance, lower muscle strength, and other age-related neuromotor impairments (Nagai et al., 2011). However, it remains challenging to infer individual muscle contributions from joint level analyses. For example, joint level analyses will underestimate the work done by muscle-tendon units when co-contraction is present. Shear wave tensiometry is a new non-invasive technology that facilitates measurements of muscle-tendon loading during locomotion (Martin et al., 2018; Keuler et al., 2019). Tensiometry measures of tendon loading can be coupled with measures of muscle-tendon kinematics to characterize the work done at the muscle level, and thereby provide additional insight into the underlying source of diminished ankle power in older adults.

In this study, we coupled shear wave tensiometry with subject-specific moment arm measures to characterize work-loops (Josephson, 1985; Biewener and Roberts, 2000; Dickinson et al., 2000; Biewener et al., 2004) of the triceps surae during walking in young and older adults. Work loops were used to evaluate the operating lengths, effective stiffness (Rouse et al., 2013), and work done by the gastrocnemius and soleus muscle-tendon units. We hypothesized that older adults would exhibit more negative gastrocnemius and soleus muscle-tendon work than young adults, which could arise from co-activation of the plantarflexors and dorsiflexors in mid-stance (Schmitz et al., 2009). Further, we expected to observe significantly lower positive work and net work generated by both muscle-tendon units in the older adults, with the age-related deficit amplified at faster walking speeds.

METHODS

Subjects

Fourteen healthy young (7F, 26 ± 5 years, 1.77 ± 0.11 m, 73.96 ± 15.19 kg) and 14 healthy older (7F, 67 ± 5 years, 1.75 ± 0.06 m, 71.90 ± 12.21 kg) adults participated in this study. All subjects self-reported that they were able to comfortably walk on a treadmill, that they were without current (past 6 months) orthopedic or neurological impairment, and that they had no history of Achilles tendinopathy. The study protocol was approved by the University of Wisconsin-Madison Health Sciences Institutional Review Board. After providing written consent, all subjects initially walked for 5 min to acclimate to the treadmill and pre-condition the tendon (Hawkins et al., 2009). Subjects then walked on an instrumented treadmill at four speeds (0.75, 1.00, 1.25, and 1.50 m/s) while Achilles tendon shear wave speed, lower extremity kinematics (8 cameras, 190 Hz, Eagle cameras, Cortex software, Motion Analysis, Rohnert Park, CA) and ground reaction forces (Instrumented treadmill, 1,900 Hz, Bertec Corp., Columbus, OH) were collected.

Motion capture markers were placed on anatomical landmarks of the lower limb (1st and 5th metatarsal head locations over the shoe, medial and lateral malleoli, and medial and lateral femoral epicondyles) and as clusters on rigid plates secured to the thigh, shank and foot (Collins et al., 2009). Ankle and knee plantarflexion angles and torques were calculated via standard inverse kinematics and inverse dynamics calculations in Visual 3D using a 6-degree of freedom rigid body model (C-motion, Inc., Germantown, MD).

Achilles Tendon Force Measurements

Shear wave tensiometry was used to measure tendon force, as described previously (Keuler et al., 2019). Briefly, a shear wave tensiometer, consisting of a custom tapping device and accelerometer array in series, was secured over the right Achilles tendon of all participants with self-adherent wrap. The piezo-actuated (PK4JQP2, Thorlabs, Newton, NJ) tapping device was driven throughout the duration of each collection by a 50 Hz square wave via an open-loop piezo controller (MDT694B, Thorlabs, Newton, NJ). The accelerometer array consisted of two miniature accelerometers (Model 352C23, PCB Piezotronics, Depew, NY) mounted 10 mm apart in a silicone mold (Mold Star 15 SLOW, Smooth-On, Macungie, PA). Accelerometery data were collected at 100 kHz and then bandpass filtered using a second-order, zero-lag Butterworth filter with 150 and 5,000 Hz cutoff frequencies. For each tap (rising edge of the square wave), we computed the time between wave arrival at the two accelerometers by finding the delay that maximized the normalized cross-correlation of the first and second accelerometer signals over a 1 ms window after the tap event. Sub-sample interpolation was performed using a local 3-point cosine fit of the normalized cross-correlation values (Cespedes, 1995). Shear wave speed was calculated by dividing the distance (10 mm) between the accelerometers by the time delay. Performing this analysis for each tap resulted in a 50 Hz tendon wave speed signal.

Subject-specific shear wave speed-force calibration was performed independent of the walking tasks. To do this, we first measured each subject's Achilles tendon moment arm, $r(\theta)$, as a function of ankle angle θ. Moment arms were measured during passive ankle dorsiflexion by simultaneously tracking the ankle functional rotation axis via motion analysis and the Achilles tendon line of action using cine ultrasound (19 Hz, SonixTOUCH Research, BK Medical, Peabody, MA) (Keuler et al., 2019). Subjects were then asked to stand on an in-ground force plate (1,900 Hz, BP400600-2000, AMTI, Watertown, MA) and cyclically sway in the anteroposterior direction at 0.5 Hz, with rate guided by a metronome. Achilles tendon shear wave speed, lower extremity kinematics and force plate data were

simultaneously collected during the sway tasks. Inverse dynamics analysis was used to compute the ankle torque T from the kinematics and forceplate data. Achilles tendon force, F_{cal}, was then computed assuming that ankle torque was generated purely via the Achilles tendon, i.e., $F_{cal} = T/r\,(\theta)$. Tibialis anterior (TA) electromyographic signals (Trigno™, DelSys, Inc. Boston, MA) were recorded during the sway tasks and used to identify and remove periods of co-contraction, which typically occurred when subjects leaned backwards. Calibration slopes were obtained by performing a linear fit between tendon wave speed squared and F_{cal}. Additional details of our calibration procedures and results were previously reported (Ebrahimi et al., 2020).

Work-Loop Analysis

Tendon forces and excursions were calculated from the tendon wave speed and joint angle data, respectively. Analysis was performed on a minimum of 4 strides for each of the four walking speeds. Achilles tendon force (F) was computed using a prediction model of the form: $F = \beta(c^2 - c_{\text{min}}^2)$, where β is the slope of the subject-specific calibration, c is wave speed, and c_{min} is the minimum wave speed measured over all walking trials for a given individual. c_{min} is assumed to represent a zero-load state. The proportion of Achilles tendon force, normalized to body mass, partitioned to the gastrocnemius (35%, both medial and lateral heads) and soleus (65%) was based on relative physiological cross-sectional areas as measured via magnetic resonance imaging and assumed fiber lengths (Handsfield et al., 2014).

Muscle-tendon excursion was defined as the muscle-tendon length relative to its length in an upright posture. Soleus excursion represented the change in length due to ankle rotation, and was computed by integrating the subject-specific Achilles tendon moment arm with respect to the ankle dorsiflexion angle during gait. The gastrocnemius excursion represented the change in length due to both ankle and knee rotation. The change in gastrocnemius length due to knee flexion was computed by integrating an average medial gastrocnemius moment arm-angle curve (Buford et al., 1997) with respect to the knee flexion angle during gait. Soleus and gastrocnemius work loops were created by plotting force vs. muscle-tendon excursion for each muscle (**Figure 1**). Muscle-tendon power was calculated as the time derivative of excursion multiplied by force. Work was calculated over the interval from the minimum excursion during early stance (corresponding to the inflection point after loading response when the muscle-tendon begins to lengthen) to the minimum muscle-tendon unit length in initial swing. Positive and negative work values were calculated by integrating the positive and negative portions of the power curve, respectively, over this interval. Positive and negative work were summed to estimate net work (shaded area in **Figure 1**). Effective stiffness of the muscle-tendon unit was calculated as the slope of the force-excursion plot from the instance of minimum excursion during early stance to maximum excursion (asterisks in **Figure 1**). Total excursion was defined as the difference between maximum excursion and minimum excursion.

Two-way mixed ANOVAs with Bonferroni *post-hoc* corrections were used to evaluate the effects of age group and walking speed on work, effective stiffness, and excursion for the gastrocnemius and soleus ($p = 0.05$ significance). Mean values are presented with standard deviations in parentheses [i.e., mean (SD)].

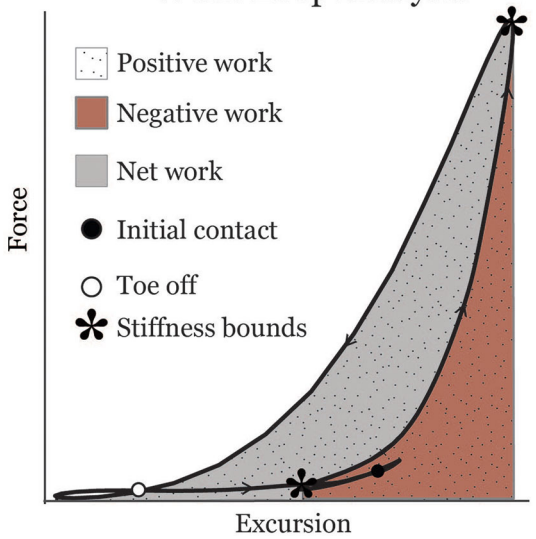

FIGURE 1 | Representative soleus muscle-tendon work-loop displaying metrics analyzed in this study. Asterisks indicate bounds from which an effective stiffness measure was calculated.

RESULTS

Work

Gastrocnemius (gas) and soleus (sol) work loops varied significantly with speed and between age groups (**Figure 2**). Muscle-tendon loading patterns during stretch were relatively invariant with walking speed for both groups. However, the subsequent loading during shortening was substantially extended with increasing walking speeds, particularly in the soleus. On average, older adults exhibited muscle-tendon work loops that were characterized by lower force magnitudes, and less positive work in shortening. Statistically, net work was significantly increased with speed (main speed effect, gas, sol: $p < 0.001$) and was lower in older adults (main age effect, gas, sol: $p < 0.005$) (**Figure 3**, **Table 1**). The age-related deficit in net work was in part due to a significant (main age effect, gas: $p = 0.03$, sol $= 0.02$) deficit in positive work. Positive work increased with speed (main speed effect, gas, sol: $p < 0.001$). No age-speed interactions were observed in net or positive work for either muscle. However, negative work exhibited an age-by-speed interaction (sol: $p < 0.002$) for the soleus. Young adults did progressively less negative work with increasing speed, as determined by *post-hoc* comparisons. However, in the older adults, negative soleus work was relatively constant across speeds, with a small reduction present only at the fastest walking speed (1.50 m/s) compared to the other speeds. For the gastrocnemius,

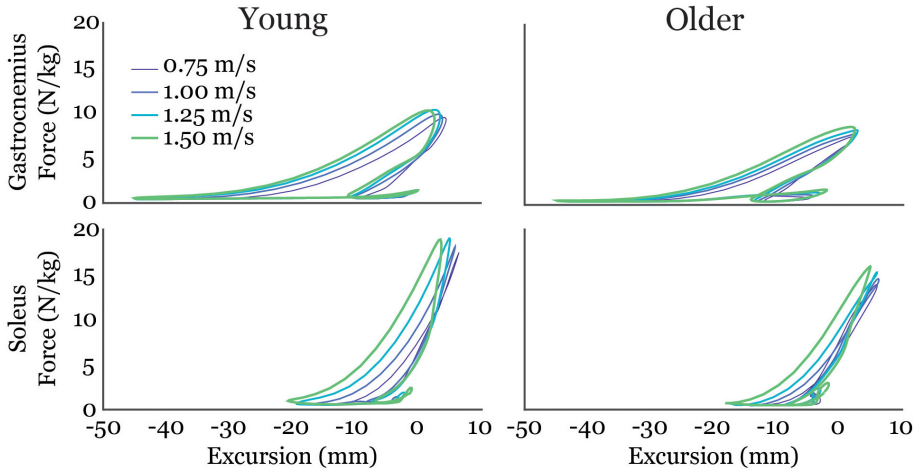

FIGURE 2 | Average gastrocnemius (top row) and soleus (bottom row) work-loops for young and older adults at each of the four walking speeds tested. Excursion of each muscle-tendon unit was defined as the muscle length relative to its length in an upright posture.

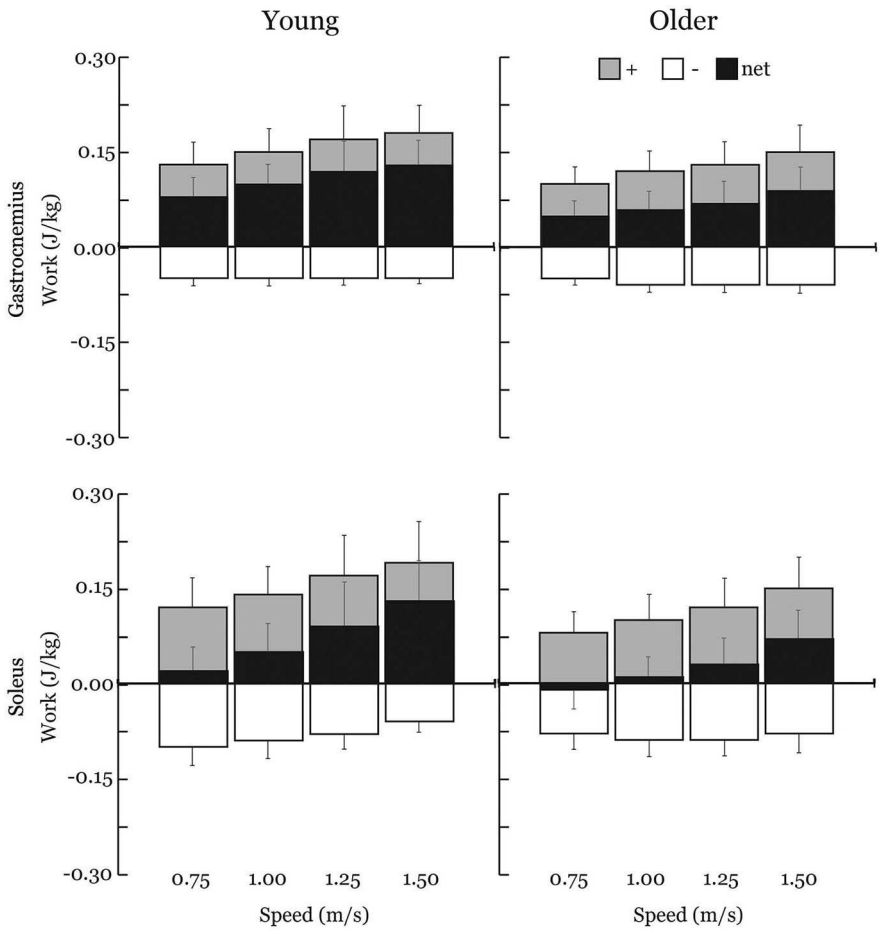

FIGURE 3 | Average positive (+), negative (–), and net muscle-tendon work across walking speeds with one-directional standard deviation error bars. Older adults exhibited substantial reductions in net work production by both the soleus (−66%) and the gastrocnemius (−36%) across all walking speeds. Positive and net work significantly increased with speed (main speed effect) and were significantly lower in older adults (main age effect) for both the gastrocnemius and soleus. Negative work exhibited an age-by-speed interaction for the soleus; only young adults did less negative work with increasing speed. Negative work was not different between young and older adults for the gastrocnemius.

TABLE 1 | Net muscle-tendon work (J/kg) significantly increased with walking speed (main speed effect, gastrocnemius, soleus: $p < 0.001$) and was lower in older adults (main age effect, gastrocnemius, soleus: $p < 0.005$).

Speed (m/s)	GASTROCNEMIUS		Soleus	
	Young	Older	Young	Older
0.75	0.08 (0.03)	0.05 (0.02)	0.02 (0.04)	−0.01 (0.03)
1.00	0.10 (0.03)	0.06 (0.03)	0.05 (0.04)	0.01 (0.03)
1.25	0.12 (0.05)	0.07 (0.03)	0.09 (0.07)	0.03 (0.04)
1.50	0.13 (0.04)	0.09 (0.04)	0.13 (0.06)	0.07 (0.04)

We did not observe a significant interaction effect (gastrocnemius: p = 0.35, soleus: p = 0.05).

TABLE 2 | Effective muscle-tendon stiffness ($N \bullet kg^{-1} \bullet mm^{-1}$) did not significantly differ with age (group main effect, gastrocnemius: $p = 0.18$, soleus: $p = 0.24$).

Speed (m/s)	GASTROCNEMIUS		Soleus	
	Young	Older	Young	Older
0.75	0.59 (0.18)	0.50 (0.24)	1.18 (0.37)	1.07 (0.50)
1.00	0.55 (0.14)	0.46 (0.20)	1.23 (0.35)	1.04 (0.40)
1.25	0.53 (0.12)	0.43 (0.20)	1.31 (0.35)	1.07 (0.43)
1.50	0.50 (0.11)	0.41 (0.20)	1.33 (0.34)	1.15 (0.51)

The soleus effective stiffness increased (speed main effect, p = 0.02) while the gastrocnemius stiffness decreased with walking speed (speed main effect, p < 0.001). We did not observe a significant interaction effect (gastrocnemius: p = 0.84, soleus: p = 0.39).

TABLE 3 | Total muscle-tendon excursion (mm) significantly increased with speed (main speed effect, gas, sol: $p < 0.001$) but did not differ between age groups (main age effect, gas, sol: $p = 0.29$).

Speed (m/s)	GASTROCNEMIUS		Soleus	
	Young	Older	Young	Older
0.75	43.08 (4.09)	41.29 (5.78)	21.26 (3.81)	19.64 (5.36)
1.00	47.02 (3.56)	44.79 (5.34)	23.51 (3.49)	21.72 (5.33)
1.25	49.47 (3.55)	47.41 (5.41)	25.74 (4.23)	23.61 (5.66)
1.50	49.32 (3.62)	48.46 (4.97)	26.05 (4.24)	24.30 (5.18)

We did not observe a significant interaction effect (gastrocnemius: p = 0.54, soleus: p = 0.90).

negative work exhibited a speed effect but not an age effect (main speed effect, gas: $p < 0.001$; main age effect, gas: $p = 0.14$).

Effective Stiffness and Total Excursion

The relationship between tendon loading and muscle-tendon excursion showed a strong linear relationship (sol: $R^2 = 0.87 \pm 0.08$, range: 0.58–0.98; gas: $R^2 = 0.90 \pm 0.06$, range: 0.74–0.98). There were no significant differences in effective stiffness with age (group main effect, gas: $p = 0.18$, sol: $p = 0.24$) (**Table 2**). However, there was a significant increase in soleus effective stiffness with walking speed (speed main effect, sol: $p = 0.02$) and a significant decrease in gastrocnemius stiffness with walking speed (speed main effect, gas: $p < 0.001$). The total excursion increased with speed (main speed effect, gas, sol: $p < 0.001$) but did not differ between age groups (main age effect, gas, sol: $p = 0.29$) (**Table 3**).

DISCUSSION

This study leveraged shear wave tensiometry to characterize the work done by the triceps surae during gait. We show that muscle-tendon lengthening behavior (effective stiffness) varies with speed, but is generally similar between age groups. However, we observed a marked age-related deficit in net soleus (−66% on average) and gastrocnemius (−36%) work across all walking speeds. The soleus results are consistent with prior reports of an age-related deficit in ankle power, though joint level analyses have often only found significant deficits at faster walking speeds (Silder et al., 2008). Notably, we did not observe an age-speed interaction effect on work; suggesting the age-related deficit in triceps surae output in walking is pervasive and not linked to increasing mechanical demands of the task.

The effective stiffness exhibited by the triceps surae was dependent on speed, but did not vary with age. Gastrocnemius stiffness decreased with walking speed, reflecting greater compliance at the muscle-tendon level. The increased compliance is attributable to gastrocnemius shortening with knee flexion in stance, which increases with walking speed. Both young and older adults exhibit greater effective soleus stiffness with increasing speed, a result that is consistent with ankle stiffness. Effective ankle stiffness, based on the slope of the moment-angle curve, also increases with speed (Frigo et al., 1996; Shamaei et al., 2013) but exhibits no difference between young and older adults walking at the same normalized speed (Crenna and Frigo, 2011). Another study found effective ankle stiffness did not correlate with age in a group of older adult women (65–91 years old) (Collins et al., 2018). Interestingly, the structural behavior of older adult tendon has been shown to differ from young adults, with there being an age-related increase in tendon compliance (Onambele et al., 2006; Stenroth et al., 2012). Thus, older adults likely maintain functionally similar effective stiffness at the muscle-tendon level by altering muscle contraction behavior. Indeed, prior studies have revealed age-related differences in soleus activation patterns (Schmitz et al., 2009) and fascicle behavior under matched walking speed conditions (Panizzolo et al., 2013). There is evidence that older adults utilize co-activation of the soleus and tibialis anterior to modulate ankle stiffness in mid-stance (Schmitz et al., 2009), which may in part be a compensation for increased tendon compliance.

There were age-related distinctions in how triceps surae work was modulated with speed. Young adults increased net soleus work by not only doing more positive work, but also doing less negative work at faster speeds. Older adults, however, did not show this trend and instead exhibited similar negative work across speeds. Ultrasound studies show soleus force-elongation behavior in stance tends to correspond with isometric behavior at the fascicle level (Cronin et al., 2013). Age-related increases in mid-stance soleus activity (Schmitz et al., 2009) may contribute to the relatively greater amounts of negative work at the faster

walking speeds observed in this study. Speed-related distinctions in the work loop curves (**Figure 2**) emerged as the muscle-tendon reached peak stretch in stance and began shortening. Muscle fascicles are rapidly shortening in this period, with the rate of shortening increasing with walking speed (Lai et al., 2015). There are thus two possible contributors to the age-dependent deficit in positive work in this phase. First, older adult muscles may simply be less capable of generating force at higher contraction rates (Thelen, 2003). Second, an increase in tendon compliance could necessitate faster muscle shortening as the tendon stretches and then recoils during push-off. Further investigations that couple shear wave tensiometry with imaging of muscle-tendon interactions could provide insight into the relative influence of these factors.

Some notable assumptions and limitations should be considered. Subject-specific calibration was used to transform the wave speed measures to Achilles tendon loading. Our calibration approach for estimating tendon force from ankle torque relied on assumptions about muscle load sharing (Ebrahimi et al., 2020). While we did use EMG measures to ensure co-contraction was not present, we did not account for plantarflexors other than the triceps surae and this likely resulted in a slight overestimate of Achilles tendon force. We also measured subject-specific moment arms of the Achilles tendon, but our gastrocnemius excursion estimates relied on generic knee moment arm measures from the literature (Buford et al., 1997). We acknowledge that the standing sway calibration inherently produces a relatively lower force than arises during typical gait, and extrapolation is necessary to calculate tendon loading during gait. For example, max Achilles tendon forces during the sway calibration used here were an average of 46% lower than the peak Achilles tendon total forces walking at 1.25 m/s. We distributed net triceps surae load based on relative physiological cross-sectional area of the gastrocnemius and soleus (Hof et al., 2002). However, it is possible that the load distribution between triceps surae muscles varies between individuals and over time. Hence while our tensiometer approach allows us to characterize the net force and work done by the Achilles tendon, there remains uncertainty when decomposing the contributions of individual muscles. Our study analyzed muscle work patterns under controlled laboratory conditions which may not reflect real-world behavior. We are currently working on a portable shear wave tensiometer that could be coupled with wearable kinematic sensors to characterize muscle-tendon behavior during real-world gait. Several comparative biomechanists have effectively used similar coupled kinematic-kinetic approaches to understand animal muscle-tendon mechanics during real world locomotion (Roberts et al., 1997; Dickinson et al., 2000; Biewener et al., 2004; Daley et al., 2009).

In conclusion, this study demonstrates the novel use of tensiometry to characterize differences in triceps surae behavior during walking. Our results show that age-related deficit in triceps surae work production are evident even at slow walking speeds. These observations suggest that aging is associated with a fundamental decline in the reliance on the triceps surae to power walking and that this shift seems unrelated to the absolute mechanical demands of the task.

DATA AVAILABILITY STATEMENT

The datasets generated for this study are available on request to the corresponding author.

ETHICS STATEMENT

The studies involving human participants were reviewed and approved by University of Wisconsin-Madison Health Sciences Institutional Review Board. The patients/participants provided their written informed consent to participate in this study.

AUTHOR CONTRIBUTIONS

AE, JM, and DT designed the study. AE collected and analyzed data, and prepared original draft and created figures. AE, JM, DS, and DT interpreted data. JM, DS, and DT reviewed, edited, and contributed to text. DT secured funding. All authors contributed to the article and approved the submitted version.

FUNDING

The funding was provided by NIH HD092697 and AG051748.

ACKNOWLEDGMENTS

We thank Isaac Loegering and Robin Pomeroy for assistance with data collection and processing related to this work.

REFERENCES

Biewener, A. A., McGowan, C., Card, G. M., and Baudinette, R. V. (2004). Dynamics of leg muscle function in tammar wallabies (*M. eugenii*) during level versus incline hopping. *J. Exp. Biol.* 207, 211–223. doi: 10.1242/jeb.00764

Biewener, A. A., and Roberts, T. J. (2000). Muscle and tendon contributions to force, work, and elastic energy savings: a comparative perspective. *Exerc. Sport Sci. Rev.* 28, 99–107.

Buford, J., Ivey, J., Malone, J. D., Patterson, R. M., Peare, G. L., Nguyen, D. K., et al. (1997). Muscle balance at the knee - Moment arms for the normal knee and the ACL-minus knee. *IEEE Trans. Rehabil. Eng.* 5, 367–379. doi: 10.1109/86.650292

Cespedes, I. (1995). Methods for estimation of subsample time delays of digitized echo signals. *Ultrason. Imaging* 17, 142–171. doi: 10.1006/uimg.1995.1007

Cofré, L. E., Lythgo, N., Morgan, D., and Galea, M. P. (2011). Aging modifies joint power and work when gait speeds are matched. *Gait Posture* 33, 484–489. doi: 10.1016/j.gaitpost.2010.12.030

Collins, J. D., Arch, E. S., Crenshaw, J. R., Bernhardt, K. A., Khosla, S., Amin, S., et al. (2018). Net ankle quasi-stiffness is influenced by walking speed but not age for older adult women. *Gait Posture* 62, 311–316. doi: 10.1016/j.gaitpost.2018.03.031

Collins, T. D., Ghoussayni, S. N., Ewins, D. J., and Kent, J. A. (2009). A six degrees-of-freedom marker set for gait analysis: repeatability and

comparison with a modified Helen Hayes set. *Gait Posture* 30, 173–180. doi: 10.1016/j.gaitpost.2009.04.004

Conway, K. A., and Franz, J. R. (2020). Shorter gastrocnemius fascicle lengths in older adults associate with worse capacity to enhance push-off intensity in walking. *Gait Posture* 77, 89–94. doi: 10.1016/j.gaitpost.2020.01.018

Crenna, P., and Frigo, C. (2011). Dynamics of the ankle joint analyzed through moment-angle loops during human walking: gender and age effects. *Hum. Mov. Sci.* 30, 1185–1198. doi: 10.1016/j.humov.2011.02.009

Cronin, N. J., Avela, J., Finni, T., and Peltonen, J. (2013). Differences in contractile behaviour between the soleus and medial gastrocnemius muscles during human walking. *J. Exp. Biol.* 216, 909–914. doi: 10.1242/jeb.078196

Daley, M. A., Voloshina, A., and Biewener, A. A. (2009). The role of intrinsic muscle mechanics in the neuromuscular control of stable running in the guinea fowl. *J. Physiol.* 587, 2693–2707. doi: 10.1113/jphysiol.2009.171017

DeVita, P., and Hortobagyi, T. (2000). Age causes a redistribution of joint torques and powers during gait. *J. Appl. Physiol.* 88, 1804–1811. doi: 10.1152/jappl.2000.88.5.1804

Dickinson, M. H., Farley, C. T., Full, R. J., Koehl, M. A. R., Kram, R., Lehamn, S. (2000). How animals move: an integrative view. *Science* 288, 100–106. doi: 10.1126/science.288.5463.100

Ebrahimi, A., Goldberg, S. R., and Stanhope, S. J. (2017). Changes in relative work of the lower extremity joints and distal foot with walking speed. *J. Biomech.* 58, 212–216. doi: 10.1016/j.jbiomech.2017.04.012

Ebrahimi, A., Loegering, I. F., Martin, J. A., Pomeroy, R. L., Roth, J. D., and Thelen, D. G. (2020). Achilles tendon loading is lower in older adults than young adults across a broad range of walking speeds. *Exp. Gerontol.* 137:110966. doi: 10.1016/j.exger.2020.110966

Frigo, C., Crenna, P., and Jensen, L. M. (1996). Moment-angle relationship at lower limb joints during human walking at different velocities. *J. Electromyogr. Kinesiol.* 6, 177–90.

Handsfield, G. G., Meyer, C. H., Hart, J. M., Abel, M. F., and Blemker, S. S. (2014). Relationships of 35 lower limb muscles to height and body mass quantified using MRI. *J. Biomech.* 47, 631–638. doi: 10.1016/j.jbiomech.2013.12.002

Hawkins, D., Lum, C., Gaydos, D., and Dunning, R. (2009). Dynamic creep and pre-conditioning of the Achilles tendon *in-vivo*. *J. Biomech.* 42:2813–2817. doi: 10.1016/j.jbiomech.2009.08.023

Hof, A. L., Van Zandwijk, J. P., and Bobbert, M. F. (2002). Mechanics of human triceps surae muscle in walking, running and jumping. *Acta Physiol. Scand.* 174, 17–30. doi: 10.1046/j.1365-201x.2002.00917.x

Josephson, R. K. (1985). Mechanical power output from striated muscle during cyclic contraction. *J. Exp. Biol.* 114, 493–512.

Judge, J. O., Davis, R. B., and Ounpuu, S. (1996). Step length reductions in advanced age: the role of ankle and hip kinetics. *J. Gerontol. A Biol. Sci. Med. Sci.* 51, M303–M312.

Kerrigan, D. C., Todd, M. K., Della Croce, U., Lipsitz, L. A., and Collins, J. J. (1998). Biomechanical gait alterations independent of speed in the healthy elderly: evidence for specific limiting impairments. *Arch. Phys. Med. Rehabil.* 79, 317–322. doi: 10.1016/S0003-9993(98)90013-2

Keuler, E., Loegering, I., Martin, J., Roth, J., and Thelen, D. (2019). Shear wave predictions of Achilles tendon loading during human walking. *Sci. Rep.* 9, 1–9. doi: 10.1038/s41598-019-49063-7

Lai, A., Lichtwark, G. A., Schache, A. G., Lin, Y. C., Brown, N. A. T., and Pandy, M. G. (2015). *In vivo* behavior of the human soleus muscle with increasing walking and running speeds. *J. Appl. Physiol.* 118, 1266–1275. doi: 10.1152/japplphysiol.00128.2015

Martin, J. A.,Brandon, S. C. E., Keuler, E. M., Hermus, J. R., Ehlers, A. C., Segalman, D. J., et al. (2018). Gauging force by tapping tendons. *Nat. Commun.* 9, 1–9. doi: 10.1038/s41467-018-03797-6

McGowan, C. P., Neptune, R. R., and Kram, R. (2008). Independent effects of weight and mass on plantar flexor activity during walking: implications for their contributions to body support and forward propulsion. *J. Appl. Physiol.* 105, 486–494. doi: 10.1152/japplphysiol.90448.2008

Nagai, K., Yamada, M., Uemura, K., Yamada, Y., Ichihashi, N., and Tsuboyama, T. (2011). Differences in muscle coactivation during postural control between healthy older and young adults. *Arch. Gerontol. Geriatr.* 53, 338–343. doi: 10.1016/j.archger.2011.01.003

Onambele, G. L., Narici, M. V., and Maganaris, C. N. (2006). Calf muscle-tendon properties and postural balance in old age. *J. Appl. Physiol.* 100, 2048–2056. doi: 10.1152/japplphysiol.01442.2005

Panizzolo, F. A., Green, D. J., Lloyd, D. G., Maiorana, A. J., and Rubenson, J. (2013). Soleus fascicle length changes are conserved between young and old adults at their preferred walking speed. *Gait Posture* 38, 764–769. doi: 10.1016/j.gaitpost.2013.03.021

Roberts, T. J., Marsh, R. L., Weyand, P. G., and Taylor, C. R. (1997). Muscular force in running turkeys: the economy of minimizing work. *Science* 275, 1113–1115. doi: 10.1126/science.275.5303.1113

Rouse, E. J., Gregg, R. D., Hargrove, L. J., and Sensinger, J. W. (2013). The difference between stiffness and quasi-stiffness in the context of biomechanical modeling. *IEEE Trans. Biomed. Eng.* 60, 562–568. doi: 10.1109/TBME.2012.2230261

Sawicki, G. S., Lewis, C. L., and Ferris, D. P. (2009). It pays to have a spring in your step. *Exerc. Sport Sci. Rev.* 37, 130–138. doi: 10.1097/JES.0b013e31819c2df6

Schmitz, A., Silder, A., Heiderscheit, B., Mahoney, J., and Thelen, D. G. (2009). Differences in lower-extremity muscular activation during walking between healthy older and young adults. *J. Electromyogr. Kinesiol.* 19, 1085–1091. doi: 10.1016/j.jelekin.2008.10.008

Shamaei, K., Sawicki, G. S., and Dollar, A. M. (2013). Estimation of quasi-stiffness and propulsive work of the human ankle in the stance phase of walking. *PLoS ONE.* 8:e59935. doi: 10.1371/journal.pone.0059935

Silder, A., Heiderscheit, B., and Thelen, D. G. (2008). Active and passive contributions to joint kinetics during walking in older adults. *J. Biomech.* 41, 1520–1527. doi: 10.1016/j.jbiomech.2008.02.016

Stenroth, L., Peltonen, J., Cronin, N. J., Sipila, S., and Finni, T. (2012). Age-related differences in Achilles tendon properties and triceps surae muscle architecture *in vivo*. *J. Appl. Physiol.* 113, 1537–1544. doi: 10.1152/japplphysiol.00782.2012

Thelen, D. G. (2003). Adjustment of muscle mechanics model parameters to simulate dynamic contractions in older adults. *J. Biomech. Eng.* 125, 70–77. doi: 10.1115/1.1531112

Winter, D. E., Patla, A. S., Frank, J. E., and Walt, S. (1990). Biomechanical walking pattern changes in the fit and healthy elderly. *Phys. Ther.* 70, 340–347. doi: 10.1093/ptj/70.6.340

Conflict of Interest: JM and DT are co-inventors on a patent for tensiometer technology (U.S. Patent No. 10631775).

The remaining authors declare that the research was conducted in the absence of any commercial or financial relationships that could be construed as a potential conflict of interest.

frontiers in Sports and Active Living

ORIGINAL RESEARCH
published: 23 June 2020
doi: 10.3389/fspor.2020.00070

Achilles Subtendon Structure and Behavior as Evidenced From Tendon Imaging and Computational Modeling

Geoffrey G. Handsfield[1], Joachim Greiner[2,3], Josef Madl[2,3], Eva A. Rog-Zielinska[2,3], Enzo Hollville[4], Benedicte Vanwanseele[4] and Vickie Shim[1]*

[1] Auckland Bioengineering Institute, University of Auckland, Auckland, New Zealand, [2] Institute for Experimental Cardiovascular Medicine, University Heart Center Freiburg Bad Krozingen, Bad Krozingen, Germany, [3] Faculty of Medicine, University of Freiburg, Freiburg, Germany, [4] Human Movement Biomechanics Research Group, Department of Movement Sciences, KU Leuven, Leuven, Belgium

OPEN ACCESS

Edited by:
Huub Maas,
Vrije Universiteit
Amsterdam, Netherlands

Reviewed by:
Raad Khair,
University of Jyväskylä, Finland
Chavaunne Thorpe,
Royal Veterinary College (RVC),
United Kingdom

****Correspondence:***
Geoffrey G. Handsfield
g.handsfield@auckland.ac.nz

Specialty section:
This article was submitted to Biomechanics and Control of Human Movement, a section of the journal Frontiers in Sports and Active Living

Received: *31 March 2020*
Accepted: *19 May 2020*
Published: *23 June 2020*

Citation:
Handsfield GG, Greiner J, Madl J, Rog-Zielinska EA, Hollville E, Vanwanseele B and Shim V (2020) Achilles Subtendon Structure and Behavior as Evidenced From Tendon Imaging and Computational Modeling. Front. Sports Act. Living 2:70. doi: 10.3389/fspor.2020.00070

The Achilles tendon is the largest and strongest tendon in the human body and is essential for storing elastic energy and positioning the foot for walking and running. Recent research into Achilles tendon anatomy and mechanics has revealed the importance of the Achilles subtendons, which are unique and semi-independent structures arising from each of the three muscular heads of the triceps surae. Of particular importance is the ability for the subtendons to slide, the role that this has in healthy tendons, and the alteration of this property in aging and disease. In this work, we discuss technical approaches that have led to the current understanding of Achilles subtendons, particularly imaging and computational modeling. We introduce a 3D geometrical model of the Achilles subtendons, built from dual-echo UTE MRI. We revisit and discuss computational models of Achilles subtendon twisting suggesting that optimal twist reduces both rupture loads and stress concentrations by distributing stresses. Second harmonic generation imaging shows collagenous subtendons within a rabbit Achilles tendon; a clear absence of signal between the subtendons indicates an inter-subtendon region on the order of 30 μm in our rabbit animal model. Entry of wheat germ agglutinin in both the inter-fascicular and the inter-subtendon regions suggests a glycoprotein-containing inter-subtendon matrix which may facilitate low friction sliding of the subtendons in healthy mammals. Lastly, we present a new computational model coupled with human exercise trials to demonstrate the magnitude of Achilles subtendon sliding which occurs during rehabilitation exercises for Achilles tendinopathy, and shows that specific exercise can maximize subtendon sliding and interface strains, without maximizing subtendon strains. This work demonstrates the value of imaging and computational modeling for probing tendon structure-function relationships and may serve to inform and develop treatments for Achilles tendinopathy.

Keywords: finite element, MRI, second harmonic, biomechanics, function

INTRODUCTION

In the last decade, research has expanded rapidly in the areas of Achilles tendon structure and mechanics. One particularly exciting research direction pertains to the Achilles subtendons, the presence and behavior of which have only recently been reported (Szaro et al., 2009; Handsfield et al., 2016). Achilles subtendons are separate and semi-independent regions of the Achilles tendon, each arising from a different muscular head of the triceps surae—soleus, medial gastrocnemius (MG), and lateral gastrocnemius (LG) (Handsfield et al., 2016). Functionally, each subtendon is similar to a unique tendon as it transmits force from a single muscle belly. Yet each is part of the larger superstructure of the Achilles tendon and does not have fully independent motion and function. The earliest identification of the subtendons as semi-independent structures was reported by Szaro et al. (2009) when that group conducted careful dissection of human cadaveric Achilles tendons, but dissected from muscle belly toward the calcaneus. In doing so, Szaro et al. recognized and documented the presence of unique independent structures of the Achilles tendon, each associated with one of the heads of the triceps surae, and this work was subsequently replicated (Edama et al., 2014, 2016). The importance of this work may have been underappreciated as these groups reported the structures as fascicles of the Achilles tendon, and they were thus not recognized as previously unidentified structures. Handsfield et al. (2016) argued that the structures these groups had probed were on a larger size scale than fascicles and must represent a previously unreported meso-scale structure. Subtendons are composed of many fascicles and represent a functional portion of the whole Achilles tendon (Handsfield et al., 2016).

Since the recognition and reporting of subtendons, there has been a surge in tendon and subtendon research, including imaging (Handsfield et al., 2017; Clark and Franz, 2020), computational modeling (Handsfield et al., 2017; Shim et al., 2018), anatomical dissection (Pekala et al., 2017; Mahan et al., 2020), and experimental approaches (Finni et al., 2018; Maas et al., 2020). Structurally, the subtendons display an internal torsion or twisting, which can be seen by the naked eye by observing the trajectory of collagen fascicles within the Achilles (White, 1943; van Gils et al., 1996). Functionally, subtendon sliding has been proposed, as subtendons are believed to slide past one another semi-independently, similar to what has been demonstrated for fascicles (Thorpe et al., 2013, 2015). This potential mechanism offered an explanation to non-intuitive motion observed *in vivo* in the human Achilles that had previously been unexplained (Arndt et al., 2012; Slane and Thelen, 2014; Franz et al., 2015). Like the sliding that occurs between fascicles of energy-storing tendons, sliding between subtendons may be a normal property of healthy Achilles tendons that may be diminished in aging or tendinopathic tendons (Slane and Thelen, 2014; Clark and Franz, 2020). Sliding of Achilles subtendons has now been demonstrated in computational models and animal experiments (Handsfield et al., 2017; Finni et al., 2018; Maas et al., 2020), and is consistent with *in vivo* observations of dynamic movements using ultrasound imaging (Slane and Thelen, 2014; Franz et al., 2015). The nature of the interface between the subtendons is still unknown and this critically limits our understanding of the mechanics of inter-subtendon sliding.

Considerable progress in the field of tendon biomechanics has come from advances in imaging and computational modeling. *In vivo* imaging methods are a powerful tool for studying human tendon as they allow for direct investigations into the anatomy of a living patient or volunteer. Anatomy can then be assessed, compared to functional measurements of that individual, or used to build subject-specific or generalized computational models. Ultrashort echo time (UTE) MRI, for instance, allows for in-depth human tendon modeling and subject-specific analysis of tendon structure and mechanics. Imaging of animal models with second harmonic generation (SHG) imaging (Campagnola and Loew, 2003) allows a deeper probing into the micro-scale structure of the tendon. Computational modeling can explore tendon mechanics based on imaging-derived geometry and creates the opportunity for *in silico* experimentation where features and boundary conditions can be added, removed, or altered in order to explore the effects on tendon mechanics and behavior in ways that are impractical or impossible for experimental approaches. For example, *in silico* experiments can be used to explore the effect of diverse structural features or boundary conditions on the muscle-tendon system (Handsfield et al., 2017; Shim et al., 2018). Much more is still to be learned about subtendon behavior in humans, and computational modeling is an avenue for exploring subtendon motion during the activities of daily living, where force and motion data can be experimentally measured and subtendon mechanics can be modeled and probed.

In this work, we aim to reexamine our understanding of Achilles subtendon structure and mechanics, particularly that which we have explored with imaging and computational modeling. We discuss UTE MRI in its contribution to Achilles tendon imaging and present an optimized method for obtaining high-signal high-contrast images of the tendon. We perform SHG imaging in animal models to provide preliminary evidence for the existence of an inter-subtendon matrix in the Achilles tendon, defined by an absence of fibrillary collagen. Lastly, we introduce a new computational finite element model that predicts the motion of subtendons and the amount of subtendon sliding based on experimentally recorded muscle forces and joint motions during rehabilitation exercises for tendinopathy, which is discussed in the context of previous computational models revealing the mechanisms of fascicle twist and subtendon twist and sliding in the Achilles tendon.

MATERIALS AND METHODS

Ultrashort Echo Time MRI

Imaging collagen-rich tissues with very short T2* decay properties, such as tendons, is a challenge for conventional MRI (Fullerton et al., 1985) since signal cannot generally be obtained from tendon or other collagen-rich tissues when echo times (TE)

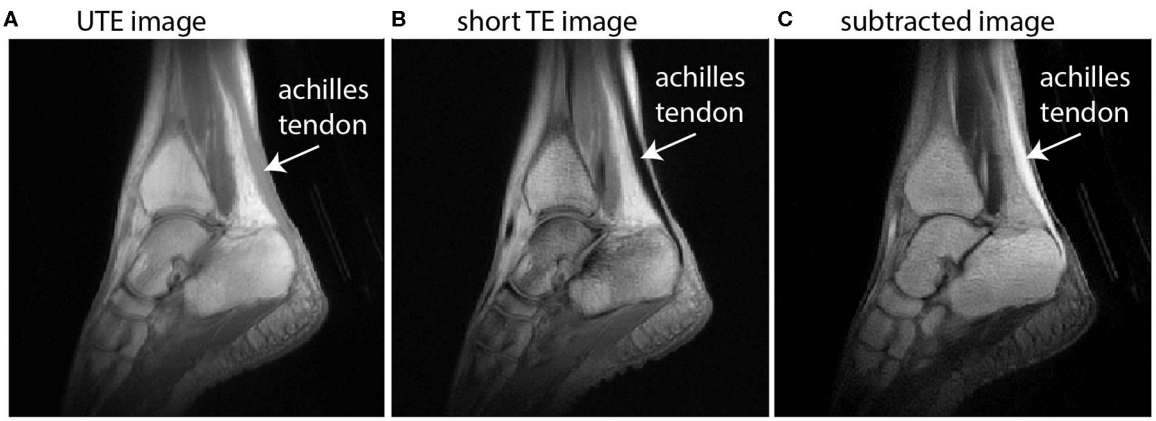

FIGURE 1 | Sagittal images of the ankle illustrate the principle of dual-echo UTE imaging of the tendon. UTE images **(A)** implement a TE that is short enough to acquire signal in the Achilles tendon but with low signal and low contrast between other tissues, particularly muscle. A conventional proton-density weighted image with short TE **(B)** is absent of any signal from the Achilles tendon. The subtracted image **(C)** offers high signal in the Achilles tendon and high contrast with neighboring tissues.

exceed ∼1 ms (see **Figure 1B**). UTE MRI uses non-Cartesian k-space trajectories to acquire images at ultrashort TEs (e.g., TE < 0.1 ms). UTE imaging has been achieved in the past using stacks of spirals (Qian and Boada, 2008; Qian et al., 2012) or 3D radial spoke acquisitions (Miller et al., 2015). For Achilles tendon MRI, UTE methods need to (i) acquire signal in the Achilles tendon and (ii) achieve contrast between the Achilles tendon and its neighboring tissues. Neighboring tissues may be subcutaneous fat, retrocalcaneal bursa, cortical bone, free fluid in the ankle, or adjacent muscles, e.g., the soleus or flexor hallucis longus.

In this work, we use dual-echo UTE imaging and image subtraction—where two images taken at the same location are subtracted to change the signal characteristics—to overcome these challenges and achieve *in vivo* images with high signal throughout the Achilles tendon and high contrast between the Achilles and its neighboring tissues (see **Figure 1**). Briefly, dual-echo UTE MRI acquires signal at two echo times—an ultrashort TE (here: 0.08 ms) and a short TE (here: 2.54 ms). Since image subtraction is implemented, the second echo time should be long enough that nearly all of the tendon signal has decayed away, but short enough that the muscle signal is similar between the two echoes. With increasingly long second TEs, image subtraction produces higher signal in the muscle tissue, which diminishes contrast between tendon and muscle. UTE images were acquired from a healthy female volunteer (height/mass/age: 163 cm/52 kg/27 years) on a 3T Siemens Trio MRI Scanner. Imaging sequence details have been described previously (Handsfield et al., 2017) and the non-Cartesian acquisition method is based on Miller et al. (2015). Here, we report an optimized sequence for dual-echo UTE and present new images to illustrate the methodological advantages of using dual-echo UTE for tendon imaging. Briefly, our sequence used the parameters TE1(UTE)/TE2(shTE)/TR/α: 0.08 ms/2.54 ms/6 ms/10°. In plane spatial resolution was 0.8 mm × 0.8 mm × 0.8 mm. Short TE images were subtracted from UTE images to maximize tendon signal and contrast (**Figure 1**).

Modeling Tendon and Subtendon Geometry From Dual-echo UTE

The creation of a 3D geometrical model of the Achilles subtendons entailed, first: segmenting the Achilles tendon in subtracted dual-echo UTE images (see **Figure 1C**). Segmentations were used to reconstruct a 3D model of the Achilles tendon in Autodesk Inventor software (Autodesk, San Rafael, CA, USA). Note that our imaging routine did not enable us to resolve individual subtendons, so our initial 3D model was of the whole Achilles. To explore subtendons within the 3D tendon, anatomical literature was used to inform the location of the three subtendons of the Achilles at the inferior/distal end of the free tendon (Sarrafian, 1993; Szaro et al., 2009). At the superior/proximal end of the free tendon, the locations of the subtendons were determined based on the anatomical location of the associated muscle. For example, at the proximal free tendon, the lateral gastrocnemius (LG) subtendon was modeled as the lateral posterior aspect of the tendon. Cutting planes were created in Autodesk Inventor that twisted 90° and subdivided the Achilles subtendons continuously from the proximal to the distal end of the free tendon. The calcaneal insertion was defined as the region of the tendon that was adjacent to the calcaneus. Cutting planes were made to extend through the calcaneal insertion region without twisting, as this is the region where subtendons fuse with the calcaneus. The cutting planes resulted in three subtendons that were consistent with literature descriptions of subtendons (Edama et al., 2014, 2016).

Second Harmonic Generation (SHG) Imaging

Second harmonic generation (SHG) imaging is a label-free microscopy method that utilizes a non-linear optical effect to visualize certain molecular structures, such as collagen fibers (Campagnola and Loew, 2003; Kahn et al., 2013). It can be combined with two-photon fluorescence microscopy

which then allows visualizing of non-collagenous structures. All investigations reported in this study conformed to the German animal welfare laws (TierSchG and TierSchVersV), compatible with the guidelines stated in Directive 2010/63/EU of the European Parliament on the protection of animals used for scientific purposes, and they were approved by the local Institutional Animal Care and Use Committees in Germany (Regierungspräsidium Freiburg, X-16/10R). Animal housing and handling was conducted in accordance with good animal practice, as defined by the Federation of European Laboratory Animal Science Association, FELASA. The Achilles tendons from one 10-months-old female New Zealand white rabbit were dissected after sacrifice by injection with sodium pentobarbital solution. Rabbits are a convenient model as they are among the largest of animals that can be housed in small animal suites, their Achilles tendons are relatively large and elastic, and their Achilles is composed of distinguishable subtendons (Doherty et al., 2006). One tendon was immediately transferred to phosphate-buffered saline (PBS) and imaged using SHG (see description below). The second tendon was transferred to a solution of 1 μg/ml Alexa Fluor 555 labeled WGA (wheat germ agglutinin, Thermo Fisher Scientific, Waltham, MA, USA) in PBS. This sample was incubated for 1 h in a 37° C bath. WGA was used here as a general tissue marker and intended in this case to localize to glycoproteins and proteoglycans in non-collagenous/non-fibrillar matrix of the tendon. After incubation, tendon samples were thoroughly rinsed in a PBS bath at room temperature to remove excess WGA. Immediately prior to imaging, samples were bisected with a scalpel either longitudinally (in the first tendon) or transversely (in the second) in order to view subtendon structure in these two planes. The cut side faced upwards toward the microscope objective.

Tendons were imaged on an upright multiphoton microscope (TCS SP8 DIVE; Leica Microsystems, Wetzlar, Germany) using a water immersion objective (IRAPO L 25×/1.00 W; Leica Microsystems) and a pulsed laser (InSight X3 Dual; Spectra-Physics, Santa Clara, CA, USA). Collagen was visualized by SHG imaging microscopy using the 920 nm laser line for excitation and a small detection window centered at 460 nm. The fluorescence of WGA-Alexa Fluor 555 was imaged in two-photon fluorescence excitation using the 1,045 nm laser line and a detection window from 577 to 633 nm. 3D imaging was performed by recording z-stacks (442.9 μm × 442.9 μm in x-y, between 80 and 225 μm z-range). In order to image over 2–4 mm in x- and y-direction, several z-stacks were recorded in tile scanning mode. Stitching and image processing was done in Leica LAS-X (Leica Microsystems).

Finite Element Modeling of Achilles Subtendons

In this study, we used ten subject-specific FE models of the Achilles tendon generated from human cadavers and performed *in silico* experiments in various aspects of tendon fascicle twist angles. The finite element (FE) mesh of the human Achilles tendon was developed using the Visible Human dataset (Ackerman, 1998) using high order cubic Hermite elements that preserve both the continuity of nodal values and their first derivatives. As in our previous tendon studies (Shim et al., 2014, 2018; Hansen et al., 2017), we used Free Form Deformation (Fernandez et al., 2004, 2018) to morph the generic tendon mesh to match morphometrical features of individual participants whose tendons were scanned with ultrasound. Features included length, average cross-sectional area, anterior-posterior length, and medial-lateral length at 50% of the tendon length.

Fascicle twist was incorporated into the model with the structure-based material coordinate system using an FE field fitting procedure. First, the structure-based material coordinate system was rotated to reflect the degree of fascicle twist and then the initial FE reference material coordinate system was rotated using three sequential rotations based on Euler angles to align it with the prescribed fascicle twist. These Euler angles were then fitted as a finite element field (Mithraratne et al., 2010). We repeated this for four different twist angles−15, 30, 45, and 60°–for 10 subject-specific FE models of the tendon from our previous study (Shim et al., 2014). We then performed tendon rupture experiments with these models by performing uniaxial stretch and measuring von Mises stress until it reached the failure load (Wren et al., 2001). The predicted rupture loads for different twist angles were analyzed using one-way ANOVA to test for significant differences between twist angles ($p < 0.05$). Sensitivity analyses were performed to comparatively characterize the influence of the following factors on tendon strength: (1) fascicle twist angles, (2) cross sectional area (CSA), and (3) tendon stiffness. Parameters were varied according to means and standard deviations reported in the literature (van Gils et al., 1996; Wren et al., 2001, 2003).

Subtendon models were generated from the morphed subject-specific model, and based on the subtendon geometry described above. For computational simplification, we combined the medial and lateral gastrocnemius subtendons into a single "gastrocnemius subtendon," creating a model consisting of a soleus subtendon and gastrocnemius subtendon. Note that while this model is appropriate for probing the sliding mechanics between the gastrocnemius and soleus subtendons, it should not be taken to imply non-independence of the two gastrocnemius subtendons. The element boundary between our subtendons was formed using the previous anatomical studies that showed subtendon boundaries in dissected human Achilles tendons (Szaro et al., 2009; Pekala et al., 2017).

The material model used here was based on a transversely isotropic hyperelastic material model that treats the tendon as a composite of collagen fascicles embedded in a matrix of ground substance (Weiss et al., 1996). Values for material property terms were taken as the average *in vivo* material properties estimated in our previous study (Hansen et al., 2017). Briefly, in that study we used 3D ultrasound *in vivo* to measure tendon deformation under maximum voluntary isometric contraction (MVIC). Using resting and 70% MVIC value, we found optimum parameters for the following three terms in the material model—the stiffness of ground substance, rate of collagen fiber loading, and Young's modulus of straightened fibers. Values used were the average from eight participants involved in the aforementioned study.

We modeled the contact condition between subtendons as frictionless contact. Differential muscle forces for soleus and gastrocnemius muscles were estimated by combining experimental data and musculoskeletal modeling that used a dynamic optimization algorithm by taking into account muscle-tendon dynamics of lower limb muscles (Swinnen et al., 2018) Briefly, four male participants ($n = 4$, age: 25.0 ± 2.4 years, height: 180.8 ± 3.0 cm, body mass: 69.7 ± 4.3 kg) performed rehabilitation exercises based on Alfredson's protocol (Alfredson et al., 1998) while we performed 3D motion capture (100 Hz; Vicon, Oxford Metrics, UK). Rehabilitation exercise protocols were ethically approved by the University Hospital Leuven Protocol S63532, and all participants provided informed written consent. The exercises included one-legged heel drop with and without bent knee, two-legged heel drop with and without extra weight (10 kg), toe- and heel walking and one-legged hopping. Ground reaction force during exercises were measured using a force plate embedded in the ground at a sampling frequency of 1,000 Hz. Each exercise was performed three times. We scaled a generic gait2392 model to subject-specific dimensions using OpenSim 3.3 (Opensim, Stanford, USA)(Delp et al., 2007). Joint angles were calculated using Kalman Smoothing and joint moments using an inverse dynamics approach. The muscle forces were then estimated using dynamic optimization with joint moments, muscle-tendon unit lengths and moment arms as inputs to solve the muscle redundancy problem by minimizing muscle activations squared (De Groote et al., 2016). For each exercise the peak soleus muscle force was found, and the soleus and gastrocnemius muscle forces at that point were applied to the subtendon sliding model as force boundary conditions where the bottom of the mesh was fixed, and the force was applied to the top surface of each subtendon as distributed forces. Two different contact conditions were used in our simulation—(1) frictionless contact to simulate subtendon sliding; (2) tied contact to simulate impaired subtendon sliding. We measured maximum displacement of each subtendon and maximum strain at the interface between subtendons. Note that differential motion between subtendons occurs even with a tied contact interface via tendon shearing.

The FE analysis was performed using CMISS (https://www.cmiss.org/), the computational framework developed as a part of the International Union of Physiological Society (IUPS) Physiome Project (Hunter et al., 2002; Hunter and Borg, 2003). The software is freely available for academic use (http://physiomeproject.org/software/opencmiss).

RESULTS

Fascicle Twist and Sliding

When tendon fascicles were modeled using a continuum-based approach, we observed a minimization of peak stresses that occurs at the typical human fascicle twist angle, implying a functional role for the structure of fascicle twisting, which is to even out peak stress/strains within the tissue. As can be seen in **Figure 2**, stress distribution patterns varied with the different amount of fascicle twist angles. When no fascicle twists are present (0° twist), the stress concentration occurs on the medial side of the tendon. However, introduction of fascicle twist from 15 to 60° redistributes this stress concentration from the medial to lateral side. When the fascicle twist angle is around 30°, there occurs a nearly even distribution of the peak stresses on the medial and lateral sides, essentially relieving stress concentrations. Interestingly, this value of fascicle twist roughly coincides with the findings from a previous anatomical study by van Gils et al. (1996) who measured fascicle twist angles from 16 human cadaver specimens and found an average of 37°.

The change in stress distribution pattern has a direct bearing on the tissue strength. When tendon rupture was simulated using the failure criteria based on a previous experimental study that reported tendon rupture load (Wren et al., 2001), we found that fascicle twist angles of 15 and 30° demonstrated improved tendon strength up to 40% compared to other twist angles (**Figure 3**). However, when the fascicle twist was put in perspective with respect to other structural features, such as cross sectional areas (CSA) and stiffness, we found the changes in CSA led to the significant changes in tissue strength while variations in the other structural features of fascicle twist and tissue stiffness did not lead to as great of changes as variations in CSA.

Subtendon Structure and Twist

Our geometrical model was used to explore the 3D structure of the Achilles subtendons. The external geometry was determined from dual-echo UTE imaging of the Achilles. We used literature descriptions of the inferior aspect of the free tendon, as well as knowledge of the locations of the triceps surae muscles, to define the proximal and distal locations of the three subtendons. From this, interpolated cutting planes defined the 3D orientation of the subtendons (**Figure 4A**), which was consistent with anatomical literature. We probed the model with axial slices at relative locations through the length of the free tendon (**Figure 4B**). The LG subtendon originates on the posterior lateral aspect of the free tendon and inserts into the anterior lateral aspect. The MG subtendon originates on the medial posterior portion of the tendon, inserting onto the lateral posterior aspect, and represents the posterior aspect of the tendon through the center of the free tendon (see e.g., **Figure 4B**, 50% slice). The soleus subtendon originates on the anterior aspect of the free tendon and inserts on the medial aspect of the free tendon.

Using this model we separated the subtendons into individual structures (**Figure 5**). The soleus subtendon is the largest of the three and has the greatest area in the calcaneal region. The LG subtendon was shorter than the other two subtendons as it inserts into the calcaneus proximal to the MG subtendon. The LG subtendon was narrower in the distal free tendon as a consequence of this proximal insertion.

Intersubtendon Matrix

Longitudinal images of rabbit Achilles tendons displayed subtendon structures within the tendon. Subtendons showed longitudinal collagen structures with evidence of collagen twisting within subtendons (**Figure 6**). Between subtendons was a non-collagenous region on the order of 30 μm in width (**Figure 6**).

We observed entry of WGA dye in the accessible region between the subtendons of the rabbit Achilles tendon in cross-sectional combined SHG and fluorescence images (**Figure 7**).

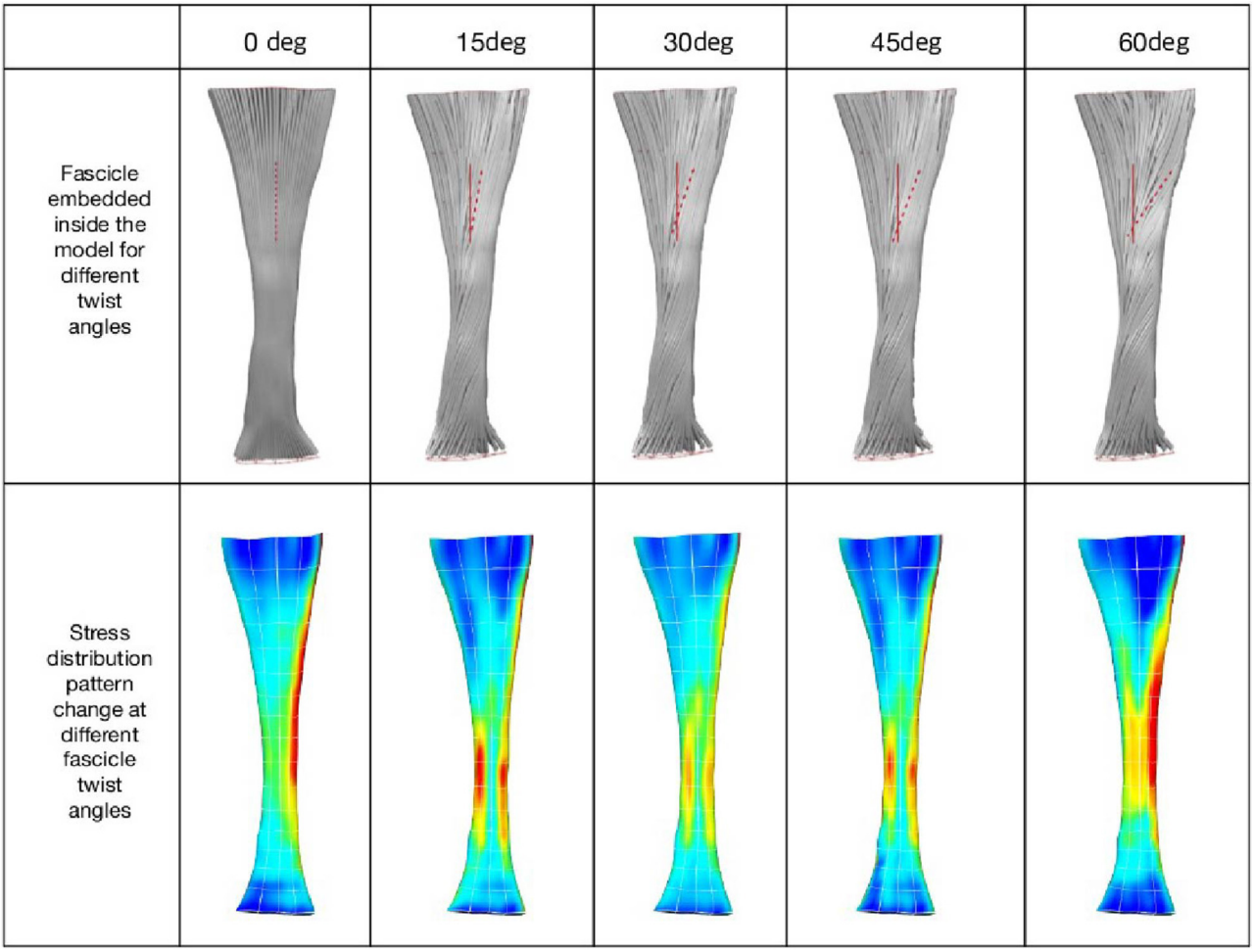

FIGURE 2 | (Top) Fascicle twist implemented in our FE models. It is an anterior view with medial on the left and lateral on the right. **(Bottom)** von Mises stress distribution across five fascicle twist angles. Posterior view with medial on the right and lateral on the left side. Adapted from Shim et al. (2018).

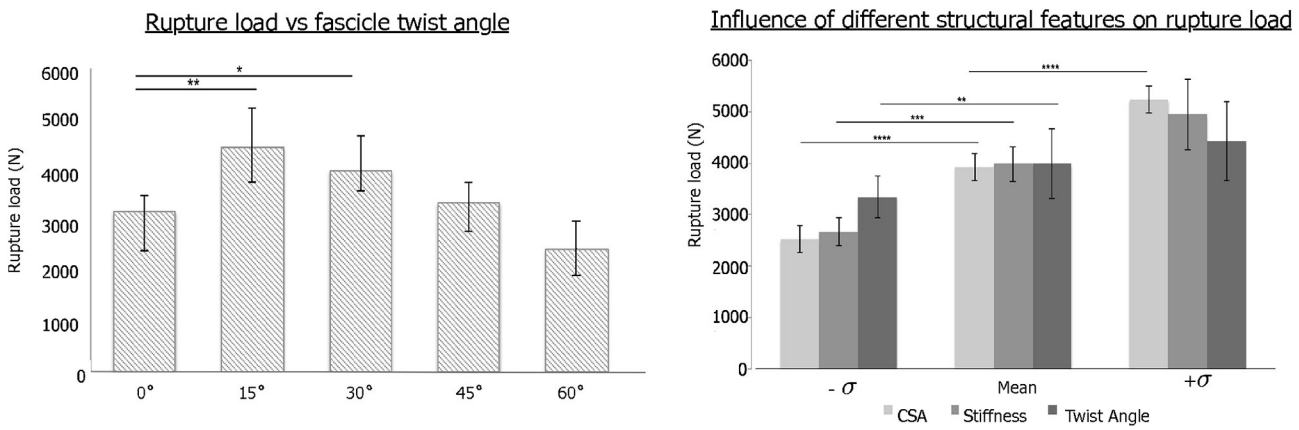

FIGURE 3 | (Left) Tendon strength significantly improved by up to 40% when the fascicle twist angle is <30° ($n = 10$ with $^{*}p < 0.05$, $^{**}p < 0.01$, $^{***}p < 0.001$). **(Right)** Sensitivity analysis revealed that tissue strength improves with increases in CSA, stiffness and fascicle angle. However, Twist angle contributes less to the tissue strength than either stiffness or CSA ($n = 10$ with $^{*}p < 0.05$, $^{**}p < 0.01$, $^{***}p < 0.001$, and $^{****}p < 0.0001$) [error bars represent standard deviation]. Adapted from Shim et al. (2018).

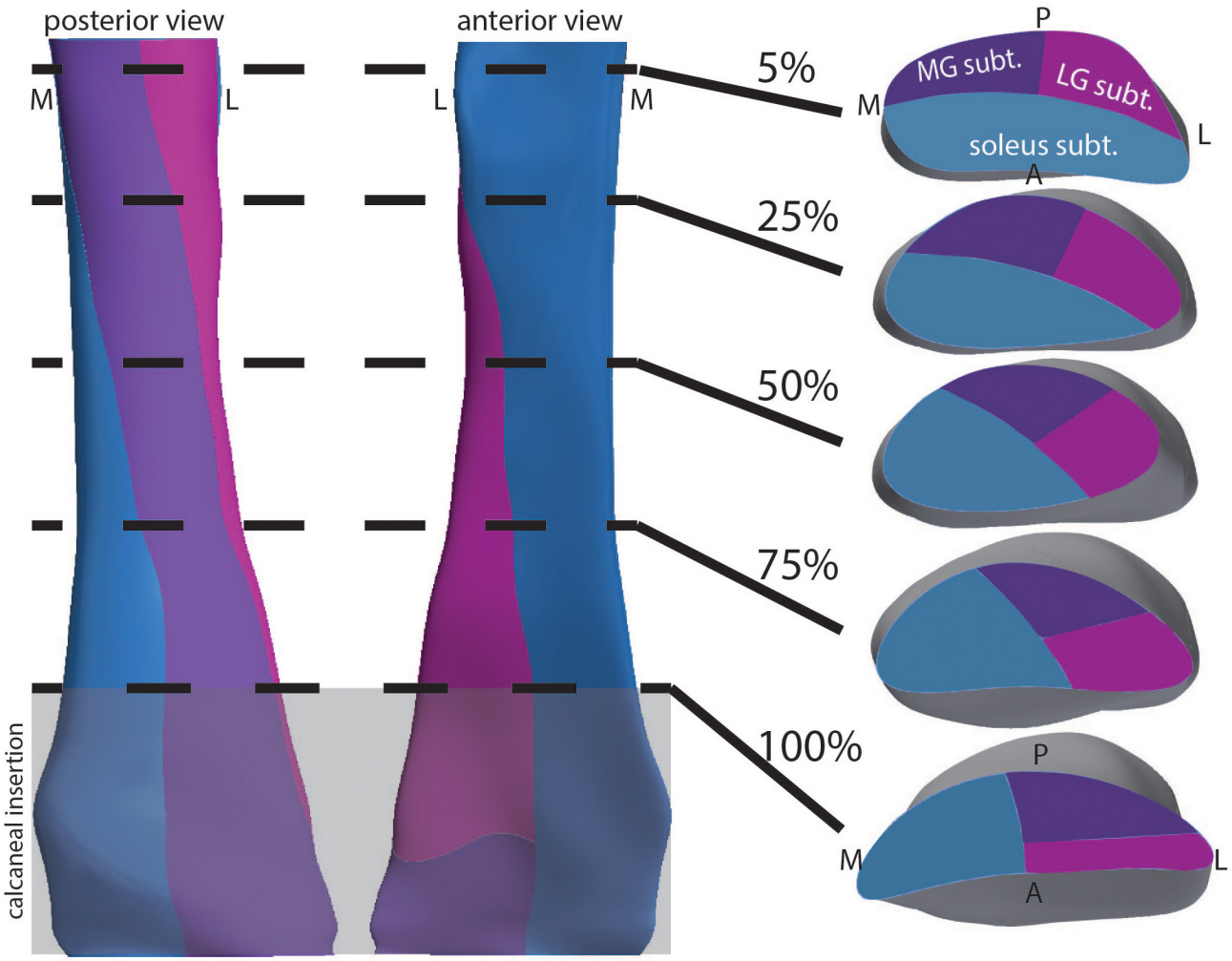

FIGURE 4 | Depiction of the 3D structure of Achilles subtendons in whole tendon and cross-section. **(A)** Posterior and anterior views of the Achilles tendon show twisting subtendons. **(B)** Cross-sectional views at relative locations from the superior to inferior aspect of the free tendon, defined as the tendon distal to muscle and proximal to calcaneus. Calcaneal insertion is windowed in gray.

Here, the SHG channel showed three subtendons in cross-section (**Figure 7A**). Fascicles are apparent within subtendons. The second channel shows fluorescently-labeled WGA that diffused into the inter-fascicular matrix as well as into the region between subtendons and bound there (**Figure 7B**), suggesting presence of an inter-subtendon matrix.

Subtendon Sliding and Interaction With Muscles

The average material property values used in subtendon sliding analysis as well as the average muscle forces used are given in **Tables 1**, **2**, respectively.

Our simulation results show that the amount of sliding and maximum strain developed at the interface are dependent on the activity type, specifically the amount of muscle forces applied to each subtendon (**Figure 8**). Under the condition of frictionless subtendon sliding, the amount of muscle forces had influenced the maximum strain values in a directly proportional manner. Muscle forces also influenced the amount of subtendon sliding but the subtendon sliding was also dependent on the type of activity. As can be seen from **Figure 8**, the amount of subtendon sliding was higher for one legged heel drop exercise with knee bent than hopping despite having smaller muscle forces associated with it. However, the amount of strain developed at the interface was almost directly proportional to the amount of muscle force applied.

The contact condition also played a role in the subtendon sliding and interface strains. When tied contact was used between the soleus and gastrocnemius subtendons in order to mimic the impaired sliding between the two subtendons,

FIGURE 5 | Anterior views of the three subtendons of the Achilles.

both sliding distance and interface strain developed were consistently lower and the differences were greater in the interface strains (**Figure 9**).

DISCUSSION

In this work, we used imaging and computational modeling to investigate the form and function of the subtendons of the Achilles tendon, to understand their behavior and how they may contribute to whole tendon function and disease. In this pursuit, we used non-Cartesian dual-echo MRI to acquire *in vivo* images of the Achilles tendon, 3D modeling to examine twisted subtendon geometry, SHG imaging to investigate the intersubtendon region in a rabbit model, and computational finite element modeling to explore the relationship between muscle forces and subtendon sliding during functional rehabilitation tasks. We further examined the functional role of fascicle twist using finite element modeling.

Ultrashort TE (UTE) MRI is an effective technique for imaging tendons in the human body and, in this study, was used to acquire 3D images of the Achilles tendon. While UTE uses an echo short enough to obtain signal from tendon and other collagenous tissues, similar signal intensity may concomitantly be obtained from surrounding tissues, especially muscle. To eliminate this unwanted signal and create high-signal-high-contrast images of the Achilles tendon, we performed dual echo UTE, where the second echo was acquired at a conventional short TE. Our final images were produced by subtracting the second echo from the first. Other imaging approaches have been used in the past to acquire tendon images, for instance ultrasound and magic angle imaging (Oatridge et al., 2001). Ultrasound is often limited to 2D planes, making it difficult to reconstruct the anatomy in 3D, although recent 3D ultrasound methods seem promising (Devaprakash et al., 2019). Magic angle imaging requires that the collagen fibers be aligned at 55° to the B0 field. This can prove cumbersome, particularly when the collagen does not have a linear trajectory within the tendon or when the tendon does not have a linear trajectory in the body, as is the case in the human Achilles.

Using the dual-echo UTE images, we performed image segmentation and developed 3D models of the Achilles tendon and its three subtendons. Subtendon geometry was created by subdividing the tendon into three parts at the superior aspect of the free tendon, and three parts at the superior aspect of the calcaneus. These locations were informed by literature descriptions of the subtendon locations (Sarrafian, 1993; Szaro et al., 2009). Using 3D modeling, the boundaries of the three subtendons were then interpolated from the superior to the inferior aspects, creating the 3D geometry of these structures. The created geometries display the internal torsion of Achilles substructures that have frequently been described and also illustrate the insertion location of each subtendon. Anatomical dissection studies have shown that collagen fibers, and the subtendons containing them, rotate about the central axis of the Achilles (White, 1943; van Gils et al., 1996; Edama et al., 2014, 2016). Furthermore, the specific orientations of the Achilles subtendons appear to be somewhat subject-specific (Edama et al., 2014; Pekala et al., 2017). Ideally, it would be beneficial to resolve the different subtendons of the Achilles tendon using *in vivo* imaging. This would allow for the creation of subject-specific models of healthy and tendinopathic individuals for simulation and investigation. Our present MRI methods did not allow us to resolve the Achilles tendon into unique subtendons—the subtendons we modeled were the result of assumptions based on literature information. Because we assume that each subtendon within an individual has similar material composition, imaging of subtendons requires that we resolve the matrix that separates the subtendons. Current resolution of our MRI methods is 800 μm. Given the apparent inter-subtendon matrix in rabbit, we propose that we would need 4–8× greater resolution in order to resolve the intersubtendon matrix in humans.

We used SHG imaging to explore the microstructure of subtendons in a rabbit animal model. SHG is a non-linear optical effect that can occur on non-centrosymmetric molecular structures, such as collagen fibrils and bundles. The SHG channel revealed strong signal in the subtendons of the Achilles and in the fascicles within the subtendons, and revealed a 30 μm region between subtendons. Fluorescence imaging of the WGA stain, which we used as a more general tissue marker, revealed that WGA diffuses into the region between the subtendons, which we believe indicates the presence of an inter-subtendon

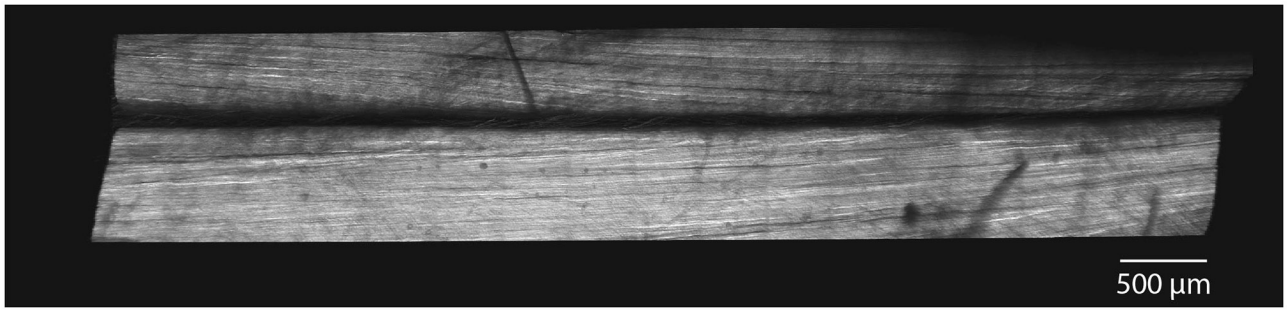

FIGURE 6 | SHG imaging demonstrate distinct subtendons in rabbit Achilles tendons. In longitudinal section, images show two distinct subtendons with collagen fascicles present within each. A non-collagenous region exists between the subtendons with a width on the order of 30 µm.

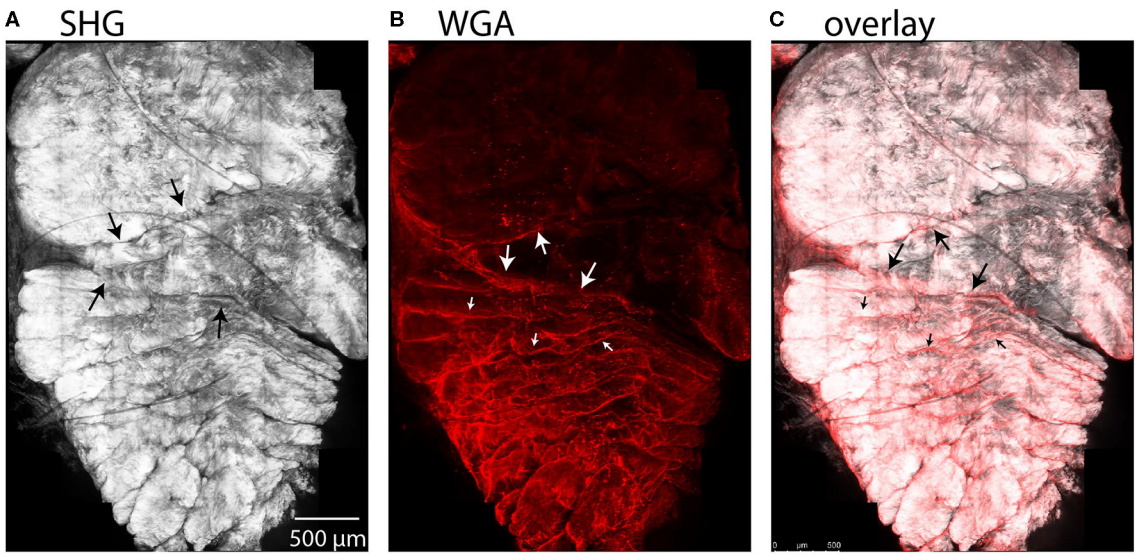

FIGURE 7 | Maximum intensity projections in a cross-sectional view of rabbit tendon over 10 z-slices. **(A)** SHG imaging demonstrated fascicles within the subtendons of the rabbit Achilles tendon. **(B)** Two-photon fluorescence microscopy revealed that WGA is present in the inter-fascicular matrix (small arrows), as well as in the region between subtendons (large arrows), indicative of an inter-subtendon matrix. **(C)** Overlay of **(A)** and **(B)**.

matrix, since this region is without signal in SHG imaging. WGA interacts with GIcNAc or sialic acid residues and thereby visualizes the presence of such glyco-moieties in this region. Furthermore, within subtendons, WGA appeared to delineate fascicles; since an inter-fascicular matrix has previously been described (Thorpe et al., 2015, 2016), this suggests that there may be compositional similarity between the region between subtendons and the matrix between fascicles within the tendon. The presence of a matrix between subtendons would lend the structures to sliding, which has been suggested in previous computational models (Handsfield et al., 2017), experimental animal models (Finni et al., 2018), and imaging experiments (Slane and Thelen, 2014; Franz et al., 2015). It is unclear why there were regional differences in both surface binding and penetration of WGA. These may be related to differences in protein content between subtendons. Further work into the composition of this matrix is needed, particularly histological and protein analysis to probe more deeply the chemical nature of this region. Further work may help in determining the friction properties that may influence inter-subtendon sliding in the Achilles tendon. Caution is always warranted when applying results from animal models to understanding human anatomy. While the rabbit Achilles has often been used as an animal Achilles model and it displays subtendons within the Achilles complex, there are anatomical differences between human and rabbit Achilles which should be considered (Doherty et al., 2006).

TABLE 1 | Material properties used in the simulation.

Ground substance stiffness	40 Mpa
Collagen fiber uncrimping rate	13
Young's Modulus of straightened fiber	1390 Mpa

In previous work, we used a continuum level finite element model to elucidate fascicle mechanics within the Achilles

TABLE 2 | Muscle forces used in the subtendon sliding simulation from four subjects for five different activities.

Activity	Two legged heel drop	One legged heel drop	One legged heel drop with knee bent	Toe walking	Hopping
Max Soleus muscle force (N)	680.6	1464.0	2371.2	1242.6	3777.4
Max Gastroc muscle force (N)	457.6	836.4	475.1	457.6	1816.8

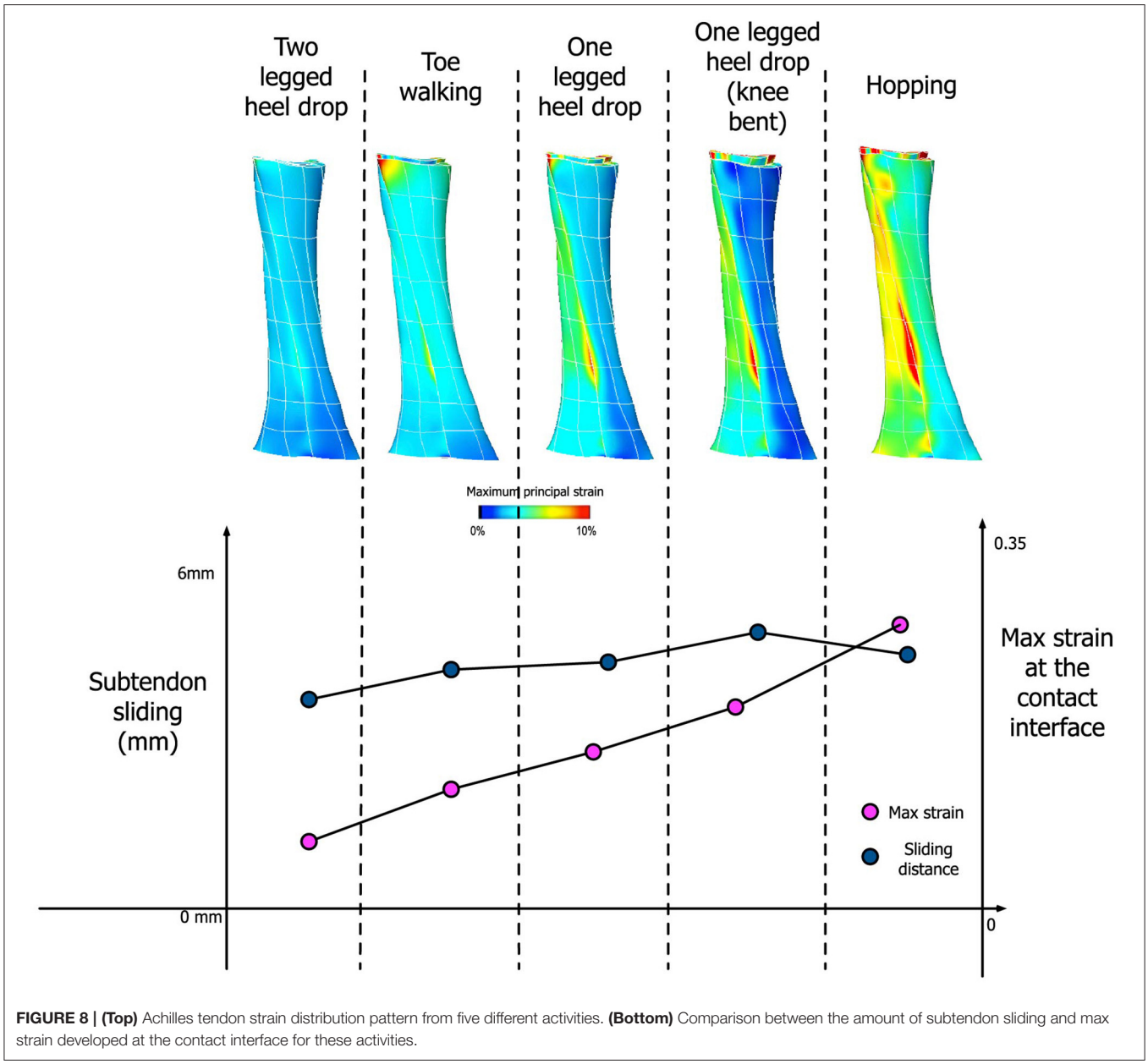

FIGURE 8 | (Top) Achilles tendon strain distribution pattern from five different activities. **(Bottom)** Comparison between the amount of subtendon sliding and max strain developed at the contact interface for these activities.

tendon. Our focus was on fascicle twist, especially its role in heterogeneous strain distribution within the tissue. We implemented a series of subject-specific Achilles tendon models to quantitatively describe the role that fascicle twist plays in tendon biomechanics. This was of particular interest as some previous studies identified heterogenous strain distribution within the tendon to be a precursor to overuse injuries and tendinopathy (Maganaris et al., 2004; Magnusson et al., 2008). Our results demonstrate that the feature of fascicle twist redistributes stress concentrations from one side of the tendon to both sides, improving overall tissue strength by up to 40%. Notably, the fascicle twist revealed as the optimum by this work is between 15 and 45°, where stress concentrations were diminished and the load required for rupture was high. This may

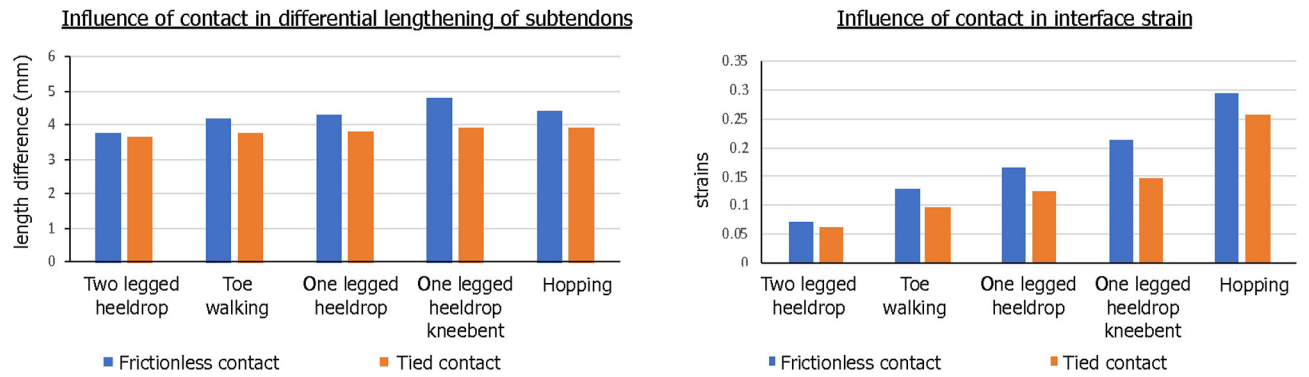

FIGURE 9 | Influence of contact condition in differential motion of subtendons and interface strains. Both the differential lengthening distance and interface strain were lower for tied contact, simulating impaired sliding interface between subtendons.

be compared to the work of van Gils et al. (1996) who found a mean fascicle twist angle of 37° in humans.

In the present study, we further developed this continuum level FE model to incorporate separate subtendon models and their sliding effects under a number of different activities. Our modeling results confirmed that differential motions of subtendons occur for various different activities, such as heel drop exercises, toe walking or hopping. What is of particular interest is the relationship between muscle forces and the degree of sliding between subtendons. Generally, the amount of subtendon sliding increased when the amount of applied muscle force increased. However, sliding distance was also dependent on the type of activity. For example, hopping resulted in the highest muscle forces but that did not translate into the largest sliding distance between subtendons. Rather, heel drop with knee bent exercise led to the largest amount of subtendon sliding. This means that those activities that generate larger differential muscle forces between the soleus and gastrocnemius muscles are likely to generate more subtendon sliding, indicating the importance of the type of exercise performed when promoting subtendon sliding. An interesting question is whether inter-subject differences in tendons are such that different individuals may require markedly different exercises to achieve differential motion and sliding of their tendons. In this study, we only collected data on 4 males of relatively similar size and fitness. Expansion of this study in the future may suggest how specifically tailored an exercise need be in order to promote Achilles rehabilitation.

Our subtendon sliding model is consistent with previous findings indicating intratendinous sliding may be reduced in aging tendons (Thorpe et al., 2013; Slane and Thelen, 2015). We showed in simulation that when subtendon sliding was impaired—via a tied contact between subtendons—both interface strains and intratendinous sliding were significantly reduced, which we propose to be a mechanism of tendon degeneration in tendinopathic tendons (Wang, 2006). Moreover, considering the imbalance of muscle excitations and force between the three heads of the triceps surae, which varied greatly between people (Crouzier et al., 2018, 2019), subtendon sliding is likely to play a major role in designing rehabilitation exercise for tendinopathy. Our results showed that individual force-sharing strategies are influenced by the type of exercise and level of contraction (different muscle force magnitude and contribution between exercises) likely leading to different subtendon stress and strain. Such variations in individual responses may imply different structural adaptations when doing the same rehabilitation program for Achilles tendinopathy. This highlights a need for better individualized and personalized training contents using experimental data and simulations, as demonstrated by the existence of "sweet spot" or optimal tendon loading by Pizzolato et al. (2019). Beyond this, it is interesting to note the differences in tendon stresses across the rehabilitation exercises—for instance, toe walking is associated with lower overall stresses than calf-raises, which are performed early in the rehabilitation process. Simulation-informed rehabilitation may be useful in the future when tailoring prescriptions for Achilles tendinopathy.

Subtendon structure and mechanics have broad implications on Achilles tendinopathy and aging in humans. It is well-established that Achilles tendinopathy is more common in middle-aged or older individuals, as well as in distance runners (Kader et al., 2002; Slane and Thelen, 2015). Given the tendency for greater differential displacements within the Achilles tendon among younger humans (Slane and Thelen, 2015), we posit that age-related changes to the subtendons and the inter-subtendon matrix may be related to the presentation of Achilles tendinopathy. With this in mind, we hypothesize age-related changes that may contribute to Achilles tendinopathy independently or in conjunction: (1) focal adhesions that develop in the inter-subtendon matrix and limit subtendon sliding, (2) age-related stiffening of the intersubtendon matrix, (3) diminished strength in the gastrocnemius muscles that prevents the forces necessary to engage subtendon sliding. Previous research on the fascicular matrix and the interfascicular matrix (IFM) shows higher turnover of collagen and other proteins within the IFM and suggests that an age-related decline in this turnover may result in a buildup of proteins in the IFM that could diminish sliding (Thorpe et al., 2016). There may

be parallels between mechanisms at the fascicle level and the subtendon level, and it is worth hypothesizing that a buildup of damaged proteins in the intersubtendon matrix may stiffen the intersubtendon matrix with aging, inhibiting sliding and contributing to tendinopathy. Prior work has established that the Achilles becomes more compliant with aging (Stenroth et al., 2012). It is unclear how this may relate to subtendon sliding, alterations of the inter-subtendon matrix, or the development of Achilles tendinopathy. Further research is needed to test these and related hypotheses and to probe the mechanisms that predispose young distance runners to tendinopathy. It may be that altered neuromuscular control with endurance training may affect muscle activation or protein turnover in a way that diminishes subtendon sliding, but this is hypothetical and warrants further investigation.

How might diminished inter-subtendon sliding promote Achilles tendinopathy? We believe this is a complex question where factors at multiple scales may influence the mechanics. We propose that inter-subtendon sliding may stimulate tenocytes in a way that promotes collagen turnover and healing of damaged tendon. A decline in sliding may cause a buildup of damaged collagen tissue which eventually becomes catastrophic and leads to overall swelling at the macroscale. We note that the finite element model presented here suggests a decline in inter-subtendon strain when sliding was prevented via a tied contact. This supports the idea that lack of sliding reduces strains, and may fall below a mechanical threshold needed to stimulate the tissue and promote health. Therapeutically, ice massage and eccentric exercises have been reported to alleviate Achilles tendinopathy (Kedia et al., 2014). It is possible that these methods work according to the same mechanism, by stimulating the tissue and promoting tenocyte activation. While we believe these are consistent ideas, at this time they remain hypothetical.

SUMMARY AND CONCLUSIONS

The Achilles tendon is composed of three subtendons—each arising from different heads of the triceps surae muscle, twisting about one another in an internally rotated direction that is somewhat subject specific, and having the ability to differentially move and slide past one another in healthy subjects. Imaging and computational modeling were used here to probe the structure and behavior of the subtendons, and deepen our understanding of the structure-function relationships of features of the tendon. Dual-echo UTE MRI was used to acquire high contrast images of the Achilles tendon. Image-based finite element models suggest that the role of twist in subtendon structure is to reduce the tendon's rupture load and distribute stresses to avoid regional stress concentrations. Consistent with literature on observed twist angles in humans, computational modeling suggests an optimum twist between 15 and 45° optimizes rupture load and stress distributions. We found a 30 μm region between rabbit subtendons with SHG imaging, suggesting a non-collagenous inter-subtendon matrix which may facilitate subtendon sliding in the Achilles. Tendon rehabilitation exercises were studied and modeled to probe their effects on subtendon motion. We found that different exercises load the subtendons differently, where a one-legged knee-bent heel drop exercise maximizes subtendon sliding without maximizing subtendon strain. Inhibition of subtendon sliding reduced the interface strains and the differential displacement of subtendons in the Achilles. More work is needed in these exciting areas of research. Understanding the fundamental structure and mechanics of the Achilles and its subtendons is an important pursuit for identifying the pathogenesis of Achilles tendinopathy and for suggesting treatment and mitigation strategies in the future.

DATA AVAILABILITY STATEMENT

The raw data supporting the conclusions of this article will be made available by the authors, without undue reservation.

ETHICS STATEMENT

The studies involving human participants were reviewed and approved by University Hospital Leuven S63532. The patients/participants provided their written informed consent to participate in this study. The animal study was reviewed and approved by Regierungspräsidium Freiburg, X-16/10R).

AUTHOR CONTRIBUTIONS

GH organized the team, wrote the bulk of the document, planned the section contributions, revised and prepared the document, and was the primary researcher on the MRI, geometrical modeling, and the SHG portion of the work. JG contributed to the development and data collection of the SHG portion of the work, and proofread, edited, and wrote sections of the document. JM conducted the technical aspects of the SHG work, oversaw data collection, and contributed sections to the document. ER-Z contributed to the experimental aspect of the SHG portion of this manuscript, oversaw sample preparation, interpreted results, proofread, and edited the document. EH and BV contributed technical aspects of the rehabilitation exercise portion of this work including data collection and analysis, contributed sections, proofread, and edited document. VS co-led the organization of this work, performed the continuum modeling portion of this work, wrote sections of the document, proofread, and edited.

FUNDING

Funding support was provided by the Aotearoa Fellowship from the Julian Robertson Foundation (Award 3715249) and institutional support from the Auckland Bioengineering Institute. EZ is an Emmy Noether Fellow of the German Research Foundation.

ACKNOWLEDGMENTS

The authors wish to acknowledge students and staff at the Institute for Experimental Cardiovascular Medicine

(IEKM) at the University of Freiburg. The authors acknowledge the microscopy facility SCI-MED (Super-Resolution Confocal/Multiphoton Imaging for Multiparametric Experimental Designs) at IEKM for providing access to the multiphoton-/SHG-imaging microscope. We would like to thank G. Wilson Miller for his contributions to our MRI work, Dane Gerneke for image processing consultation, and Sam Van Rossom for his help with dynamic optimization.

REFERENCES

Ackerman, M. J. (1998). The visible human project. *Proc. IEEE* 86, 504–511. doi: 10.1109/5.662875

Alfredson, H., Nordström, P., and Lorentzon, R. (1998). Prolonged progressive calcaneal bone loss despite early weightbearing rehabilitation in patients surgically treated for achilles tendinosis. *Calcif. Tissue Int.* 62, 166–171. doi: 10.1007/s002239900411

Arndt, A., Bengtsson, A. S., Peolsson, M., Thorstensson, A., and Movin, T. (2012). Non-uniform displacement within the achilles tendon during passive ankle joint motion. *Knee Surg. Sport. Traumatol. Arthrosc.* 20, 1868–1874. doi: 10.1007/s00167-011-1801-9

Campagnola, P. J., and Loew, L. M. (2003). Second-harmonic imaging microscopy for visualizing biomolecular arrays in cells, tissues and organisms. *Nat. Biotechnol.* 21, 1356–1360. doi: 10.1038/nbt894

Clark, W. H., and Franz, J. R. (2020). Triceps surae muscle–subtendon interaction differs between young and older adults. *Connect. Tissue Res.* 61, 104–113. doi: 10.1080/03008207.2019.1612384

Crouzier, M., Lacourpaille, L., Nordez, A., Tucker, K., and Hug, F. (2018). Neuromechanical coupling within the human triceps surae and its consequence on individual force-sharing strategies. *J. Exp. Biol.* 221, 1–13. doi: 10.1242/jeb.187260

Crouzier, M., Tucker, K., Lacourpaille, L., Doguet, V., Fayet, G., Dauty, M., et al. (2019). Force-sharing within the triceps surae: an achilles heel in achilles tendinopathy. *Med. Sci. Sport. Exerc.* 52, 1076–1087. doi: 10.1249/MSS.0000000000002229

De Groote, F., Kinney, A. L., Rao, A. V., and Fregly, B. J. (2016). Evaluation of direct collocation optimal control problem formulations for solving the muscle redundancy problem. *Ann. Biomed. Eng.* 44, 2922–2936. doi: 10.1007/s10439-016-1591-9

Delp, S. L., Anderson, F. C., Arnold, A. S., Loan, P., Habib, A., John, C. T., et al. (2007). OpenSim: open-source software to create and analyze dynamic simulations of movement. *IEEE Trans. Biomed. Eng.* 54, 1940–1950. doi: 10.1109/TBME.2007.901024

Devaprakash, D., Lloyd, D. G., Barrett, R. S., Obst, S. J., Kennedy, B., Adams, K. L., et al. (2019). Magnetic resonance imaging and freehand 3-d ultrasound provide similar estimates of free achilles tendon shape and 3-D geometry. *Ultrasound Med. Biol.* 45, 2898–2905. doi: 10.1016/j.ultrasmedbio.2019.07.679

Doherty, G. P., Koike, Y., Uhthoff, H. K., Lecompte, M., and Trudel, G. (2006). Comparative anatomy of rabbit and human achilles tendons with magnetic resonance and ultrasound imaging. *Comp. Med.* 56, 68–74.

Edama, M., Kubo, M., Onishi, H., Takabayashi, T., Inai, T., Yokoyama, E., et al. (2014). The twisted structure of the human achilles tendon. *Scand. J. Med. Sci. Sports* 25, e497–e503. doi: 10.1111/sms.12342

Edama, M., Kubo, M., Onishi, H., Takabayashi, T., Yokoyama, E., Inai, T., et al. (2016). Structure of the achilles tendon at the insertion on the calcaneal tuberosity. *J. Anat.* 229, 610–614. doi: 10.1111/joa.12514

Fernandez, J., Zhang, J., Shim, V.,Munro, J. T., Sartori,M., Besier, T., et al. (2018). "Musculoskeletal modelling and the physiome project," in *Multiscale Mechanobiology of Bone Remodeling and Adaptation* (Courses and Lectures), ed P. Pivonka, Vol. 578. (Cham: Springer; CISM International Centre for Mechanical Sciences). doi: 10.1007/978-3-319-58845-2_3

Fernandez, J. W., Mithraratne, P., Thrupp, S. F., Tawhai, M. H., and Hunter, P. J. (2004). Anatomically based geometric modelling of the musculo-skeletal system and other organs. *Biomech. Model. Mechanobiol.* 2, 139–155. doi: 10.1007/s10237-003-0036-1

Finni, T., Bernabei, M., Baan, G. C., Noort, W., Tijs, C., and Maas, H. (2018). Non-uniform displacement and strain between the soleus and gastrocnemius subtendons of rat achilles tendon. *Scand. J. Med. Sci. Sport.* 28, 1009–1017. doi: 10.1111/sms.13001

Franz, J. R., Slane, L. C., Rasske, K., and Thelen, D. G. (2015). Non-uniform *in vivo* deformations of the human Achilles tendon during walking. *Gait Posture* 41, 192–197. doi: 10.1016/j.gaitpost.2014.10.001

Fullerton, G. D., Cameron, I. L., and Ord, V. A. (1985). Orientation of tendons in the magnetic field and its effect on T2 relaxation times. *Radiology* 155, 433–435. doi: 10.1148/radiology.155.2.3983395

Handsfield, G. G., Inouye, J. M., Slane, L. C., Thelen, D. G., Miller, G. W., and Blemker, S. S. (2017). A 3D model of the achilles tendon to determine the mechanisms underlying nonuniform tendon displacements. *J. Biomech.* 51, 17–25. doi: 10.1016/j.jbiomech.2016.11.062

Handsfield, G. G., Slane, L. C., and Screen, H. R. C. (2016). Nomenclature of the tendon hierarchy: an overview of inconsistent terminology and a proposed size-based naming scheme with terminology for multi-muscle tendons. *J. Biomech.* 49, 3122–3124. doi: 10.1016/j.jbiomech.2016.06.028

Hansen, W., Shim, V. B., Obst, S., Lloyd, D. G., Newsham-West, R., and Barrett, R. S. (2017). Achilles tendon stress is more sensitive to subject-specific geometry than subject-specific material properties: a finite element analysis. *J. Biomech.* 56, 26–31. doi: 10.1016/j.jbiomech.2017.02.031

Hunter, P., Robbins, P., and Noble, D. (2002). The IUPS human physiome project. *Pflugers Arch.* 445, 1–9. doi: 10.1007/s00424-002-0890-1

Hunter, P. J., and Borg, T. K. (2003). Integration from proteins to organs: the physiome project. *Nat. Rev. Mol. Cell Biol.* 4, 237–243. doi: 10.1038/nrm1054

Kader, D., Saxena, A., Movin, T., and Maffulli, N. (2002). Achilles tendinopathy: some aspects of basic science and clinical management. *Br. J. Sports Med.* 36, 239–249. doi: 10.1136/bjsm.36.4.239

Kahn, C. J. F., Dumas, D., Arab-Tehrany, E., Marie, V., Tran, N., Wang, X., et al. (2013). Structural and mechanical multi-scale characterization of white New-Zealand rabbit achilles tendon. *J. Mech. Behav. Biomed. Mater.* 26, 81–89. doi: 10.1016/j.jmbbm.2013.05.028

Kedia, M., Williams, M., Jain, L., Barron, M., Bird, N., Blackwell, B., et al. (2014). The effects of conventional physical therapy and eccentric strengthening for insertional achilles tendinopathy. *Int. J. Sports Phys. Ther.* 9, 488–497.

Maas, H., Noort, W., Baan, G. C., and Finni, T. (2020). Non-uniformity of displacement and strain within the achilles tendon is affected by joint angle configuration and differential muscle loading. *J. Biomech.* 101:109634. doi: 10.1016/j.jbiomech.2020.109634

Maganaris, C. N., Narici, M. V., Almekinders, L. C., and Maffulli, N. (2004). Biomechanics and pathophysiology of overuse tendon injuries: ideas on insertional tendinopathy. *Sport. Med.* 34, 1005–1017. doi: 10.2165/00007256-200434140-00005

Magnusson, S. P., Narici, M. V., Maganaris, C. N., and Kjaer, M. (2008). Human tendon behaviour and adaptation, *in vivo*. *J. Physiol.* 586, 71–81. doi: 10.1113/jphysiol.2007.139105

Mahan, J., Damodar, D., Trapana, E., Barnhill, S., Nuno, A. U., Smyth, N. A., et al. (2020). Achilles tendon complex: the anatomy of its insertional footprint on the calcaneus and clinical implications. *J. Orthop.* 17, 221–227. doi: 10.1016/j.jor.2019.06.008

Miller, G. W., Eames, M., Snell, J., and Aubry, J. F. (2015). Ultrashort echo-time MRI versus CT for skull aberration correction in MR-guided transcranial focused ultrasound: *in vitro* comparison on human calvaria. *Med. Phys.* 42, 2223–2233. doi: 10.1118/1.4916656

Mithraratne, K., Hung, A., Sagar, M., and Hunter, P. J. (2010). "An efficient heterogeneous continuum model to simulate active contraction of facial soft tissue structures," in *6th World Congress of Biomechanics (WCB 2010). August 1–6, 2010 Singapore*, eds C. T. Lim and J. C. H. Goh (Berlin; Heidelberg: Springer Berlin Heidelberg), 1024–1027. doi: 10.1007/978-3-642-14515-5_261

Oatridge, A., Herlihy, A. H., Thomas, R. W., Wallace, A. L., Curati, W. L., Hajnal, J. V., et al. (2001). Magnetic resonance: magic angle imaging of the achilles tendon. *Lancet* 358, 1610–1611. doi: 10.1016/S0140-6736(01)06661-2

Pekala, P., Mlyniec, A., and Tomaszewski, K. (2017). The twisted structure of the achilles tendon unraveled–a detailed quantitative and qualitative anatomical investigation of the achilles tendon and its fascicles. *Scand. J. Med. Sci. Sport.* 27, 1705–1715. doi: 10.1111/sms.12835

Pizzolato, C., Lloyd, D. G., Zheng, M. H., Besier, T. F., Shim, V. B., Obst, S. J., et al. (2019). Finding the sweet spot via personalised achilles tendon training: the future is within reach. *Br. J. Sports Med.* 53, 11–12. doi: 10.1136/bjsports-2018-099020

Qian, Y., and Boada, F. E. (2008). Acquisition-weighted stack of spirals for fast high-resolution three-dimensional ultra-short echo time MR imaging. *Magn. Reson. Med.* 60, 135–145. doi: 10.1002/mrm.21620

Qian, Y., Williams, A. A., Chu, C. R., and Boada, F. E. (2012). High-resolution ultrashort echo time (UTE) imaging on human knee with AWSOS sequence at 3.0 T. *J. Magn. Reson. Imaging* 35, 204–210. doi: 10.1002/jmri.22639

Sarrafian, S. K. (1993). "Calcaneal (achilles) tendon," in *Anatomy of the Foot and Ankle: Descriptive Topographic Functional* (Philadelphia: J.B. Lippincott Company), 280–282.

Shim, V. B., Fernandez, J. W., Gamage, P. B., Regnery, C., Smith, D. W., Gardiner, B. S., et al. (2014). Subject-specific finite element analysis to characterize the influence of geometry and material properties in Achilles tendon rupture. *J. Biomech.* 47, 3598–3604. doi: 10.1016/j.jbiomech.2014.10.001

Shim, V. B., Handsfield, G. G., Fernandez, J. W., Lloyd, D. G., and Besier, T. F. (2018). Combining *in silico* and *in vitro* experiments to characterize the role of fascicle twist in the achilles tendon. *Sci. Rep.* 8:13856. doi: 10.1038/s41598-018-31587-z

Slane, L. C., and Thelen, D. G. (2014). Non-uniform displacements within the achilles tendon observed during passive and eccentric loading. *J. Biomech.* 47, 2831–2835. doi: 10.1016/j.jbiomech.2014.07.032

Slane, L. C., and Thelen, D. G. (2015). Achilles tendon displacement patterns during passive stretch and eccentric loading are altered in middle-aged adults. *Med. Eng. Phys.* 37, 712–716. doi: 10.1016/j.medengphy.2015.04.004

Stenroth, L., Peltonen, J., Cronin, N. J., Sipilä, S., and Finni, T. (2012). Age-related differences in achilles tendon properties and triceps surae muscle architecture *in vivo*. *J. Appl. Physiol.* 113, 1537–1544. doi: 10.1152/japplphysiol.00782.2012

Swinnen, W., Hoogkamer, W., Delabastita, T., Aeles, J., De Groote, F., and Vanwanseele, B. (2018). Effect of habitual foot-strike pattern on the gastrocnemius medialis muscle-tendon interaction and muscle force production during running. *J. Appl. Physiol.* 126, 708–716. doi: 10.1152/japplphysiol.00768.2018

Szaro, P., Witkowski, G., Smigielski, R., Krajewski, P., and Ciszek, B. (2009). Fascicles of the adult human achilles tendon–an anatomical study. *Ann. Anat.* 191, 586–593. doi: 10.1016/j.aanat.2009.07.006

Thorpe, C. T., Godinho, M. S. C., Riley, G. P., Birch, H. L., Clegg, P. D., and Screen, H. R. C. (2015). The interfascicular matrix enables fascicle sliding and recovery in tendon, and behaves more elastically in energy storing tendons. *J. Mech. Behav. Biomed. Mater.* 52, 85–94. doi: 10.1016/j.jmbbm.2015.04.009

Thorpe, C. T., Peffers, M. J., Simpson, D., Halliwell, E., Screen, H. R. C., and Clegg, P. D. (2016). Anatomical heterogeneity of tendon: fascicular and interfascicular tendon compartments have distinct proteomic composition. *Sci. Rep.* 6:20455. doi: 10.1038/srep20455

Thorpe, C. T., Udeze, C. P., Birch, H. L., Clegg, P. D., and Screen, H. R. (2013). Capacity for sliding between tendon fascicles decreases with ageing in injury prone equine tendons: a possible mechanism for age-related tendinopathy? *Eur. Cell. Mater.* 25, 48–60. doi: 10.22203/eCM.v025a04

van Gils, C. C., Steed, R. H., and Page, J. C. (1996). Torsion of the human achilles tendon. *J. Foot Ankle Surg.* 35, 41–48. doi: 10.1016/S1067-2516(96)80011-1

Wang, J. H. C. (2006). Mechanobiology of tendon. *J. Biomech.* 39, 1563–1582. doi: 10.1016/j.jbiomech.2005.05.011

Weiss, J. A., Maker, B. N., and Govindjee, S. (1996). Finite element implementation of incompressible, transversely isotropic hyperelasticity. *Comput. Methods Appl. Mech. Eng.* 135, 107–128. doi: 10.1016/0045-7825(96)01035-3

White, J. W. (1943). Torsion of the achilles tendon: its surgical significance. *Arch. Surg.* 46, 784–787. doi: 10.1001/archsurg.1943.01220110200033

Wren, T. A. L., Lindsey, D. P., Beaupré, G. S., and Carter, D. R. (2003). Effects of creep and cyclic loading on the mechanical properties and failure of human achilles tendons. *Ann. Biomed. Eng.* 31, 710–717. doi: 10.1114/1.1569267

Wren, T. A. L., Yerby, S. A., Beaupr, G. S., and Carter, D. R. (2001). Mechanical properties of the human achilles tendon. *Clin. Biomech.* 16, 245–251. doi: 10.1016/S0268-0033(00)00089-9

Conflict of Interest: The authors declare that the research was conducted in the absence of any commercial or financial relationships that could be construed as a potential conflict of interest.

frontiers in Bioengineering and Biotechnology

ORIGINAL RESEARCH
published: 17 July 2020
doi: 10.3389/fbioe.2020.00700

Force Transmission Between the Gastrocnemius and Soleus Sub-Tendons of the Achilles Tendon in Rat

Connor C. Gains[1], Janaina C. Correia[2], Guus C. Baan[2], Wendy Noort[2], Hazel R. C. Screen[1] and Huub Maas[2]*

[1] Institute of Bioengineering, School of Engineering and Materials Science, Queen Mary University of London, London, United Kingdom, [2] Department of Human Movement Sciences, Faculty of Behavioural and Movement Sciences, Vrije Universiteit Amsterdam, Amsterdam Movement Sciences, Amsterdam, Netherlands

The Achilles tendon (AT) is comprised of three distinct sub-tendons bound together by the inter-subtendon matrix (ISTM). The interactions between sub-tendons will have important implications for AT function. The aim of this study was to investigate the extent to which the ISTM facilitates relative sliding between sub-tendons, and serves as a pathway for force transmission between the gastrocnemius (GAS) and soleus (SOL) sub-tendons of the rat AT. In this study, ATs were harvested from Wistar rats, and the mechanical behavior and composition of the ISTM were explored. To determine force transmission between sub-tendons, the proximal and distal ends of the GAS and SOL sub-tendons were secured, and the forces at each of these locations were measured during proximal loading of the GAS. To determine the ISTM mechanical behavior, only the proximal GAS and distal SOL were secured, and the ISTM was loaded in shear. Finally, for compositional analysis, histological examination assessed the distribution of matrix proteins throughout sub-tendons and the ISTM. The results revealed distinct differences between the forces at the proximal and distal ends of both sub-tendons when proximal loading was applied to the GAS, indicating force transmission between GAS and SOL sub-tendons. Inter-subtendon matrix tests demonstrated an extended initial low stiffness toe region to enable some sub-tendon sliding, coupled with high stiffness linear region such that force transmission between sub-tendons is ensured. Histological data demonstrate an enrichment of collagen III, elastin, lubricin and hyaluronic acid in the ISTM. We conclude that ISTM composition and mechanical behavior are specialized to allow some independent sub-tendon movement, whilst still ensuring capacity for force transmission between the sub-tendons of the AT.

Keywords: Achilles tendon, force transmission, interfascicular matrix, shear, immunohistochemistry

OPEN ACCESS

Edited by:
Bernardo Innocenti, Université libre de Bruxelles, Belgium

Reviewed by:
Panagiotis Chatzistergos, Staffordshire University, United Kingdom
Chiara Giulia Fontanella, University of Padua, Italy

****Correspondence:***
Connor C. Gains
c.c.gains@qmul.ac.uk

Specialty section:
This article was submitted to Biomechanics, a section of the journal Frontiers in Bioengineering and Biotechnology

Received: *14 February 2020*
Accepted: *04 June 2020*
Published: *17 July 2020*

Citation:
Gains CC, Correia JC, Baan GC, Noort W, Screen HRC and Maas H (2020) Force Transmission Between the Gastrocnemius and Soleus Sub-Tendons of the Achilles Tendon in Rat. Front. Bioeng. Biotechnol. 8:700. doi: 10.3389/fbioe.2020.00700

INTRODUCTION

The Achilles tendon (AT) is the largest and strongest tendon in the human body. It forms a fundamental component of the musculoskeletal system, enabling everyday movements by bearing high loads and storing energy to reduce their energetic cost (Alexander, 1984; Komi, 1990; Fukashiro et al., 1995). In humans, the AT is exposed to forces exceeding 12 times bodyweight

during running (Komi et al., 1992), and strains of up to 16% during a one-legged hop *in vivo* (Lichtwark and Wilson, 2005). It is estimated to store up to 35% of the total energy lost and regained during locomotion (Ker et al., 1987; Alexander, 1991). Such high strains mean that the AT functions markedly close to its failure properties (Wren et al., 2001), and is consequently vulnerable to injury. Tendinopathy of the AT is a highly debilitating condition. It accounts for up to half of all sports-related injuries (Kaux et al., 2011; Freedman et al., 2014; Lantto et al., 2015; Li et al., 2017), and a notable rise in the frequency of cases among the sedentary and aging populations is also reported over recent decades (de Jonge et al., 2011). Repetitive overload has been postulated as a major precursor for tendinopathy, but due to insufficient understanding of AT structure-function relationships, the causative mechanisms behind tendinopathy remain poorly understood (Wang et al., 2006; Riley, 2008).

Tendons are hierarchical fiber-composites, in which collagen molecules aggregate to form highly ordered sub-units of increasing diameter, up to the whole tendon level. At the larger length-scales, the collagenous sub-units are interspersed with a highly hydrated proteoglycan-rich matrix (Thorpe et al., 2013a). The hierarchical structure of tendon has long been established (Kastelic et al., 1978), yet discrepancies remain prevalent in the literature regarding the correct nomenclature to define the sub-units at each length scale. This is compounded by the differences in tendon hierarchical organization seen between functionally distinct tendons, and those seen across species of different sizes. Fascicles have typically been considered to be the largest sub-unit in tendon beneath the whole tendon level, but the AT is an exception, as the tendon derives from the three distinct muscles bellies of the triceps surae complex (Bojsen-møller and Magnusson, 2015). As such, the AT includes an additional macro level between fascicles and tendon, where the elements of the AT arising from each muscle belly of the triceps surae form separate soleus (SOL) and gastrocnemius (GAS) "sub-tendons" (Handsfield et al., 2016). As the GAS and SOL sub-tendons of the AT descend from their respective muscles, they laterally rotate and insert onto the calcaneal bone (Edama et al., 2015). Along their given lengths, the AT sub-tendons are bound together by the inter-subtendon matrix (ISTM; **Figure 1**). Although the sub-tendons are tightly fused together by the ISTM, anatomical studies have shown the sub-tendons to differ morphologically, allowing them to be macroscopically distinguished and dissected (Szaro et al., 2009; Edama et al., 2015; Finni et al., 2018).

Recent human studies have demonstrated non-uniform displacements in the AT, revealing that the anterior portion of the AT experiences greater displacements than the posterior portion during passive ankle motions (Arndt et al., 2012), eccentric plantarflexor contractions (Slane and Thelen, 2014), and isometric contractions, irrespective of the knee angle or level of force produced (Bogaerts et al., 2018). While these studies in human subjects were not able to attribute the non-uniform behavior to specific sub-tendons, recent work has shown that the SOL sub-tendon in the rat AT experiences significantly different displacements and strains than the lateral GAS sub-tendon during isometric contractions (Finni et al., 2018; Maas et al., 2020), indicating non-uniform deformations of the AT sub-tendons.

Several factors are likely to be responsible for the non-uniformities observed within the AT. While the specialized macroscopic design of AT may play an important role (Bojsen-møller and Magnusson, 2015; Edama et al., 2015; Pękala et al., 2016), the ISTM at the microscopic level is also highly likely to contribute. The matrix between fascicles (interfascicular matrix; IFM) has been shown to enable fascicle sliding in both human and equine tendons, a crucial component of enabling tendon extension and recoil (Thorpe et al., 2012, 2013b, 2015b; Franz et al., 2015; Franz and Thelen, 2016). In the same manner, the ISTM may permit the relative sliding between the AT sub-tendons to enable non-uniform AT loading. However, the role of ISTM in enabling sub-tendon sliding or serving as a pathway to transmit forces between sub-tendons and distribute load through the AT is currently unknown. This may have significant implications, as the transmission of force across sub-tendons may act to distribute loads across a greater cross-sectional area (CSA), thereby reducing peak stresses to mitigate the risk of tissue overload (Maas and Finni, 2018).

Studies attempting to characterize the distribution of proteins within the different compartments of tendon, particularly in the non-collagenous matrix at the larger length scales, are limited. In the horse superficial digital flexor tendon (SDFT), the IFM has a distinct proteomic profile compared to that of the surrounding fascicles, displaying a greater number of proteins (Thorpe et al., 2016b). Further evidence suggests differences exist in the cell populations present in the IFM and within fascicles, where those in the former appear morphologically more rounded, and reside at a significant greater density (Thorpe et al., 2015a). Immunohistochemical studies have shown both lubricin (Sun et al., 2006, 2015; Funakoshi et al., 2008; Thorpe et al., 2016a), and elastin (Smith et al., 2011; Grant et al., 2013; Godinho et al., 2017) to be highly localized to the IFM, where it is suggested they may contribute to the specialized composition of IFM which enables its highly elastic mechanical behavior. The protein distribution of the ISTM in the AT, however, remains poorly characterized, preventing further correlation between its specialized composition and distinct mechanical properties.

The aims of the current study were (i) to investigate to what extent the ISTM facilitates relative sliding between sub-tendons and/or serves as a pathway for force transmission to distribute forces through the AT, (ii) to assess the mechanical behavior of the ISTM, and (iii) to characterize the composition of the ISTM. We hypothesized that the ISTM provides a mechanical linkage between GAS and SOL sub-tendons, with mechanical behavior that enables some inter-subtendon sliding, whilst also ensuring force transmission between sub-tendons. We also hypothesized that the distribution of proteins, and organization of cells would differ between the ISTM and sub-tendon compartments.

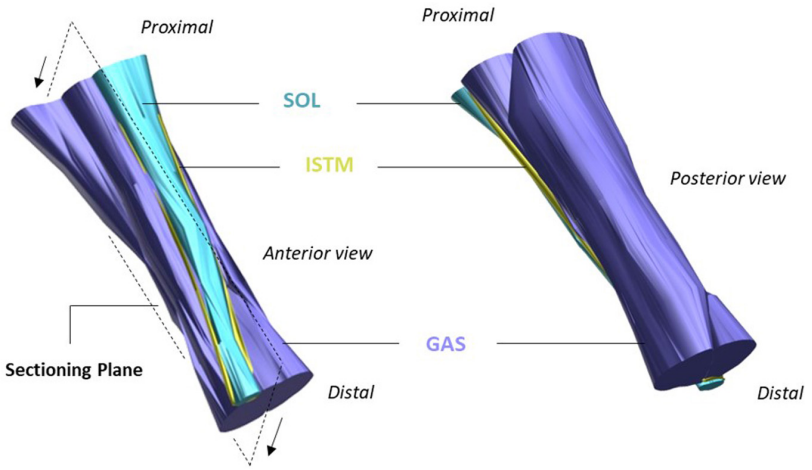

FIGURE 1 | Structure of the rat Achilles tendon (AT). The gastrocnemius (GAS, purple), and soleus (SOL, blue) sub-tendons are bound together by the inter-subtendon matrix (ISTM, yellow). The plane in which samples were sectioned for histology/immunohistochemistry is shown, with arrows indicating the cutting direction. Adapted from Finni et al. (2018).

MATERIALS AND METHODS

Animals

For mechanical characterization, a single hindlimb from 10 Wistar rats (7 female, 3 male, body mass 240–360 g) was excised and frozen (−80°C) immediately after sacrifice with an intracardial overdose injection of pentobarbital sodium (Euthasol 20%), along with double-sided pneumothorax. For immunohistochemical studies, one hindlimb from eight Wistar rats (sex unknown, body mass 200–220 g) was excised and prepared for embedding immediately after an overdose of isoflurane and decapitation. All procedures were in strict agreement with the regulations set out in EU law and approved by local university ethical committees, with limbs taken as left-over tissue from other unrelated studies.

Sample Preparation

On the day of mechanical testing, hindlimbs were allowed to thaw at room temperature. To obtain access to the triceps surae muscle complex, the limbs were shaved, followed by removal of the skin and biceps femoris muscle. The AT was then exposed by removing all remaining connective and fat tissues surrounding the tendon structure. The GAS and SOL muscles were identified and separated down to the muscle-tendon junction to allow preparation of the proximal ends of the GAS and SOL sub-tendons. Distal separation of GAS and SOL sub-tendons was achieved by gently dissecting through a small region of the ISTM at the calcaneal insertion. Metal rings were then attached to the proximal and distal ends of the GAS and SOL sub-tendons via threaded knots to allow connection to the mechanical testing set-up (**Figure 2A**). The distance between rings is referred to as the grip-to-grip distance hereafter. Marker knots were sutured onto the surface of the GAS sub-tendon to assess internal strains within the mid-portion of the GAS sub-tendon (the middle 1/3 of the total tendon length).

AT samples intended for immunohistochemistry were dissected immediately after sacrifice, embedded longitudinally (n = 5–8) in optimal cutting temperature compound (OCT) and snap-frozen in hexane cooled on dry ice. Cryosections covering the full length of the AT were cut 15 μm thick, transferred to polylysine slides, and stored at −80°C until required for staining (**Table 1**).

Mechanical Testing Set-Up

The AT samples were secured within the loading rig by connecting the metal rings attached to the proximal and distal ends of the GAS and SOL sub-tendons to hooks on the rig loading arms (**Figure 2**). Each loading arm was linked to a force transducer (ALPHA load beam transducer, 25 N maximum capacity, maximum output error <0.1%, compliance 0.0162 mm/N, BLH Electronics Inc.), mounted on a single-axis micro-positioner. The force transducer linked to the loading arm at the proximal end of the GAS sub-tendon was mounted on a servo-motor (MTS50C-Z8, T-Cube Servo-motor driver, Thorlabs, Cambridgeshire, United Kingdom), to impose displacements to the proximal end of the GAS sub-tendon (**Figure 2**). A video camera (Panasonic HC-V720, resolution: 1 pixel ∼0.03 mm) was positioned above the loading set-up to record the grip-to-grip distance and strains between suture markers in the GAS sub-tendon, with a millimeter ruler positioned besides the AT samples for calibration.

Mechanical Testing Protocols

Two different loading protocols were applied (**Figure 3**). Protocol A was designed to assess force transmission between the GAS and SOL sub-tendons, simulating two different levels of physiological GAS muscle activation and muscle belly shortening, while the SOL muscle length remains largely unchanged. Such conditions reflect the preferential recruitment of the GAS muscle in the triceps surae, as observed *in vivo* during isometric plantarflexor

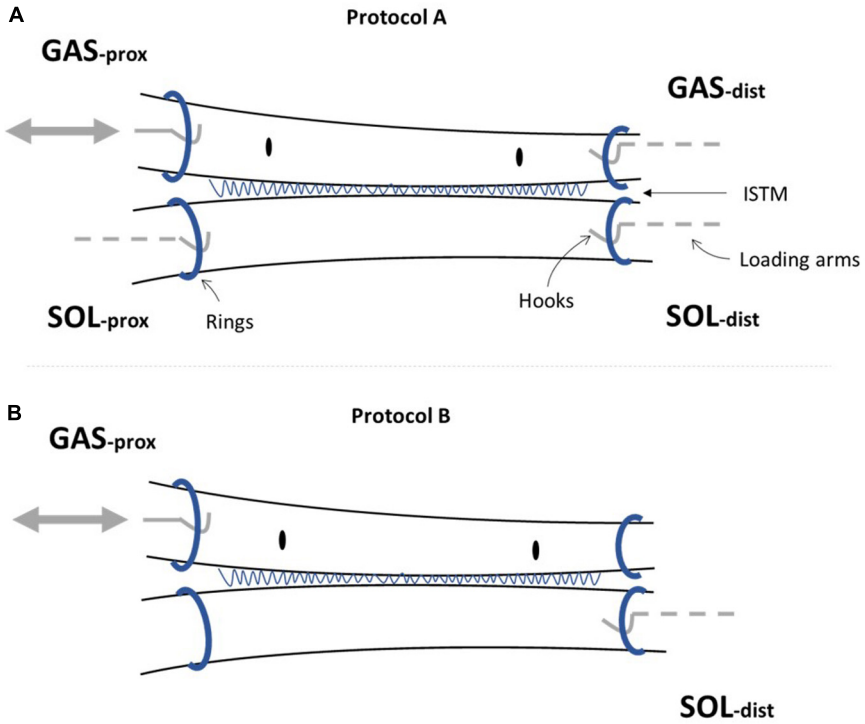

FIGURE 2 | Achilles tendon (AT) sample preparation for mechanical testing. Metal rings were attached to the proximal (prox) and distal (dist) ends of the gastrocnemius (GAS) and soleus (SOL) sub-tendons to secure samples to the rig set-up. The sub-tendons are bound together by the inter-subtendon matrix (ISTM). **(A)** For protocol A [(i) and (ii)], all four ends of the AT sample were attached to the loading arms with force transducers (GASprox,GASdist, SOLprox and SOLdist), where a servo-motor was additionally connected to the GASprox, allowing the tendon to be stretched at a given speed and length according to the loading protocol. **(B)** To determine the mechanical behavior of the inter-subtendon matrix (ISTM) in protocol B, only the proximal gastrocnemius (GASprox) and distal soleus (SOLdist) rings remained connected to the set-up, with displacement still applied via the motor connected to the GASprox to load the ISTM in shear. Black dots indicate the sutured markers on the GAS sub-tendon used for internal strain analysis.

TABLE 1 | Details of the primary antibodies used for immunohistochemical staining.

Antibody	Host species	Mono/polyclonal	Epitope recognized	Concentration	Manufacturer (product code)
Decorin	Rabbit IgG	Polyclonal	Core protein	1:500	Atlas Antibodies (HPA003315)
Collagen type III	Rabbit IgG	Polyclonal	Core protein	1:150	Abcam (ab7778)
Elastin	Rabbit IgG	Polyclonal	Core protein	1:50	Abcam (ab21610)
Lubricin	Mouse IgG	Monoclonal	C-terminal domain	1:50	MD Bioproducts (1045015)

contractions at varying knee joint angles (Cresswell et al., 1995) and maximal knee extension (Bojsen-møller et al., 2004). Protocol B was designed to indirectly determine the mechanical behavior of ISTM. Each sample was tested through protocols A and B in this order, and all tests were performed at room temperature.

For protocol A, preloads of 0.025 and 0.015 N were applied to the GAS and SOL sub-tendons respectively. These preloads were designed to account for the differences we measured in the GAS and SOL sub-tendon cross sectional areas (**Table 2**), and to ensure consistent pre-stress conditions. Protocol A(i) applied a 1mm ramp displacement to the loading arm attached to the proximal end of the GAS sub-tendon at an average speed of 1.1 mm/s (0.9 s:1.3 s:0.9 s stretch:hold:release) for 10 cycles (**Figure 3A**). Directly after completing protocol A(i), the pre-loads were re-applied, and protocol A(ii) was initiated, imposing a 2 mm stretch at an average speed of 1.3 mm/s (1.6 s:1.2 s:1.6 s stretch:hold:release) to the loading arm for 10 cycles (**Figure 3A**). On completion of protocol A, the hooks attached to the distal GAS and proximal SOL were disconnected from the mechanical set-up, thus leaving only the proximal GAS and distal SOL secured to the loading arms (**Figure 2B**). Under this configuration (protocol B), displacement of the proximal GAS loaded the ISTM in shear. A pre-load of 0.015 N was applied to the sample to remove any slack. Samples were then subjected to 10 stretch cycles of 0.5 mm using a triangular waveform at a speed of 0.1 mm/s (5.0 s:5.0 s stretch:release) (**Figure 3B**). All exposed tissues were regularly irrigated with phosphate-buffered saline (PBS) throughout preparation to maintain sample hydration.

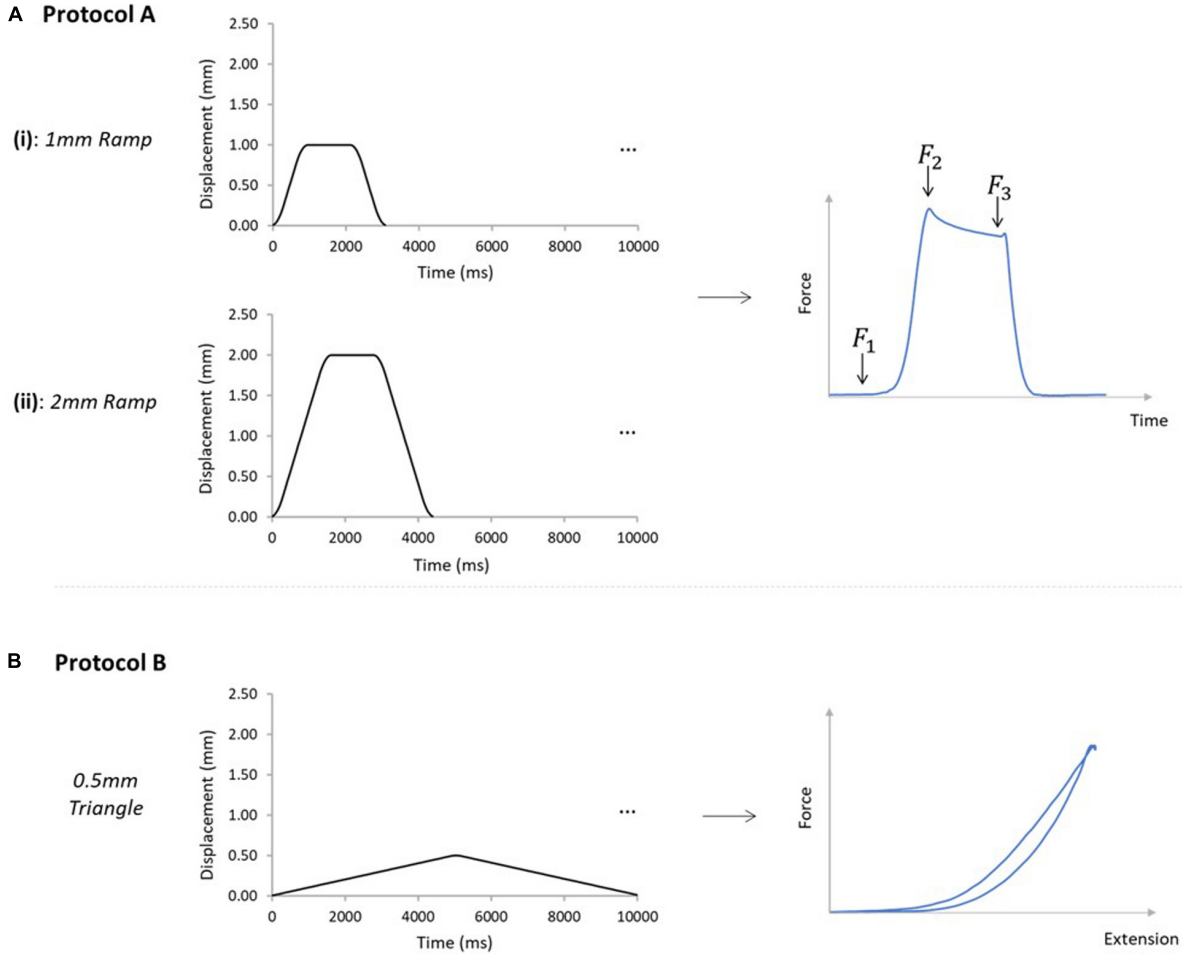

FIGURE 3 | Mechanical testing protocols applied to AT samples. **(A)** Samples were subjected to protocols A [(i) and (ii)], and B, in order on all analyzed samples. Protocol A(i) applied a 1mm ramp protocol to the GASprox, at an average speed of 1.1 mm/s for 10 cycles. Protocol A(ii) applied using the same displacement waveform but to a peak displacement of 2 mm, at an average speed of 1.3 mm/s for 10 cycles. Protocol A was devised to investigate force transmission between the sub-tendons, where the force before the stretch (F_1), peak force (F_2), and force in the steady state (F_3) were analyzed. **(B)** Protocol B was applied with only the GASprox and SOLdist attached to their respective loading arms and force transducers, where a 0.5 mm triangular waveform (0.1 mm/s, 10 cycles) was imposed to the GASprox to load the inter-subtendon matrix in shear and assess its mechanical behavior.

After mechanical testing, the sub-tendons of the AT were manually separated, to assess whether the GAS and SOL sub-tendons had been correctly isolated. Samples where the sub-tendons were entirely separated along their lengths (termed "isolated" samples) were analyzed as one group. In samples where a fiber remained (termed non-isolated samples), that fiber may contribute toward force measurements if running from proximal GAS to distal SOL, or be subject to no load if running from proximal SOL to distal GAS. Non-isolated samples with a fiber running from the proximal SOL to the distal GAS were included in the analysis as a secondary group. A comparison of data from isolated and the non-isolated samples confirmed no impact on force measurements (four isolated samples; six non-isolated isolated; comparison of forces exerted at the sub-tendons distally, $p = 0.171$), hence data from both conditions were pooled in the analysis. In non-isolated samples where fibers ran from the proximal GAS to the distal SOL, or across both directions, fibers would undoubtedly introduce significant errors to the estimation of force transmission via the ISTM, so samples were excluded from further analysis.

After manual separation, the total tendon sample length and the CSA of the GAS and SOL sub-tendons were measured. The samples lengths were measured through analysis of the video recordings. To measure CSA, the sub-tendons were cut transversely, imaged with a microscope camera (Bresser MicroCam 5.0), and measured using ImageJ (Schneider et al., 2017).

Data Recording and Analysis

Force signals were sampled at 1000 Hz, processed through a low-pass Butterworth filter with a cut-off frequency of 10 Hz, and stored for analysis. Images of the AT during loading were recorded at 50 frames/s (Panasonic HC-V720).

Protocol A [(i) and (ii)]

The force prior to the stretch (F_1), the peak force at the end of stretch (F_2), and the steady state force at the end of the hold phase (F_3), were measured from all four force transducers across all 10 cycles (**Figure 3A**). The percentage reduction in the peak force was calculated across the 10 cycles, providing a measure of the stress relaxation behavior during pre-conditioning (hereafter referred to as "stress relaxation"). The steady state force (F_3) of cycle 10 was used to compare force values across the four force transducers, and, thus, assess force transmission between sub-tendons. Percentage differences between the forces at the proximal and distal ends of each sub-tendon were calculated by dividing the difference between proximal and distal steady-state forces of each sub-tendon in cycle 10, by the mean of the two force values. Data obtained from 10 samples was analyzed using a custom-written MATLAB code (R2018a, MathWorks, Natick, MA, United States). Strains relating to the GAS sub-tendon were assessed during loading, through analysis of the video recordings using Tracker (Tracker Video Analysis and Modeling Tool, 5.0.7, D. Brown and Cox, 2009). External strains were calculated through analysis of the grip-to-grip length changes between the proximal and distal GAS rings. Internal strains were assessed through the mid-portion length changes, measured between the suture markers. Video recordings from seven samples were available for external strain analysis. Internal strains were calculated from five samples, as it was not possible to suture markers on the SOL sub-tendon of all samples. Values for the internal strains were compared with the applied strain, and the external strains in the 10th cycle of each ramp protocol.

Protocol B

For each stretch cycle, hysteresis was calculated as the difference in area between the loading and unloading curves, while total hysteresis was calculated as the difference between the loading curve of cycle 1 and the unloading curve of cycle 10. Stress relaxation was calculated as the percentage reduction in the peak force across the 10 cycles. Maximal stiffness was calculated by measuring the continual stiffness over each cycle from the slope of the force-displacement data (500 data points per cycle), and taking the maximum value from cycles 1 to 10. Values were then compared from cycles 1 to 10 to assess changes. Data were obtained from nine samples, as for one experiment Protocol B was not imposed due to a technical issue.

To ensure the ISTM was being loaded in shear, the grip-to-grip distances were used to measure the external strains in each of the GAS and SOL sub-tendons and also the relative movement between the two sub-tendons using the Tracker software. ISTM strains were calculated from the distance between the proximal GAS and distal SOL rings. Video recordings from seven samples were available for external strain analysis.

Immunohistochemistry

Immunohistochemistry was used to assess the distribution of several proteins (decorin, collagen type III, elastin, and lubricin) in the ISTM and sub-tendon (ST) regions of the AT. The choice of proteins for staining was guided by the low stiffness, highly elastic behavior we observed in the ISTM from Protocol B. Sections were allowed to thaw at room temperature, before fixing in ice-cold acetone (−20°C) for 10 min. Slides were then washed three times in tris-buffered saline (TBS), and to improve permeability, pre-treated with either Chondroitinase ABC (0.2 U/ml) for 1 h (decorin), or hyaluronidase [4800 U/ml in PBS containing protease inhibitor cocktail (complete Mini, Roche)] overnight (collagen type III and elastin) at room temperature. Two further washes in TBS followed, before sections were incubated with blocking buffer, consisting of 10% serum in TBS + 0.1% bovine serum albumin (BSA) for 2 h at room temperature. Slides were then drained, and primary antibodies diluted in blocking buffer (**Table 1**) applied to sections and incubated overnight at 4°C. The slides were drained the following day and washed twice with TBS, before sections were incubated with 0.3% H_2O_2 in TBS for 15 min at room temperature to inhibit endogenous peroxidase activity. Directly after decanting, slides were incubated with secondary antibodies (1:50 in 10% serum in TBS + 0.1% BSA) for 1 h at room temperature. Sections were then rinsed three times in TBS, before the staining was developed using 3,3'-diaminobenzidine (DAB). Sections were counterstained using Gill's hematoxylin, dehydrated in increasing concentrations of ethanol and xylene, and coverslipped using DPX mountant. Negative controls included sections incubated with (i) no primary antibody, to check for non-specific binding of the secondary antibody and (ii) a non-specific rabbit IgG antibody at the same concentration as elastin (highest concentration used for all antibodies raised in rabbit), to check for non-specific binding of the primary antibodies. The non-specific rabbit IgG was incubated on sections pre-treated with chondroitinase ABC and hyaluronidase (on separate sections) to validate non-specific binding of all primary antibodies. No staining was observed in any of these controls.

Immunohistochemistry for Lubricin

Sections were allowed to thaw at room temperature, before fixing in 10% neutral buffered formalin for 5 min. Slides were then washed three times in PBS containing 3% Triton X-100, followed by blocking in 10% serum in TBST (TBS containing 0.5% Triton X-100) + 0.1% BSA (blocking buffer) for 2 h at room temperature. Samples were then incubated with lubricin monoclonal antibody diluted in blocking buffer overnight at 4°C. Sections were washed three times in TBST, and treated with 3% H_2O_2 for 1 h at room temperature to quench endogenous peroxidase activity. The samples were incubated with a biotinylated horse anti-mouse (rat absorbed) secondary antibody (1:50 in blocking buffer) for 1 h at room temperature, followed by incubation with avidin–biotin complex (ABC) reagent (Vectastain® Elite ABC HRP Kit, Vector laboratories, United Kingdom) for 1 h at room temperature. After three washes in PBS, staining was developed with DAB. Sections were then dehydrated in increasing concentrations of ethanol and xylene, and coverslipped using DPX mountant. No counterstaining was performed on sections stained for lubricin, due to previous reports indicating the presence of intracellular lubricin in tendon (Sun et al., 2015; Thorpe et al.,

TABLE 2 | Forces measured at the proximal and distal ends of the GAS and SOL sub-tendons in the 10th cycle of the 1 mm [protocol A(i)] and 2mm [protocol A(ii)] stretch imposed at the proximal GAS.

	Protocol A(i)				Protocol A(ii)			
	GASprox	**GASdist**	**SOLprox**	**SOLdist**	**GASprox**	**GASdist**	**SOLprox**	**SOLdist**
F_1 (N)	0.002 ± 0.001	0.001 ± 0.001	0.002 ± 0.002	0.001 ± 0.001	0.000 ± 0.002	0.001 ± 0.002	0.003 ± 0.003	0.000 ± 0.001
F_2 (N)	0.364 ± 0.218	0.285 ± 0.215	0.008 ± 0.008	0.084 ± 0.051	1.418 ± 0.825	1.081 ± 0.759	0.007 ± 0.007	0.341 ± 0.163
F_3 (N)	0.324 ± 0.203	0.253 ± 0.198	0.005 ± 0.007	0.075 ± 0.046	1.285 ± 0.774	0.982 ± 0.715	0.004 ± 0.006	0.306 ± 0.149
Stress relaxation (%)	34.9 ± 6.8	32.5 ± 6.5	49.4 ± 20.4	35.4 ± 7.5	44.2 ± 5.4	45.5 ± 10.8	57.7 ± 21.9	43.8 ± 5.4
Total AT length (mm)		8.66 ± 1.13						
GAS CSA (mm^2)		1.19 ± 0.26						
SOL CSA (mm^2)		0.60 ± 0.44						

Stress relaxation measured at each load cell over all 10 cycles of protocol A(i) and A(ii). Geometric properties of the samples measured after mechanical testing, including the total AT length, and the cross-sectional area (CSA) of the GAS and SOL sub-tendons.

2016a). Negative controls included sections incubated with (i) no primary antibody, to check for non-specific binding of secondary antibody, (ii) no primary or secondary antibody, to check for non-specific binding of the ABC reagent, and (iii) a non-specific mouse IgG antibody at the same concentration as the primary antibody, to check for non-specific binding of the primary antibody. No staining was observed in any negative controls.

Histochemistry for Hyaluronic Acid

Histochemical staining was used to assess the distribution of hyaluronic acid (HA) in the ISTM and ST regions of the rat AT. Sections were allowed to thaw at room temperature, before fixing in ice-cold acetone (−20°C) for 10 min. Negative controls for HA were washed three times in TBS, and pre-digested with 30U of hyaluronidase (from *Streptomyces hyalurolyticus*, Sigma H1136) overnight at room temperature, before proceeding with the staining procedure. Slides were washed three times in TBS, followed by blocking in 10% serum in TBS + 0.1% BSA for 2 h at room temperature. Sections were then drained, and incubated with biotinylated HA binding protein (bHABP, 1:100) overnight at 4°C. The slides were drained the following day and washed twice with TBS, before sections were incubated with 0.3% H_2O_2 in TBS for 15 min at room temperature to quench endogenous peroxidase activity. After two further washes in TBS, sections were incubated with the ABC reagent (Vectastain® Elite ABC HRP Kit, Vector laboratories, United Kingdom) for 1 h at room temperature. Three washes in TBS followed, before the staining was developed using DAB, counterstained using Gill's hematoxylin, dehydrated in increasing concentrations of ethanol and xylene, and coverslipped using DPX mountant. An additional negative control was included which involved sections incubated without the bHABP, to check for non-specific reactions of the ABC reagent. No staining was observed in all negative controls.

Histology

To assess the general structure and cellular organization of the ISTM and sub-tendon regions in the rat AT, longitudinal sections were stained with hematoxylin and eosin (H&E). Once sections had been thawed at room temperature, and fixed with ice-cold acetone (−20°C) for 10 min, slides were stained with H&E using the standard staining procedure (Stevens and Bancroft, 1990) and mounted.

Image Acquisition

Two to three sections from each sample were stained with each of the five stains. Sections were imaged using a Leica DMIL light microscope at low magnification (×10), and high magnification (x20). To ensure the ISTM was within the field of view of all images, sections were first visualized under phase contrast enabling identification of the ISTM region without bias (**Figure 6A**).

Image Scoring

Semi-quantitative methods were adopted to assess the distribution of proteins in the sub-tendons and ISTM of the AT. Two independent assessors scored the intensity of staining in immunohistochemical images, by grading the staining intensity in the sub-tendons and ISTM regions separately from 0 to 5, where 0 indicates no staining, and 5 represents very intense staining. The two assessors also graded cellularity, and the nuclear shape of cells within ISTM and sub-tendon regions using the H&E stained sections. For cellularity, images were graded from 0 to 5, where 0 indicates no cells present, and 5 indicates a very high number of cells. Nuclear shape was graded in each image from 0 to 5, where 0 indicates a highly elongated, spindle-like morphology, and 5 represents a rounded, circular nuclear shape. Inter-observer variability was assessed through linear weighted Kappa statistics (Viera and Garrett, 2005), using an online software tool[1]. Scorers were asked to grade every image twice to allow the calculation of intra-observer variability, where images were re-arranged on the second occasion to prevent bias scoring. Intra-observer variability was also calculated using linear weighted Kappa statistics.

Statistics

Normality of all data sets was first determined using a Shapiro–Wilk test, after which non-parametric statistics was adopted

[1]http://vassarstats.net/kappa.html

for protocol A data, and parametric statistics for protocol B and immunohistochemical data. Wilcoxon rank sum tests were used to test for differences between steady-state forces across the GAS or SOL sub-tendons. A Mann Whitney test was conducted to assess differences in the steady-state forces at the distal end of the GAS and SOL sub-tendons of isolated and non-isolated samples. To assess the effects of cycle number on the ISTM mechanical behavior, a one-way analysis of variance (ANOVA) was performed. To assess the differences in staining intensity between the sub-tendon and ISTM regions, a one-way nested ANOVA was used. Statistical analysis was performed using GraphPad Prism 8 (GraphPad, Inc., San Diego, CA, United States), unless stated otherwise. Statistical significance was defined as $p < 0.05$. All data were displayed as mean ± SD, unless stated otherwise.

RESULTS

Force Transmission Between the GAS and SOL Sub-Tendons

The grip-to-grip length changes (external strain) imposed on the GAS sub-tendon during the last cycle of protocol A(i) was 0.45 ± 0.25 mm (7.8% strain). Mid-portion length changes (internal strains) were substantially smaller (3.7%). The same behavior was true for protocol A(ii), where 0.83 ± 0.27 mm grip-to-grip lengthening (13.9% external strain) was measured in the GAS sub-tendon in the 10th cycle of the 2 mm stretch, accompanied by mid-portion length changes of 5.8% internal strain, suggesting non-uniform strain distributions along the GAS sub-tendon in both loading protocols.

A typical force response of the proximal and distal ends of the GAS and SOL sub-tendons in the 10th cycle of protocol A(i), 1mm stretch, is presented in **Figure 4A**. The values for the force prior to stretch, (F_1), peak force at the end of stretch (F_2), steady state force at the end of the hold phase (F_3), and percentage stress relaxation from cycle 1 to 10 for each load cell are presented in **Table 2**. With respect to the GAS sub-tendon, the forces exerted at both ends increased when subjected to the 1 mm stretch. However, the steady state force was significantly greater at the proximal end ($p = 0.002$; difference = 0.07 N, 31%) than the distal end (**Figure 4B**). The SOL sub-tendon similarly demonstrated significant differences between the steady state force at the proximal and distal ends, but in the opposite direction, i.e., greater force was measured at the distal end ($p = 0.002$; difference = 0.07 N, 173%) than at the proximal end (**Figure 4B**).

A typical force response from the four ends of the AT samples in the 10th cycle of protocol A(ii), 2 mm stretch, is presented in **Figure 4C**. The values for F_1, F_2, F_3, and percentage stress relaxation from cycle 1 to 10 for each load cell are presented in **Table 2**. As seen during protocol A(i), the steady state force measured at the proximal end of the GAS sub-tendon was significantly higher ($p = 0.002$; difference = 0.30 N, 27%) than at the distal end, whilst a greater force was measured at the distal end of the SOL sub-tendon ($p = 0.002$; difference = 0.16 N, 194%) compared to proximal end (**Figure 4D**).

Mechanical Behavior of the ISTM

Displacement of the proximal GAS and distal SOL rings was compared with applied displacement of the loading arm, confirming that the applied deformation was transferred to the ISTM during each loading cycle of the test. Changes in the distance between the proximal GAS and distal SOL in the 10^{th} cycle of protocol B measured 0.39 ± 0.06 mm. Strains in the sub-tendons during protocol B were found to be negligible (<0.6% strain), confirming the ISTM was exclusively strained in shear. Typical force-displacement curves for the 10 cycles of protocol B are presented in **Figure 5A**. We observed 57.1 ± 4.7% hysteresis in the first cycle, which decreased to 34.2 ± 7.7% in the 10th cycle. Over all 10 cycles, the total hysteresis was 62.4 ± 8.5% (**Figure 5D**). Hysteresis significantly changed from cycles 1 to 2 ($p < 0.001$), but analysis of cycles 2 to 10 showed an insignificant effect of cycle number on hysteresis ($p = 1.000$). Analysis of the early stages of stress relaxation showed the percentage force reduction over all 10 cycles was 20.1 ± 12.9% (**Figure 5C**), and the peak force did not significantly change with cycle number ($p = 1.000$). With respect to ISTM stiffness, a slight, but insignificant ($p = 1.000$) increase was observed over the 10 cycles, with the maximal stiffness in the 10th cycle measuring 0.89 ± 0.45 N/mm (**Figure 5B**).

General AT Structure and ISTM Histology

Representative H&E staining of the AT is presented in **Figure 6B**. There was a significantly higher cellularity localized to the ISTM, than within sub-tendons ($p < 0.001$; **Figure 6C**). The nuclear shape of cells within ISTM and sub-tendons were also significantly different ($p < 0.001$), where nuclei in the ISTM were significantly rounder (**Figure 6D**).

Decorin Distribution

Typical images of decorin staining are presented in **Figure 6G**. There were no significant differences in staining intensity between the ISTM and sub-tendon regions ($p = 0.081$; **Figure 6H**), with decorin appearing throughout the AT structure.

HA Distribution

Typical images of HA staining are presented in **Figure 6E**. Hyaluronic acid was seen throughout the ISTM, where the staining intensity was significantly greater than within sub-tendons ($p < 0.001$; **Figure 6F**).

Collagen Type III Distribution

Typical images of collagen type III staining are presented in **Figure 6I**. There was a significant difference between the staining intensity of the ISTM and sub-tendon regions ($p < 0.001$; **Figure 6J**). Collagen type III appears to be predominately localized to the ISTM, with light staining also sparsely distributed throughout the sub-tendon regions between fibers.

Lubricin Distribution

Typical images of lubricin staining are presented in **Figure 6M**. There was a significant difference between the staining intensity of the ISTM and STM regions ($p < 0.001$), where lubricin was

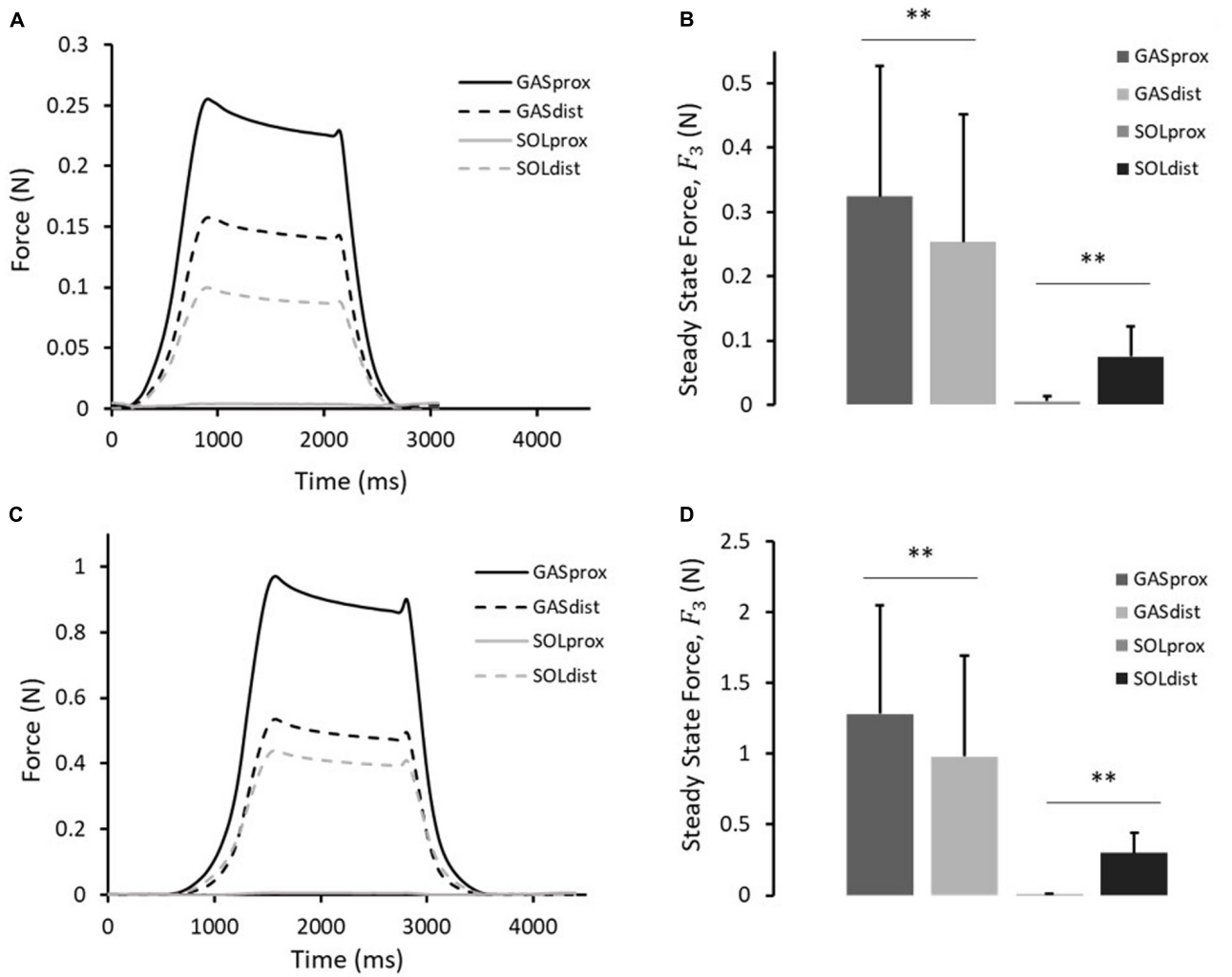

FIGURE 4 | (A) Typical force response, and **(B)** the steady-state force, F_3, measured at the proximal and distal ends of the GAS and SOL sub-tendons in 10th cycle of protocol A(i). **(C)** Typical force response, and **(D)** the steady-state force, F_3, measured at the proximal and distal ends of the GAS and SOL sub-tendons in 10th cycle of protocol A(ii). Data presented as mean ± SD. Significant differences: $^{**}p < 0.01$.

predominately localized to the ISTM (**Figure 6N**). Lubricin was also evident within the sub-tendons, specifically at the interfaces between adjacent fibers.

Elastin Distribution

Typical images of elastin staining are presented in **Figure 6K**. There was a significant difference between the staining intensity of the ISTM and sub-tendon regions ($p < 0.001$), with elastin predominately localized to the ISTM (**Figure 6L**). Staining for elastin was also present within sub-tendons, where it was localized to the interfaces between adjacent fibers.

Assessor Variation

The overall Kappa score was 0.70, indicating a good agreement between the two blinded assessors. When focusing on the intra-observer agreement specifically, a Kappa score of 0.79 confirms consistency in scoring by each individual. There were no differences between the Kappa statistics for individual stains, or cellular parameters relating to the H&E staining.

DISCUSSION

The aim of this study was to investigate the capacity for force transmission between the GAS and SOL sub-tendons, testing the hypothesis that forces can be transmitted between the AT sub-tendons. We further aimed to assess the mechanical behavior and composition of the ISTM. We present the first data to clearly demonstrate force transmission between GAS to SOL sub-tendons. A direct analysis of ISTM mechanical behavior also demonstrated a non-linear loading curve, revealing an initial extended low stiffness region, followed by a swift rise in stiffness with increased applied force. Exploring specialization of the ISTM to enable this behavior, we provide the first investigation

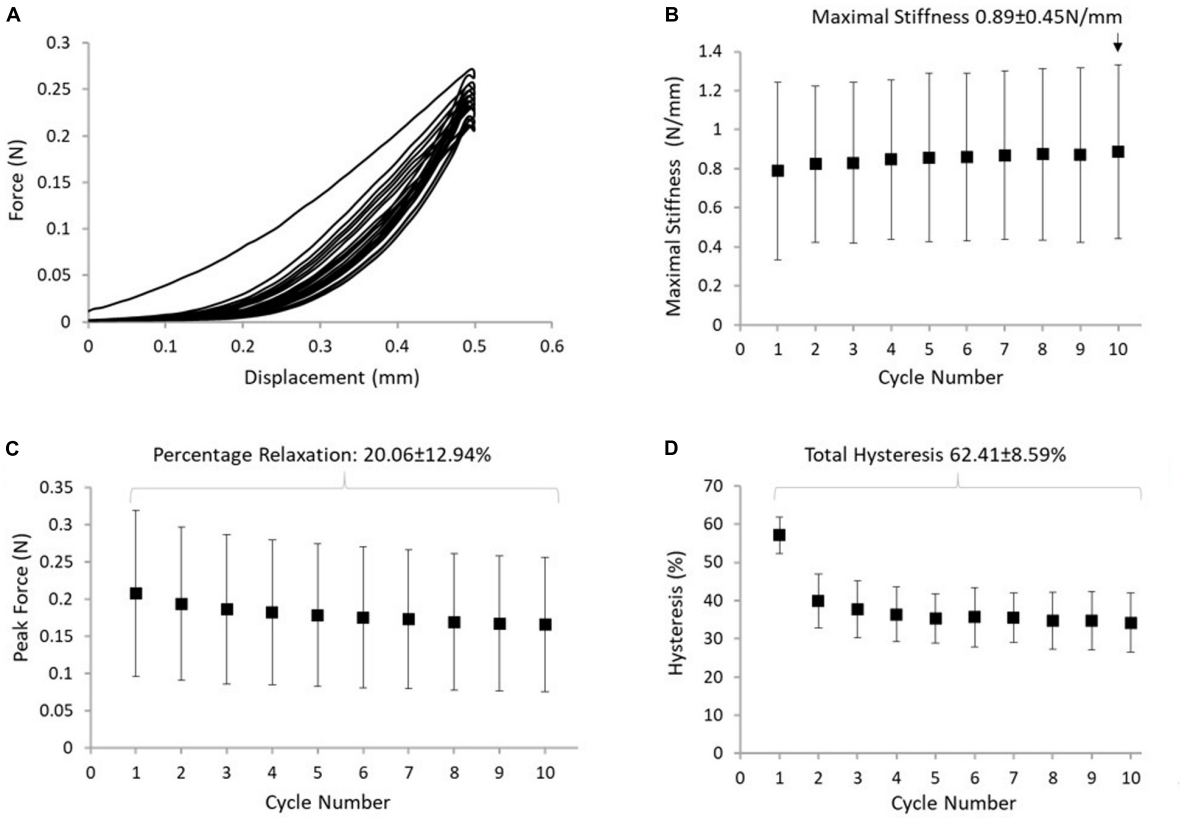

FIGURE 5 | (A) Typical response of the ISTM to protocol B. **(B)** The maximum stiffness reached in the ISTM in each cycle of protocol, with the highest value measured in cycle 10 indicated above the data point. **(C)** The reduction in peak force, with the stress relaxation calculated over all 10 cycles indicated above the data points. **(D)** Hysteresis measured in the ISTM across all 10 cycles, with the total hysteresis over protocol B indicated above the data points. Data presented as mean ± SD.

of protein distribution in the rat AT, which in support of our hypothesis, demonstrates a localization of elastin, lubricin, HA, and collagen type III to the ISTM.

This study is not without limitations. It is notable that sample preparation for mechanical testing was hindered by the small size of samples and the varying degrees of AT twist which led to a highly variable location of the ISTM. This made it difficult to carry out mechanical characterization in a repeatable manner, and meant that the overall number of samples were constrained. However, post-test analysis of the samples ensured that we could confidently pool data from isolated and non-isolated samples for analysis. Grip-to-grip strains are nearly always influenced by the gripping method, particularly in short samples such as a rodent AT. Here, the fixation of rings to the tendons may have led to increased compliance at the tendon-ring interface. However, surface markers were used in attempt to mitigate this error during strain analysis, so the applied strains could be correlated to those measured locally within sub-tendons. Whilst the sex of the animals for mechanical characterization was known, this was not the case for histological samples, and it is possible variation may exist in the composition of the AT among sexes. However, care was taken to remain semi-quantitative in the analysis of histological data, and recent work has also indicated that sex differences are largely insignificant in rodent ATs (Sarver et al., 2017). Indeed, the semi-quantitative nature of immunohistochemistry means care must also be taken in the interpretation. Staining intensity does not correlate to protein abundance, and is impacted by sample preparation. However, all samples were stained and imaged using a consistent protocol, and data focused on relative differences between different regions of the image, which would be less affected by such parameters. Whilst additional, quantitative approaches to analysis are necessary to determine relative amounts of proteins in the different regions of the AT, controls confirmed specificity of the stains, and good inter- and intra-observer agreement provide confidence in the reported outcomes.

Considering ISTM mechanics in light of the likely *in vivo* loading conditions, an extended low stiffness toe region of the ISTM loading curve would allow for sliding between the AT sub-tendons, and thus permit them a degree of mechanical independence. However, as the applied load increases, the rapid rise in ISTM stiffness would ensure force transmission between sub-tendons, and enable the AT to function as an integrated force transmitting structure. The capacity for inter-subtendon sliding in the AT has commonly led to the suggestion that the AT sub-tendons largely act independently under mechanical

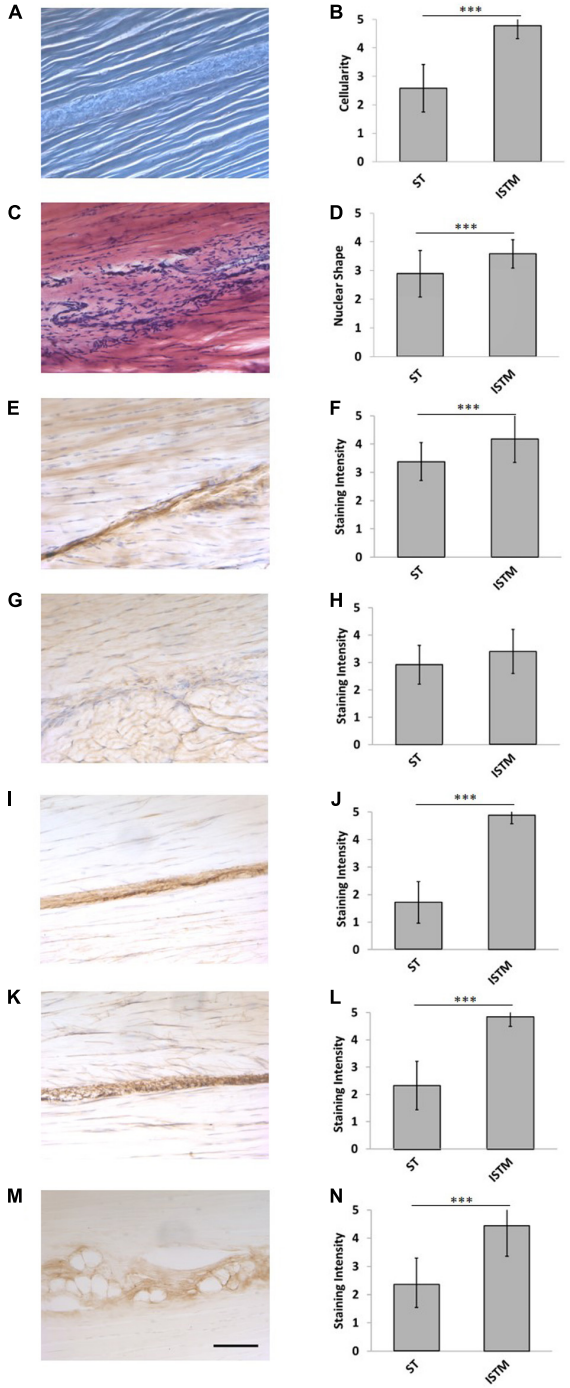

FIGURE 6 | Representative histology and immunohistochemistry. **(A)** Histological section of the rat Achilles tendon imaged under phase contrast, demonstrating the GAS and SOL sub-tendon (ST) regions are bound together by the inter-subtendon matrix (ISTM). **(C)** H&E staining. There was a significant difference in the panel **(B)** celluarity, and **(D)** nuclear of shapes between the ISTM and sub-tendons. **(E)** Representative histochemical staining for HA. Representative immunohistochemical staining for **(G)** decorin, **(I)** collagen type III, **(K)** elastin, and **(M)** lubricin. Staining intensity for **(F)** HA, **(J)** collagen type III, **(L)** elastin, and **(N)** lubricin was significantly greater in the ISTM. Staining intensity for **(H)** decorin was not significantly different between regions. Scale bar: 100 μm. Data are displayed as mean ± SD.***$p < 0.001$.

load. Such behavior could theoretically allow fibers within the GAS and SOL muscles to operate at independent lengths, which may be more optimal for their respective force production needs (Franz and Thelen, 2015; Franz et al., 2015). Indeed, two studies report negligible force transmission through the IFM in human (Haraldsson et al., 2008) and bovine AT (Purslow, 2009). Contrary to these reports, investigations into both equine and porcine flexor tendons have shown that whilst the IFM enables interfascicular sliding, it is also engaged in transmitting significant forces between adjacent fascicles (Thorpe et al., 2012, 2013b, 2015b; Kondratko-Mittnacht et al., 2015). The redistribution of load through the IFM similarly occurs in the rat tail tendon (Kondratko-Mittnacht et al., 2015). The current data provide further support to the importance of the ISTM in the rat AT in transmitting substantial forces between sub-tendons, enabling the AT to internally distribute stresses.

Our observations regarding the viscoelastic properties of the ISTM suggests greater hysteresis than seen in previous equine IFM tests, but comparable levels of percentage force reduction during the early stages of stress relaxation (Thorpe et al., 2015b), which may be related to the more complex, twisted structure of the AT or the complexity of the sample gripping arrangement. Despite this, it is evident the ISTM can effectively withstand and recover from cyclic loading. Recent studies indicate that aging reduces the elasticity of the IFM in the SDFT (Thorpe et al., 2015b), and rat tail tendon (Muench et al., 2019). Whether the same age-related changes occur in the ISTM of the AT is unknown, but such a response may be associated with the increased predisposition to AT injury with aging.

In support of our hypothesis, the ISTM demonstrated a distinctive protein composition and cellular organization, compared to that within sub-tendons, with collagen type III, elastin, HA, lubricin, and cellularity all enriched in the ISTM. In agreement with previous reports (Thorpe et al., 2015a, 2016b; Rowson et al., 2016), further analysis of the resident AT cells also revealed the nuclear morphology of the cells within the ISTM to be significantly rounder, which is likely to derive from the distinction between the physical cues imposed on the cells within each region (softer ISTM permits a more rounded shape, as opposed to the stiffer aligned collagen within sub-tendons restricting cell nuclei to aligning more toward the fiber direction).

Staining for decorin was not significantly different between the ISTM and sub-tendon regions of the rat AT. These results are in agreement with those observed in the equine SDFT, which have similarly shown staining for decorin throughout the IFM and fascicle regions (Kim et al., 2010; Thorpe et al., 2016a). Conversely, we found collagen type III to be significantly more enriched in the ISTM. Collagen type III is traditionally thought to be negligible in adult tendon unless tendinopathic (Maffulli et al., 2000; Eriksen et al., 2002; Södersten et al., 2013). However, whilst fascicles lose their collagen type III expression past development, the IFM has been shown to become significantly more enriched (Birk and Mayne, 1997), which is in line with our findings. These results may indicate a role for collagen III beyond that of repair, which we propose may be mechanical. Tissues with a high degree of elasticity, such as skin, blood vessels, and lung, demonstrate a significantly higher ratio of collagen type

III:type I (Keene et al., 1987; Gelse et al., 2003), perhaps explained by the greater compliance of type III (Asgari et al., 2017). The endomysium around muscle fibers of GAS and SOL muscles in rat is similarly rich in collagen type III, where it is suggested to permit force transmission between muscle fibers (Kurose et al., 2006). It is possible, that this same mechanism also exists in the ISTM of the AT. Observed staining for type III collagen between the fibers of sub-tendons suggests it may also contribute the same mechanism at a fiber-level.

Elastin and lubricin were also highly localized to the ISTM, reflecting findings in the IFM of other energy storing tendons, where it is suggested lubricin enables interfascicular sliding, whilst elastin facilitates recoil (Ritty et al., 2002; Sun et al., 2006, 2009, 2015; Funakoshi et al., 2008; Kohrs et al., 2011; Grant et al., 2013; Fang and Lake, 2016; Thorpe et al., 2016a; Eekhoff et al., 2017; Godinho et al., 2017). Lubricin is a mucinous glycoprotein, which provides articular cartilage with boundary lubrication (Swann et al., 1977). Knockout studies have shown an absence of lubricin leads to an increase in interfascicular friction (Kohrs et al., 2011) and alterations in the viscoelastic properties of the fascicles (Reuvers et al., 2011). Elastin forms the core of elastic fibers, which are rich in tissues subjected to long-term repetitive loading [e.g., cardiovascular tissues (Li et al., 1998)], due to its ability to reversibly deform up to 100% strain with minimal energy loss (Gosline et al., 2002). Recent studies indicate elastin may also contribute to the mechanics of energy-storing tendons under both tension and shear, by facilitating the efficient recoil between fascicles (Grant et al., 2015; Fang and Lake, 2016; Eekhoff et al., 2017). Taken together, it is highly likely the localization of the lubricin and elastin in the ISTM is to support the elastic sliding and recovery of the ISTM as observed in this study.

It is notable that staining for lubricin was not homogeneous along the length of the ISTM, but far more prominent in the mid-portion and distal regions of the AT, which is directly in line with observations made in the human AT (Sun et al., 2015). Spiralization of the Achilles sub-tendons generates an area of concentrated stress ∼3–6 cm above the calcaneal insertion in humans (Doral et al., 2010), which correlates to the region of the tendon with the narrowest CSA (Kongsgaard et al., 2005), and highest concentration of lubricin (Sun et al., 2015). While we did not analyze lubricin in quantitative amounts, we established that the region of intense staining in the rat Achilles ISTM correlated to the same approximate region as reported in the human AT. Interestingly, we found that the concentration of HA mirrored that of lubricin, with particular enrichment in the distal ISTM. Hyaluronic acid has been identified in the compressive regions of flexor tendons (Robbins and Vogel, 1994; Rees et al., 2005; Vogel and Peters, 2005), but also within the sheath, where it primarily serves a tribological role (Hagberg et al., 1992; Uchiyama et al., 1997). Co-localization of HA and lubricin in the ISTM may indicate both play similar mechanical roles in tendon, potentially protecting against increased compressive and shear forces in this region. However, a recent study revealed that a synergistic relationship between HA and lubricin was fundamental in providing articular cartilage with its remarkably low friction lubrication (Bonnevie et al., 2015), providing support to the hypothesis that these components may also work together in tendon to facilitate sub-tendon sliding. It is notable that the region of concentrated lubricin and HA also correlates to the region of the AT most prone to tendinopathy, which may indicate an association between sub-tendon sliding and injury (Theobald et al., 2005; Shim et al., 2014).

CONCLUSION

This study is the first to investigate ISTM mechanical behavior and demonstrate force transmission between AT sub-tendons. Non-linear mechanical behavior of the ISTM combines an initial low stiffness region with a region of high linear stiffness. Together, these data reveal that the ISTM is capable of enabling non-uniform AT loading whilst still ensuring force transmission occurs between the AT sub-tendons. An analysis of ISTM composition highlights localization of HA, lubricin, and elastin to the ISTM region, proteins likely to play a role in facilitating the sliding and recovery of the ISTM. Our results provide important advances into the understanding of AT structure and function. Further studies into the effects of aging on force transmission may reveal the factors which predispose the AT to injury, thus assisting in the development of appropriate preventative therapies.

DATA AVAILABILITY STATEMENT

All datasets generated for this study are included in the article/supplementary material.

ETHICS STATEMENT

Ethical review and approval was not required for the animal study because tissue taken as waste tissue from other unrelated studies.

AUTHOR CONTRIBUTIONS

HM conceived and designed the experiments and edited the manuscript. HS assisted with the experimental design and edited the manuscript. CG performed the immunohistochemistry, analyzed all the data, and drafted the manuscript. JC, GB, and WN performed the mechanical experiments. All authors contributed to the article and approved the submitted version.

FUNDING

This research was funded by an EPSRC Doctoral Training Grant Research Studentship (EP/R51259X/1), and part funded by TRB Chemedica Limited.

ACKNOWLEDGMENTS

The authors gratefully acknowledge Sjoerd Bruijn for his assistance with the MATLAB scripting.

REFERENCES

Alexander, M. (1991). Energy-saving mechanisms in walking and running. *J. Exp. Biol.* 160, 55–69.

Alexander, R. (1984). Elastic energy stores in runnng vertebrates. *Am. Zool.* 24, 85–94. doi: 10.1093/icb/24.1.85

Arndt, A., Bengtsson, A. S., Peolsson, M., Thorstensson, A., Movin, T. (2012). Non-uniform displacement within the Achilles tendon during passive ankle joint motion. *Knee Surgery Sports Traumatol. Arthrosc.* 20, 1868–1874. doi: 10.1007/s00167-011-1801-1809

Asgari, M., Latifi, N., Heris, H. K., Vali, H., Mongeau, L. (2017). In vitro fibrillogenesis of tropocollagen type III in collagen type I affects its relative fibrillar topology and mechanics. *Sci. Rep.* 7:1392. doi: 10.1038/s41598-017-01476-y

Birk, D. E., and Mayne, R. (1997). Localization of collagen types I, III and V during tendon development. Changes in collagen types I and III are correlated with changes in fibril diameter. *Eur. J. Cell Biol.* 72, 352–361.

Bogaerts, S., De Brito Carvalho, C., De Groef, A., Suetens, P., and Peers, K. (2018). Non-uniformity in pre- -insertional Achilles tendon is not influenced by changing knee angle during isometric contractions. *Scand. J. Med. Sci. Sports* 28, 2322–2329. doi: 10.1111/sms.13230

Bojsen-møller, J., Hansen, P., Aagaard, P., Svantesson, U., Kjaer, M., and Magnusson, S. P., et al. (2004). Differential displacement of the human soleus and medial gastrocnemius aponeuroses during isometric plantar flexor contractions in vivo. *J. Appl. Physiol.* 97, 1908–1914. doi: 10.1152/japplphysiol.00084.2004

Bojsen-møller, J., and Magnusson, S. P. (2015). Heterogeneous Loading of the Human Achilles Tendon In Vivo. *Exerc. Sport Sci. Rev.* 43, 190–197. doi: 10.1249/JES.0000000000000062

Bonnevie, E. D., Galesso, D., Secchieri, C., Cohen, I., and Bonassar, L. J., et al. (2015). Elastoviscous Transitions of Articular Cartilage Reveal a Mechanism of Synergy between Lubricin and Hyaluronic Acid. *PLoS One* 10:e143415. doi: 10.1371/journal.pone.0143415

Brown, D., and Cox, A. J. (2009). Innovative uses of video analysis. *Phys. Teach.* 47, 145–150. doi: 10.1119/1.3081296

Cresswell, A. G., Loscher, W., and Thorstensson, A. (1995). Influence of gastrocnemius muscle length on triceps surae torque development and electromyographic Activity in Man. *Exp. Brain Res.* 105, 283–290.

Doral, M. N., Alam, M., Bozkurt, M., Turhan, E., Atay, O. A., and Dönmez, G., et al. (2010). Functional anatomy of the Achilles tendon. *Knee Surgery Sports Traumatol. Arthrosc.* 18, 638–643. doi: 10.1007/s00167-010-1083-1087

Edama, M., Kubo, M., Onishi, H., Takabayashi, T., Inai, T., and Yokoyama, E., et al. (2015). The twisted structure of the human Achilles tendon. *Scand. J. Med. Sci. Sports* 25, e497–e503. doi: 10.1111/sms.12342

Eekhoff, J. D., Fang, F., Kahan, L. G., Espinosa, G., Cocciolone, A. J., and Wagenseil, J. E., et al. (2017). Functionally distinct tendons from elastin haploinsufficient mice exhibit mild stiffening and tendon-specific structural alteration. *J. Biomech. Eng.* 139, 1110031–1110039. doi: 10.1115/1.4037932

Eriksen, H. A., Pajala, A., Leppilahti, J., and Risteli, J. (2002). Increased content of type I11 collagen at the rupture site of human Achilles tendon. *J. Orthopaedic Res.* 20, 1352–1357. doi: 10.1016/s0736-0266(02)00064-5

Fang, F., and Lake, S. P. (2016). Multiscale mechanical integrity of human supraspinatus tendon in shear after elastin depletion. *J. Mech. Behav. Biomed. Mater.* 63, 443–455. doi: 10.1016/j.jmbbm.2016.06.032

Finni, T., Bernabei, M., Baan, G. C., Noort, W., Tijs, C., Maas, H., et al. (2018). Non-uniform displacement and strain between the soleus and gastrocnemius subtendons of rat Achilles tendon. *Scand. J. Med. Sci. Sports* 28, 1009–1017. doi: 10.1111/sms.13001

Franz, J. R., Slane, L. C., Rasske, K., and Thelen, D. G. (2015). Non-uniform in vivo deformations of the human Achilles tendon during walking. *Gait Posture*, 41, 192–197. doi: 10.1016/j.gaitpost.2014.10.001

Franz, J. R., and Thelen, D. G. (2015). Depth-dependent variations in Achilles tendon deformations with age are associated with reduced plantarflexor performance during walking. *J. Appl. Physiol.* 119, 242–249. doi: 10.1152/japplphysiol.00114.2015

Franz, J. R., and Thelen, D. G. (2016). Imaging and simulation of Achilles tendon dynamics: implications for walking performance in the elderly. *J. Biomech.* 49, 1403–1410. doi: 10.1016/j.jbiomech.2016.04.032

Freedman, B. R., and Gordon, J. A., Soslowsky, L. J. (2014). The Achilles tendon: fundamental properties and mechanisms governing healing. *Muscles Ligaments Tendons J.* 4, 245–255.

Fukashiro, S., Komi, P. V., Järvinen, M., Miyashita, M. (1995). In vivo Achilles tendon loading during jumping in humans. *Eur. J. Appl. Occupat. Physiol.* 71, 453–458. doi: 10.1007/bf00635880

Funakoshi, B. T., Schmid, T., Hsu, H-P., and Spector, M. (2008). Lubricin Distribution in the Goat Infraspinatus Tendon: a Basis for Interfascicular Lubrication. *J. Bone Joint Surg.* 90, 803–814. doi: 10.2106/JBJS.G.00627

Gelse, K., Poschl, E., and Aigner, T. (2003). Collagens — structure, function, and biosynthesis. *Adv. Drug Deliv. Rev.* 55, 1531–1546. doi: 10.1016/j.addr.2003.08.002

Godinho, M. S. C., Thorpe, C. T., Greenwald, S. E., and Screen, H. R. C. (2017). Elastin is Localised to the Interfascicular Matrix of Energy Storing Tendons and Becomes Increasingly Disorganised With Ageing, *Sci. Rep.* 7:9713. doi: 10.1038/s41598-017-09995-9994

Gosline, J., Lillie, M., Carrington, E., Guerette, P., Ortlepp, C., and Savage, K., et al. (2002). Elastic proteins: biological roles and mechanical properties. *Philos. Trans. R. Soc. Lond. B Biol. Sci.* 357, 121–132. doi: 10.1098/rstb.2001.1022

Grant, T. M., Thompson, M. S., Urban, J., and Yu, J. (2013). Elastic fibres are broadly distributed in tendon and highly localized around tenocytes. *J. Anat.*, 222, 573–579. doi: 10.1111/joa.12048

Grant, T. M., Yapp, C., Chen, Q., Czernuszka, J. T., and Thompson, M. S. (2015). The Mechanical, Structural, and Compositional Changes of Tendon Exposed to Elastase. *Ann. Biomed. Eng.* 43, 2477–2486. doi: 10.1007/s10439-015-1308-1305

Hagberg, L., Heinegård, D., and Ohlsson, K. (1992). The contents of macromolecule solutes in flexor tendon sheath fluid and their relation to synovial fluid. A quantitative analysis. *J. Hand. Surg. Br.* 17, 167–171. doi: 10.1016/0266-7681(92)90081-c

Handsfield, G. G., Slane, L. C., and Screen, H. R. C. (2016). Nomenclature of the tendon hierarchy: an overview of inconsistent terminology and a proposed size-based naming scheme with terminology for multi-muscle tendons. *J. Biomech.* 49, 3122–3124. doi: 10.1016/j.jbiomech.2016.06.028

Haraldsson, B. T., Aagaard, P., Qvortrup, K., Bojsen-Moller J., Krogsgaard M., and Koskinen, S., et al. (2008). Lateral force transmission between human tendon fascicles. *Matrix Biol.* 27, 86–95. doi: 10.1016/j.matbio.2007.09.001

de Jonge, S., van den Berg, C., de Vos, R. J., van der Heide, H. J. L., Weir, A., Verhaar, J. A. N., et al. (2011). Incidence of midportion Achilles tendinopathy in the general population. *Br. J. Sports Med.* 45, 1026–1028. doi: 10.1136/bjsports-2011-090342

Kastelic, J., Galeski, A., and Baer, E. (1978). The multicomposite structure of tendon. *Connect Tissue Res.* 1, 11–23. doi: 10.3109/030082078091 52283

Kaux, J. F., Forthomme, B., Goff, C. L., Crielaard, J. M., and Croisier, J. L. (2011). Current opinions on tendinopathy. *J. Sports Sci. Med.* 10, 238–253.

Keene, D., Sakai, L. Y., Bächinger, H. P., and Burgeson, R. E. (1987). Type III collagen can be present on banded collagen fibrils regardless of fibril diameter. *J. Cell Biol.* 105, 2393–2402. doi: 10.1083/jcb.105.5.2393

Ker, R. F., Bennett, M. B., Bibby, S. R., Kester, R. C., and Alexander, R. M. (1987). The spring in the arch of the human foot. *Nature* 325, 147–149. doi: 10.1038/325147a0

Kim, B., Yoon, J. H., Zhang, J., Mueller, P O E., and Halper, J. (2010). Glycan profiling of a defect in decorin glycosylation in equine systemic proteoglycan accumulation, a potential model of progeroid form of Ehlers-Danlos syndrome. *Arch. Biochem. Biophys.* 501, 221–231. doi: 10.1016/j.abb.2010.06.017

Kohrs, R. T., Zhao, C., Sun, Y-.L., Jay, G. D., Zhang, L., and Warman, M. L., et al. (2011). Tendon fascicle gliding in wild type, heterozygous, and lubricin knockout mice. *J. Orthopaedic Res.* 29, 384–389. doi: 10.1002/jor.21247

Komi, P. V. (1990). Relevance of In vivo Force Measurements to Human Biomechanics. *J. Biomech.* 23, 23–34. doi: 10.1016/0021-9290(90)90038-5

Komi, P. V., Fukashiro, S., and Jarvinen, M. (1992). Biomechanical loading of Achilles tendon during normal locomotion. *Clin. J. Sport Med.* 11, 521–531.

Kondratko-Mittnacht, J., Duenwald-Kuehl, S., Lakes R., and Vanderby, R. Jr. (2015). Shear load transfer in high and low stress tendons. *J. Mech. Behav. Biomed. Mater.* 45, 109–120. doi: 10.1016/j.jmbbm.2015.01.021

Kongsgaard, M., Aagaard, P., Kjaer, M., Magnusson, S. P. (2005). Structural Achilles tendon properties in athletes subjected to different exercise modes and in Achilles tendon rupture patients. *J. Appl. Physiol.* 99, 1965–1971. doi: 10.1152/japplphysiol.00384.2005

Kurose, T., Asai, Y., Mori, E., Daitoku, D., Kawamata, S. (2006). Distribution and Change of Collagen Types I and III and Elastin in Developing Leg Muscle in Rat. *Hiroshima J. Med. Sci.*, 55, 85–91.

Lantto, I., Heikkinen, J., Flinkkilä, T., Ohtonen, P., Leppilahti, J. (2015). Epidemiology of Achilles tendon ruptures: increasing incidence over a 33-year period. *Scand. J. Med. Sci. Sports* 25, 133–138. doi: 10.1111/sms.12253

Li, D. Y., Brooke, B., Davis, E. C., Mecham, R. P., Sorensen, L. K., and Boak, B. B., et al. (1998). Elastin is an essential determinant of arterial morphogenesis. *Nature* 393, 276–280. doi: 10.1038/30522

Li, H. Y., Yasui, Y., Han, S. H., Miyamoto, W., Hua, Y. H. (2017). Achilles tendinopathy: from the basic science to the clinic. *BioMed. Res. Int.* 2017, 2–4. doi: 10.1155/2017/9534125

Lichtwark, G. A., and Wilson, A. M. (2005). In vivo mechanical properties of the human Achilles tendon during one-legged hopping. *J. Exp. Biol.* 208, 4715–4725. doi: 10.1242/jeb.01950

Maas, H., Noort, W., Baan, G. C., and Finni, T. (2020). Non-uniformity of displacement and strain within the Achilles tendon is affected by joint angle configuration and differential muscle loading. *J. Biomech.* doi: 10.1016/j.jbiomech.2020.109634

Maas, H., and Finni, T. (2018). Mechanical Coupling Between Muscle-Tendon Units Reduces Peak Stresses. *Exerc. Sport Sci. Rev.* 46, 26–33. doi: 10.1249/JES.0000000000000132

Maffulli, N., Ewen, S. W., Waterston, S. W., Reaper, J., Barrass, V. (2000). Tenocytes from Ruptured and Tendinopathic Achilles Tendons Produce Greater Quantities of Type III Collagen than Tenocytes from Normal Achilles Tendons An In Vitro Model of Human Tendon Healing. *Am. J. Sports Med.* 28, 499–505. doi: 10.1177/03635465000280040901

Muench, J. R., Thelen, D. G., and Henak, C. R. (2019). *Interfibrillar Shear Behavior is Altered in Aging Tendon Fascicles. Biomechanics and Modeling in Mechanobiology*. Berlin: Springer Berlin Heidelberg, 1–9. doi: 10.1007/s10237-019-01251-1250

Pękala, P. A., Henry, B. M., Ochała, A., Kopacz, P., Tatoń, G., Młyniec, A., et al. (2016). The twisted structure of the Achilles tendon unraveled: a detailed quantitative and qualitative anatomical investigation. *Scand. J. Med. Sci. Sports* 27, 1705–1715. doi: 10.1111/sms.12835

Purslow, P. P. (2009). "The shear modulus of connections between tendon fascicles," in *Proceedings of the IEEE Toronto International Conference on Science and Technology for Humanity*, Toronto, 10–13. doi: 10.1109/TIC-STH.2009.5444520.

Rees, S. G., Curtis, C. L., Dent, C. M., Caterson, B. (2005). Catabolism of aggrecan proteoglycan aggregate components in short-term explant cultures of tendon. *Matrix Biol.* 24, 219–231. doi: 10.1016/j.matbio.2005.02.002

Reuvers, J., Thoreson, A. R., Zhao, C., Zhang, L., Jay, G. D., An, K. N. (2011). The mechanical properties of tail tendon fascicles from lubricin knockout, wild type and heterozygous mice. *J. Struct. Biol.* 176, 41–45. doi: 10.1016/j.jsb.2011.07.013

Riley, G. (2008). Tendinopathy - From basic science to treatment. *Nat. Clin. Pract. Rheumatol.* 4, 82–89. doi: 10.1038/ncprheum0700

Ritty, T. M., Ditsios, K., and Starcher, B. C. (2002). Distribution of the elastic fiber and associated proteins in flexor tendon reflects function. *Anat. Rec.* 268, 430–440. doi: 10.1002/ar.10175

Robbins, J., and Vogel, K. (1994). Regional expression of mRNA for proteoglycans and collagen in tendon. *Eur. J. Cell Biol.* 64, 264–270.

Rowson, D., Knight, M. M., and Screen, H. R. C. (2016). Zonal Variation in Primary Cilia Elongation Correlates With Localized Biomechanical Degradation in Stress Deprived Tendon. *J. Orthopaedic Res.* 34, 2146–2153. doi: 10.1002/jor.23229

Sarver, D. C., Kharaz, Y. A., Sugg, K. B., Gumucio, J. P., Comerford, E., Mendias, C. L. (2017). Sex Differences in Tendon Structure and Function. *J. Orthopaedic Res.* 35, 2117–2126. doi: 10.1002/jor.23516

Schneider, C. A., Rasband, W. S., and Eliceiri, K. W. (2017). NIH Image to ImageJ: 25 years of Image Analysis. *Nat. Methods* 9, 671–675. doi: 10.1038/nmeth.2089

Shim, V. B., Fernandez, J. W., Gamage, P. B., Regnery, C., Smith, D. W., Gardiner, B. S., et al. (2014). Subject-specific finite element analysis to characterize the in fl uence of geometry and material properties in Achilles tendon rupture. *J. Biomech.* 47, 3598–3604. doi: 10.1016/j.jbiomech.2014.10.001

Slane, L. C., and Thelen, D. G. (2014). Non-uniform displacements within the Achilles tendon observed during passive and eccentric loading. *J. Biomech.* 47, 2831–2835. doi: 10.1016/j.jbiomech.2014.07.032

Smith, K. D., Vaughan-Thomas, A., Spiller, D. G., Innes, J. F., Clegg, P. D., Comerford, E. J., et al. (2011). The organisation of elastin and fibrillins 1 and 2 in the cruciate ligament complex. *J. Anat.* 218, 600–607. doi: 10.1111/j.1469-7580.2011.01374.x

Södersten, F., Hultenby, K. R., Heinegard, D., Johnston, C., and Ekman, S. (2013). Immunolocalization of collagens and III) and cartilage oligomeric matrix protein in the normal and injured equine superficial digital flexor tendon. *Connect. Tissue Res.* 54, 62–69. doi: 10.3109/03008207.2012.734879

Stevens, A., and Bancroft, J. D. (1990). "Carbohydrates /Harry C. Cook," in *Theory and Practice of Histological Techniques*, eds J. D. Bancroft, A. Stevens (London: Churchill Livingstone).

Sun, Y., Berger, E. J., Zhao, C., Jay, G. D., An, K. N., Amadio, P. C., et al. (2006). Expression and mapping of lubricin in canine flexor tendon. *J. Orthopaedic Res.* 1861–1868. doi: 10.1002/jor.20239.

Sun, Y., Berger, E. J., Zhao, C., An, K. N., Amadio, P. C., Jay, G., et al. (2009). Mapping lubricin in canine musculoskeletal tissues mapping lubricin in canine musculoskeletal tissues. *Connect. Tissue Res.* 47, 215–221. doi: 10.1080/03008200600846754

Sun, Y. L., Wei, Z., Zhao, C., Jay, G. D., Schmid, T. M., Amadio, P. C., et al. (2015). Lubricin in human achilles tendon: the evidence of intratendinous sliding motion and shear force in achilles tendon. *J. Orthopaedic Res.* 33, 932–937. doi: 10.1002/jor.22897

Swann, D. A., Sotman, S., Dixon, M., and Brooks, C. (1977). The Isolation and Partial Characterization of the Major Glycoprotein (LGP-I) from the Articular Lubricating Fraction from Bovine Synovial Fluid. *Biochem. J.* 161, 473–485. doi: 10.1042/bj1610473

Szaro, P., Witkowski, G., Smigielski, R., Krajewski, P., Ciszek, B. (2009). Fascicles of the adult human Achilles tendon - An anatomical study. *Ann. Anat.* 191, 586–593. doi: 10.1016/j.aanat.2009.07.006

Theobald, P., Benjamin, M., Nokes, L., Pugh, N. (2005). Review of the vascularisation of the human Achilles tendon. *Int. J. Care Inj.* 36, 1267–1272. doi: 10.1016/j.injury.2005.02.012

Thorpe, C. T., Udeze, C. P., Birch, H. L., Clegg, P. D., and Screen, H. R. (2012). Specialization of tendon mechanical properties results from interfascicular differences. *J. R. Soc. Interf.* 9, 3108–3117. doi: 10.1098/rsif.2012.0362

Thorpe, C. T., Udeze, C. P., Birch, H. L., Clegg, P. D., Screen, H. R. (2013b). Capacity for sliding between tendon fascicles decreases with ageing in injury prone equine tendons: a possible mechanism for age-related tendinopathy. *Eur. Cells Mater.* 25, 48–60. doi: 10.22203/eCM.v025a04

Thorpe, C. T., Birch, H. L., Clegg, P. D., Screen, H. R. (2013a). The role of the non-collagenous matrix in tendon function. *Int. J. Exp. Pathol.* 248–259. doi: 10.1111/iep.12027

Thorpe, C. T., Chaudhry, S., Lei, I. I., Varone, A., Riley, G. P., Birch, H. L., et al. (2015a). Tendon overload results in alterations in cell shape and increased markers of inflammation and matrix degradation. *Scand. J. Med. Sci. Sports* 25, 381–391. doi: 10.1111/sms.12333

Thorpe, C. T., Godinho, M. S. C., Riley, G. P., Birch, H. L., Clegg, P. D., Screen, H. R. C., et al. (2015b). The interfascicular matrix enables fascicle sliding and recovery in tendon, and behaves more elastically in energy storing tendons. *J. Mech. Behav. Biomed. Mater.* 52, 85–94. doi: 10.1016/j.jmbbm.2015.04.009

Thorpe, C. T., Peffers, M. J., Simpson, D., Halliwell, E., Screen, H. R., Clegg, P. D., et al. (2016b). Anatomical heterogeneity of tendon: fascicular and interfascicular tendon compartments have distinct proteomic composition. *Sci. Rep.* 6, 1–12. doi: 10.1038/srep20455

Thorpe, C. T., Karunaseelan, K. J., Ng, A., Chieng H. J., Riley, G. P., Birch, H. L., Clegg, P. D., et al. (2016a). Distribution of proteins within different compartments of tendon varies according to tendon type. *J. Anat.* 229, 450–458. doi: 10.1111/joa.12485

Uchiyama, B. Y. S., Amadio, P. C., Ishikawa, J., An, K. N. (1997). Boundary Lubrication between the Tendon and the Pulley in the Finger . *J. Bone Joint Surg.* 7, 213–218.

Viera, A. J., and Garrett, J. M. (2005). Understanding interobserver agreement: the kappa statistic. *Fam. Med.* 37, 360–363.

Vogel, K. G., and Peters, J. A. (2005). Histochemistry defines a proteoglycan-rich layer in bovine flexor tendon subjected to bending. *J. Musculoskeletal Neuronal Interact.* 5, 64–69.

Wang, J. H., Iosifidis, M. I., and Fu, F. H. (2006). Biomechanical basis for tendinopathy. *Clin. Orthop. Relat. Res.* 443, 320–332. doi: 10.1097/01.blo.0000195927.81845.46

Wren, T. A. L., Yerby, S. A., Beaupré, G. S., and Carder, D. R. (2001). Mechanical properties of the human achilles tendon. *Clin. Biomech.*, 16, 245–251.

Conflict of Interest: The authors declare that the research was conducted in the absence of any commercial or financial relationships that could be construed as a potential conflict of interest.

frontiers in Sports and Active Living

ORIGINAL RESEARCH
published: 06 August 2020
doi: 10.3389/fspor.2020.00088

Achilles Tendon Morphology Is Related to Triceps Surae Muscle Size and Peak Plantarflexion Torques During Walking in Young but Not Older Adults

*Katherine R. Knaus[1], Anahid Ebrahimi[2], Jack A. Martin[2,3], Isaac F. Loegering[4], Darryl G. Thelen[2,3,4] and Silvia S. Blemker[1,5]**

[1] Department of Biomedical Engineering, University of Virginia, Charlottesville, VA, United States, [2] Department of Mechanical Engineering, University of Wisconsin-Madison, Madison, WI, United States, [3] Department of Orthopedics and Rehabilitation, University of Wisconsin-Madison, Madison, WI, United States, [4] Department of Biomedical Engineering, University of Wisconsin-Madison, Madison, WI, United States, [5] Department of Mechanical and Aerospace Engineering, University of Virginia, Charlottesville, VA, United States

OPEN ACCESS

Edited by:
Huub Maas, Vrije Universiteit Amsterdam, Netherlands

Reviewed by:
Kiros Karamanidis, London South Bank University, United Kingdom
Rod S. Barrett, Griffith University, Australia

***Correspondence:**
Silvia S. Blemker
ssblemker@virginia.edu

Specialty section:
This article was submitted to Biomechanics and Control of Human Movement, a section of the journal Frontiers in Sports and Active Living

Received: *29 February 2020*
Accepted: *04 June 2020*
Published: *06 August 2020*

Citation:
Knaus KR, Ebrahimi A, Martin JA, Loegering IF, Thelen DG and Blemker SS (2020) Achilles Tendon Morphology Is Related to Triceps Surae Muscle Size and Peak Plantarflexion Torques During Walking in Young but Not Older Adults. Front. Sports Act. Living 2:88. doi: 10.3389/fspor.2020.00088

The interaction of the triceps surae muscles and the Achilles tendon is critical in producing the ankle plantarflexion torque required for human walking. Deficits in plantarflexor output are a hallmark of reduced mobility in older adults and are likely associated with changes in the triceps surae muscles that occur with age. Structural differences between young and older adults have been observed in the Achilles tendon and in the triceps surae muscles. However, less is known about how age-related differences in muscle and tendon morphology correspond with each other and, furthermore, how those morphology differences correlate with age-related deficits in function. The goal of this work was to investigate whether there is a correlation between age-related differences in triceps surae muscle size and Achilles tendon cross-sectional area (CSA) and whether either is predictive of ankle plantarflexion torque during walking. We used magnetic resonance imaging (MRI) to measure triceps surae muscle volumes and tendon CSAs in young ($n = 14$, age: 26 ± 4 years) and older ($n = 7$, age: 66 ± 5 years) adults, and we determined peak plantarflexion torques during treadmill walking. We found that individual muscle volumes as a percentage of the total triceps surae volume did not differ between young and older adults, though muscle volumes per body size (normalized by the product of height and mass) were smaller in older adults. Achilles tendon CSA was correlated with body size and muscle volumes in young adults but not in older adults. The ratio of tendon CSA to total triceps surae muscle volume was significantly greater in older adults. Peak ankle plantarflexion torque during walking correlated with body size and triceps surae volume in young and older adults but was correlated with tendon CSA only in the young adults. Structure–function relationships that seem to exist between the Achilles tendon and the triceps surae muscles in young adults are no longer evident in all older adults. Understanding mechanisms that determine altered Achilles tendon CSA in older adults may provide insight into age-related changes in function.

Keywords: aging gait, gastrocnemius, soleus, plantarflexion torque, muscle volume, tendon cross-sectional area

INTRODUCTION

The interaction of the triceps surae muscles with the Achilles tendon is critically important to human walking. This complex muscle–tendon interplay is the primary source of plantarflexion torque at the ankle and is implicated in the development of walking deficits that occur with age. Gait differences between young and older adults are clearly associated with differences in plantarflexor output (Winter et al., 1990; Kerrigan et al., 1998; DeVita and Hortobagyi, 2000; Boyer et al., 2017). Numerous studies have investigated age-related differences in the morphology and the mechanical properties of the Achilles tendon and triceps surae muscles (Karamanidis and Arampatzis, 2006; Onambele et al., 2006; Stenroth et al., 2012), but it remains unclear how muscle and tendon structure relate to each other in both young and older adults. Further, the association between age-related changes in muscle and tendon structure and changes in plantarflexor output has not been fully explored.

The triceps surae muscles share a common series elastic element in the Achilles tendon but are an anatomically complicated group of muscles that may experience complex changes with age. The biarticular gastrocnemius and uniarticular soleus muscles within this group differ greatly in volume (Ward et al., 2009; Handsfield et al., 2014), architecture (Ward et al., 2009; Rana et al., 2013; Dalmau-Pastor et al., 2014; Bolsterlee et al., 2019), and fiber type (Johnson et al., 1973). It is not surprising that empirical and modeling studies suggest functional differences between these muscles, predicting unequal contributions to propulsion and support during walking (Neptune et al., 2001; Anderson and Pandy, 2003; McGowan et al., 2008; Francis et al., 2013). Each muscle's function is rooted in its intricate architecture. The gastrocnemius comprises distinct medial and lateral heads with different origins (Dalmau-Pastor et al., 2014). The soleus is divided by its aponeuroses into bipennate anterior compartments and unipennate posterior compartments (Agur et al., 2003; Hodgson et al., 2006; Bolsterlee et al., 2018). Age-related sarcopenia leads to reduced muscle volumes in the triceps surae as a whole (Janssen et al., 2000; Morse et al., 2005); however, it is unclear whether sarcopenia similarly affects each individual triceps surae muscle. It is possible that the individual muscles' susceptibility to atrophy may vary due to differences in mechanical stimuli and fiber-type composition (Nilwik et al., 2013).

Triceps surae muscle volume is indicative of ankle plantarflexion torque capacity (Fukunaga et al., 2001), such that a smaller triceps surae volume may explain why older adults employ lower ankle plantarflexion torques than young adults when walking at the same speed (DeVita and Hortobagyi, 2000; Franz and Thelen, 2015). However, direct comparisons between plantarflexion torques during walking and triceps surae muscle volumes have not been performed across age groups to assess age-related differences. Further, given the functional differences between triceps surae muscles, age-related changes in individual components of this muscle group may better explain torque deficits.

In contrast to changes in muscle size, Achilles tendon cross-sectional area (CSA) is maintained or even increased with age (Onambele et al., 2006; Stenroth et al., 2012). Healthy tendons adapt to changes in mechanical loading (Bohm et al., 2015), suggesting that the ratio of muscle size to tendon size should remain constant. However, the correlation between muscle size and tendon size has not been well studied, nor have age-related differences in this correlation been observed. Understanding the morphological relationship between the Achilles tendon and individual components of the triceps surae, in addition to the full muscle group, may provide further insight into age-related changes in walking.

The goal of this work was to investigate how triceps surae muscle volumes collectively and individually differed with age. We aimed to determine (1) if age-related differences in muscle size correlated with age-related differences in Achilles tendon CSA and (2) if age-related differences in muscle size and tendon CSA were predictive of age-related differences in joint torque during walking. We used magnetic resonance imaging (MRI) to measure muscle volumes and tendon CSAs in young and older adults and determined peak plantarflexion torques during treadmill walking. We tested the hypotheses that (i) triceps surae muscle volumes would negatively correlate with age and positively correlate with body size while Achilles tendon CSA would positively correlate with both age and body size, (ii) age-related changes in volume would differ between individual muscles of the triceps surae, and (iii) differences in tendon and muscle size would positively correlate with differences in ankle plantarflexion torque during walking in both young and older adults.

METHODS

Subjects

Fourteen healthy young adults (six females/eight males, age: 26 $\pm$ 4 years, height: 1.78 $\pm$ 0.10 m, mass: 74.87 $\pm$ 12.11 kg) and seven healthy older adults (four females/three males, age: 66 $\pm$ 5 years, height: 1.76 $\pm$ 0.07 m, mass: 74.57 $\pm$ 15.26 kg) participated in this study (**Table 1**). No subjects had a history of orthopedic or neurological impairment or injury to the lower limb, and all could walk comfortably on a treadmill. All older adult subjects reported participating in daily physical activity. All subjects provided written consent, and the study protocol was approved by the University of Wisconsin–Madison Health Sciences Institutional Review Board.

Triceps Surae Muscle Volume Measurements

The triceps surae muscles and Achilles tendon were imaged with a 3-T Signa PET/magnetic resonance (MR) scanner (GE Healthcare) using a spoiled gradient recall-echo sequence that used iterative decomposition of water and fat with echo asymmetry and least squares estimation (IDEAL-SPGR) (Reeder et al., 2007). Subjects lay supine with their right ankle relaxed and wrapped in a GEM Medium Flex Coil. Two sets of three-dimensional images were collected with the following scanning parameters: in-plane resolution: 0.72 $\times$ 0.72 mm; slice thickness: 2 mm; imaging matrix: 512 $\times$ 512 $\times$ 76; flip angle: 14°.

TABLE 1 | Subject characteristics (mean ± standard deviation).

	Age (years)	Height (m)	Mass (kg)	Tendon CSA (mm^2)	Moment arm (mm)
Young	25.5 ± 4.3	1.78 ± 0.1	74.87 ± 12.11	61.35 ± 12.24	46.64 ± 3.87
Older	66 ± 4.8	1.76 ± 0.07	74.57 ± 15.26	65.54 ± 6.96	43.54 ± 8.13
p-value	**0.0003**	0.601	0.911	0.248	0.086
	Peak ankle torque (Nm)	**Stride length (m)**	**Step length (m)**	**Stride time (s)**	**Cadence (steps/min)**
Young	114.23 ± 24.01	1.38 ± 0.09	0.69 ± 0.04	1.11 ± 0.07	108.74 ± 6.83
Older	106.04 ± 27.72	1.27 ± 0.1	0.64 ± 0.05	1.02 ± 0.08	118.48 ± 9.84
p-value	0.478	**0.036**	**0.035**	**0.036**	**0.040**

All gait characteristics are reported for subjects walking at a speed of 1.25 m/s. Young and older adults did not differ significantly in body size, Achilles tendon geometry, or peak torque produced during walking. However, young and older adults did differ in their gait spatiotemporal parameters, with older adults using shorter strides at a higher cadence than young adults walking at 1.25 m/s. $p < 0.05$ was considered significant and written in bold.

Continuous axial images were obtained from the calcaneus to the femur proximal to the condyles.

The triceps surae muscles in the right limb were segmented using a Matlab (MathWorks Inc., Natick, MA, USA) software package that was developed in the Multiscale Muscle Mechanophysiology lab at the University of Virginia for measuring lower-limb muscle volumes (Handsfield et al., 2014). In each axial image, a single researcher manually outlined the boundaries of four unique muscles: the medial gastrocnemius (MG), the lateral gastrocnemius (LG), the posterior soleus (PS), and the anterior soleus (AS) (**Figure 1**). The heads of the gastrocnemius and the soleus muscles were identified based on a detailed slice-by-slice segmentation atlas of lower-limb muscles (Handsfield et al., 2014), and the posterior and anterior compartments of the soleus were identified based on descriptions of the aponeurosis that visibly separates these regions of the muscle (Hodgson et al., 2006; Bolsterlee et al., 2018). Individual muscle volumes were calculated by summing the volume of voxels from the segmentation in each slice. Previously, we determined the average intra-user variability in measuring muscle volumes using this segmentation method to be 4.4% (Handsfield et al., 2016). Total triceps surae muscle volume was defined as the sum of the volumes of the four individual muscles. Relative muscle volumes were determined by dividing individual muscle volumes by the total triceps surae muscle volume.

To determine differences in muscle size independent of body size differences, we normalized individual and total muscle volumes by dividing by the product of subject height and mass. Triceps surae muscle volumes have been shown to vary with height * mass as a metric of body size in healthy adults (Handsfield et al., 2014).

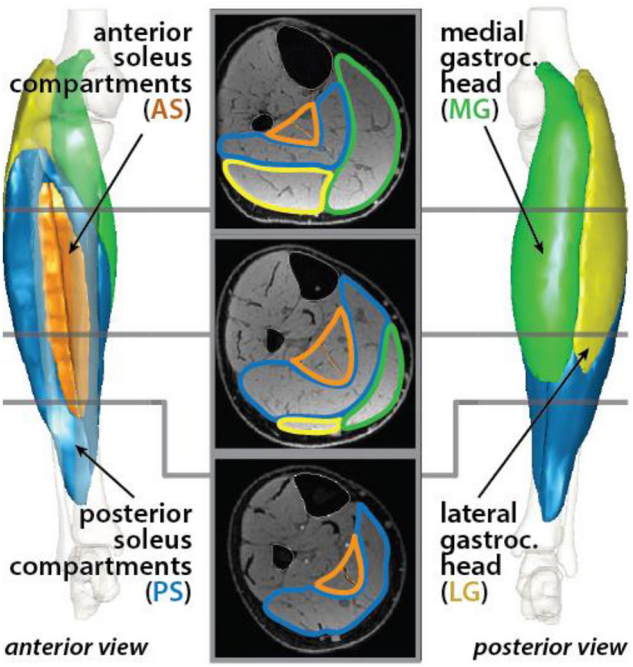

FIGURE 1 | Triceps surae muscles were segmented in axial MR images. The muscle cross sections were defined for the medial (green) and lateral (yellow) heads of the gastrocnemius and the posterior (blue) and anterior (orange) compartments of the soleus. Each muscle was reconstructed in 3-D.

Achilles Tendon CSA Measurements

The Achilles free tendon was also segmented in the axial MR images from the most proximal image where the calcaneus was visible to the soleus muscle–tendon junction (MTJ), which was defined as the most distal image where the soleus was visible. The tendon volume was determined from the summed CSA multiplied by the slice thickness, while the tendon length was computed as the summed distance between the centroids of adjacent cross sections (Handsfield et al., 2014).

To test our hypotheses, a representative Achilles CSA was determined from the middle slice of the free tendon. A ratio of tendon size per muscle size was calculated by dividing Achilles

tendon CSA by individual and total triceps surae muscle volumes, just as tendon size per body size was found by dividing tendon CSA by the product of height and mass.

Achilles Tendon Moment Arm Measurements

Achilles tendon moment arms were measured using a previously described method combining ultrasonography and motion capture (Rasske et al., 2017; Keuler et al., 2019; Ebrahimi et al., 2020). Briefly, subjects lay prone with their right knees flexed 20° while their ankles were rotated from maximum dorsiflexion to maximum plantarflexion. Subjects were asked to provide resistance during ankle rotation to engage their triceps surae muscles. An ultrasound transducer positioned over the Achilles tendon was used to collect B-mode images. The superficial and deep edges of the tendon were manually identified, and a tendon line of action was determined from the best fit between them. Marker clusters on the shank, foot, and transducer were used to record kinematics in order to transform ultrasound images into the reference frame of the shank. A best-fit screw axis that described the foot motion with respect to the shank was computed to define a functional axis (Siston et al., 2005). Achilles tendon moment arm was computed in each image frame as the perpendicular distance between the tendon line of action and the functional axis (Wade et al., 2019). The moment arm was estimated for a 0° posture using a quadratic fit of moment arm relative to ankle angle.

Peak Ankle Torque Measurements During Walking

Subjects walked on an instrumented treadmill (sample rate: 1,900 Hz, Bertec Corp.) at 1.25 m/s. Ground reaction forces were recorded during at least two 10-s trials (minimum 10 strides). Motion capture (sample rate: 190 Hz, Motion Analysis Corp.) was used to record 3-D trajectories of markers positioned on the pelvis, thigh, and shank during walking. Lower-extremity kinematics and kinetics were computed using standard inverse dynamics techniques (Visual3D, C-Motion, Inc.). Peak ankle plantarflexion moments were averaged across gait cycles for each subject. Plantarflexion torque was assumed to be generated entirely by the triceps surae muscles. Peak ankle torque was divided by Achilles tendon moment arm to provide an estimate of Achilles tendon force at these peaks.

Statistical Analyses

We used a Mann–Whitney rank sum test, a non-parametric test, to determine differences in our measurements between young and older subject groups. For tests that were repeated over the four individual muscles, we corrected for family-wise error rate using the Holm–Bonferroni method. Linear regression analysis was used to determine correlations between different measurements in either young or older subjects. Significance was set at $p = 0.05$.

RESULTS

Relative Volumes of Triceps Surae Muscles Did Not Differ Between Young and Older Adults

Relative volumes of individual triceps surae muscles, compared to total volume, were similar in young (percentage of total volume: $PS = 41.9\%$, $AS = 8.8\%$, $MG = 30.9\%$, $LG = 18.3\%$) and older ($PS = 42.4\%$, $AS = 8.5\%$, $MG = 29.7\%$, $LG = 19.4\%$) adults (**Figure 2**), with no significant difference for any muscle (**Table 2**).

Triceps Surae Muscle Volumes Were Correlated With Body Size and Were Smaller per Body Size in Older Adults

Total triceps surae volume was positively correlated with the product of height and mass in both young and older adults (**Figure 3A**). The scaling relationship between total triceps surae muscle volume and body size as well as the relationships for all individual muscles in young adults and older adults is provided in **Table 3**. Triceps surae volumes normalized by height * mass were smaller in older adults (**Figure 3B**), and all individual muscles were smaller per body size in older adults (percentage difference: $PS = 15.4\%$, $AS = 17.9\%$, $MG = 20.3\%$, $LG = 10.7\%$) (**Figure 3C**). Triceps surae muscle volumes were not significantly different between young and older adults but trended toward being smaller in older adults (percentage difference: $PS = 17.2\%$, $AS = 22.7\%$, $MG = 23.1\%$, $LG = 14.2\%$) (**Table 2**).

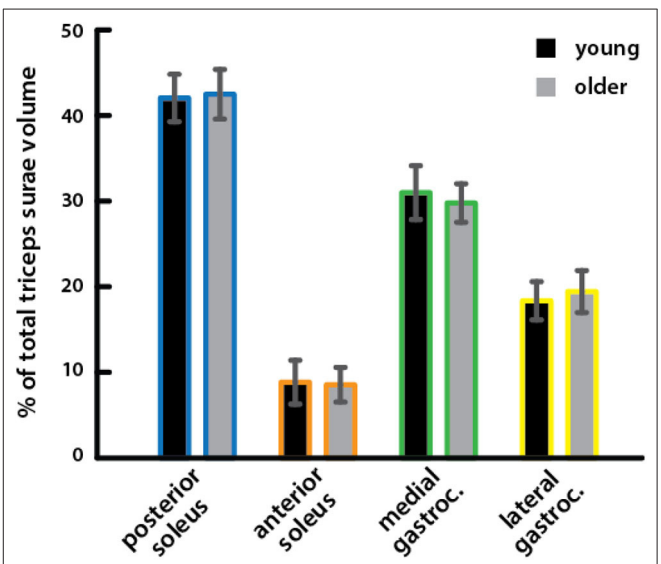

FIGURE 2 | Relative volumes of triceps surae muscles did not differ between young and older adults. Relative volumes of individual triceps surae muscles as a percentage of the total triceps surae volume are shown for young (black) and older (gray) adults. A Mann–Whitney rank sum test detected no significant differences between young and older adults for any muscle (**Table 2**).

TABLE 2 | Triceps surae muscle volumes (mean ± standard deviation) compared between young and older adults.

		Posterior soleus	Anterior soleus	Medial gastrocnemius	Lateral gastrocnemius	Total triceps surae
Muscle volume (cm^3)	Young	391.4 ± 84.3	83.8 ± 32.0	291.6 ± 81.9	175.1 ± 54.3	941.9 ± 229.9
	Older	329.4 ± 81.7	66.7 ± 20.5	231.1 ± 56.1	151.9 ± 47.2	779.1 ± 189.6
	p-value	0.668	0.668	0.576	0.436	0.167
Normalized volume (cm^3/kg*m)	Young	2.93 ± 0.26	0.62 ± 0.19	2.17 ± 0.3	1.28 ± 0.21	7.00 ± 0.60
	Older	2.51 ± 0.35	0.52 ± 0.18	1.77 ± 0.3	1.15 ± 0.24	5.95 ± 0.93
	p-value	0.060	0.218	0.060	0.248	**0.015**
Relative volume (%)	Young	41.94 ± 2.76	8.83 ± 2.55	30.91 ± 3.13	18.32 ± 2.23	N/A
	Older	42.38 ± 2.89	8.53 ± 2.02	29.7 ± 2.25	19.39 ± 2.44	N/A
	p-value	1.588	1.588	1.256	1.256	N/A
Tendon CSA/volume (cm^{-1})	Young	1.58 ± 0.18e−3	8.38 ± 3.77e−3	2.15 ± 0.27e−4	3.71 ± 0.88e−4	6.62 ± 0.77e−5
	Older	2.09 ± 0.55e−3	1.14 ± 0.66 e−2	3.03 ± 0.10e−4	4.68 ± 1.56 e−3	8.91 ± 2.68e−4
	p-value	0.069	0.069	**0.048**	0.218	**0.019**

Muscle volumes were normalized to account for body size differences by dividing by the product of each subject's height and mass. Relative volumes are the individual muscle volumes compared to the total triceps surae volume. Older adults had smaller absolute muscle volumes than young adults, but differences were not significant. The Mann–Whitney rank sum test was used to determine significance. The Holm–Bonferroni method was used to correct for family-wise error in tests repeated for individual muscle volumes. $p < 0.05$ was considered significant and appear in bold.

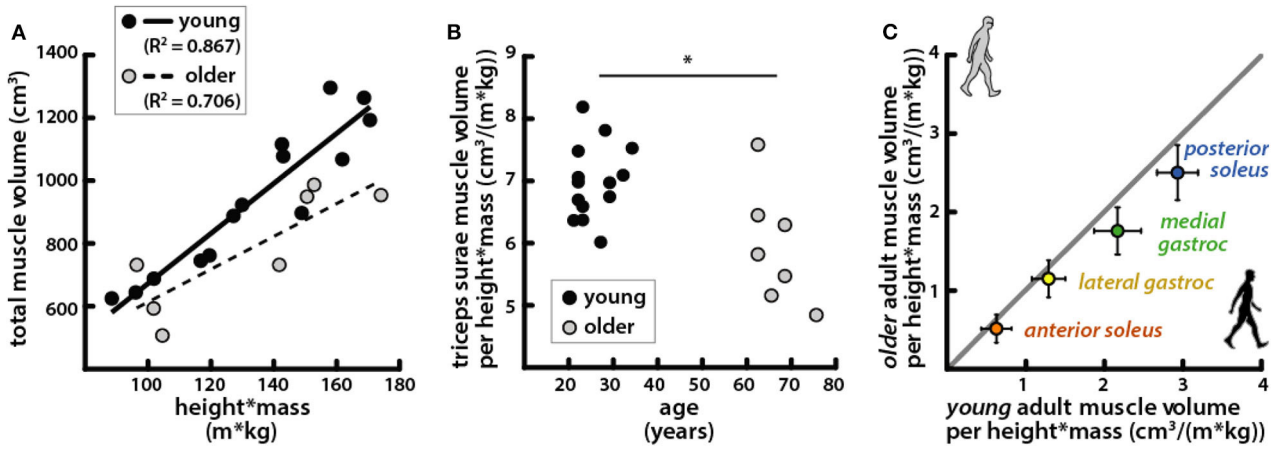

FIGURE 3 | Triceps surae muscle volumes per body size were correlated with body size and were smaller per body size in older adults. **(A)** Total triceps surae volumes vs. the product of height and mass for young (black circles, solid line: $R^2 = 0.867$, $p = 1.33e{-}6$) and older (gray circles, dashed line: $R^2 = 0.706$, $p = 0.018$) adults. **(B)** Total triceps surae muscle volumes normalized by height * mass vs. age; a Mann–Whitney rank sum test determined muscle volume normalized by body size was significantly different between young and older adults ($p = 0.015$). **(C)** Average individual triceps surae muscle volumes normalized by height * mass for older adults vs. young adults; error bars indicate standard deviation. Points falling below the unity line (gray) indicate muscles that are smaller in older adults than in young adults (**Table 2**). *Indicates significant difference between young and old adults.

Tendon CSA Was Correlated With Body and Muscle Size in Young Adults but Not in Older Adults

Achilles tendon CSA varied along its length from the top of the calcaneus to the soleus MTJ (**Figure 4**). There were no significant differences in average CSA between young (53.71 ± 14.88 mm^2) and older (51.22 ± 13.18 mm^2) adults or in CSA measured at the top of the calcaneus (young = 64.87 ± 16.34 mm^2; older = 51.59 ± 18.02 mm^2) and CSA measured at the soleus MTJ (young = 49.76 ± 14.05 mm^2; older = 51.83 ± 10.89 mm^2). Free tendon lengths also varied greatly between individuals but were not significantly different between young (50.95 ± 17.94 mm) and older (45.26 ± 20.39 mm) adults (**Figures 4A,D**). There were no significant differences in free tendon volume between young (2.65 ± 1.05 cm^3) and older (2.25 ± 1.07 cm^3) adults. CSA at half of the free tendon's length was used for further analysis and is subsequently referred to as Achilles tendon CSA.

Achilles tendon CSA trended toward being larger in older adults, but the difference was not significant (**Table 1**). Tendon CSA was positively correlated with height * mass in young adults but not in older adults (**Figure 5A**). Similarly, tendon CSA was positively correlated with total

TABLE 3 | Linear regression was used to determine the relationship between individual and total muscle volumes and body size, calculated as height * mass; Achilles tendon CSA; peak plantarflexion torque during walking at 1.25 m/s; and peak Achilles tendon force, estimated by dividing peak torque by moment arm, in young and older adults.

			Posterior soleus muscle volume (cm^3)	Anterior soleus muscle volume (cm^3)	Medial gastrocnemius muscle volume (cm^3)	Lateral gastrocnemius muscle volume (cm^3)	Total triceps surae muscle volume (cm^3)
Height * mass (kg*m)	Young	R^2	0.801	0.412	0.713	0.812	0.867
		Equation	$0.29x + 22.09$	$0.54x + 88.64$	$0.28x + 53.05$	$0.45x + 55.7$	$0.11x + 31.26$
		p-value	**<0.001**	**0.013**	**<0.001**	**<0.001**	**<0.001**
	Older	R^2	0.762	0.253	0.658	0.465	0.706
		Equation	$0.33x + 24.39$	$0.75x + 81.81$	$0.44x + 29.79$	$0.44x + 64.81$	$0.14x + 26.36$
		p-value	**0.010**	0.250	**0.027**	0.092	**0.018**
Achilles tendon CSA (mm^2)	Young	R^2	0.749	0.229	0.838	0.602	0.798
		Equation	$0.13x + 12.17$	$0.18x + 46.01$	$0.14x + 21.47$	$0.17x + 30.73$	$0.05x + 16.56$
		p-value	**<0.001**	0.084	**<0.001**	**0.001**	**<0.001**
	Older	R^2	0.041	0.027	0.033	0.028	<0.001
		Equation	$0.02x + 59.84$	$0.06x + 61.84$	$-0.02x + 70.75$	$-0.02x + 69.28$	$0.00x + 65.26$
		p-value	0.662	0.726	0.697	0.721	0.983
Peak plantarflexion torque (Nm)	Young	R^2	0.808	0.294	0.644	0.745	0.801
		Equation	$0.26x + 14.03$	$0.41x + 80.12$	$0.24x + 45.65$	$0.38x + 47.39$	$0.09x + 26.22$
		p-value	**<0.001**	**0.045**	**<0.001**	**<0.001**	**<0.001**
	Older	R^2	0.725	0.279	0.650	0.707	0.760
		Equation	$0.29x + 10.9$	$0.71x + 58.41$	$0.40x + 14.05$	$0.49x + 31.10$	$0.13x + 6.75$
		p-value	**0.015**	0.223	**0.029**	**0.018**	**0.010**
Estimated peak tendon force (N)	Young	R^2	0.765	0.163	0.621	0.668	0.723
		Equation	$5.44x + 329.21$	$6.62x + 1{,}904.10$	$5.04x + 988.16$	$7.89x + 1{,}077.13$	$1.94x + 631.56$
		p-value	**<0.001**	0.153	**<0.001**	**<0.001**	**<0.001**
	Older	R^2	0.313	0.167	0.653	0.204	0.406
		Equation	$4.19x + 1{,}078.59$	$12.19x + 1{,}645.40$	$8.81x + 423.04$	$5.85x + 1{,}569.86$	$2.05x + 857.57$
		p-value	0.191	0.363	**0.028**	0.309	0.124

The equation and R^2-value for each linear regression are reported. $p < 0.05$ was considered significant and appear in bold.

triceps surae muscle volume in young adults (**Figure 5B**), while CSA was not related to total muscle volume in older adults.

Tendon CSA normalized to height * mass increased with age but was not significantly different between young and older adults (**Figure 5C**). However, tendon CSA normalized to total triceps surae muscle volume was significantly greater in older adults (**Figure 5D**). Additionally, the ratio of tendon size to muscle size was greater in older adults for all individual muscles, though the difference was only significant for the MG (**Table 2**).

Peak Ankle Plantarflexion Torque During Walking Was Correlated With Body and Muscle Size in Young and Older Adults but Was Correlated With Tendon Size Only in Young Adults

Peak torque during walking at 1.25 m/s was positively correlated with height * mass (**Figure 6B**) and was not significantly different between age groups (**Table 1**, **Figure 6A**). Peak torque was positively correlated with total triceps surae muscle volume in young and older adults (**Figure 6C**). Peak torque was positively correlated with Achilles tendon CSA in young adults but not in older adults (**Figure 6D**).

Estimated Peak Achilles Tendon Force Was Correlated With Triceps Surae Muscle Volume in Young Adults but Not in Older Adults

Achilles tendon moment arms were slightly smaller in older adults compared to young adults, but the difference was not significant (**Table 1**). Estimated peak Achilles tendon forces were also positively correlated with the total triceps surae volume in young adults (**Figure 6E**). However, in older adults, estimated peak force was not significantly correlated with total triceps surae muscle volume.

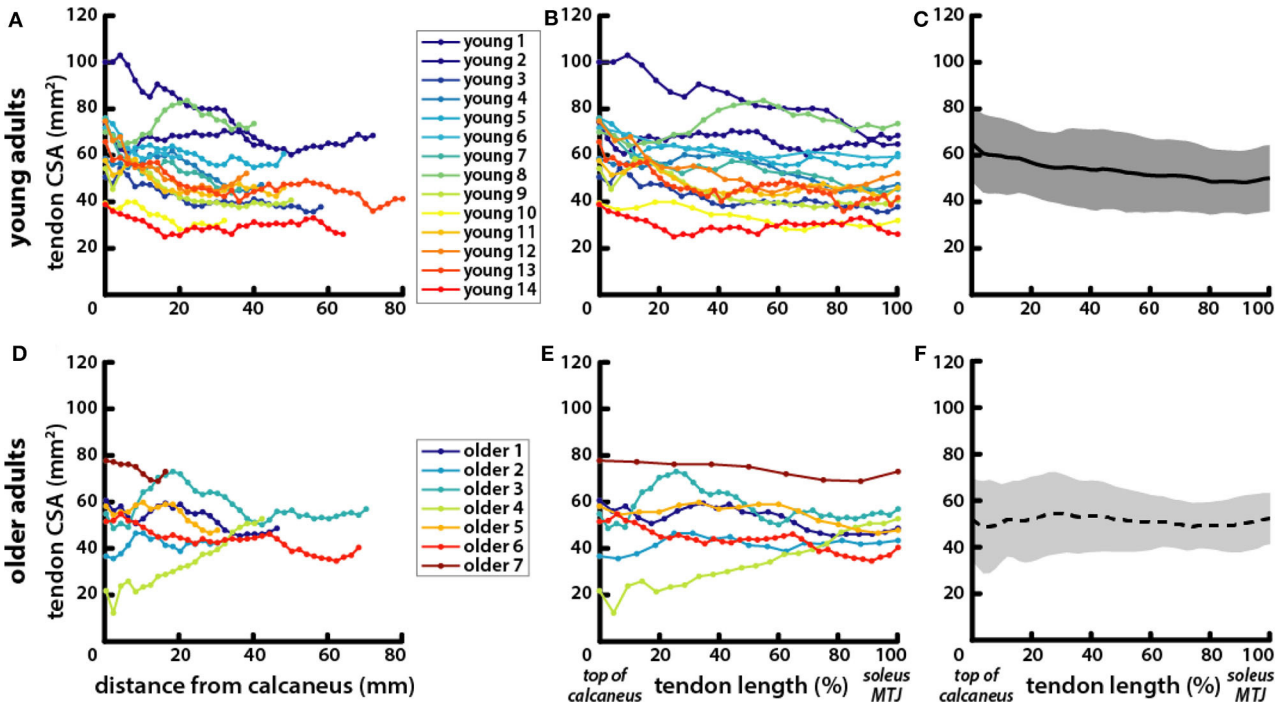

FIGURE 4 | Tendons exhibited greater variation in length and CSA within age groups than between young and older adults. Achilles tendon CSA was measured in axial MR images of **(A)** young and **(D)** older adults from the most proximal image where the calcaneus was visible to the most distal image where the soleus was visible. CSA locations are reported as their distance from the calcaneus in the proximal–distal direction. To account for variations in free tendon length, CSA locations were normalized to length for **(B)** young and **(E)** older adults with the top of the calcaneus being the most distal point at 0% and the soleus MTJ the most proximal point at 100%. Average tendon CSA is plotted with normalized tendon length in **(C)** young (solid line, gray shading for standard deviation) and **(F)** older (dotted line, light gray shading) adults.

DISCUSSION

We investigated how triceps surae muscle volumes and Achilles tendon CSA correlate with each other, body size, and peak ankle plantarflexion torque during walking and determined how those relationships differ between age groups. Although peak plantarflexion torques did not differ between young and older adults walking at the same speed, we found evidence of sarcopenia as triceps surae muscle volume per body size was lower in older adults. However, the relative volumes of the triceps surae muscles were the same in young and older adults. Both young and older adults' triceps surae muscle volumes were positively correlated with both body size and peak walking torques, but triceps surae muscle volumes were positively correlated with Achilles tendon size only in young adults.

We found that volume distribution between the gastrocnemius and soleus was similar between age groups and furthermore that the volume distributions between the unique heads and compartments within the respective muscles were also similar between age groups (**Figure 2**). The distribution of triceps surae muscle volume between the soleus and the heads of the gastrocnemius is similar to what has been reported previously in young adults (Albracht et al., 2008). A previous study found that although physiological CSA (PCSA) distribution of the gastrocnemius heads and soleus within the triceps surae was similar in young and older adults, volume distribution between these muscles differed with age (Morse et al., 2005). The authors considered the soleus as a whole and did not image the full muscle, estimating volume of the distal portion using local multiple regression in each subject. Our findings were not consistent with our hypothesis that we would see age-related differences in volume distribution between the individual muscles of the triceps surae, which we expected due to the different functional roles of each muscle. Specifically, we expected that the gastrocnemius would experience greater atrophy because it is composed of a higher percentage of fast twitch fibers than the soleus (Johnson et al., 1973; Nilwik et al., 2013). Additionally, we posited that differences in gait between young and older adults might be explained by an altered balance of force production between muscles with different contributions to propulsion and support in walking (Neptune et al., 2001; Anderson and Pandy, 2003; McGowan et al., 2008; Francis et al., 2013). Older adults can respond to biofeedback to match the propulsive forces that young adults produce during walking but also increase support forces (Franz et al., 2014). If the soleus contributes more to support while the gastrocnemius contributes more to propulsion (Francis et al., 2013), a greater soleus-to-gastrocnemius size ratio could correspond with greater support to propulsive force generation. However, we did not see a redistribution of muscle volumes that would correspond with an imbalance between propulsive and support forces.

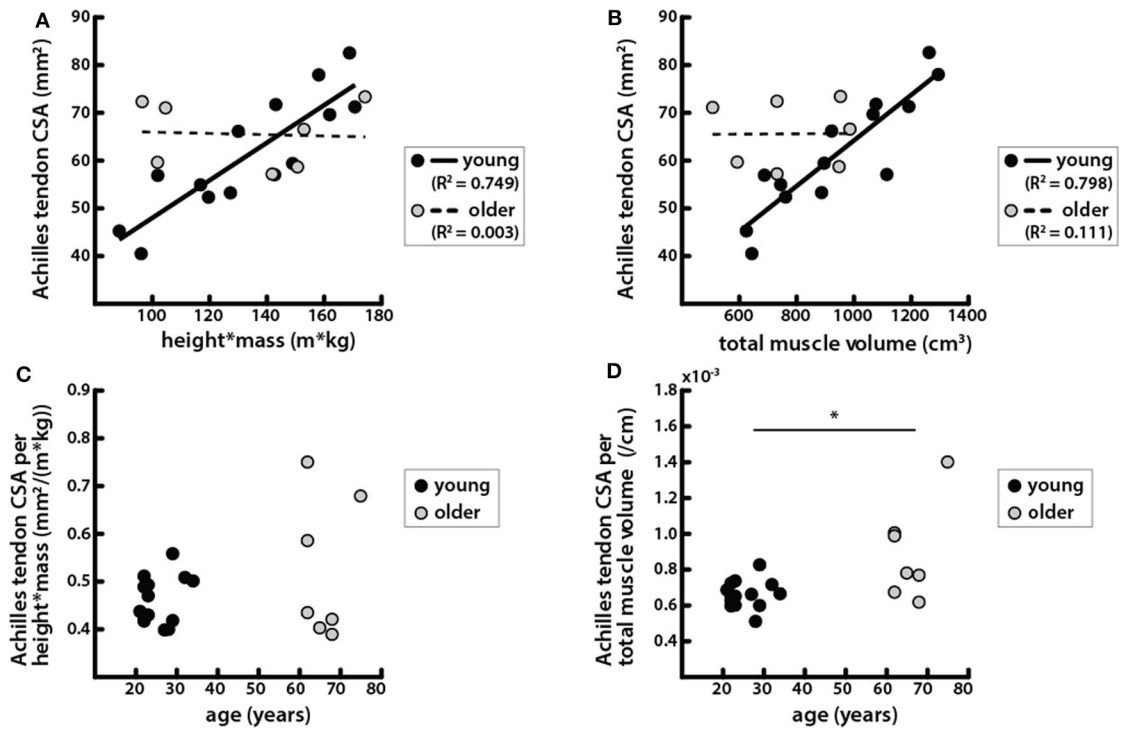

FIGURE 5 | Achilles tendon CSA was correlated with body and muscle size in young adults but not in older adults. **(A)** Achilles tendon CSAs vs. the product of height and mass in young (black circles, solid line: $R^2 = 0.749$, $p = 6.42e{-}5$) and older (gray circles, dashed line: $R^2 = 0.003$, $p = 0.901$) adults. **(B)** Achilles tendon CSA vs. total triceps surae muscle volume in young (black circles, solid line: $R^2 = 0.798$, $p = 1.69e{-}5$) and older (gray circles, dashed line: $R^2 = 0.111$, $p = 0.139$) adults. **(C)** Achilles tendon CSA normalized by height * mass vs. age; a Mann-Whitney rank sum test determined that there were no significant differences between age groups in tendon CSA normalized by body size ($p = 0.737$). **(D)** Achilles tendon CSA normalized by total triceps surae muscle volume vs. age; a Mann–Whitey rank sum test determined that tendon CSA normalized by muscle size was significantly different between young and older adults ($p = 0.019$). *Indicates significant difference between young and old adults.

Older adults exhibited a proportional relationship between triceps surae muscle volumes and body size (**Figure 3A**) but with a lower ratio of muscle volume to body size than that in young adults (**Figures 3B,C**). This is consistent with prior work in healthy young adults which showed that lower-limb muscle volumes scale with body size, computed as the product of height and mass (Handsfield et al., 2014). In our current work, we found that the posterior and anterior compartments of the soleus each exhibit a scaling relationship between their volume and height * mass, which has been previously unexplored. Our results demonstrate that this relationship is generally preserved with sarcopenia but with a smaller scaling factor. In previous studies, individual triceps surae muscle volumes were found to also be predicted by the product of the maximum anatomical CSA and the muscle length when combined with a shape factor (Albracht et al., 2008; Karamanidis et al., 2019). Interestingly, a unique shape factor was required to accurately predict muscle volumes in older adults, as the use of the shape factor for muscle volumes measured in young adults (Albracht et al., 2008) overestimated volumes of older adult muscles (Karamanidis et al., 2019). Our work provides further evidence that while the muscle scaling relationships that are present in young adults are not eliminated by aging, they are certainly altered.

Achilles tendon CSA scaled with body size as well as with triceps surae muscle volumes in young adults (**Figures 5A,B**), which is consistent with the hypothesis that there is a mechanical relationship between muscle loading and tendon adaptation that determines CSA (Bohm et al., 2015). The correspondence of tendon CSA with muscle volumes that we have shown provides morphological evidence of the structure–function relationship between muscle and tendon in young adults. This work complements previous mechanical evidence showing correlations between normalized Achilles tendon stiffness and tendon forces estimated during maximum isometric voluntary plantarflexion contractions (Arampatzis et al., 2007). The lack of relationship between muscle and tendon size in older adults suggests that an alternative mechanism may be driving tendon adaptation. Altered tendon adaptation does not appear to result in a positive correlation between CSA and age; we did not find that Achilles tendon CSA was significantly larger in older adults (**Figure 4C**) as has been found in previous studies (Onambele et al., 2006; Stenroth et al., 2012). Those studies also found that tendon material properties change with age, showing that older adults have more compliant tendons. Increases in tendon CSA may be an adaptation to conserve the level of strain experienced in physiologic loading conditions in order to avoid failure, which occurs at similar strain levels even as material properties vary

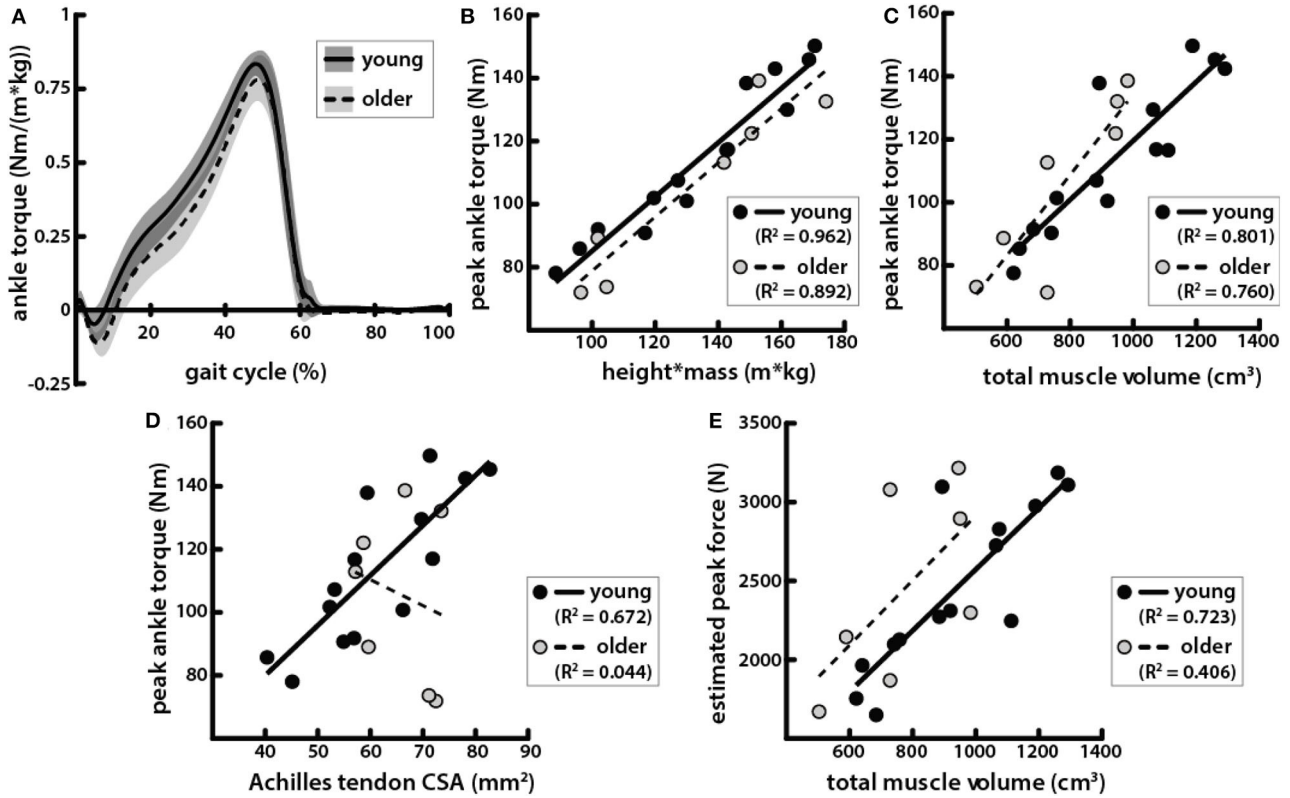

FIGURE 6 | Peak ankle plantarflexion torque during walking was correlated with body and muscle size in young and older adults but correlated with tendon size only in young adults. **(A)** Average ankle torque normalized by body size, calculated as the product of height and mass, in young (solid line, gray shading for standard deviation) and older (dotted line, light gray shading) adults walking at 1.25 m/s plotted over one gait cycle. **(B)** Peak plantarflexion torque during walking at 1.25 m/s vs. the product of height and mass in young (black circles, solid line: $R^2 = 0.926$, $p = 3.77e{-}8$) and older (gray circles, dashed line: $R^2 = 0.892$, $p = 1.35e{-}3$) adults. **(C)** Peak torque vs. total triceps surae muscle volume in young (black circles, solid line: $R^2 = 0.801$, $p = 1.56e\text{-}5$) and older (gray circles, dashed line: $R^2 = 0.760$, $p = 0.010$) adults. **(D)** Peak torque vs. Achilles tendon CSA in young (black circles, solid line: $R^2 = 0.672$, $p = 3.31e{-}4$) and older (gray circles, dashed line: $R^2 = 0.044$, $p = 0.651$) adults. **(E)** Estimated peak forces, calculated by dividing peak torques by Achilles tendon moment arms, vs. total triceps surae muscle volume in young (black circles, solid line: $R^2 = 0.723$, $p = 1.16e{-}4$) and older (gray circles, dashed line: $R^2 = 0.406$, $p = 0.124$) adults.

(LaCroix et al., 2013). This theory is supported by our finding that older adults had a significantly larger ratio of tendon CSA to muscle volume compared with the young adults (**Figure 5D**). The relationship between tendon and muscle size can be used to assess how much older adults deviate morphologically from young adults (**Figure 5B**) and may be indicative of the quality of the structure–function relationship between the Achilles tendon and triceps surae muscles in older adults. Such a metric might provide a more biomechanically relevant way to estimate the functional potential of adults, instead of the number of years they have been alive.

Peak plantarflexion torques during walking were positively correlated with body size, and the ratio of peak torque to height * mass was very similar in young and older adults (**Figure 6B**). This result is not surprising since the mechanical demands of walking are tied to body size. Body mass determines the load applied at the center of mass, while height is proportional to the lever arm of that load. Peak plantarflexion torques have been shown to differ between young and old adults when walking at the same speed (DeVita and Hortobagyi, 2000; Franz and Thelen, 2015; Boyer et al., 2017). Older adults in our studies did not walk with significantly lower peak torques, but it should be noted that the heights and masses of the young and older adults were similar in our study and also that they walked at a speed of 1.25 m/s, which was slower than in some previous studies (DeVita and Hortobagyi, 2000; Boyer et al., 2017). We did observe age-related differences in spatiotemporal parameters (**Table 1**). Peak torques during walking observed here were positively correlated with triceps surae muscle volumes (**Figure 6C**). Previous studies have shown positive correlations in young adults between plantarflexion muscle volumes and maximal plantarflexion torques measured both isokinetically and isometrically with a dynamometer (Morse et al., 2004; Baxter and Stephen, 2014), but the correlations were not as strong as those found in this study. In one of these studies, torque measured during maximum voluntary isometric contraction in older adults was not found to be significantly correlated with muscle volumes (Morse et al., 2004).

Achilles tendon CSA was positively correlated with body and muscle size, as well as with peak plantarflexion torque in young adults, but was correlated with none of these in older adults (**Figure 6D**). These results indicate that the mechanical relationships governing tendon size may differ between young

and older adults. Additionally, estimated Achilles tendon forces were not correlated with triceps surae muscle volumes in older adults. We expected that accounting for moment arms would improve correlations between plantarflexor output and muscle size by removing variation due to differences in musculoskeletal geometry such that muscle size would be compared directly to force production. In a previous study, Achilles tendon moment arms were shown to positively correlate with plantarflexion torque measured by dynamometry, as well as with plantarflexor muscle volumes (Baxter and Stephen, 2014). In our study, moment arms were not directly correlated with muscle volumes, body size, or peak plantarflexion torques during walking in either young or older adults. Older adults in our study had slightly smaller moment arms than the young adults, as has been shown previously (Rasske and Franz, 2018), though the difference was not significant here.

There are several limitations of this study that should be mentioned. First, we were limited by a relatively small sample size, especially in the older adult group. Furthermore, the average age of the older adults in this study (66 ± 5 years) may have been too low to be associated with substantial age-related changes in function, considering adults can be considered in "midlife" under the age of 65 years old (Boyer et al., 2017). Previous authors have posited that age-related changes in tendon and muscle exhibit different time courses, as they observed lower muscle strength but similar tendon properties in older adults in their sixties (Karamanidis and Arampatzis, 2006). The observed age-related differences in muscle–tendon relationships may vary in older adults in their late seventies and eighties. Also, we did not control for physical activity level between the two age groups. All older adults reported engaging in regular physical activity, and while seven of the young adults also engaged in regular physical activity, we did not have reports from the other seven subjects, so we cannot confirm a similar activity level between groups. We may have been more likely to see differences in peak plantarflexion torque between young and older adults in a group over 75 years old. However, we did see differences between triceps surae muscles and Achilles tendons between our age groups, suggesting that structural changes may precede mobility deficits that arise with aging. Here, we used volume as a metric of muscle size, and therefore strength, since we did not measure fascicle or sarcomere lengths necessary for computing PCSA. Because the ratio of muscle belly length to muscle fiber length in the triceps surae was shown not to differ with age (Morse et al., 2005), we assumed volume remains reasonably proportional with strength in a comparison between young and older adults. Furthermore, moment arms used to estimate peak force were measured at an ankle position of 0° rather than the joint position at which peak torque occurred. However, peak torque occurred at very similar plantarflexion angles, so we do not believe this contributed to differences in estimated peak force between young and older adults.

This study reveals that the relationship between plantarflexor muscle and tendon structure may differ between young and older adults. The distribution of individual muscle volumes within the triceps surae was similar between young and older adults, as was the positive correlation between muscle volume and both body size and ankle plantarflexion torque. However, the same was not true for Achilles tendon CSA; CSA was only clearly related to body size and plantarflexion torque in young adults. Structure–function relationships that seem to exist between the Achilles tendon and the triceps surae muscles in young adults are no longer evident in all older adults. It appears that mechanisms affecting Achilles tendon morphology may be somehow altered with aging. Future work aimed at identifying factors affecting muscle–tendon relationships may provide a target for efforts to improve mobility in aging adults.

DATA AVAILABILITY STATEMENT

The datasets generated for this study are available on request to the corresponding author.

ETHICS STATEMENT

The studies involving human participants were reviewed and approved by University of Wisconsin-Madison Health Sciences Institutional Review Board. The patients/participants provided their written informed consent to participate in this study.

AUTHOR CONTRIBUTIONS

KK, AE, JM, DT, and SB designed the study. AE and IL collected the data. KK analyzed the data, prepared the original draft, and created the figures. KK, AE, JM, DT, and SB interpreted the data. KK, AE, JM, IL, DT, and SB reviewed, edited, and contributed to the text. DT and SB secured the funding. All authors contributed to the article and approved the submitted version.

FUNDING

Funding for the completion of this study was provided by the National Institutes of Health grants R01AG051748 and AG000213.

ACKNOWLEDGMENTS

The authors would like to acknowledge Emily Keuler, Robin Pomeroy, and Sruthi Gopinathan for their assistance on this project.

REFERENCES

Agur, A. M., Thow-Hing, V. G., Ball, K. A., Fiume, E., and Hunt McKee, N. (2003). Documentation and three-dimensional modelling of human soleus muscle architecture. *Clin. Anatomy* 16, 285–293. doi: 10.1002/ca.10112

Albracht, K., Arampatzis, A., and Baltzopoulos, V. (2008). Assessment of muscle volume and physiological cross-sectional area of the human triceps surae muscle *in vivo*. *J. Biomech.* 41, 2211–218. doi: 10.1016/j.jbiomech.2008.04.020

Anderson, F. C., and Pandy, M. G. (2003). Individual muscle contributions to support in normal walking. *Gait Posture* 17, 159–169. doi: 10.1016/S0966-6362(02)00073-5

Arampatzis, A., Karamanidis, K., Morey-Klapsing, G., De Monte, G., and Stafilidis, S. (2007). Mechanical properties of the triceps surae tendon and aponeurosis in relation to intensity of sport activity. *J. Biomech.* 40, 1946–1952. doi: 10.1016/j.jbiomech.2006.09.005

Baxter, J. R., and Stephen, J. P. (2014). Plantar flexor moment arm and muscle volume predict torque-generating capacity in young men. *J. Appl. Physiol.* 116, 538–544. doi: 10.1152/japplphysiol.01140.2013

Bohm, S., Mersmann, F., and Arampatzis, A. (2015). Human tendon adaptation in response to mechanical loading: a systematic review and meta-analysis of exercise intervention studies on healthy adults. *Sports Med. Open* 1:7. doi: 10.1186/s40798-015-0009-9

Bolsterlee, B., D'Souza, A., and Herbert, R. D. (2019). Reliability and robustness of muscle architecture measurements obtained using diffusion tensor imaging with anatomically constrained tractography. *J. Biomech.* 86, 71–78. doi: 10.1016/j.jbiomech.2019.01.043

Bolsterlee, B., Finni, T., D'Souza, A., Eguchi, J., Clarke, E. C., and Herbert, R. D. (2018). Three-dimensional architecture of the whole human soleus muscle *in vivo*. *Peer J.* 6:e4610. doi: 10.7717/peerj.4610

Boyer, K. A., Johnson, R. T., Banks, J. J., Jewell, C., and Hafer, J. F. (2017). Systematic review and meta-analysis of gait mechanics in young and older adults. *Exp. Gerontol.* 95, 63–70. doi: 10.1016/j.exger.2017.05.005

Dalmau-Pastor, M., Fargues-Polo, B., Casanova-Martínez, D., Vega, J., and Golanó, P. (2014). Anatomy of the triceps surae: A pictorial essay. *Foot Ankle Clin.* 19, 603–635. doi: 10.1016/j.fcl.2014.08.002

DeVita, P., and Hortobagyi, T. (2000). Age causes a redistribution of joint torques and powers during gait. *J. Appl. Physiol.* 88, 1804–1811. doi: 10.1152/jappl.2000.88.5.1804

Ebrahimi, A., Loegering, I. F., Martin, J. A., Pomeroy, R. L., Roth, J. D., and Thelen, D. G. (2020). Achilles tendon loading is lower in older adults than young adults across a broad range of walking speeds. *Exp. Gerontol.* 137:110966. doi: 10.1016/j.exger.2020.110966

Francis, C. A., Lenz, A. L., Lenhart, R. L., and Thelen, D. G. (2013). The modulation of forward propulsion, vertical support, and center of pressure by the plantarflexors during human walking. *Gait Posture*. 38, 993–997. doi: 10.1016/j.gaitpost.2013.05.009

Franz, J. R., Maletis, M., and Kram, R. (2014). Real-time feedback enhances forward propulsion during walking in old adults. *Clin. Biomech.* 29, 68–74. doi: 10.1016/j.clinbiomech.2013.10.018

Franz, J. R., and Thelen, D. G. (2015). Depth-dependent variations in achilles tendon deformations with age are associated with reduced plantarflexor performance during walking. *J. Appl. Physiol.* 119242–119249. doi: 10.1152/japplphysiol.00114.2015

Fukunaga, T., Miyatani, M., Tachi, M., Kouzaki, M., Kawakami, Y., and Kanehisa, H. (2001). Muscle volume is a major determinant of joint torque in humans. *Acta Physiol. Scandinav.* 172, 249–255. doi: 10.1046/j.1365-201x.2001.00867.x

Handsfield, G. G., Meyer, C. H., Abel, M. F., and Blemker, S. S. (2016). Heterogeneity of muscle sizes in the lower limbs of children with cerebral palsy. *Muscle Nerve* 53, 933–945. doi: 10.1002/mus.24972

Handsfield, G. G., Meyer, C. H., Hart, J. M., Abel, M. F., and Blemker, S. S. (2014). Relationships of 35 lower limb muscles to height and body mass quantified using MRI. *J. Biomech.* 47, 631–638. doi: 10.1016/j.jbiomech.2013.12.002

Hodgson, J. A., Finni, T., Lai, A. M., Reggie Edgerton, V., and Sinha, S. (2006). Influence of structure on the tissue dynamics of the human soleus muscle observed in MRI studies during isometric contractions. *J. Morphol.* 267, 584–601. doi: 10.1002/jmor.10421

Janssen, I., Heymsfield, S. B., Mian Wang, Z., and Ross, R. (2000). Skeletal muscle mass and distribution in 468 men and women aged 18-88 Yr. *J. Appl. Physiol.* 89, 81–88. doi: 10.1152/jappl.2000.89.1.81

Johnson, M. A., Polgar, J., Weightman, D., and Appleton, D. (1973). Data on the distribution of fibre types in thirty-six human muscles: an autopsy study. *J. Neurol. Sci.* 18, 111–129. doi: 10.1016/0022-510X(73)90023-3

Karamanidis, K., and Arampatzis, A. (2006). Mechanical and morphological properties of human quadriceps femoris and triceps surae muscle-tendon unit in relation to aging and running. *J. Biomech.* 39, 406–417. doi: 10.1016/j.jbiomech.2004.12.017

Karamanidis, K., Epro, G., König, M., Mersmann, F., and Arampatzis, A. (2019). Simplified triceps surae muscle volume assessment in older adults. *Front. Physiol.* 10:1299. doi: 10.3389/fphys.2019.01299

Kerrigan, D. C., Todd, M. K., Della Croce, U., Lipsitz, L. A., and Collins, J. J. (1998). Biomechanical gait alterations independent of speed in the healthy elderly: evidence for specific limiting impairments. *Archiv. Phys. Med. Rehabilit.* 79, 317–322. doi: 10.1016/S0003-9993(98)90013-2

Keuler, E. M., Loegering, I. F., Martin, J. A., Roth, J. D., and Thelen, D. G. (2019). Shear wave predictions of achilles tendon loading during human walking. *Sci. Rep.* 9:13419. doi: 10.1038/s41598-019-49063-7

LaCroix, A. S., Duenwald-Kuehl, S. E., Lakes, R. S., and Vanderby, R. (2013). Relationship between tendon stiffness and failure: a metaanalysis. *J. Appl. Physiol.* 115, 43–51. doi: 10.1152/japplphysiol.01449.2012

McGowan, C. P., Neptune, R. R., and Kram, R. (2008). Independent effects of weight and mass on plantar flexor activity during walking: implications for their contributions to body support and forward propulsion. *J. Appl. Physiol.* 105, 486–494. doi: 10.1152/japplphysiol.90448.2008

Morse, C. I., Thom, J. M., Birch, K. M., and Narici, M. V. (2005). Changes in triceps surae muscle architecture with sarcopenia. *Acta Physiol. Scandin.* 183, 291–298. doi: 10.1111/j.1365-201X.2004.01404.x

Morse, C. I., Thom, J. M., Davis, M. G., Fox, K. R., Birch, K. M., and Narici, M. V. (2004). Reduced plantarflexor specific torque in the elderly is associated with a lower activation capacity. *Euro. J. Appl. Physiol.* 92, 219–226. doi: 10.1007/s00421-004-1056-y

Neptune, R. R., Kautz, S. A., and Zajac, F. E. (2001). Contributions of the individual ankle plantar flexors to support, forward progression and swing initiation during walking. *J. Biomech.* 34, 1387–1398. doi: 10.1016/S0021-9290(01)00105-1

Nilwik, R., Snijders, T., Leenders, M., Groen, B. L., van Kranenburg, J., Verdijk, L. B., et al. (2013). The decline in skeletal muscle mass with aging is mainly attributed to a reduction in type II muscle fiber size. *Exp. Gerontol.* 48, 492–498. doi: 10.1016/j.exger.2013.02.012

Onambele, G. L., Narici, M. V., and Maganaris, C. N. (2006). Calf muscle-tendon properties and postural balance in old age. *J. Appl. Physiol.* 100, 2048–2056. doi: 10.1152/japplphysiol.01442.2005

Rana, M., Hamarneh, G., and Wakeling, J. M. (2013). 3D fascicle orientations in triceps surae. *J. Appl. Physiol.* 115, 116–1125. doi: 10.1152/japplphysiol.01090.2012

Rasske, K., and Franz, J. R. (2018). Aging effects on the achilles tendon moment arm during walking. *J. Biomech.* 77, 34–39. doi: 10.1016/j.jbiomech.2018.06.001

Rasske, K., Thelen, D. G., and Franz, J. R. (2017). Variation in the human achilles tendon moment arm during walking. *Comp. Methods Biomech. Biomed. Eng.* 20, 201–205. doi: 10.1080/10255842.2016.1213818

Reeder, S. B., McKenzie, C. A., Pineda, A. R., Yu, H., Shimakawa, A., Brau, A. C., et al. (2007). Water–fat separation with IDEAL gradient-echo Imaging. *J. Magnetic Resonance Imaging* 25, 644–652. doi: 10.1002/jmri.20831

Siston, R. A., Daub, A. C., Giori, N. J., Goodman, S. B., and Delp, S. L. (2005). Evaluation of methods that locate the center of the ankle for computer-assisted total knee arthroplasty. *Clin. Orthop. Related Res.* 439, 129–135. doi: 10.1097/01.blo.0000170873.88306.56

Stenroth, L., Peltonen, J., Cronin, N. J., Sipil,ä, S., and Finni, T. (2012). Age-related differences in achilles tendon properties and triceps surae muscle architecture *in vivo*. *J. Appl. Physiol.* 113, 1537–1544. doi: 10.1152/japplphysiol.00782.2012

Wade, F. E., Lewis, G. S., and Piazza, S. J. (2019). Estimates of achilles tendon moment arm differ when axis of ankle rotation is derived from ankle motion. *J. Biomech.* 90, 71–77. doi: 10.1016/j.jbiomech.2019.04.032

Ward, S. R., Eng, C. M., Smallwood, L. H., and Lieber, R. L. (2009). Are current measurements of lower extremity muscle architecture accurate? *Clin. Orthop. Related Res.* 467, 1074–1082. doi: 10.1007/s11999-008-0594-8

Winter, D. A., Patla, A. E., Frank, J. S., and Walt, S. E. (1990). Biomechanical walking pattern changes in the fit and healthy elderly. *Physical. Therapy* 70, 340–347. doi: 10.1093/ptj/70.6.340

Conflict of Interest: The authors declare that the research was conducted in the absence of any commercial or financial relationships that could be construed as a potential conflict of interest.

frontiers in Bioengineering and Biotechnology

ORIGINAL RESEARCH
published: 12 August 2020
doi: 10.3389/fbioe.2020.00878

Targeted Achilles Tendon Training and Rehabilitation Using Personalized and Real-Time Multiscale Models of the Neuromusculoskeletal System

Claudio Pizzolato[1,2], Vickie B. Shim[1,3], David G. Lloyd[1,2], Daniel Devaprakash[1,2], Steven J. Obst[1,4], Richard Newsham-West[1], David F. Graham[1,5], Thor F. Besier[3], Ming Hao Zheng[6] and Rod S. Barrett[1,2]*

[1] School of Allied Health Sciences, Griffith University, Gold Coast, QLD, Australia, [2] Griffith Centre of Biomedical and Rehabilitation Engineering, Menzies Health Institute Queensland, Griffith University, Gold Coast, QLD, Australia, [3] Auckland Bioengineering Institute, The University of Auckland, Auckland, New Zealand, [4] School of Health, Medical and Applied Sciences, Central Queensland University, Bundaberg, QLD, Australia, [5] Department of Health and Human Development, Montana State University, Bozeman, MT, United States, [6] Centre for Orthopaedic Translational Research, School of Surgery, The University of Western Australia, Nedlands, WA, Australia

OPEN ACCESS

Edited by:
Jason Franz,
The University of North Carolina at Chapel Hill, United States

Reviewed by:
Alkiviadis Tsamis,
University of Leicester, United Kingdom
Chiara Giulia Fontanella,
University of Padua, Italy
Joshua Daniel Roth,
University of Wisconsin–Madison, United States

***Correspondence:**
Claudio Pizzolato
c.pizzolato@griffith.edu.au

Specialty section:
This article was submitted to Biomechanics, a section of the journal Frontiers in Bioengineering and Biotechnology

Received: 09 April 2020
Accepted: 09 July 2020
Published: 12 August 2020

Citation:
Pizzolato C, Shim VB, Lloyd DG, Devaprakash D, Obst SJ, Newsham-West R, Graham DF, Besier TF, Zheng MH and Barrett RS (2020) Targeted Achilles Tendon Training and Rehabilitation Using Personalized and Real-Time Multiscale Models of the Neuromusculoskeletal System. Front. Bioeng. Biotechnol. 8:878. doi: 10.3389/fbioe.2020.00878

Musculoskeletal tissues, including tendons, are sensitive to their mechanical environment, with both excessive and insufficient loading resulting in reduced tissue strength. Tendons appear to be particularly sensitive to mechanical strain magnitude, and there appears to be an optimal range of tendon strain that results in the greatest positive tendon adaptation. At present, there are no tools that allow localized tendon strain to be measured or estimated in training or a clinical environment. In this paper, we first review the current literature regarding Achilles tendon adaptation, providing an overview of the individual technologies that so far have been used in isolation to understand *in vivo* Achilles tendon mechanics, including 3D tendon imaging, motion capture, personalized neuromusculoskeletal rigid body models, and finite element models. We then describe how these technologies can be integrated in a novel framework to provide real-time feedback of localized Achilles tendon strain during dynamic motor tasks. In a proof of concept application, Achilles tendon localized strains were calculated in real-time for a single subject during walking, single leg hopping, and eccentric heel drop. Data was processed at 250 Hz and streamed on a smartphone for visualization. Achilles tendon peak localized strains ranged from ∼3 to ∼11% for walking, ∼5 to ∼15% during single leg hop, and ∼2 to ∼9% during single eccentric leg heel drop, overall showing large strain variation within the tendon. Our integrated framework connects, across size scales, knowledge from isolated tendons and whole-body biomechanics, and offers a new approach to Achilles tendon rehabilitation and training. A key feature is personalization of model components, such as tendon geometry, material properties, muscle geometry, muscle-tendon paths, moment arms, muscle

activation, and movement patterns, all of which have the potential to affect tendon strain estimates. Model personalization is important because tendon strain can differ substantially between individuals performing the same exercise due to inter-individual differences in these model components.

Keywords: biomechanics, strain, mechanobiology, adaptation, Achilles tendon

INTRODUCTION

The human Achilles tendon is a complex three-dimensional structure that enhances power production and efficiency of the triceps surae muscle-tendon complex during movement (Lichtwark and Wilson, 2005; Handsfield et al., 2017; Pekala et al., 2017; Wiesinger et al., 2017). The Achilles tendon experiences strain when the triceps surae muscle force increases, and the energy stored in the tendon can be rapidly recovered during subsequent unloading, thereby facilitating efficient locomotion. In extreme cases, the Achilles tendon can completely rupture, but more commonly undergoes tendinopathic changes and symptoms, which include reduced Young's modulus, focal pain, and associated motor dysfunction (Paavola et al., 2002; Arya and Kulig, 2010; Obst et al., 2018; McAuliffe et al., 2019). It is currently difficult to predict individuals at risk of tendon injury, and the individual responses to an exercise-based Achilles tendon rehabilitation protocol. Changes in mechanical properties and geometry of tendon have been reported as a response to mechanical stimuli (Arampatzis et al., 2010). However, the mechanical stimuli provided to the tendon during exercise or rehabilitation cannot be estimated from external biomechanics (Pizzolato et al., 2017a), which possibly explains why the loading dose and modality of training protocols for the management of tendinopathy remain unclear (Wilson et al., 2018).

In this article, we first provide a brief overview of Achilles tendon biomechanics, mechanobiology, and adaptation. We then propose an integrated framework to better understand localized mechanical environment of the tendon during motor tasks, which is required to help prevent Achilles tendon damage/injury and enhance outcomes from Achilles tendon training and rehabilitation. Finally, we provide a proof of concept application of our framework by estimating localized strain within the Achilles tendon in real-time during walking, single leg hopping, and eccentric heel drop exercises.

ACHILLES TENDON BIOMECHANICS, MECHANOBIOLOGY, AND ADAPTATION

Musculoskeletal tissues are sensitive to their mechanical environment, with both excessive and insufficient loading resulting in reduced tissue strength (Wang et al., 2013, 2015). Whereas bone appears to be most sensitive to loading at high strain rates (Turner et al., 1995; Hsieh and Turner, 2001; Hart et al., 2017), tendon instead appears to be particularly sensitive to the magnitude of tissue strain (Wang, 2006; Heinemeier and Kjaer, 2011; Galloway et al., 2013). *In vitro* bioreactor studies in rabbit Achilles tendons revealed tendons that experienced strain magnitudes of 6% at 0.25 Hz for 8 h per day for 6 days had greater expression of type I collagen (characterized by high stiffness and superior mechanical properties) and lower expression of type III collagen (characterized by inferior mechanical properties) than tendons that experienced either 3% or 9% strains at the same duration and frequency (Wang et al., 2013). Furthermore, tendons that were load-deprived for 12 days experienced increased type III collagen expression and had reduced mechanical strength, but were able to increase type I collagen expression and material properties following a loading regime that produced 6% strain (6 days, 8 h/day, 0.25 Hz) (Wang et al., 2015). *In vivo* studies have also systematically manipulated Achilles tendon loading parameters including strain magnitude, duration, rate, and frequency. For example, Arampatzis et al. (2010) reported an increase in elastic modulus of the Achilles tendon following isometric plantar flexor training (20 repetitions, 5 sets/session, 4 days/week) performed at a strain magnitude of ∼5%, and no improvement when the same training total volume was performed at a lower strain magnitude (∼3%). The same authors also reported that an increase in strain rate from 0.17 to 0.5 Hz resulted in only a moderate improvement of Achilles tendon mechanical properties (Arampatzis et al., 2010). A systematic review of human tendon adaptation in response to mechanical loading further concluded that, on the basis of 27 included studies, while tendons are responsive to a range of loading conditions, loading magnitude (and hence strain), in particular, plays a key role in tendon adaptation (Bohm et al., 2015). While there remains much to learn about the specific loading conditions (i.e., strain magnitude, strain duration, strain frequency, and strain rate) that maximize tendon adaptation and the mechanobiological pathway involved (Smith et al., 2013; Young et al., 2016), tendon strain magnitude appears to play a fundamental role.

Based on the presumption that strain magnitude is a key control variable for tendon adaptation, it follows that the efficacy of exercise-based training and rehabilitation programs might be improved by ensuring that the strain magnitude experienced by the Achilles tendon during exercise is in the anabolic range of approximately 5–6%, where tendon remodeling exceeds strain-induced tendon damage (Pizzolato et al., 2019). However, there are no tools available that allow localized tendon strain to be measured or estimated in either the training or clinical environment. Arguably, the best non-invasive method of direct measurement available at present involves attaching an ultrasound probe to the leg to track the motion of the gastrocnemius muscle-tendon junction and estimating the change in tendon length relative to a motion

capture marker placed on the calcaneus (Stenroth et al., 2012; Zelik and Franz, 2017). While this approach has provided new and important insight into the strains experienced during tasks such as walking, running and jumping, the approach remains technically challenging and impractical outside of the laboratory environment. Alternative approaches to strain mapping of the Achilles tendon during functional movements are therefore required.

In this article, we propose and demonstrate a framework that combines 3D tendon imaging, motion capture, and personalized neuromusculoskeletal (NMS) rigid body and finite element (FE) models to assess the localized stress and/or strain in the free Achilles tendon (region spanning from the calcaneal insertion to soleus muscle tendon junction) for the purpose of providing instantaneous feedback during dynamic motor tasks. A key feature of the framework is personalization of model features with the potential to affect calculation of strain, which include tendon geometry and material properties, muscle geometry and muscle-tendon paths and/or moment arms, and muscle activation and movement patterns. This is important because tendon stress and/or strain could differ substantially between individuals performing the same exercise prescription such as eccentric heel drops used in treatment of tendinopathy (Alfredson et al., 1998), even if they are matched for age, size, gender, training history, and clinical status. The proposed framework will help to clarify the optimum loading dose for training and rehabilitation of the Achilles tendon by facilitating exercise prescription based on internal tissue loading.

FRAMEWORK FOR REAL-TIME ESTIMATION OF LOCALIZED ACHILLES TENDON STRESS AND STRAIN

The proposed framework for estimating Achilles tendon stress and strain in real-time involves integration of motion capture, electromyography, medical imaging, and NMS and FE models (**Figure 1**). Body kinematics and muscle activation patterns are used as inputs into a rigid body electromyogram (EMG) – informed NMS model that computes the triceps sure muscle forces applied to the Achilles tendon. These muscle forces are subsequently applied to a personalized FE model of the Achilles tendon based on geometry and material properties determined from a combination of 3D medical imaging, isometric measurements, and model fitting. Real-time estimates of Achilles tendon stress and/or strain are enabled by the use of a surrogate FE model that is first generated offline, and then solved for a feasible set of muscle forces. The corresponding stress/strain calculated via the personalized Achilles tendon FE model are then used to create a surrogate model via polynomial fitting, regression methods, or other machine learning approaches. Each of these steps is described in detail in the following sections.

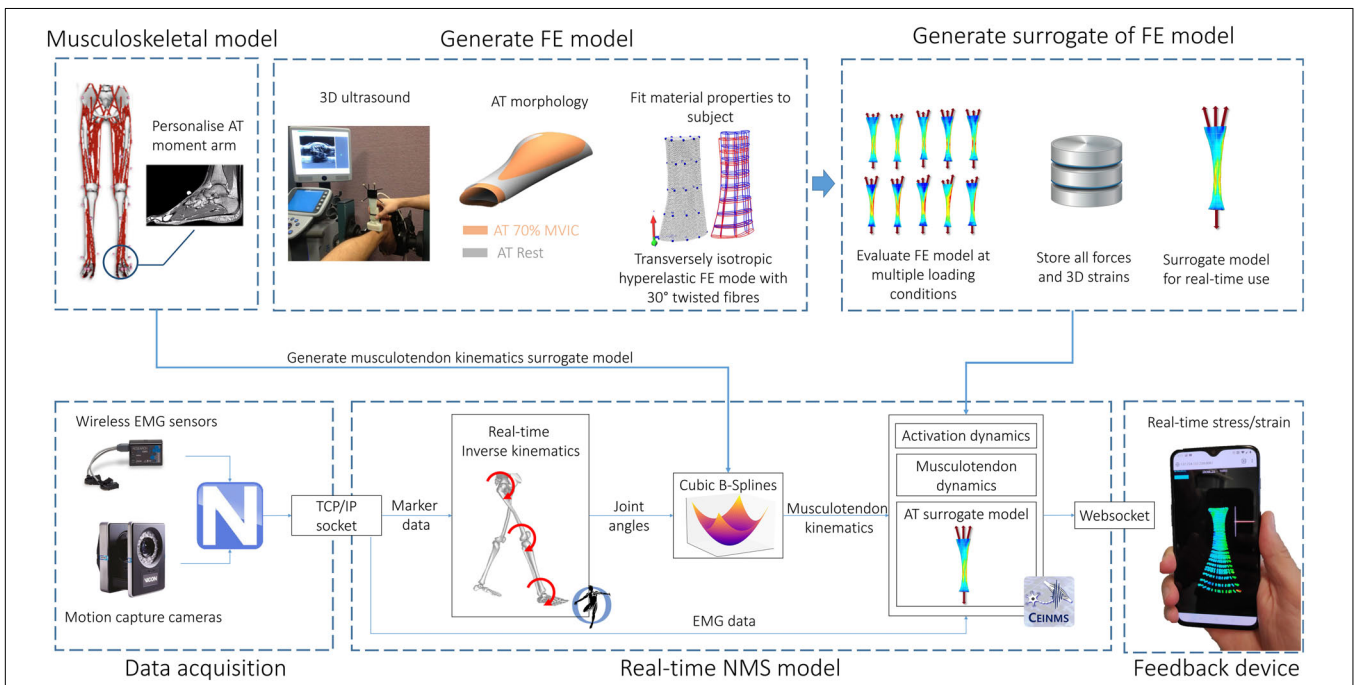

FIGURE 1 | Model creation and data processing pipeline. A generic OpenSim musculoskeletal model (gait2392) was linearly scaled to the individual using motion capture data. The moment arm of medial gastrocnemius, lateral gastrocnemius, and soleus muscle-tendon units were adjusted to match the Achilles tendon moment arm measured via magnetic resonance imaging. FE model of the Achilles tendon was created from 3D ultrasound following established methods. A surrogate of the FE model was used to predict localized strains at 2048 Gauss points throughout the Achilles tendon. Joint angles were calculated via real-time inverse kinematics. Muscle-tendon lengths, calculated via multidimensional cubic B-splines, and surface EMG were used to drive a Calibrated EMG-informed NMS model (CEINMS) in open-loop. Muscle forces predicted by CEINMS were used as input for the Achilles tendon surrogate model, enabling estimation of localized strains. Real-time visual feedback of strain was implemented in Javascript three.js (r100) and visualized on a mobile phone via internet browser (Mozilla Firefox).

Personalized Achilles Tendon 3D Geometry and Deformation From Freehand 3D Ultrasound

Conventional 2D brightness-mode (b-mode) ultrasound has been widely used to quantify the length, thickness, and cross-sectional area of the Achilles tendon. 2D b-mode ultrasound may also be used to create 3D reconstruction of the Achilles tendon when used in conjunction with motion capture (Devaprakash et al., 2019). This approach, termed freehand 3D ultrasound, involves simultaneously recording the position and orientation of the ultrasound probe in 3D space as it is swept along the free Achilles tendon. The generated stack of 2D images is then positioned and orientated in a global coordinate system. Image slices are then segmented to generate a volumetric reconstruction of the Achilles tendon. Estimates of free Achilles volume, length, and cross-sectional area from freehand 3D ultrasound have been shown to be both highly repeatable (Obst et al., 2014a) and in close agreement with corresponding estimates obtained from high resolution magnetic resonance imaging (MRI) scans (Devaprakash et al., 2019). The main limitation of freehand 3D ultrasound is that the free Achilles tendon must remain stationary during the freehand scan and so the method is confined to resting or isometric conditions. However, unlike MRI, freehand 3D ultrasound allows macroscopic Achilles tendon geometry to be readily measured in the laboratory environment at rest and during voluntary isometric loading.

Experimental studies to date using freehand 3D ultrasound have demonstrated that longitudinal strain of the free Achilles tendon is more than double the longitudinal strain experienced by the proximal aponeurosis (Obst et al., 2016), and that the free Achilles tendon experiences twist during loading (Obst et al., 2014b). Studies of 3D tendon deformation during and following tendon conditioning (Nuri et al., 2016, 2018a) and following eccentric heel drop exercise (Obst et al., 2015, 2016) have further confirmed that changes in strain behavior under a constant isometric load are primarily confined to the free Achilles tendon, rather than the proximal tendon or the aponeurosis. In contrast to the healthy free Achilles tendon, which becomes narrower along the medial-lateral axis and bulges along the anterior-posterior axis during longitudinal deformation, the tendinopathic Achilles tendon experiences deformation along both transverse plane axes, as well as a corresponding volume reduction during sustained longitudinal deformation (Nuri et al., 2017, 2018b). Geometry and 3D deformation of the Achilles tendon under loading condition can be used create personalized FE models and estimate localized stress/strain.

Personalized Finite Element Models of the Achilles Tendon

Finite element analysis allows the localized tissue stress or strain to be computed as a function of the personalized tissue geometry and material properties in response to externally applied loads (i.e., boundary conditions). Prior to FE analysis, a generic tendon mesh is morphed to match the resting 3D geometry of tendon measured using freehand 3D ultrasound via free form deformation (Fernandez et al., 2004). The constitutive mechanical behavior of the free Achilles tendon can be modeled using a transversely isotropic hyperelastic formulation, which has been successfully applied to both cadaveric (Shim et al., 2014) and *in vivo* analyses (Hansen et al., 2017; Shim et al., 2018, 2019). Material properties of the Achilles tendon can be estimated using an inverse FE approach, wherein an optimization procedure identifies the subject-specific material properties parameters that produce the best match between the geometry of the loaded subject-specific FE mesh and the geometry of the free Achilles tendon measured under submaximal loading conditions using freehand 3D ultrasound (Hansen et al., 2017). Achilles tendon forces required as boundary conditions during the inverse FE approach (**Figure 2**) can be readily calculated from measured angle joint moment and Achilles tendon moment arm. After this procedure, the personalized FE model of the Achilles tendon can estimate all principal component stress/strains, which can

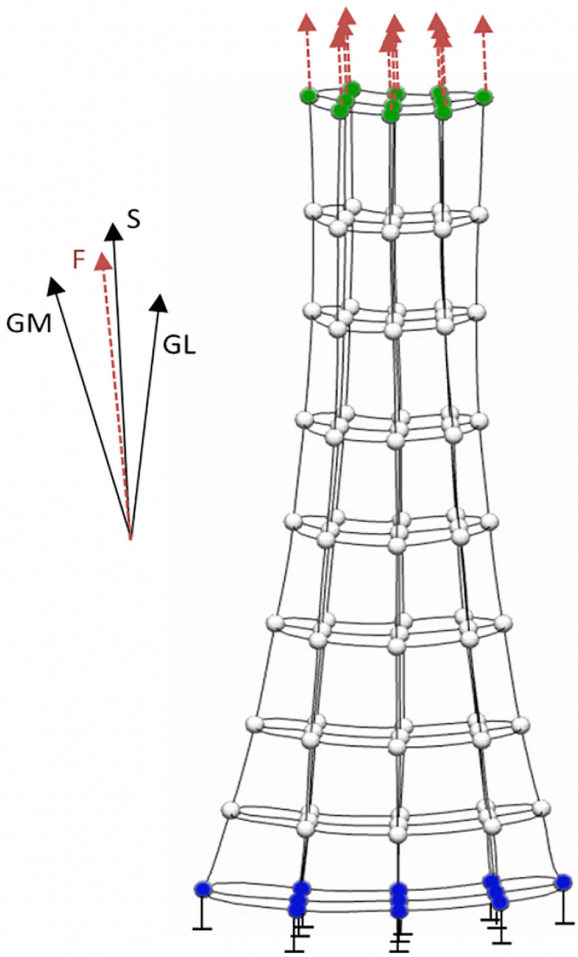

FIGURE 2 | Boundary conditions applied to the finite element model of the Achilles tendon. The model's distal nodes (blue) are constrained and not allowed to move. Boundary force from gastrocnemius medialis (GM), gastrocnemius lateralis (GL) and soleus (S) is equally distributed on the proximal nodes (green) of the model.

be re-aligned with anatomical directions (i.e., proximal-distal, medial-lateral, and anterior-posterior) (Shim et al., 2018), for a range of triceps sure forces.

In the healthy free Achilles tendon, stress is more sensitive to subject-specific differences in tendon geometry than subject-specific differences in tendon material properties (Hansen et al., 2017). The location of peak tendon stress and the predicted rupture location vary considerably between cadaveric tendon samples under equivalent loading conditions (Shim et al., 2014). As both tendon geometry and material properties (Arya and Kulig, 2010; Obst et al., 2018) are altered in Achilles tendinopathy, it is also important to determine how these alterations affect Achilles tendon stress distributions in tendinopathic Achilles tendons. Shim et al. (2019) reported that tendinopathic tendons have a 30% larger cross-sectional area and 50% lower modulus compared to healthy tendons, but that the lower modulus resulted in only an 8% increase in average tendon stress during a 70% submaximal isometric contraction, compared to a 30% decrease in average tendon stress due to the larger cross-sectional area. It was therefore suggested that the larger cross-sectional area reported in tendinopathic Achilles tendons (Arya and Kulig, 2010) could be protective against higher tendon stresses, but could also result in regions of underloading/stress shielding with associated catabolic effects on the tendon.

The aforementioned FE models of the Achilles tendon were developed from the macroscopic 3D tendon geometry assessed using freehand 3D ultrasound, and therefore do not incorporate more detailed substructural Achilles tendon geometry such as the twisted substructure of individual sub-tendons (Edama et al., 2015; Pekala et al., 2017) and the proximal aponeurosis. By including fascicle twist in a FE model of the human Achilles tendon, Shim et al. (2018) demonstrated that twist increased the predicted rupture load by 40%, and that ∼30° minimized tendon stress, with higher and lower twist angles resulting in higher tendon stress. Future Achilles tendon models should include more detailed substructural estimates of spatial distribution of material properties. While there is some initial evidence that a tendinopathic inclusion alters the stress distribution in the vicinity of the lesion (Maganaris et al., 2017), further research is required to more fully characterize the mechanical environment in and around the lesion in tendinopathy.

A current limitation of FE analysis in the context of the proposed use as a biofeedback tool, is that FE models are computationally intensive and therefore not amenable to real-time application. This is circumvented by first solving the FE model offline for a large number of feasible triceps sure muscle force combinations, then use machine learning approaches (sometimes called surrogate methods), such as partial least squares regression or polynomial fitting, to estimate the tendon stress/strain distribution in real-time with minimal computational requirements.

Personalized Real-Time Neuromusculoskeletal Models

Neuromusculoskeletal models are causal physics-based representations of an individual's bones, muscles, tendons, and joints. The skeletal structure is represented as a rigid multi-body system. Muscles are modeled as Hill-type actuators, and joints are subjected to mechanical constraints that represent their real counterpart (Delp et al., 2007). Motion capture (e.g., stereophotogrammetry marker-based systems or inertial measurement units) and external force data (e.g., ground reaction forces) are used to determine joint angles and moments using inverse kinematics and inverse dynamics approaches, respectively. Mechanical methods based on metabolic expenditure optimization criterion, such as static or dynamic optimization, can be used to solve the muscle redundancy problem; however, these approaches do not account for the individual's motor control and have repeatedly shown to be unable to appropriately predict muscle co-contractions that are evident in measured EMG data (Hoang et al., 2018; Davico et al., 2019b; Veerkamp et al., 2019). Alternatively, EMG data can be directly used to inform forward dynamic simulations of muscles contraction and calculate muscle forces (Lloyd and Besier, 2003; Pizzolato et al., 2015, 2017c). When personalized to the individual (e.g., via system identification methods or direct measurement) EMG-informed NMS models can predict physiologically plausible muscle forces across different motor tasks and different populations varying by age and pathology (Gerus et al., 2013; Hoang et al., 2018; Davico et al., 2019b; Veerkamp et al., 2019).

Personalization of NMS models may involve musculoskeletal geometry (e.g., bone shape and dimensions, muscle-tendon insertion points and pathways, joint mechanics) and neuromuscular parameters (e.g., maximum isometric forces of muscles, tendon slack length, optimal fiber length, activation dynamics) (Saxby et al., 2020). A rudimentary form of musculoskeletal geometry personalization is linear scaling of bone geometry based on discrete anthropometric measurements. While this approach is easy to implement, the resulting geometry may poorly represent the individual, affecting muscle-tendon attachment points and pathways, and consequent estimation of muscle-tendon forces (Gerus et al., 2013; Bahl et al., 2019). More advanced and promising methods use medical imaging databases to build population-based statistical shape models (Zhang et al., 2014; Zhang and Besier, 2017; Davico et al., 2019a). Sparse data, such as anatomical landmarks, of individuals not previously included in the database are then used to reconstruct the geometry of bones. In the context of the Achilles tendon, statistical shape models of primary foot bone segments, as well as tibia-fibula and femur, can be reconstructed with minimal error (Davico et al., 2019a; Grant et al., 2020), but future work should investigate whether these accurate predictions of bone geometry are also reflected in accurate predictions of Achilles tendon moment arm.

Neuromuscular parameters affect the amplitude and timing of predicted muscle-tendon forces and personalization has been shown essential in predicting physiologically plausible muscle and joint contact forces (Hoang et al., 2018). While some parameters, such as maximum isometric force of individual muscle, can be inferred from medical imaging data (O'Brien et al., 2010; Handsfield et al., 2014), optimization algorithms are required to calibrate parameters that cannot be observed

(Pizzolato et al., 2015; Hoang et al., 2018). Calibration involves minimizing the error between the joint moments estimated from EMG-informed NMS models and from inverse dynamics, while satisfying a variety of physiological constraints (e.g., muscle fascicles working within a plausible range of their force-length characteristic) (Pizzolato et al., 2015). Including a variety of different tasks and trials in the calibration also ensures that the NMS model is appropriately calibrated within a large solution space (Lloyd and Besier, 2003; Saxby et al., 2016). After calibration, the NMS model can predict novel trials and tasks for the same subject.

Recent advances in NMS modeling have also made it possible to execute EMG-informed NMS models in real-time (Manal et al., 2012; Pizzolato et al., 2017c; Durandau et al., 2018), enabling instantaneous estimates of the state of internal musculoskeletal tissues. This has extended the potential application of physiologically sound models to training and rehabilitation (Pizzolato et al., 2017a); a feat previously considered unattainable. This technology has been used to estimate internal knee loading during gait, showing that a person can change their gait patterns to volitionally modulate the amplitude of their knee contact force (Pizzolato et al., 2017c), and to estimate the amount of force experienced by the Achilles tendon during post-rupture rehabilitation (Manal et al., 2012). These prior examples of real-time estimation of internal biomechanics have been limited to forces alone, which only partially represent the mechanical stimuli responsible for tissue adaptation (Pizzolato et al., 2017a). Recent advances in computational rigid body NMS and FE modeling has resulted in technologies that are sufficiently mature to be combined into personalized real-time multi-scale models of the person and their tissues. We present a proof of concept of this integrated technology applied to estimation of free Achilles tendon localized strain during dynamic motor tasks. We show that the developed multiscale model can calculate the strain field within the free Achilles tendon in real-time and with minimal computational effort using as input EMG and motion capture data alone. Future refinement of this technology should involve rapid creation of personalized rigid-body and FE models to create a clinic-ready system for advanced training and rehabilitation.

PROOF OF CONCEPT APPLICATION

One healthy individual (age: 21, mass: 70.5 kg, height: 1.75 m) gave written informed consent to participate in this study (Griffith University ethics approval number 2017/020).

Experimental Setup and Data Acquisition

Prior to all testing, the participant followed a standardized protocol for Achilles tendon preconditioning (Hawkins et al., 2009). Anatomical MRI scans of the ankle joint, including foot and distal tibia-fibula, were acquired on a Philips Ingenia 3.0 Tesla scanner (Amsterdam, Netherlands) using an 8-channel ankle coil (PDW 3D TSE, TR/TE 1000/41 ms) with the participant lying in a supine position with the hip in neutral position and knee fully extended. The foot was supported inside the coil by a pad to ensure that the ankle was in a neutral position (0° dorsiflexion).

Achilles tendon geometry measurements were performed as follows. The participant was positioned prone on a bed with their foot firmly secured to the dynamometer foot plate, which was locked with the ankle in a neutral position (0°). The knee joint was fully extended, and the hip joint was in neutral position. Freehand 3D ultrasound data were acquired using a 2D ultrasound (Aplio 500, Canon Medical Systems, Otawara, Japan) and motion capture system (Vicon MX T-series, Vicon Motion Systems Ltd., Oxford, United Kingdom), as described in Devaprakash et al. (2019). A dynamometer (HUMAC NORM, Stoughton, MA, United States) was used to concurrently measure ankle plantarflexion torque. All equipment was synchronized via a hardware trigger. After preconditioning, freehand 3D ultrasound data of the Achilles tendon was collected at rest and at 25, 50, and 70% of maximum voluntary isometric contraction (MVIC). Measurements were repeated three times per condition.

A 20-camera motion capture system (Vicon, Oxford, United Kingdom) and 8 force plates (Kistler Instrument Corporation, Amherst, NY, United States) were used to collect marker trajectories (250 Hz) and ground reaction forces (1000 Hz) during walking, running, single leg hopping, and eccentric heel drops. Surface EMG (TELEmyo DTS, Noraxon U.S.A. Inc., Scottsdale, AZ, United States) were also acquired (1500 Hz) from 16 sites on a single leg: medial gastrocnemius, lateral gastrocnemius, soleus, flexor digitorum hallucis longus, peroneus longus, peroneus brevis, tibialis anterior, extensor hallucis longus, vastus medialis, vastus lateralis, rectus femoris, semitendinosus, biceps femoris, sartorius, tensor fascia latae, and gracilis. All the systems were synchronized via hardware trigger.

Neuromusculoskeletal and Finite Element Models

A generic OpenSim (Delp et al., 2007) model (gait2392) was linearly scaled to the individual. The moment arms of the medial and lateral gastrocnemius and soleus muscles were automatically adjusted in the scaled OpenSim model in order to reflect the experimental measure from MRI data (Alexander et al., 2017). This was achieved by optimizing the distal attachment point of the three musculotendon units. Multidimensional cubic B-splines were used to create a surrogate model of the model's musculoskeletal geometry for real-time estimation of muscle-tendon lengths and moment arms (Sartori et al., 2012).

Experimental free Achilles tendon elongations were calculated from isometric freehand 3D ultrasound measurements, as the distance between the calcaneal notch and soleus muscle-tendon junction. Isometric ankle torque data and Achilles tendon moment arm experimentally measured from MRI were then combined with tendon elongation measurements to calculate normalized force-elongation points. The following piecewise function (Schutte, 1993)

$$\begin{cases} f(\varepsilon) = 0, & \varepsilon < 0 \\ f(\varepsilon) = a\varepsilon^2, & \varepsilon < \varepsilon_0 \\ f(\varepsilon) = m\varepsilon + q, & \varepsilon \geq \varepsilon_0 \end{cases}$$

was fitted to the experimental values by optimizing a, m, q, and ε_0 while ensuring C^1 continuity, where f represents force and ε strain. This resulted in a continuous dimensionless curve that was applied to tendon of the medial gastrocnemius, lateral gastrocnemius, and soleus muscle-tendon units in the NMS model. Tendon force elongation curves for the other muscle-tendon units in the model were based on literature data (Millard et al., 2013). Maximum isometric forces for each of the triceps surae muscles were estimated from MRI measured muscle volumes and muscle optimal fiber lengths (from gait2392 OpenSim model) using a specific tension of 55 N/cm^3 (O'Brien et al., 2010). The remaining NMS model parameters were then calibrated via established methods (Pizzolato et al., 2015) using one trial from each experimental dynamic task in the calibration procedure. Optimized parameters included optimal fiber length, tendon slack length, and maximum isometric forces of the muscles not measured, as well as muscle activation/deactivation time constants (Pizzolato et al., 2015).

A FE model of the free Achilles tendon was modeled using CMISS[1] as an incompressible, transversely isotropic hyperelastic material with 30° twisted fibers, and geometry personalized via freehand 3D ultrasound, as well as material properties parameters calculated via inverse FE approaches (Shim et al., 2014, 2019; Hansen et al., 2017). To enable calculation of longitudinal principal component strains (i.e., localized), the reference FE material coordinate system was rotated to align with the fiber orientation of the tendon, which run in the proximal-distal direction (Shim et al., 2018). The material behavior of the model was defined via six coefficients (Hansen et al., 2017), C1 to C6. Coefficients C2 was set from literature (C2 = 0 to describe a Neo-Hookean material). Coefficient C5, corresponding to Young's modulus, was calculated from experimental 3D ultrasound data as the ratio between tendon stiffness and average free Achilles tendon cross-sectional area (C5 = 0.58 GPa). Coefficients C1, C3 (scaling of the exponential stress), and C4 (rate of collagen fiber loading) were optimized by minimizing the root mean square error (RMSE) between the longitudinal tendon elongation in the FE model under load and the corresponding measured experimental tendon elongation at 70% MVIC. Finally, coefficient C6 was calculated as function of C2, C4, and C5 (Hansen et al., 2017). After creating the personalized FE model of the free Achilles tendon, localized strains were calculated for 2048 Gauss points (i.e., integration points) by solving the FE problem for a range of boundary conditions. Specifically, the model was constrained at the distal end and forces that ranged from 0 to 200% MVIC at 10% intervals were evenly applied to the surface of the proximal end of the tendon, in the direction corresponding to the longitudinal (i.e., proximal-distal) axis of inertia of the tendon. This resulted in a total of 21 localized strain data points per Gauss point that were a function of the force applied as boundary condition, which were then used as training data for the surrogate FE model. Three different surrogate methods were assessed in their ability to reproduce FE data (RMSE; coefficient of correlation, R) using a leave-one-out validation. The three tested models were: partial least square regression, cubic spline interpolation, and basis spline interpolation. For both the spline-based models, one spline per Gauss node (n = 2048) was used to interpolate the localized strain as a function of the force applied to the free Achilles tendon.

[1]https://www.cmiss.org

Real-Time Estimation of Achilles Tendon Strain

Real-time conditions were simulated using Vicon Virtual System (v1.4.1), which allows emulating the connection with live streaming cameras and analog devices. Vicon Nexus 2.8 was used to acquire the stream and perform automatic and real-time marker labeling. Labeled, but unfiltered, marker and EMG data were streamed to a custom, multithreaded software pipeline implemented in C++. The software pipeline (**Figure 1**) used real-time components previously described and validated (Pizzolato et al., 2017b,c) that allowed for computationally efficient estimation of real-time muscle-tendon forces, and it was extended to include surrogate FE model of the free Achilles tendon. In brief, marker data was used to estimate joint angles using a real-time OpenSim inverse kinematics algorithm (Pizzolato et al., 2017b), which were then filtered and used to estimate muscle-tendon kinematics (i.e., lengths and moment arms) of the lower limb. Musculotendon kinematics and surface EMG were then used to drive a three-degrees of freedom (knee flexion extension, ankle plantar-dorsiflexion and pronation-supination), calibrated EMG-informed NMS model in open-loop using CEINMS software (Pizzolato et al., 2015). Predicted triceps surae muscle forces were summed and used in input for the surrogate model of the free Achilles tendon, enabling estimation of localized strains. A real-time visual feedback of strain was implemented in Javascript three.js (r100) and visualized in a web browser (Mozilla Firefox) on a mobile phone (OnePlus 6T, OnePlus) via websocket (**Figure 1**). Computations were all performed on a laptop workstation (Windows 7, i7-6820HQ @ 2.7 Hz, 32 GB RAM).

Free Achilles tendon localized strains during walking, single leg hopping, and eccentric heel drop, as well as real-time performance were reported. The real-time pipeline was also assessed to correctly function in real laboratory conditions, but due to the unavailability of the same subject used to generate the personalized models, only simulated real-time data were reported.

Results

The surrogate model based on cubic splines outperformed both partial least square regression and basis spline interpolation in the leave-one-out validation (**Figure 3**) and was consequently used in the real-time pipeline to calculate Achilles tendon strain.

In walking, the greatest amount of free Achilles tendon strain was present in the push-off phase, which also corresponded to the production of maximal plantar-flexion moment. At push-off, the localized strains within the tendon varied from ∼3 to ∼11%, while global strain (proximal to distal elongation normalized by resting length) was ∼6.5% (**Figure 4**). During single leg hopping, maximum strain also corresponded to the production of maximal plantar-flexion moment, but greater plantarflexion torque in the

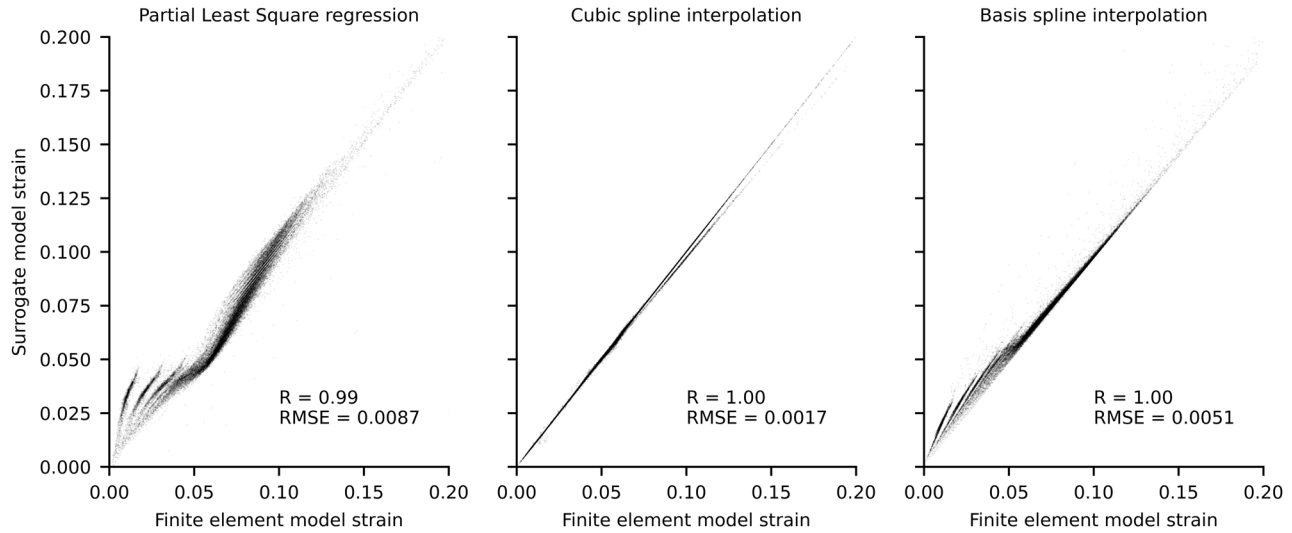

FIGURE 3 | Scatterplots of localized strains of each Gauss point for finite element model and surrogate models. Data was produced using a leave one out procedure, wherein each surrogate model was trained n times on n-1 conditions and used to predict the condition not included in the training. The force boundary condition used to execute the finite element model ranged between 0 and 2 times the experimental maximum voluntary isometric contraction (MVIC), at 0.1 MVIC increments, which resulted in $n = 21$.

landing phase compared to the take-off phase did not correspond to greater free Achilles tendon strains. During these phases, localized strains within the tendon varied from ∼5 to ∼15%, while global strain was ∼10% (**Figure 5**). The greatest magnitude of localized strain was present in the mid-portion and on the proximal medial side of the free Achilles tendon. During eccentric heel drops, localized strains within the tendon varied on average from ∼2 to ∼9%, increasing of ∼1% in full dorsiflexion, while the global free Achilles tendon strain peaked at ∼6% (**Figure 6**).

A total of 10,000 data frames computed in real-time were analyzed to assess performance of the integrated system. Each data frame was computed on average in 3.02 ms, which is 1.3 times faster than the time sampling of experimental marker data from the motion capture system (i.e., 250 Hz or 4 ms). Of all analyzed data frames, 95% were computed in less than 3.86 ms, which includes all the calculations from raw marker data to tendon strain computation (**Figure 7**).

DISCUSSION AND FUTURE DIRECTIONS

This paper demonstrates proof of concept that an integrated technology-based approach may be used to provide real-time feedback in a training and/or rehabilitation setting to ensure that a targeted dose of mechanical stimuli is delivered to the musculoskeletal tissue. We have demonstrated that it is possible to estimate localized tissue strain in the free Achilles tendon during walking, hopping and eccentric heel drops, in real-time using an EMG-informed NMS model combined with a surrogate FE model. While some further development and validation of our framework is required, we foresee that in the near future it will be possible to provide instantaneous feedback of Achilles tendon tissue strain in a clinical or training environment, thereby facilitating personalized training and/or rehabilitation of the Achilles tendon that targets the loading range that elicits positive tendon adaptation (hypertrophy).

Using standard laboratory-based equipment, we have demonstrated it is possible to estimate Achilles tendon strain in real-time with minimal delay (less than 3.86 ms for 95% of the data), which is essential to provide appropriate and timely feedback to the user (Kannape and Blanke, 2013). Real-time biofeedback of triceps surae muscle-tendon forces (Manal et al., 2012) and tibiofemoral joint contact force (Pizzolato et al., 2017c) from EMG-informed musculoskeletal models have been previously being used to modify an individual's gait patterns. The proposed framework takes these studies one step further by reporting localized tissue level Achilles tendon strain. As a proof of concept, we have developed a simple visual feedback interfaces that runs on a smartphone to instantly show localized Achilles tendon strain to the user (**Figure 1**), but we are yet to perform human-in-the-loop experiments where the person changes their training or rehabilitation to optimize tissue strains. In a simple implementation, this form of feedback could be provided to indicate when the predicted peak or average tendon strain is either within or outside the desired target range.

It is important to highlight some limitations of the proposed real-time framework. While inverse kinematics was performed in real-time using OpenSim using a previously validated method (Pizzolato et al., 2017b), marker-based motion capture may suffer from marker occlusions. As such, particular care must be taken by the experimenter to appropriately place infrared cameras and calibrate the capture volume to enable for auto labeling of markers to function correctly. Our 20-cameras setup prevented marker occlusions during the evaluated tasks, but motion capture solutions based on inertial measurement units may simplify the data acquisition setup in the future. We

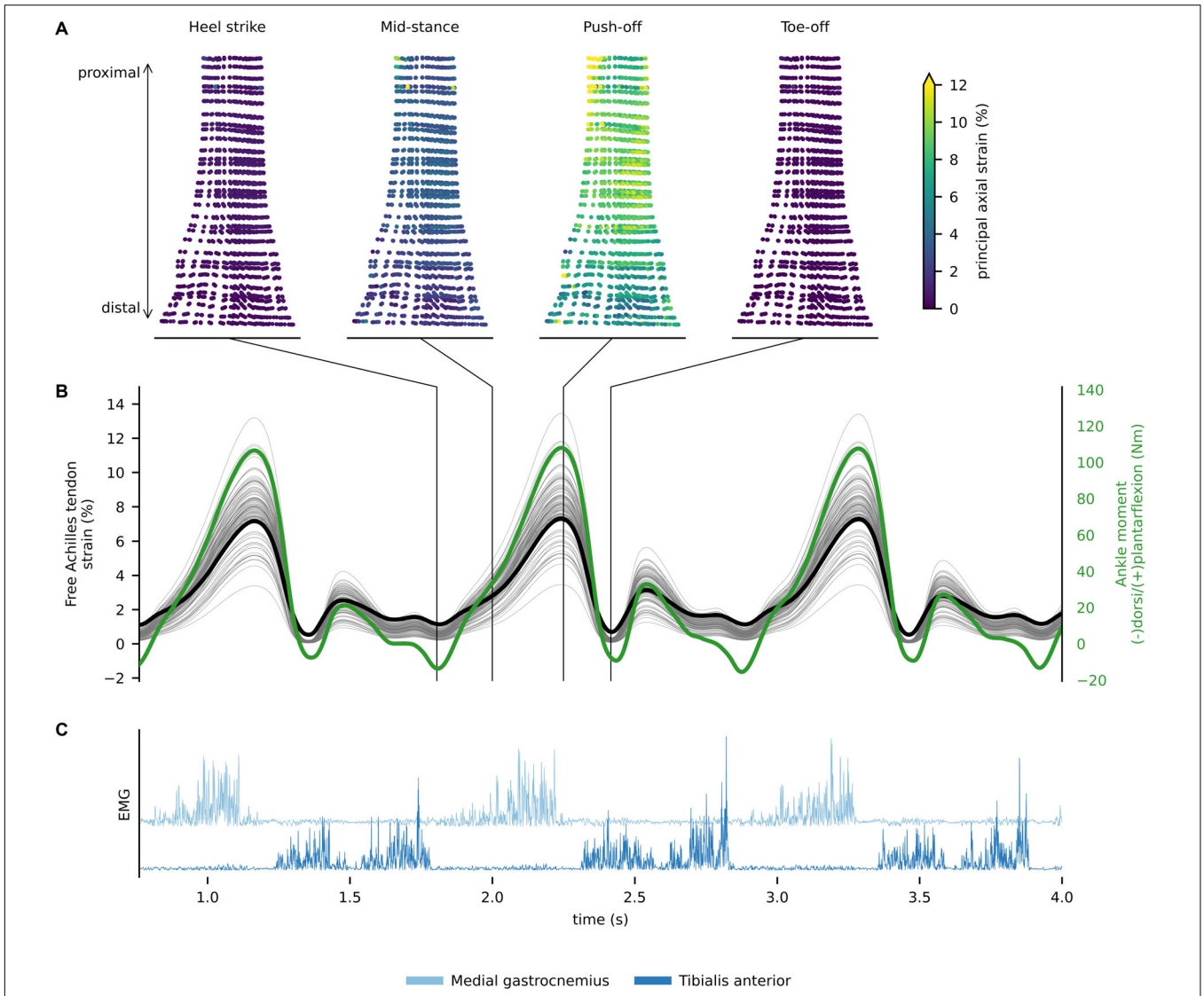

FIGURE 4 | (A) *In vivo* free Achilles tendon localized strains for discrete events of the gait cycle. **(B)** Free Achilles tendon global (thick black line), localized strain (thin gray lines) for each Gauss point, and ankle moment (green line) during walking. **(C)** Rectified electromyograms of tibialis anterior and medial gastrocnemius showing phasic muscle activity during walking.

used multidimensional cubic B-splines to enable calculation of muscle-tendon lengths and moment arms (Sartori et al., 2012), which may appear a simplification. However, multidimensional cubic B-splines have been previously shown to be superior to polynomial fitting and to introduce negligible estimates errors for muscle-tendon kinematics (Sartori et al., 2012). Another limitation of real-time executions is the inability to use non-causal filters, such as zero-lag Butterworth filters commonly used in analysis of biomechanical data. Following previously established methods (Pizzolato et al., 2017c), we filtered EMG and joint angle data using the same causal Butterworth filter, thus minimizing errors caused by phase delays which has been shown to produce excellent agreement between real-time and offline simulations (Pizzolato et al., 2017c). Model calibration is fundamental to obtain physiologically plausible muscle-tendon forces (Hoang et al., 2018) but at the current stage this process is still computationally intensive and must be performed offline. Online calibration procedures, such as Bueno and Montano (2017), should be implemented in the future to minimize idle times. Finally, as the FE method is computationally intensive, a surrogate FE model was used to enable real-time estimation of Achilles tendon strain. Of the three evaluated methods, cubic interpolation showed the best performance, with associated strain RMSE of 0.0017. Different surrogate methods should be explored to adapt the proposed framework to more complex FE models (e.g., with subtendons). Nonetheless, prior to translation it will be necessary to conduct a comprehensive methodological evaluation of the proposed framework, including studies to determine the validity and reliability of tendon strains estimates, and sensitivity of such estimates to model parameters.

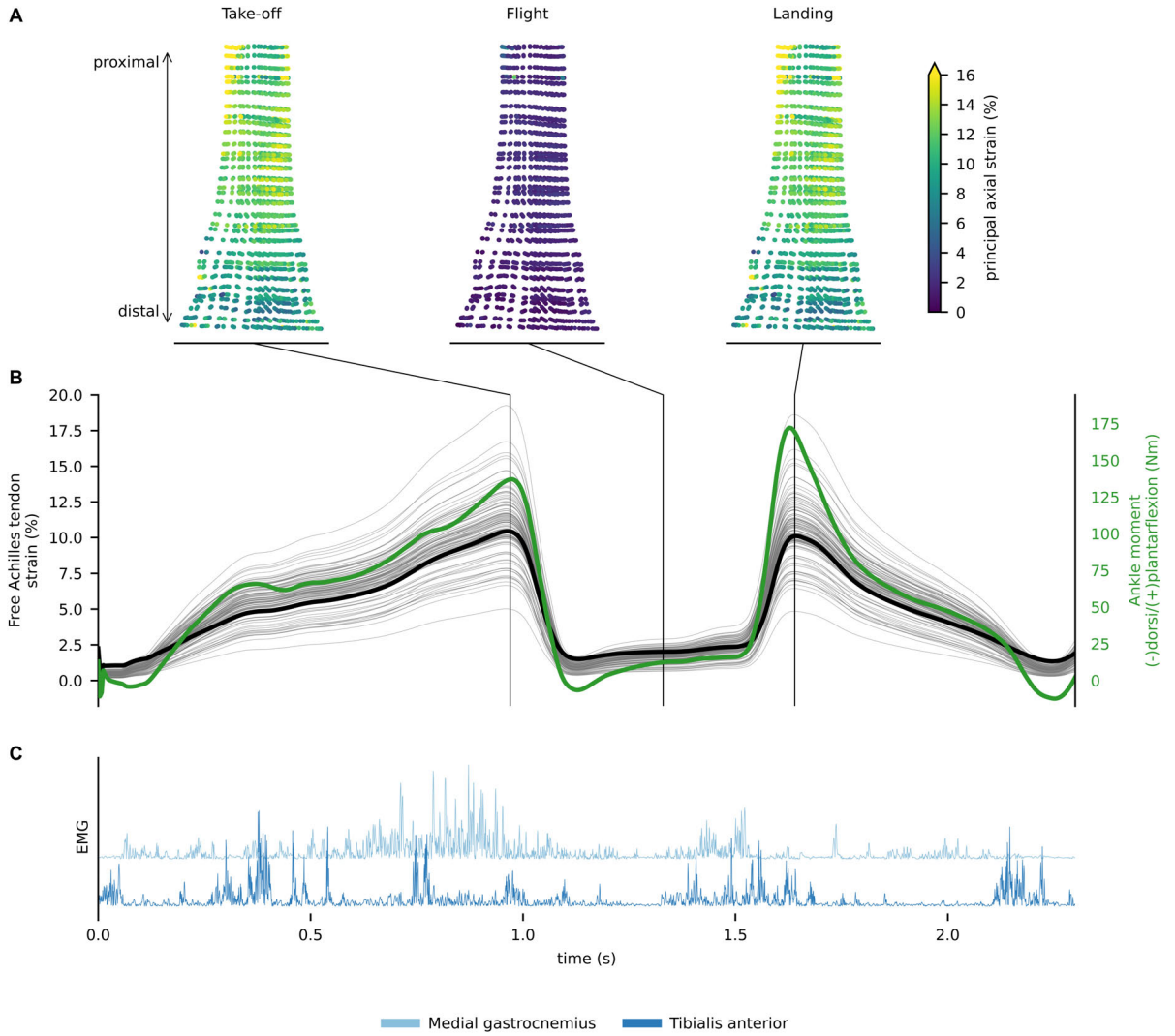

FIGURE 5 | (A) *In vivo* free Achilles tendon localized strains for discrete events of the single leg hoping. **(B)** Free Achilles tendon global (thick black line), localized strain (thin gray lines) for each Gauss point, and ankle moment (green line) during single leg hopping. **(C)** Rectified electromyograms of tibialis anterior and medial gastrocnemius.

The peak global Achilles tendon strains estimated via our multiscale model (6.5% for walking and 10% for single leg hop) were higher than the maximum strain measured with 2D ultrasound from previous research (4.8% for walking and 8.2% for single leg hop) (Lichtwark and Wilson, 2005, 2006). However, previous research measured global strains of the free Achilles tendon and aponeurosis combined (i.e., calcaneal notch to medial gastrocnemius muscle-tendon junction) while we provided a strain estimate of the free Achilles tendon alone (i.e., calcaneal notch to soleus muscle-tendon junction). Importantly, longitudinal free Achilles tendon strain has been shown to be greater than the longitudinal strain of the Achilles tendon aponeurosis (Magnusson et al., 2003), which at least partially explains differences between our predicted global strains and previous measurements during dynamics tasks. Single leg hop exercises resulted in the highest free Achilles tendon global strains, which is likely related to some combination of higher muscle activation and more favorable force-length-velocity behavior (i.e., longer triceps surae muscle lengths and faster lengthening speeds) than for walking and eccentric heel drops. It is however, important to consider that we presented data from a single subject and the results are likely to differ when analyzing Achilles tendon strain distribution in multiple individuals and pathological tendons (Hansen et al., 2017; Shim et al., 2019).

The FE model used in this study has been previously employed in cadaveric experiments, demonstrating excellent ability to predict tendon rupture in quasi-static conditions (Shim et al., 2014). However, the employed FE model did not fully account for each of the individual subtendons (Pekala et al., 2017), thus preventing the prediction of differential strains between deep and superficial Achilles tendon that have been described in literature (Franz et al., 2015). In future it will be

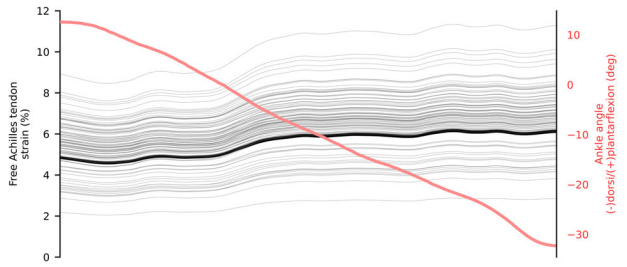

FIGURE 6 | Mean *in vivo* free Achilles tendon global (thick black) and localized (thin gray) strain from 5 repetition of eccentric heel drop. The ankle angle is represented in red.

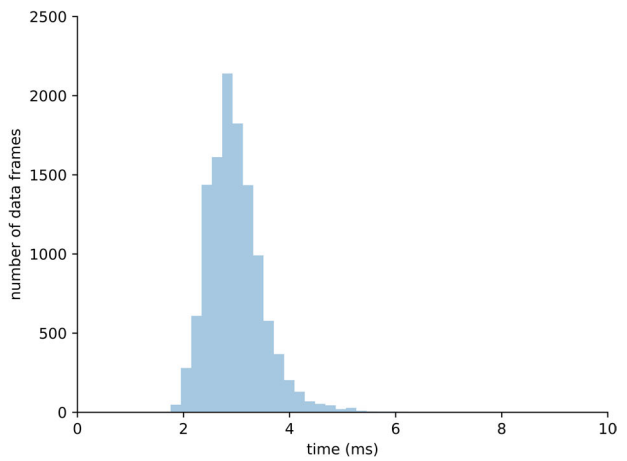

FIGURE 7 | Distribution of computational time required to process 10,000 data frames within the complete real-time pipeline.

of benefit to incorporate more detailed representation of the complex substructural geometry of the tendon and localized material properties (e.g., via elastography) for normal and pathological tendons (DeWall et al., 2014). Localized AT strains ranged from 3 to 11% during walking, 5 to 15% during single leg hopping, and 2 to 9% during the eccentric heel drop and suggest that tendon strain distribution within the Achilles tendon may be highly heterogenous. The highest localized strains tended to correspond with the tendon mid-region where the tendon cross-sectional area was minimal. However, our model used a homogeneous spatial distribution of material properties and a transversely isotropic hyperelastic formulation, which does not account for the viscous behavior of human tendons. While elastic properties have been shown to prevail over viscous properties in the human Achilles tendon (Peltonen et al., 2013), a better estimate of localized tendon strain would still be expected if localized tendon material properties were included in our model. Furthermore, we used a twist of 30°, which has been shown to prevent strain concentrations (Shim et al., 2018), so our estimate of localized strain might be conservative.

Validation of localized strain prediction using strain mapping techniques will be required to confirm the true extent of strain magnitude and heterogeneity in the Achilles tendon. It is however, important to consider that direct measurement of Achilles tendon strain distribution during dynamic task is an extremely challenging task (Maganaris et al., 2017). Franz et al. (2015) provided direct measurements of Achilles tendon displacement during walking; however, tendon displacements were only assessed on a single plane, and within a region of interest of 38 mm within the mid portion of the tendon. Other approaches, such as the use of speckle-tracking based methods under controlled contractile conditions also show potential at this time (Slane and Thelen, 2015). Despite the lack of direct validation of our results, the individual components of our modeling pipeline have been tested and validated (or verified) individually. Our rigid-body EMG-informed NMS model has been used in multiple applications, showing to produce physiologically plausible muscle forces across the lower and upper limbs (Hoang et al., 2018; Kian et al., 2019; Assila et al., 2020; Maniar et al., 2020). Additionally, the personalization via ultrasound and MRI measurements, the calibration of the neuromuscular parameters in the rigid body model, and the tuning of the material properties of the FE model, all contribute to generate physiologically plausible results. Nonetheless, it will be necessary to define some creative ways to further validate and refine our modeling pipeline. Following this methodological evaluation and validation, a detailed survey of interindividual variation of free Achilles tendon strains in a broad range of functional tasks will be of benefit to guide practitioners in prescribing exercise for Achilles tendon training and rehabilitation that are likely to have anabolic or therapeutic benefit. Clinical trials will also be required to demonstrate whether the efficacy of targeted training and rehabilitation informed by real-time feedback of free Achilles tendon strain is enhanced relative to traditional exercise prescriptions where tissue strain is not explicitly targeted.

In vitro and *in vivo* studies have identified strain magnitude as an important parameter for maximizing tendon adaptation (Wang, 2006; Arampatzis et al., 2007; Wang et al., 2013, 2015), but more studies are required to better locate the mechanobiological sweet spot for normal as well as pathological tendons. Such studies should explore the effect of different combinations strain magnitude, duration, frequency and rate on tendon remodeling, and identify the optimal combination. A further imperative will be to substantially reduce the time required to generate and run personalized models. A current bottleneck in the process is the time taken to manually segment medical images, which may be addressed in the future using auto-segmentation methods (Cunningham et al., 2016) or statistical shape modeling approaches (Zhang and Besier, 2017). In the context of the present application, statistical shape modeling would involve using machine learning methods to interrogate a large database of 3D tendon geometries to create a personalized 3D tendon geometry based on sparse geometric data obtained from the individual. While no such database currently exists, efforts to do so are recommended.

A further barrier to clinical translation is the current need to directly measure whole body kinematics, ground reaction

forces, and muscle activation patterns in order to first calibrate the NMS model and then estimate triceps surae muscle-tendon forces. Although these measurements may be routinely made in a laboratory environment, they are generally not feasible in either the field or a typical clinic. A necessary development will therefore be to develop wearable technologies, such as inertial measurement units to replace marker-based motion capture, which may be imbedded into garments together with wireless EMG sensors. Such systems are already commercially available but would need to be registered to an underlying anatomical model and evaluated against marker-based motion capture systems in terms of their ability to drive a NMS model. Several recent developments also point to the possibility that the current need to directly measure ground reaction forces using a force plate could be eliminated. For example Martin et al. (2018) and Keuler et al. (2019) described a non-invasive method that involves measuring the speed of the of the shear wave generated in response to tapping the tendon to estimate Achilles tendon loading during locomotion. Further, Johnson and colleagues used reduced motion capture marker sets or wearable technology and big data/machine learning to accurately estimate ground reaction forces and moments (Johnson et al., 2018, 2019a, 2020) and knee joint moments (Johnson et al., 2019b) from kinematic motion capture data alone. Developments such as these are important because of their potential make direct measurement of ground reaction forces redundant.

CONCLUSION

It is clear from both *in vitro* and *in vivo* studies that the Achilles tendon is highly sensitive to its mechanical environment and that there appears to be a strain range that results in positive tendon adaptation. We have demonstrated in this paper that it is possible to generate data that could be used to provide real-time feedback in a training and/or rehabilitation setting to that ensure a targeted dose of mechanical stimuli can be delivered to the Achilles tendon. The main point of difference with this approach, compared to existing approaches in tendon training and rehabilitation, is that the prescribed loading regime for the tendon is defined at the tissue level in terms of localized tendon stresses and/or strains, rather than by whole-body or joint level biomechanics, via a generic set of exercises and dosages. This is an important distinction because (1) the correspondence between external and internal tissue loading is weak due to the high degree of variability between individuals in movement patterns, muscle activation patterns, musculoskeletal geometry and material properties, and (2) defining loading at the level of the tissue (tendon) connects, across size scales, these two previously distinct fields of research, thereby providing the ability to alter exercise prescription to target the mechanobiological sweet-spot for the tendon. We also foresee the potential of targeted training and rehabilitation informed by real-time feedback of localized tissues loading to guide remodeling of other musculoskeletal tissues such as bone, muscle and cartilage, and in the management of other musculoskeletal conditions including osteoarthritis and osteoporosis.

DATA AVAILABILITY STATEMENT

Upon request, the raw data supporting the conclusions of this article will be made available by the authors, without undue reservation.

ETHICS STATEMENT

The studies involving human participants were reviewed and approved by the Griffith University Human Research Ethics Committee. The participant provided their written informed consent to participate in this study.

AUTHOR CONTRIBUTIONS

CP and VS contributed to the model, analyze the data, and conceptualized, drafted, critically revised, and approved the final version of the manuscript. DD contributed to the data collection, and conceptualized, drafted, critically revised, and approved the final version of the manuscript. DL, SO, RN-W, DG, TB, MZ, and RB contributed to the conceptualization, and critically revised and approved the final version of the manuscript. All authors contributed to the article and approved the submitted version.

FUNDING

This work was supported by the Australian Research Council (LP150100905).

REFERENCES

Alexander, C., Lum, I., Reid, S., Clarke, E., Stannage, K., Abd, A. E.-S., et al. (2017). A simple but reliable method for measuring 3D Achilles tendon moment arm geometry from a single, static magnetic resonance scan. *J. Biomec.* 55, 134–138. doi: 10.1016/j.jbiomech.2017.01.038

Alfredson, H., Pietila, T., Jonsson, P., and Lorentzon, R. (1998). Heavy-load eccentric calf muscle training for the treatment of chronic Achilles tendinosis. *Am. J. Sports Med.* 26, 360–366. doi: 10.1177/03635465980260030301

Arampatzis, A., Karamanidis, K., and Albracht, K. (2007). Adaptational responses of the human Achilles tendon by modulation of the applied cyclic strain magnitude. *J. Exp. Biol.* 210(Pt 15), 2743–2753. doi: 10.1242/jeb.003814

Arampatzis, A., Peper, A., Bierbaum, S., and Albracht, K. (2010). Plasticity of human Achilles tendon mechanical and morphological properties in response to cyclic strain. *J. Biomech.* 43, 3073–3079. doi: 10.1016/j.jbiomech.2010.08.014

Arya, S., and Kulig, K. (2010). Tendinopathy alters mechanical and material properties of the Achilles tendon. *J. Appl. Physiol.* 108, 670–675. doi: 10.1152/japplphysiol.00259.2009

Assila, N., Pizzolato, C., Martinez, R., Lloyd, D.G., and Begon, M. (2020). EMG-assisted algorithm to account for shoulder muscles co-contraction in overhead manual handling. *Appl. Sci.* doi: 10.3390/app10103522

Bahl, J. S., Zhang, J., Killen, B. A., Taylor, M., Solomon, L. B., Arnold, J. B., et al. (2019). Statistical shape modelling versus linear scaling: effects on predictions of hip joint centre location and muscle moment arms in people with hip osteoarthritis. *J. Biomech.* 85, 164–172. doi: 10.1016/j.jbiomech.2019.01.031

Bohm, S., Mersmann, F., and Arampatzis, A. (2015). Human tendon adaptation in response to mechanical loading: a systematic review and meta-analysis of exercise intervention studies on healthy adults. *Sports Med. Open.* 1:7.

Bueno, D. R., and Montano, L. (2017). Neuromusculoskeletal model self-calibration for on-line sequential bayesian moment estimation. *J. Neural Eng.* 14:026011. doi: 10.1088/1741-2552/aa58f5

Cunningham, R. J., Harding, P. J., and Loram, I. D. (2016). Real-time ultrasound segmentation, analysis and visualisation of deep cervical muscle structure. *IEEE Trans. Med. Imaging* 36, 653–665. doi: 10.1109/tmi.2016.2623819

Davico, G., Pizzolato, C., Killen, B. A., Barzan, M., Suwarganda, E. K., Lloyd, D. G., et al. (2019a). Best methods and data to reconstruct paediatric lower limb bones for musculoskeletal modelling. *Biomech. Model. Mechanobiol.* doi: 10.1007/s10237-019-01245-y [Online ahead of print]

Davico, G., Pizzolato, C., Lloyd, D. G., Obst, S. J., Walsh, H. P. J., and Carty, C. P. (2019b). Increasing level of neuromusculoskeletal model personalisation to investigate joint contact forces in cerebral palsy: a twin case study. *Clin. Biomech.* 72, 141–149. doi: 10.1016/j.clinbiomech.2019.12.011

Delp, S. L., Anderson, F. C., Arnold, A. S., Loan, P., Habib, A., John, C. T., et al. (2007). OpenSim: open-source software to create and analyze dynamic simulations of movement. *IEEE Trans. Biomed. Eng.* 54, 1940–1950. doi: 10.1109/tbme.2007.901024

Devaprakash, D., Lloyd, D. G., Barrett, R. S., Obst, S. J., Kennedy, B., Adams, K. L., et al. (2019). Magnetic Resonance Imaging and Freehand 3-D Ultrasound Provide Similar Estimates of Free Achilles Tendon Shape and 3-D Geometry. *Ultrasound Med. Biol.* 45, 2898–2905. doi: 10.1016/j.ultrasmedbio.2019.07.679

DeWall, R. J., Slane, L. C., Lee, K. S., and Thelen, D. G. (2014). Spatial variations in Achilles tendon shear wave speed. *J. Biomech.* 47, 2685–2692. doi: 10.1016/j.jbiomech.2014.05.008

Durandau, G., Farina, D., and Sartori, M. (2018). Robust Real-Time Musculoskeletal Modeling Driven by Electromyograms. *IEEE Trans. Biomed. Eng.* 65, 556–564. doi: 10.1109/tbme.2017.2704085

Edama, M., Kubo, M., Onishi, H., Takabayashi, T., Inai, T., Yokoyama, E., et al. (2015). The twisted structure of the human Achilles tendon. *Scand. J. Med. Sci. Sports* 25, e497–e503.

Fernandez, J., Mithraratne, P., Thrupp, S., Tawhai, M., and Hunter, P. (2004). Anatomically based geometric modelling of the musculo-skeletal system and other organs. *Biomech. Model. Mechanobiol.* 2, 139–155. doi: 10.1007/s10237-003-0036-1

Franz, J. R., Slane, L. C., Rasske, K., and Thelen, D. G. (2015). Non-uniform in vivo deformations of the human Achilles tendon during walking. *Gait Posture* 41, 192–197. doi: 10.1016/j.gaitpost.2014.10.001

Galloway, M. T., Lalley, A. L., and Shearn, J. T. (2013). The role of mechanical loading in tendon development, maintenance, injury, and repair. *J. Bone Joint Surg. Am.* 95, 1620–1628. doi: 10.2106/jbjs.l.01004

Gerus, P., Sartori, M., Besier, T. F., Fregly, B. J., Delp, S. L., Banks, S. A., et al. (2013). Subject-specific knee joint geometry improves predictions of medial tibiofemoral contact forces. *J. Biomech.* 46, 2778–2786. doi: 10.1016/j.jbiomech.2013.09.005

Grant, T. M., Diamond, L. E., Pizzolato, C., Killen, B. A., Devaprakash, D., Kelly, L., et al. (2020). Development and validation of statistical shape models of the primary functional bone segments of the foot. *PeerJ* 8:e8397. doi: 10.7717/peerj.8397

Handsfield, G. G., Inouye, J. M., Slane, L. C., Thelen, D. G., Miller, G. W., and Blemker, S. S. (2017). A 3D model of the Achilles tendon to determine the mechanisms underlying nonuniform tendon displacements. *J. Biomech.* 51, 17–25. doi: 10.1016/j.jbiomech.2016.11.062

Handsfield, G. G., Meyer, C. H., Hart, J. M., Abel, M. F., and Blemker, S. S. (2014). Relationships of 35 lower limb muscles to height and body mass quantified using MRI. *J. Biomech.* 47, 631–638. doi: 10.1016/j.jbiomech.2013.12.002

Hansen, W., Shim, V. B., Obst, S., Lloyd, D. G., Newsham-West, R., and Barrett, R. S. (2017). Achilles tendon stress is more sensitive to subject-specific geometry than subject-specific material properties: a finite element analysis. *J. Biomech.* 56, 26–31. doi: 10.1016/j.jbiomech.2017.02.031

Hart, N. H., Nimphius, S., Rantalainen, T., Ireland, A., Siafarikas, A., and Newton, R. (2017). Mechanical basis of bone strength: influence of bone material, bone structure and muscle action. *J. Musculoskeletal Neuronal Interact.* 17:114.

Hawkins, D., Lum, C., Gaydos, D., and Dunning, R. (2009). Dynamic creep and pre-conditioning of the Achilles tendon in-vivo. *J. Biomech.* 42, 2813–2817. doi: 10.1016/j.jbiomech.2009.08.023

Heinemeier, K. M., and Kjaer, M. (2011). In vivo investigation of tendon responses to mechanical loading. *J. Musculoskelet. Neuronal Interact.* 11, 115–123.

Hoang, H. X., Pizzolato, C., Diamond, L. E., and Lloyd, D. G. (2018). Subject-specific calibration of neuromuscular parameters enables neuromusculoskeletal models to estimate physiologically plausible hip joint contact forces in healthy adults. *J. Biomech.* 80, 111–120. doi: 10.1016/j.jbiomech.2018.08.023

Hsieh, Y. F., and Turner, C. H. (2001). Effects of loading frequency on mechanically induced bone formation. *J. Bone Mineral Res.* 16, 918–924. doi: 10.1359/jbmr.2001.16.5.918

Johnson, W. R., Alderson, J., Lloyd, D., and Mian, A. (2019a). Predicting Athlete Ground Reaction Forces and Moments From Spatio-Temporal Driven CNN Models. *IEEE Trans. Biomed. Eng.* 66, 689–694. doi: 10.1109/tbme.2018.2854632

Johnson, W. R., Mian, A., Lloyd, D. G., and Alderson, J. A. (2019b). On-field player workload exposure and knee injury risk monitoring via deep learning. *J. Biomech.* 93, 185–193. doi: 10.1016/j.jbiomech.2019.07.002

Johnson, W. R., Mian, A., Donnelly, C. J., Lloyd, D., and Alderson, J. (2018). Predicting athlete ground reaction forces and moments from motion capture. *Med. Biol. Eng. Comput.* 56, 1781–1792. doi: 10.1007/s11517-018-1802-7

Johnson, W. R., Mian, A., Robinson, M. A., Verheul, J., Lloyd, D. G., and Alderson, J. A. (2020). Multidimensional ground reaction forces and moments from wearable sensor accelerations via deep learning. *IEEE Trans. Biomed. Eng.* (in press). doi: 10.1109/TBME.2020.3006158

Kannape, O. A., and Blanke, O. (2013). Self in motion: sensorimotor and cognitive mechanisms in gait agency. *J. Neurophysiol.* 110, 1837–1847. doi: 10.1152/jn.01042.2012

Keuler, E. M., Loegering, I. F., Martin, J. A., Roth, J. D., and Thelen, D. G. (2019). Shear Wave Predictions of Achilles Tendon Loading during Human Walking. *Sci. Rep.* 9:13419.

Kian, A., Pizzolato, C., Halaki, M., Ginn, K., Lloyd, D., Reed, D., et al. (2019). Static optimization underestimates antagonist muscle activity at the glenohumeral joint: a musculoskeletal modeling study. *J. Biomech.* 2019:109348. doi: 10.1016/j.jbiomech.2019.109348

Lichtwark, G., and Wilson, A. (2005). In vivo mechanical properties of the human Achilles tendon during one-legged hopping. *J. Exp. Biol.* 208, 4715–4725. doi: 10.1242/jeb.01950

Lichtwark, G., and Wilson, A. (2006). Interactions between the human gastrocnemius muscle and the Achilles tendon during incline, level and decline locomotion. *J. Exp. Biol.* 209(Pt 21), 4379–4388. doi: 10.1242/jeb.02434

Lloyd, D. G., and Besier, T. F. (2003). An EMG-driven musculoskeletal model to estimate muscle forces and knee joint moments in vivo. *J. Biomech.* 36, 765–776. doi: 10.1016/s0021-9290(03)00010-1

Maganaris, C. N., Chatzistergos, P., Reeves, N. D., and Narici, M. V. (2017). Quantification of internal stress-strain fields in human tendon: unraveling the mechanisms that underlie regional tendon adaptations and mal-adaptations to mechanical loading and the effectiveness of therapeutic eccentric exercise. *Front. Physiol.* 8:91. doi: 10.3389/fphys.2017.00091

Magnusson, S. P., Hansen, P., Aagaard, P., Brond, J., Dyhre-Poulsen, P., Bojsen-Moller, J., et al. (2003). Differential strain patterns of the human gastrocnemius aponeurosis and free tendon, in vivo. *Acta Physiol. Scand.* 177, 185–195. doi: 10.1046/j.1365-201x.2003.01048.x

Manal, K., Gravare-Silbernagel, K., and Buchanan, T. S. (2012). A Real-time EMG-driven Musculoskeletal Model of the Ankle. *Multibody Syst. Dyn.* 28, 169–180. doi: 10.1007/s11044-011-9285-4

Maniar, N., Schache, A. G., Pizzolato, C., and Opar, D. A. (2020). Muscle contributions to tibiofemoral shear forces and valgus and rotational joint moments during single leg drop landing. *Scand. J. Med. Sci. Sports* doi: 10.1111/sms.13711

Martin, J. A., Brandon, S. C. E., Keuler, E. M., Hermus, J. R., Ehlers, A. C., Segalman, D. J., et al. (2018). Gauging force by tapping tendons. *Nat. Commun.* 9:1592.

McAuliffe, S., Tabuena, A., McCreesh, K., O'Keeffe, M., Hurley, J., Comyns, T., et al. (2019). Altered strength profile in achilles tendinopathy: a systematic review and meta-analysis. *J. Athl. Train* 54, 889–900. doi: 10.4085/1062-6050-43-18

Millard, M., Uchida, T., Seth, A., and Delp, S. L. (2013). Flexing computational muscle: modeling and simulation of musculotendon dynamics. *J. Biomech. Eng.* 135:021005.

Nuri, L., Obst, S. J., Newsham-West, R., and Barrett, R. S. (2016). Regional three-dimensional deformation of human Achilles tendon during conditioning. *Scand. J. Med. Sci. Sports* 27, 1263–1272. doi: 10.1111/sms.12742

Nuri, L., Obst, S. J., Newsham-West, R., and Barrett, R. S. (2017). The tendinopathic Achilles tendon does not remain iso-volumetric upon repeated loading: insights from 3D ultrasound. *J. Exp. Biol.* 220, 3053–3061. doi: 10.1242/jeb.159764

Nuri, L., Obst, S. J., Newsham-West, R., and Barrett, R. S. (2018a). Recovery of human Achilles tendon three-dimensional deformation following conditioning. *J. Sci. Med. Sport* 21, 473–478. doi: 10.1016/j.jsams.2017.09.016

Nuri, L., Obst, S. J., Newsham-West, R., and Barrett, R. S. (2018b). Three-dimensional morphology and volume of the free Achilles tendon at rest and under load in people with unilateral mid-portion Achilles tendinopathy. *Exp. Physiol.* 103, 358–369. doi: 10.1113/ep086673

O'Brien, T. D., Reeves, N. D., Baltzopoulos, V., Jones, D. A., and Maganaris, C. N. (2010). In vivo measurements of muscle specific tension in adults and children. *Exp. Physiol.* 95, 202–210. doi: 10.1113/expphysiol.2009.048967

Obst, S. J., Newsham-West, R., and Barrett, R. S. (2014a). In vivo measurement of human Achilles tendon morphology using freehand 3-D ultrasound. *Ultrasound Med. Biol.* 40, 62–70. doi: 10.1016/j.ultrasmedbio.2013.08.009

Obst, S. J., Renault, J. B., Newsham-West, R., and Barrett, R. S. (2014b). Three-dimensional deformation and transverse rotation of the human free Achilles tendon in vivo during isometric plantarflexion contraction. *J. Appl. Physiol.* 116, 376–384. doi: 10.1152/japplphysiol.01249.2013

Obst, S. J., Newsham-West, R., and Barrett, R. S. (2015). Three-dimensional morphology and strain of the human Achilles free tendon immediately following eccentric heel drop exercise. *J. Exp. Biol.* 218(Pt 24), 3894–3900.

Obst, S. J., Newsham-West, R., and Barrett, R. S. (2016). Changes in Achilles tendon mechanical properties following eccentric heel drop exercise are specific to the free tendon. *Scand. J. Med. Sci. Sports* 26, 421–431. doi: 10.1111/sms.12466

Obst, S. J., Schrader, B. L., Davis, S. A., Dodd, K. A., Holzberger, C. J., Beavis, L. B., et al. (2018). Are the mechanical properties of the Achilles and patellar tendon altered in tendinopathy? A systematic review with meta-analysis. *Sports Med.* 48, 2179–2198. doi: 10.1007/s40279-018-0956-7

Paavola, M., Kannus, P., Jarvinen, T. A., Khan, K., Jozsa, L., and Jarvinen, M. (2002). Achilles tendinopathy. *J. Bone Joint Surg. Am.* 84, 2062–2076.

Pekala, P. A., Henry, B. M., Ochala, A., Kopacz, P., Taton, G., Mlyniec, A., et al. (2017). The twisted structure of the Achilles tendon unraveled: a detailed quantitative and qualitative anatomical investigation. *Scand. J. Med. Sci. Sports* 27, 1705–1715. doi: 10.1111/sms.12835

Peltonen, J., Cronin, N. J., Stenroth, L., Finni, T., and Avela, J. (2013). Viscoelastic properties of the Achilles tendon in vivo. *Springerplus* 2:212.

Pizzolato, C., Lloyd, D. G., Barrett, R. S., Cook, J., Zheng, M., Besier, T. F., et al. (2017a). Bioinspired technologies to connect musculoskeletal mechanobiology to the person for training and rehabilitation. *Front. Comput. Neurosci.* 11:96. doi: 10.3389/fncom.2017.00096

Pizzolato, C., Reggiani, M., Modenese, L., and Lloyd, D. G. (2017b). Real-time inverse kinematics and inverse dynamics for lower limb applications using OpenSim. *Comput. Methods Biomech. Biomed. Eng.* 20, 436–445. doi: 10.1080/10255842.2016.1240789

Pizzolato, C., Reggiani, M., Saxby, D. J., Ceseracciu, E., Modenese, L., and Lloyd, D. G. (2017c). Biofeedback for gait retraining based on real-time estimation of tibiofemoral joint contact forces. *IEEE Trans. Neural. Syst. Rehabil. Eng.* 25, 1612–1621. doi: 10.1109/tnsre.2017.2683488

Pizzolato, C., Lloyd, D. G., Sartori, M., Ceseracciu, E., Besier, T. F., Fregly, B. J., et al. (2015). CEINMS: a toolbox to investigate the influence of different neural control solutions on the prediction of muscle excitation and joint moments during dynamic motor tasks. *J. Biomech.* 48, 3929–3936. doi: 10.1016/j.jbiomech.2015.09.021

Pizzolato, C., Lloyd, D. G., Zheng, M. H., Besier, T. F., Shim, V. B., Obst, S. J., et al. (2019). Finding the sweet spot via personalised Achilles tendon training: the future is within reach. *Br. J. Sports Med.* 53, 11–12. doi: 10.1136/bjsports-2018-099020

Sartori, M., Reggiani, M., van den Bogert, A. J., and Lloyd, D. G. (2012). Estimation of musculotendon kinematics in large musculoskeletal models using multidimensional B-splines. *J. Biomech.* 45, 595–601. doi: 10.1016/j.jbiomech.2011.10.040

Saxby, D. J., Killen, B. A., Pizzolato, C., Carty, C. P., Diamond, L. E., Modenese, L., et al. (2020). Machine learning methods to support personalized neuromusculoskeletal modelling. *Biomech. Model Mechanobiol.* doi: 10.1007/s10237-020-01367-8

Saxby, D. J., Modenese, L., Bryant, A. L., Gerus, P., Killen, B., Fortin, K., et al. (2016). Tibiofemoral contact forces during walking, running and sidestepping. *Gait Posture* 49, 78–85. doi: 10.1016/j.gaitpost.2016.06.014

Schutte, L. M. (1993). *Using Musculoskeletal Models to Explore Strategies for Improving Performance in Electrical Stimulation-Induced leg Cycle Ergometry*. Stanford: Stanford University.

Shim, V. B., Fernandez, J. W., Gamage, P. B., Regnery, C., Smith, D. W., Gardiner, B. S., et al. (2014). Subject-specific finite element analysis to characterize the influence of geometry and material properties in Achilles tendon rupture. *J. Biomech.* 47, 3598–3604. doi: 10.1016/j.jbiomech.2014.10.001

Shim, V. B., Handsfield, G. G., Fernandez, J. W., Lloyd, D. G., and Besier, T. F. (2018). Combining in silico and in vitro experiments to characterize the role of fascicle twist in the Achilles tendon. *Sci. Rep.* 8:13856.

Shim, V. B., Hansen, W., Newsham-West, R., Nuri, L., Obst, S., Pizzolato, C., et al. (2019). Influence of altered geometry and material properties on tissue stress distribution under load in tendinopathic Achilles tendons - A subject-specific finite element analysis. *J. Biomech.* 82, 142–148. doi: 10.1016/j.jbiomech.2018.10.027

Slane, L. C., and Thelen, D. G. (2015). Achilles tendon displacement patterns during passive stretch and eccentric loading are altered in middle-aged adults. *Med. Eng. Phys.* 37, 712–716. doi: 10.1016/j.medengphy.2015.04.004

Smith, D. W., Rubenson, J., Lloyd, D., Zheng, M., Fernandez, J., Besier, T., et al. (2013). A conceptual framework for computational models of Achilles tendon homeostasis. *Wiley Interdiscip. Rev. Syst. Biol. Med.* 5, 523–538. doi: 10.1002/wsbm.1229

Stenroth, L., Peltonen, J., Cronin, N. J., Sipilä, S., and Finni, T. (2012). Age-related differences in Achilles tendon properties and triceps surae muscle architecture in vivo. *J. Appl. Physiol.* 113, 1537–1544. doi: 10.1152/japplphysiol.00782.2012

Turner, C. H., Owan, I., and Takano, Y. (1995). Mechanotransduction in bone: role of strain rate. *Am. J. Physiol. Endocrinol. Metab.* 269, E438–E442.

Veerkamp, K., Schallig, W., Harlaar, J., Pizzolato, C., Carty, C. P., Lloyd, D. G., et al. (2019). The effects of electromyography-assisted modelling in estimating musculotendon forces during gait in children with cerebral palsy. *J. Biomech.* 92, 45–53. doi: 10.1016/j.jbiomech.2019.05.026

Wang, J. H. (2006). Mechanobiology of tendon. *J. Biomech.* 39, 1563–1582. doi: 10.1016/j.jbiomech.2005.05.011

Wang, T., Lin, Z., Day, R. E., Gardiner, B., Landao-Bassonga, E., Rubenson, J., et al. (2013). Programmable mechanical stimulation influences tendon homeostasis in a bioreactor system. *Biotechnol. Bioeng.* 110, 1495–1507. doi: 10.1002/bit.24809

Wang, T., Lin, Z., Ni, M., Thien, C., Day, R. E., Gardiner, B., et al. (2015). Cyclic mechanical stimulation rescues achilles tendon from degeneration in a bioreactor system. *J. Orthop. Res.* 33, 1888–1896. doi: 10.1002/jor.22960

Wiesinger, H.-P., Rieder, F., Kösters, A., Müller, E., and Seynnes, O. R. (2017). Sport-specific capacity to use elastic energy in the patellar and achilles tendons of elite athletes. *Front. Physiol.* 8:132. doi: 10.3389/fphys.2017.00132

Wilson, F., Walshe, M., O'Dwyer, T., Bennett, K., Mockler, D., and Bleakley, C. (2018). Exercise, orthoses and splinting for treating Achilles tendinopathy: a systematic review with meta-analysis. *Br. J. Sports Med.* 52, 1564–1574. doi: 10.1136/bjsports-2017-098913

Young, S. R., Gardiner, B., Mehdizadeh, A., Rubenson, J., Umberger, B., and Smith, D. W. (2016). Adaptive remodeling of achilles tendon: a multi-scale computational model. *PLoS Comput. Biol.* 12:e1005106. doi: 10.1371/journal.pcbi.1005106

Zelik, K. E., and Franz, J. R. (2017). It's positive to be negative: achilles tendon work loops during human locomotion. *PLoS One* 12:e179976. doi: 10.1371/journal.pone.0179976

Zhang, J., and Besier, T. F. (2017). Accuracy of femur reconstruction from sparse geometric data using a statistical shape model. *Comput. Methods Biomech. Biomed. Eng.* 20, 566–576. doi: 10.1080/10255842.2016.1263301

Zhang, J., Malcolm, D., Hislop-Jambrich, J., Thomas, C. D. L., and Nielsen, P. M. (2014). An anatomical region-based statistical shape model of the human femur. *Comput. Methods Biomech. Biomed. Eng.* 2, 176–185. doi: 10.1080/21681163.2013.878668

Conflict of Interest: The authors declare that the research was conducted in the absence of any commercial or financial relationships that could be construed as a potential conflict of interest.

frontiers in Bioengineering and Biotechnology

ORIGINAL RESEARCH
published: 02 September 2020
doi: 10.3389/fbioe.2020.00994

Altering the Mechanical Load Environment During Growth Does Not Affect Adult Achilles Tendon Properties in an Avian Bipedal Model

Kavya Katugam[1], Suzanne M. Cox[1], Matthew Q. Salzano[1,2,3], Adam De Boef[1], Michael W. Hast[4], Thomas Neuberger[3,5], Timothy M. Ryan[6], Stephen J. Piazza[1] and Jonas Rubenson[1,2,3]**

[1] Biomechanics Laboratory, Department of Kinesiology, The Pennsylvania State University, University Park, PA, United States, [2] Integrative and Biomedical Physiology, The Pennsylvania State University, University Park, PA, United States, [3] Huck Institutes of the Life Sciences, The Pennsylvania State University, University Park, PA, United States, [4] Biedermann Lab for Orthopaedic Research, Perelman School of Medicine, University of Pennsylvania, Philadelphia, PA, United States, [5] Department of Biomedical Engineering, The Pennsylvania State University, University Park, PA, United States, [6] Department of Anthropology, The Pennsylvania State University, University Park, PA, United States

Tendon mechanical properties respond to altered load in adults, but how load history during growth affects adult tendon properties remains unclear. To address this question, we adopted an avian model in which we altered the mechanical load environment across the growth span. Animals were divided at 2 weeks of age into three groups: (1) an exercise control group given the opportunity to perform high-acceleration movements (EXE, n = 8); (2) a sedentary group restricted from high-intensity exercise (RES, n = 8); and (3) a sedentary group also restricted from high-intensity exercise and in which the gastrocnemius muscles were partially paralyzed using repeated bouts of botulinum toxin-A injections (RES-BTX, n = 8). Video analysis of bird movement confirmed the restrictions eliminated high-intensity exercise and did not alter time spent walking and sitting between groups. At skeletal maturity (33–35 weeks) animals were sacrificed for analysis, consisting of high-field MRI and material load testing, of both the entire free Achilles tendon and the tendon at the bone-tendon junction. Free tendon stiffness, modulus, and hysteresis were unaffected by variation in load environment. Further, the bone-tendon junction cross-sectional area, stress, and strain were also unaffected by variations in load environment. These results suggest that: (a) a baseline level of low-intensity activity (standing and walking) may be sufficient to maintain tendon growth; and (b) if this lower threshold of tendon load is met, non-mechanical mediated tendon growth may override the load-induced mechanotransduction signal attributed to tendon remodeling in adults of the same species. These results are important for understanding of musculoskeletal function and tendon health in growing individuals.

Keywords: tendon, growth, stiffness, modulus, development

OPEN ACCESS

Edited by:
Huub Maas,
Vrije Universiteit Amsterdam, Netherlands

Reviewed by:
Nicolai Konow,
University of Massachusetts Lowell, United States
Andrew Biewener,
Harvard University, United States

****Correspondence:***
Kavya Katugam
kxk751@psu.edu
Jonas Rubenson
jonas@psu.edu

Specialty section:
This article was submitted to Biomechanics, a section of the journal Frontiers in Bioengineering and Biotechnology

Received: *02 May 2020*
Accepted: *29 July 2020*
Published: *02 September 2020*

Citation:
Katugam K, Cox SM, Salzano MQ, De Boef A, Hast MW, Neuberger T, Ryan TM, Piazza SJ and Rubenson J (2020) Altering the Mechanical Load Environment During Growth Does Not Affect Adult Achilles Tendon Properties in an Avian Bipedal Model. Front. Bioeng. Biotechnol. 8:994. doi: 10.3389/fbioe.2020.00994

INTRODUCTION

Tendon mechanical properties change in response to variations in mechanical load history. In adult animals, including humans, increased loading increases both tendon stiffness and modulus, whereas decreased loading has had the opposite effect (for reviews see: Wren et al., 2000; Wang, 2006; Magnusson et al., 2008; Bohm et al., 2015).

While a causal link between load stimulus and tendon properties has been demonstrated for adult tissue, the few studies that have examined how variation in load across the growth period affect tendon material properties have produced contradictory findings. A comparison of adolescent athletes to non-athletes provided indirect evidence that long-term training during growth may result in increased patellar tendon stiffness (Mersmann et al., 2017a; Charcharis et al., 2019). A similar comparison between pre-adolescent athletes and non-athletes, however, found no differences in Achilles tendon stiffness (Pentidis et al., 2019). Short-term (10-week) resistance training interventions in both typically developing pre-adolescent children (Waugh et al., 2014) and in children with cerebral palsy (Kalkman et al., 2019) have been shown to increase Achilles tendon stiffness. We are not aware of any longer-term intervention studies of tendon adaptation in human children, but a 1-year longitudinal study tracking adolescent volleyball athletes undergoing strenuous training and minimally active control subjects found no significant between-group differences in the changes in patellar tendon stiffness (Mersmann et al., 2016). In this study, and in others by these authors (for a review, see Mersmann et al., 2017b), it is proposed that tendon has a slower and less pronounced response to altered load during growth compared to muscle, a phenomenon that may lead to an imbalance in the development of muscle and tendon strength.

Non-human animal models may provide insight into load-induced tendon plasticity across longer growth periods. For example, domestic fowl reared in cages that restrict movement developed Achilles tendons with a lower stiffness and elastic modulus compared to the same species reared in large pens that allowed for walking and running (Nakagaki et al., 2007), although detailed descriptions of activity in their groups were not included. More severe disuse models have found inconsistent results. Walsh et al. (1993) reported a reduction in stiffness and strength in rabbit knee ligament after immobilization. On the other hand, using botulinum toxin to paralyze murine muscle has resulted in tendon stiffness that decreases (Schwartz et al., 2013), increases (Khayyeri et al., 2017) or remains unaltered (Eliasson et al., 2007) when these interventions are applied during growth. Both of the latter two studies report a reduction in hysteresis in the unloaded tendon, which the authors interpret as impaired tendon damping (Eliasson et al., 2007; Khayyeri et al., 2017). An absence of altered tendon stiffness and tenocyte histology has similarly been observed in equine studies implementing trotting and galloping training across a substantial portion of the animals' growth span (Kasashima et al., 2008; Stanley et al., 2008). Likewise, Achilles tendon size and collagen content were found to be unaltered by high-intensity running training in growing domestic fowl (Curwin et al., 1988). Inconsistencies in the literature, such as those above, make it difficult predict how altered load during childhood will affect adult tendon. Overcoming this shortcoming is especially important in light of the trends of inadequate physical activity in growing children (Guthold et al., 2020).

Some of the uncertainty in the influence of load on tendon properties arises due to differences in measurement technique and mode, magnitude and duration of altered loads in the previous studies. For example, uncertainty in the load thresholds required for initiating tendon adaptation (Lavagnino and Arnoczky, 2005; Arampatzis et al., 2007) and their sensitivity to load frequency (Arampatzis et al., 2010) make it difficult to interpret the various outcomes from experimental load interventions. Our understanding of load-induced tendon adaptations during growth is hindered further because a number of prior investigations have not assessed tendon mechanical properties in functional contexts. In these studies, tendon properties have been assessed from portions of tendon, and then assumed to represent the entire tendon. The distal part of tendons, including the tendon-bone junction, are common sites of rupture under load (Jack, 1950; Woo et al., 1983; Woo and Buckwalter, 1988; Jarvinen, 1992), very likely due to their greater strain and stress, and smaller cross sectional area (Woo et al., 1983; Wren et al., 2000, 2001, 2003). Therefore, testing methods that exclude distal tendon regions and the bone-tendon junction may result in an over- or under-estimation of the whole-tendon mechanical properties and obscure their relevance to locomotor function.

The aim of this study was to address these limitations by (1) amplifying any possible load-induced changes in tendon properties by examining both a range of altered tendon loading, and by altering load across the entire growth period; and (2) by quantifying both whole tendon and regional properties relevant to *in vivo* function. To accomplish this, we applied a chronic load-reduction approach to the Achilles tendon in an avian bipedal model (guinea fowl; *Numida meleagris*). This permits alteration of the load stimulus over a large range of tissue size and over a substantially greater portion of the animals' growth span compared to most other model systems. Guinea fowl have substantially greater body-mass growth compared to rodent models (two orders of magnitude increase in body mass) and juvenile guinea fowl can locomote as early as 1-day-old. In this model system, we designed the experiment to induce two levels of load reduction to compare against controls. First, we reduced tendon load by restricting locomotor behavior in one group. This was achieved by eliminating high-intensity activity via space restriction (Cox et al., 2020). Secondly, in another group, we aimed to generate a more pronounced Achilles tendon load reduction by eliminating high-intensity movements and further paralyzing the gastrocnemius muscles using botulinum toxin-A (BTX-A), a neurotoxin known to offload muscle and tendon (Longino et al., 2005; Schwartz et al., 2013). In all groups we tracked the activity level throughout maturation. The experimental design intended to induce levels of decreased load over a much longer duration than most previous studies and to be able to relate these results to changes in activity level.

We assessed tendon properties of birds reared in these conditions in two functional contexts post-growth. First, we

investigated the spring-like quality of the tendon by measuring the stiffness, modulus and hysteresis of the entire free tendon. The properties of the full intact tendon most directly reflect its overall capacity to store and release elastic energy during locomotion, as well as how it will influence muscle fiber mechanics and energetics (Lichtwark and Wilson, 2008; Roberts and Azizi, 2011; Konow et al., 2012). Second, we assessed tendon properties at the bone-tendon junction. Similar to the human Achilles, the bone-tendon junction is the tendon region with the smallest cross sectional area in guinea fowl and is thus important for understanding tendon strength. Based on the response known to occur in adult tendon, we hypothesized that tendon would adapt in a load-dependent manner. Specifically, we predicted that the overall free Achilles tendon stiffness, modulus, and hysteresis would be reduced in animals in which high-intensity movements were eliminated across the growth period, and further reduced in animals administered (BTX-A). Additionally, we predicted that the distal tendon at the bone-tendon junction would exhibit smaller cross-sectional areas and undergo larger stress and strain during loading.

MATERIALS AND METHODS

Animals

Twenty-four one-day old guinea fowl keets were obtained from a regional breeder (Guinea Farm; New Vienna, IA, United States). At 2-weeks of age, animals were divided into three groups: an exercise control group (EXE, n = 8; 3 female, 5 male), a restricted movement group (RES, n = 8; 3 female, 5 male), and a Botox group (RES-BTX, n = 8; 3 female, 5 male). Animals were pen-raised (see below for details) in a 12-h/12-h light/dark cycle, with both food and water provided *ad libitum*. The experimental design was approved by The Pennsylvania State University Institutional Animal Care and Use Committee (IACUC; protocol #46435) and the Institutional Biosafety Committee (IBC; protocol #47306).

Movement Analysis

Video recordings (Foscam; C2 1080p HD cameras; Houston, TX, United States) of each pen were acquired to quantify the daily movement patterns of the animals. A single camera was placed over each pen, with each camera's field-of-view capturing the group pen. Videos were recorded four times per day, across the growth period. A random subset of 60 videos (20 EXE, 20 RES, 20 RES-BTX) recorded during the 12-h light cycle were analyzed using methods outlined previously by Cox et al. (2020). Briefly, the first 5 min of each selected video was analyzed with a custom-written MATLAB script (The MathWorks, Natick, MA, United States) that allowed users to timestamp observed activities (i.e., walking, standing, sitting, and high-acceleration actions including jumps and sprint actions) via keystroke. The percent time spent walking, standing and sitting was assessed as group ensemble, reflecting the activity of the pen, while high-acceleration movements were recorded on an individual animal basis. Each individual video was analyzed three times and averaged. These were used to compute group averages for comparisons. Individual birds were not identifiable in any videos, so bird-specific analyses were not conducted.

Treatment

All RES and RES-BTX animals were group-reared in restricted-movement pens (1 m^2 at maturity) without perches, eliminating the ability for birds to jump and highly restricting running and sprinting (Cox et al., 2020). All EXE animals were group-reared in larger pens (3.14 m^2) with perches, in which animals were free to perform high-acceleration movements expected to result in high tendon loads, including running, sprinting and jumping to and landing from perches.

We chose to examine the Achilles tendon in this study, in part because of its prominent functional role in movement (Daley and Biewener, 2003; Marsh et al., 2004; Henry et al., 2005), and because it is in series with large muscles (gastrocnemius) that are readily treated with Botulinum toxin injections. BTX-A (Allergan, Irvine, CA, United States) was applied to the lateral and medial gastrocnemius muscles (LG and MG) to induce a local unloading effect on the Achilles tendon that would be greater than that achieved by restricting movement alone. Starting at 7–8 weeks of age, RES-BTX animals received bilateral BTX-A injections (4 units (LD50)/kg per leg) into the LG and MG muscles while under general anesthesia (1.5% isoflurane). BTX-A was combined with 0.9% sodium chloride to make a concentration of 10 units/ml. BTX-A injections were administered at multiple locations in each muscle, covering the proximal-distal and medio-lateral muscle regions. Previous studies in rabbits have indicated that an amount of 3.5 units/kg was sufficient to elicit a functional muscle impairment (Longino et al., 2005; Fortuna et al., 2015).

At 7–8 weeks of age, identifying muscle boundaries from palpation alone was difficult, so the first BTX-A administration was performed using a sterile dermatotomy procedure. Skin incisions were closed with absorbable suture (4.0 Monocryl). All subsequent BTX-A injections were administered via percutaneous injection. BTX-A was re-administered every 5 weeks (week 12–13; week 17–18; week 22–23) for a total of four injections. After each BTX-A administration, RES-BTX animals were monitored for 1–2 days in 0.6 m^2 individual cages before returning to group-housing. The RES and EXE group animals received a sham saline injection in the gastrocnemius muscles using the same volume injection and at the same frequency. At 33–35 weeks of age, animals were weighed and euthanized (pentobarbital >1.6 mg/kg), at which time animals had reached sexual and skeletal maturity.

Tendon Imaging

Following euthanasia, the pelvic limb of each animal was split along the midline of the pelvis. The right limb was kept fresh-frozen (−20°C) for tendon analysis. Tendon volume and cross-sectional area (CSA) were assessed with high-field MRI (7T Biospec Avance III HD; Bruker Biospin, Billerica, MA, United States; **Figure 1A**). Before MR imaging, limbs were placed onto an acrylic board. Using wooden dowels and zip ties to mount the limbs allowed for similar orientation for all animals. The small diameter of the MRI bore required the limb to be positioned in an extended posture. By keeping the knee extended a small amount

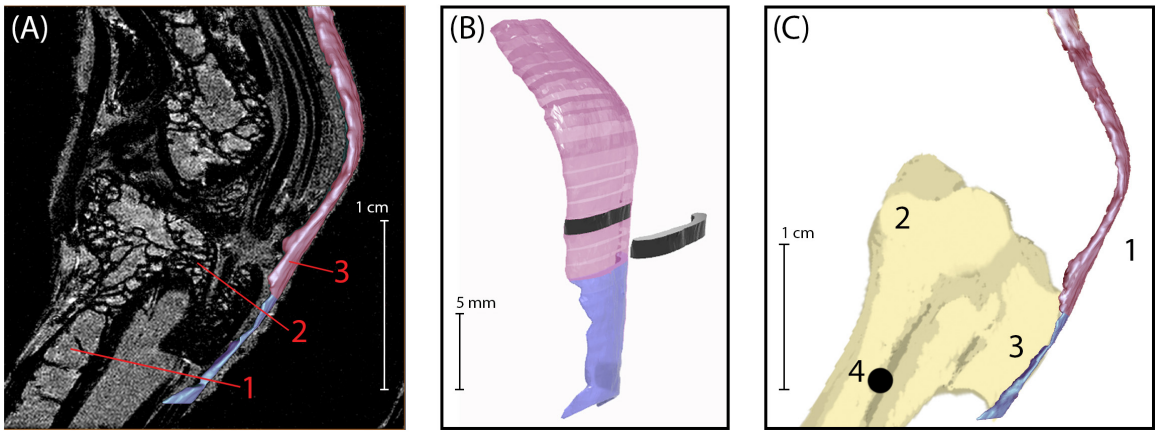

FIGURE 1 | (A) Sagittal plane MRI of the guinea fowl ankle joint. 1: tarsometatarsus bone (TMT). 2: Hypotarsus of the TMT, where the Achilles tendon inserts. 3: Achilles Tendon. **(B)** 3D rendering of the Achilles tendon, showing segmentation used to calculate cross-sectional area. The transition between colors indicates the bone-tendon-junction, which corresponds to the three-dot horizontal marker painted onto the tendons for video analysis (see **Figure 2**). Each tendon slice (shown in black) is 1 mm in thickness. **(C)** Medial view of bone-tendon specimen prepared for material testing. Prior to testing, superficial connective tissue was removed to expose the Achilles tendon (1), which inserts on the proximal end of the tarsometatarsus (2) at the hypotarsus (3). A 1.2 mm diameter hole (4) was drilled into the distal end of the tarsometatarsus bone, proximal to the hypotarsus, to allow for loading and clamping of specimen into material testing rig.

of tension was maintained on the tendon keeping the tendon alignment similar between specimens. Once mounted, limbs were sprayed with saline and covered in plastic wrap to retain moisture during the scanning procedure. After preparation, limbs were inserted into a 60 mm inner diameter quadrature driven birdcage resonator and placed into the isocenter of the magnet. A standard three-dimensional gradient echo imaging sequence with fat suppression yielded a 100-micron isotropic resolution within 33 min (repetition time: 40 ms; echo time: 3.9 ms; field of view (FOV): 35 mm × 25 mm × 20 mm; matrix size: 350 × 250 × 200; averages: 1). Data were zero filled by a factor of two in each direction using a custom MATLAB script resulting in a 50-micron isotropic pixel resolution. Image segmentation was performed using the lasso tool in Avizo (Thermo Fisher Scientific; Waltham, MA, United States).

Once segmented, tendon files were exported as stereolithography (STL) files that were imported into Rhinoceros 3D modeling software (Robert McNeel & Associates; Seattle, WA, United States) for determining overall and regional cross-sectional areas. Meshes were converted to polysurfaces and sliced every millimeter perpendicular to the lateral surface of tendon (**Figure 1B**). The cross-sectional area for each slice surface was calculated using the area tool in Rhinoceros 3D and recorded.

Tendon Preparation

Following MR imaging, the gastrocnemius muscles were detached from their origins on the tibiotarsus and femur. Muscle tissue was carefully dissected away from the proximal tendon aponeurosis. The Achilles tendon remained intact and attached to the hypotarsus, the attachment site for the Achilles tendon on the tarsometatarsus (TMT).

The fascia around the posterior ankle was carefully removed so as to isolate the free Achilles tendon. A 1.2 mm diameter hole was drilled in the proximal end of the TMT to secure the bone during material testing (**Figure 1C**). To facilitate regional strain analysis along the free tendon, small marks were placed along the length of the free tendon with insoluble acrylic lacquer paint (Krylon Products Group, Cleveland, OH, United States). The space between each mark was approximately 5% of the TMT length for each given sample (**Figure 2A**), resulting in between 13 and 20 marks per tendon. The TMT was used to standardize the tendon marks, as opposed to the tendon slack length, because the later was established after mounting the tendon (see below). The bone-tendon junction was indicated using a horizontal row of three marks, perpendicular to the length of the tendon (**Figure 2A**). Video recordings (Grasshopper3 GS3-U3-23S6C; FLIR Systems, Inc., Wilsonville, OR, United States) were used to track the tendon strain through marker movement. The entire limb was kept hydrated using a saline bath for a minimum of 30 min prior to material testing and throughout the testing procedure.

Tendon Material Testing

Mechanical properties of the tendons were measured via a material testing system (858 Mini Bionix II; MTS Systems Corp; Eden Prairie, MN, United States) using a custom-built rig (**Figure 3**). Samples were mounted vertically via custom clamps on the tendon aponeurosis and the TMT, and attached to a 50-pound load cell (MTS Systems Corp; Eden Prairie, MN, United States). The upper clamp gripped the entire aponeurosis of each sample, leaving only the free tendon exposed to loading. The transition from the free tendon to aponeurotic tendon was clearly identifiable by a marked change in tendon tissue thickness. The sample was clamped within a saline bath kept at the average active body temperature for guinea fowl (41.5 degrees Celsius; Prinzinger et al., 1991).

A tensile testing protocol was adapted from a previous study on explanted tendon (Miller et al., 2012). After tendons were

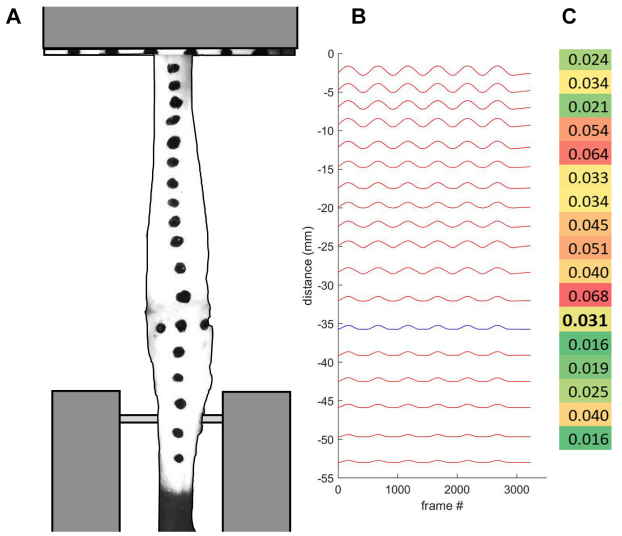

FIGURE 2 | (A) Tendon specimen were marked for regional strain analysis, and loaded into custom-built clamps. The bone-tendon junction is indicated with three horizontally aligned marks. **(B)** Displacement plot indicates bone-tendon junction distal region in blue. **(C)** Strain profile map indicates higher regional strain values in red and lower regional strain values in green. Bolded value corresponds with the tendon region proximal to the bone-tendon junction.

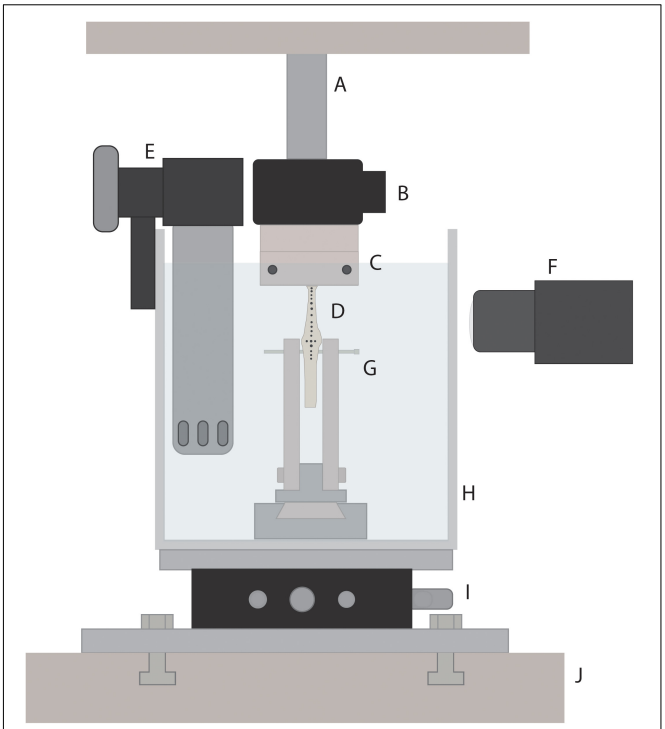

FIGURE 3 | Schematic of custom-built rig for tendon material testing. The rig was inserted into a material testing system (J; MTS Systems Corporation, Minneapolis, MN, United States) to allow for loading of tendon samples. Tendon specimen (D) were loaded via a 3D-printed tendon tissue clamp (C) at the proximal end, and a bone mount (G) at the distal end. A 50-pound load cell (B) connected the proximal end of the tendon specimen to the MTS linear actuator (A). An xy-stage (I) was used to orient the tendon, allowing for load to be applied along the long axis of the tendon. Tendons were submerged in a saline bath (H) that was heated to the average active body temperature for guinea fowl (41.5°C) using a water heater (E). A high speed camera (F) was used to track tendon marks during loading.

mounted into the custom-built rig, the upper clamp was lowered until the free-tendon was visibly slack, after which the force reading was zeroed. The upper clamp was then raised, elongating the tendon, until the force reading was approximately 5 N, and then was lowered again until the force first read 0.000 ± 0.001 N. The displacement reading was again zeroed and the free tendon slack length for each sample was measured using digital calipers as the distance from the middle of the hypotarsus to the start of the aponeurotic tendon, corresponding to the bottom of the upper clamp (**Figure 3**).

Tendons were first preconditioned by cyclic loading from 0 to 0.005 strain at 0.1 Hz for 10 cycles following Schmidt et al. (2019). Strain (ε) was calculated as the clamp displacement (ΔL) divided by the free tendon slack length (L_0, mm):

$$\varepsilon = \frac{\Delta L}{L_0}.$$

After preconditioning, tendons were loaded cyclically from 0 to 0.05 strain at 0.1 Hz for 20 cycles. Force and displacement were sampled at 102.4 Hz. Video recordings of the last five loading cycles for each tendon were captured at 50 Hz. Each sample video was spatially calibrated using still images of the clamped tendon, with a mm scale bar positioned in line with the tendon. Three images were taken of each sample, and pixel-to-millimeter conversion factors were computed for each image and averaged.

A custom-built LED circuit was used to synchronize video data with MTS output data. During the first filmed loading cycle, a TTL signal from the MTS triggered the LED light to turn on (5V high). During the last filmed loading cycle, the TTL voltage turned low, triggering the LED light to turn off. The recorded data were synchronized to the video data using a Boolean TTL variable (0–1) stored in the MTS data, the frames of video in which the LED turned on and off, and by time normalizing the MTS and video data. This was achieved by down-sampling the MTS data with spline interpolation.

Tendon Functional Stiffness, Elastic Modulus, and Hysteresis Analysis

First, force (F, N) and displacement (ΔL, mm) data were shifted to start at (0,0), as small errors in initial length measurements due to pre-conditioning cycles resulted in shifted force-length curves. As a result, maximum tendon strain exhibited some variability (mean maximum strain was 0.045 ± 0.0024 with a range between 0.04 and 0.048 strain).

Force and displacement data from the last five loading cycles were analyzed for each tendon using custom-written routines in MATLAB. Force data were filtered using a 5 Hz low-pass filter. Force-displacement curves were plotted for each sample. The force-displacement curves exhibited a typical J-shape with a clear toe region (**Figure 3**). Stiffness was calculated by fitting a

line to the force-length curve beyond the toe region, within the range of 25–95% of the tendon's maximal length (**Figure 4**). The region within this range that resulted in the lowest RMS_{error} of the linear fit,

$$RMS_{error} = \sqrt{\frac{\sum (Y_{fit} - Y_{exp})^2}{\text{number points}}},$$

was used to compute stiffness, with the minimum region set to 15% of the total tendon length and ending at 95% of the maximum tendon length (**Figure 4**). The slope of this linear fit region was used as the cycle stiffness. This process was repeated for each of the last five loading cycles for each sample, and these stiffness values were averaged across cycles to determine the functional tendon stiffness (K_{func}, N/mm) for each sample. The fitting routine was done using a custom function in MATLAB (The MathWorks, Natick, MA, United States).

Stress (σ, N/mm^2) for each sample were calculated using the average CSA for each tendon (CSA_{avg}, mm^2). The modulus of elasticity (E, MPa) for each sample was computed from the stress-strain curves in the same manner as described for determining K_{func}. To better characterize the tendon mechanical properties, we assessed the association between $K_{func}$and E and between K_{func} and CSA_{avg} in each group and across all groups using Pearson product moment correlations.

Finally, we assessed tendon hysteresis, which can influence the ability of the tendon to return energy during cyclical movement (Bennett et al., 1986; Shadwick, 1990). Strain energy was calculated as the area under the entire extension portion of each of the last five stress-strain cycles, including the toe region. The average energy storage (ϕ_{in}) was computed from these five cycles for each sample. The average energy recovered from each sample (ϕ_{out}) was calculated as the average area under the unloading portion of the last five stress-strain cycles. The energy lost (ϕ_{loss}) was calculated as the difference between ϕ_{in} and ϕ_{out} ($\phi_{loss} = \phi_{in} - \phi_{out}$). Hysteresis ($H$) was defined for each sample as:

$$H = \frac{\phi_{loss}}{\phi_{in}}.$$

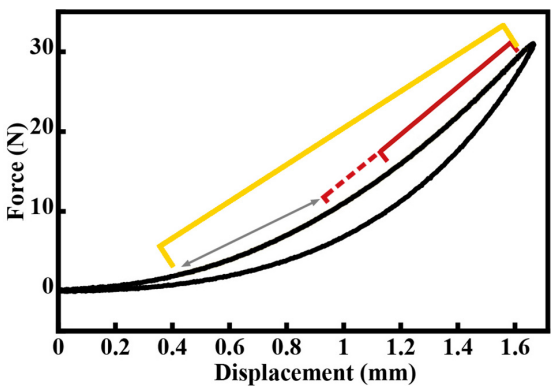

FIGURE 4 | Example force-displacement curve for a load-unload cycle of the Achilles tendon, exhibiting a typical j-shape toe region. Yellow bracket represents 25–95% of loading curve. The red bracket represents the region within the 25–95% range that resulted in the lowest RMS_{error} of the linear fit, which was then used to compute the stiffness value for this loading cycle. The red dashed bracket and arrow represents other regions for which linear fits were assessed. These regions spanned the entire length of the 25–95% region, always ending at 95% of the loading curve.

Regional Tendon Analysis

Regional strain at the bone-tendon junction was determined for each tendon sample. The ink marks on the calibrated video of the last five loading cycles for each tendon were auto digitized (ImageJ, MTrack2 Plug-in) to extract their position data. The bone-tendon junction region was defined as the section of the tendon between the center of the hypotarsus (identified by horizontal markers, as seen in **Figure 2**) and the closest proximal tendon mark. Our standardized marking procedure resulted in this region being between 3 and 5 mm (4.15 and 7.01% of L_0). A maximal regional strain value was calculated by dividing the regional displacement by the region length at L_0. The maximal regional displacement value used in this computation was taken when the total tendon strain was 0.04, since all tendons were strained at least to this amount. The bone-tendon junction tendon stress was computed as the ratio of the force applied to the tendon at this strain and the minimum cross-sectional area within the most distal tendon region (bone-tendon junction region CSA; CSA_{BTJ}, mm^2). The CSA_{BTJ} of each sample was extracted from the MRI data. This was done by matching the bone-tendon junction region on the MR images to the video data. In the video recordings, the bone-tendon junction was identified prior to material testing and marked with a horizontal row of three dots. The bone-tendon junction was identified in MR images by observation since the bone and the tendon were both identifiable. Above the tendon attachment site, the tendon CSA consistently increased by at least 50%. This change in tendon CSA was used as a proxy to identify the end of the bone-tendon junction region.

In order to assess the validity of using surface markers to measure regional tendon strain, we compared video tracking measurements of surface markers to that of insect pins placed through the tendon. The surface markers and pins were placed in the same locations, with two sets of each spaced approximately 10 mm apart. The comparison of these two techniques were used to reveal potential differences between surface (epitendon) strain and mid-substance strain.

Statistical Analysis

The influence of treatment group (EXE, RES, and RES-BTX) on animal movement data, tendon morphology and material properties, and bone-tendon junction morphology and material properties was evaluated using one-way ANOVA tests run in R (R Core Team, 2016) and Minitab (Minitab, LLC, State College, PA, United States) when criteria of normality and equal variances were met. *Post-hoc* Tukey tests were run for significant results to determine specific group effects. When criteria of normality and/or equal variance were not met, one-way non-parametric ANOVA on rank (i.e., Kruskal–Wallis) tests were run to determine influence of treatment group, with *post-hoc* Dunn tests (Dunn, 1964). The level of significance was set at $\alpha = 0.05$ *a priori*. Effect size (E.S.) values were reported as omega-squared

analyses, and were computed using the "sjstats" package in R (Lüdecke, 2019).

RESULTS

Habitual Movement

Bird movement data did not pass criteria of normality and/or equal variance. Kruskal–Wallis tests indicated no difference between treatment groups in percent time spent walking ($p = 0.393$), percent time spent standing ($p = 0.312$), and percent time spent sitting ($p = 0.286$, adjusted p for ties = 0.241), indicating that these measures were not significantly affected by the treatments (**Table 1**).

A Kruskal–Wallis test of number of sprint actions per group per day indicated significant differences between treatment groups ($p < 0.001$). A *post-hoc* Dunn test revealed that EXE birds sprinted significantly more than RES ($p < 0.001$) and RES-BTX birds ($p < 0.001$), but there was no significant difference between RES and RES-BTX birds ($p = 0.239$). EXE birds on average performed approximately 5.5 times more sprint actions than RES birds, and approximately 3.4 times more sprint actions than RES-BTX birds.

A Kruskal–Wallis test of number of jump actions per group per day indicated significant differences between treatment groups ($p < 0.001$). A *post-hoc* Dunn test revealed that EXE birds jumped significantly more than RES ($p < 0.001$) and RES-BTX birds ($p < 0.001$). EXE birds on average performed approximately 210 jump actions per group per day, while no jumps were observed in either RES or RES-BTX birds.

Tendon Functional Stiffness, Elastic Modulus, and Hysteresis

All tendon morphology and material property data passed criteria of normality and equal variance, and thus were analyzed using one-way ANOVA testing to determine differences between treatment groups. Body mass ($p = 0.755$, E.S = −0.066) and TMT length ($p = 0.769$, E.S. = −0.068) were not statistically different between groups (**Table 2**). Neither Achilles tendon length ($p = 0.79$, E.S. = −0.067) nor the average Achilles tendon CSA ($p = 0.81$, E.S. = −0.07) were statistically different between groups. Functional stiffness (K_{func}, $p = 0.951$, E.S. = −0.086), modulus of elasticity (E, $p = 0.955$, E.S. = −0.086), and hysteresis (H, $p = 0.760$, E.S. = −0.064) were similarly not statistically different between groups (**Figures 5**, **6**). Additionally, tendon stiffness across all animals correlated with modulus ($R^2 = 0.743$, $p < 0.01$), but not with average tendon cross-sectional area (CSA; mm^2) ($R^2 = 0.007$, $p = 0.698$; **Figure 7**). Hysteresis calculations may have been affected by the fact that not all tendons were pulled to exactly 0.05 strain.

TABLE 1 | Animal movement analysis.

	EXE	RES	RES-BTX
Time during growth (%)			
Standing*	69.2 ± 18.6	66.6 ± 12.4	67.2 ± 15.7
Walking*	26.6 ± 19.3	28.0 ± 12.8	27.2 ± 18.2
Sitting*	3.9 ± 6.5	5.1 ± 5.9	5.3 ± 7.1
High-intensity movements (counts per day)			
Sprints*	**347 ± 310**	**64 ± 140**†	**103 ± 143**†
Jumps*	**210 ± 360**	**0 ± 0**†	**0 ± 0**†

*Values reported as group means ± standard deviation. Bold type indicates significance with α = 0.05; *represents non-parametric Kruskal–Wallis testing and post-hoc Dunn testing where applicable; †represents values significantly different from EXE group value. Counts per group are interpolated over the 12 lighted hours.*

TABLE 2 | Tendon morphology and material properties.

	EXE	RES	RES-BTX
Body Mass (kg)	1.70 ± 0.14	1.65 ± 0.11	1.70 ± 0.20
Tarsometatarsus Length (mm)	77.7 ± 5.0	77.1 ± 3.2	78.7 ± 4.2
Achilles tendon length (L_0, mm)	38.2 ± 1.8	36.8 ± 5.4	37.9 ± 3.9
Average Achilles tendon CSA (mm^2)	5.63 ± 0.37	5.69 ± 0.53	5.53 ± 0.50
Functional stiffness (K_{func}, N/mm)	51.9 ± 6.92	51.83 ± 10.19	50.57 ± 10.32
Modulus of elasticity (E, MPa)	354.4 ± 61.2	342.3 ± 106.3	346.5 ± 69.4
Hysteresis (H)	0.24 ± 0.04	0.24 ± 0.04	0.23 ± 0.03

Values reported as group means ± standard deviation.

Regional Tendon Findings

Regional strain, minimum CSA, and tendon stress at the bone tendon-junction at 0.04 global strain did not pass criteria of normality and/or equal variance, and thus were analyzed using the Kruskal–Wallis tests (**Table 3**). Regional strain within each tendon specimen varied by up to 15% (**Figure 5**). Regional strain experienced by the thinnest portion of each sample (i.e., the bone-tendon junction region) when global strain was equal to 0.04 were not statistically different between groups ($p = 0.608$, E.S. = −0.057; **Figure 8**). CSA for the thinnest portion of each sample was 2.8% greater for RES animals and 13.7% smaller for RES-BTX animals when compared to EXE animals, but this was not a statistically significant difference ($p = 0.099$, E.S. = 0.115). Tendon stress at the bone tendon-junction at 0.04 global strain was 4.65% less for RES-BTX animals and 25.13% greater for RES animals when compared to EXE animals, but neither was this difference statistically significant ($p = 0.570$, E.S. = 0.025; **Figure 8**).

Our surface-marker to pin-marker test found that the two techniques are comparable. The techniques showed an average difference in maximal strain of the tendon region of 0.00110 ± 0.00025. This small difference equates to an approximately 5% difference between the techniques, indicating that the surface marker strain is similar to mid-substance strain.

DISCUSSION

The goal of this study was to examine developmental plasticity of growing tendon. Contrary to our hypotheses, the spring-like

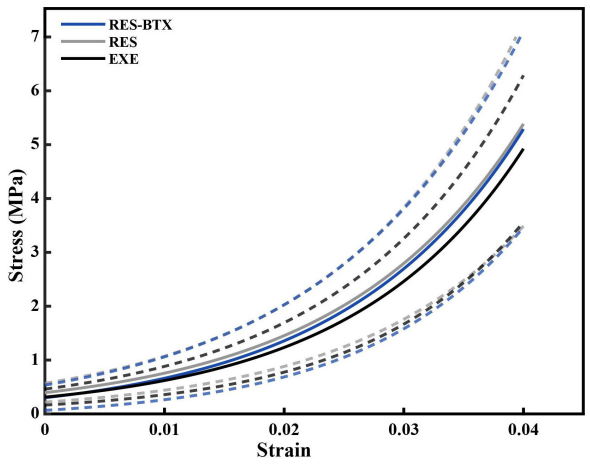

FIGURE 5 | Average stress-strain curve of the loading portion of the load cycle, by condition. Averages were calculated by fitting an exponential curve, Stress = $Ae^{B\times Strain}$ to each of the last five loading cycles up to 0.04 strain for each tendon. The constants A and B from the fitted exponential equations of the five loading cycles were averaged for each specimen, and used to generate individual curves that could be averaged across the groups (solid lines). Dashed lines indicate one standard deviation above and below the mean for each condition. Gray (RES) and blue (RES-BTX) curves were superimposed and for clarity, RES-BTX curves have been globally offset by 0.1 MPa.

characteristics of the free tendon and the bone-tendon junction were unaffected both after restricting high-intensity exercise and after restricting high-intensity exercise and additional chronic administration of botulinum toxin across the growth period. These results suggest that tendon properties, at least in the bird species studied here, may be resilient to variations in load level during the growth period.

Tendon Response to Altered Growth Conditions

Stiffness, modulus and cross sectional area values of the free tendon in all groups are very close to the values reported for comparable control animals in a previous study of adult guinea fowl (stiffness: 51.9 ± 6.92 EXE from our study vs. 50.58 ± 10.62 N/mm, modulus: 354.4 ± 61.2 EXE from our study vs. 338 ± 11 MPa, CSA: 5.63 ± 0.37 EXE from our study vs. 6.45 ± 0.30 mm^2; Buchanan and Marsh, 2001). These values are similar, despite the differences between the *in vivo* experimental techniques used to test tendon mechanics by Buchanan and Marsh (2001) and the explanted material testing methods adopted here.

Unlike the marked increase in stiffness and modulus resulting from running exercise in adult animals (Buchanan and Marsh, 2001), we did not observe tendon adaptation as a result of restricting movement or BTX-A administration in growing animals. While very little difference in tendon properties was observed between groups, there was variation in tendon stiffness within each group (**Figure 5**). In each group this variation is accounted for primarily by tendon modulus rather than tendon CSA, further indicating that the mechanical characteristics of the tendon remained similar across groups.

The similarity of tendon properties across groups is surprising considering the difference in activity level of exercised birds which engaged in substantially more daily high-intensity movements (jumping, running) than the restricted birds. These high-intensity movements are known to generate considerably higher tendon loading than those observed during walking and standing. In particular, landing from perches is expected to result in considerable eccentric muscle force. Indeed, on a daily basis, the EXE group performed approximately 210 perch jumps/landings and 347 running maneuvers. In contrast, jumping and landing was completely absent in the RES and RES-BTX animals and running maneuvers were considerably lower. It is difficult to know how this load reduction treatment compares to that applied in the previous growth study of domestic fowl by Nakagaki et al. (2007). These authors did not report specific activity levels of their groups, but attributed lower tendon stiffness in caged animals (compared to pen-reared animals) to the inability of these animals to engage in spontaneous running exercise. The change in tendon load stimulus between the EXE and both the RES and RES-BTX groups is arguably greater than the twice-weekly resistance training intervention shown to induce Achilles tendon adaptation over a 10-week

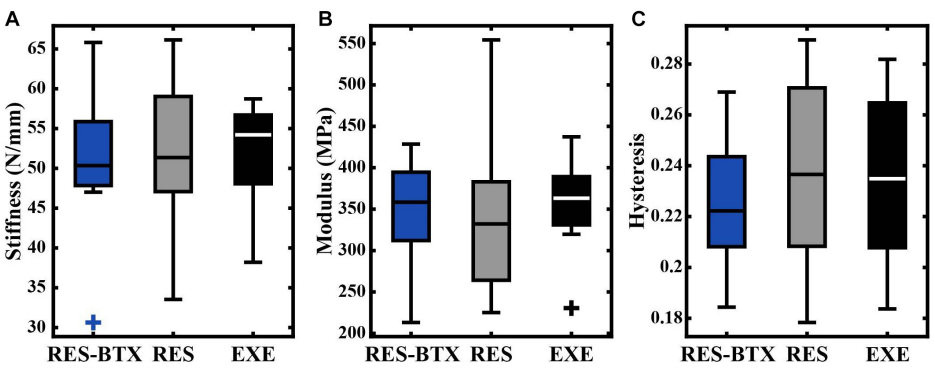

FIGURE 6 | Boxplots of **(A)** stiffness (N/mm), **(B)** modulus (MPa), and **(C)** hysteresis by condition. Crosses (+) indicate values that are outside 1.5 times the interquartile range above the upper quartile and below the lower quartile. No significant differences were found between groups.

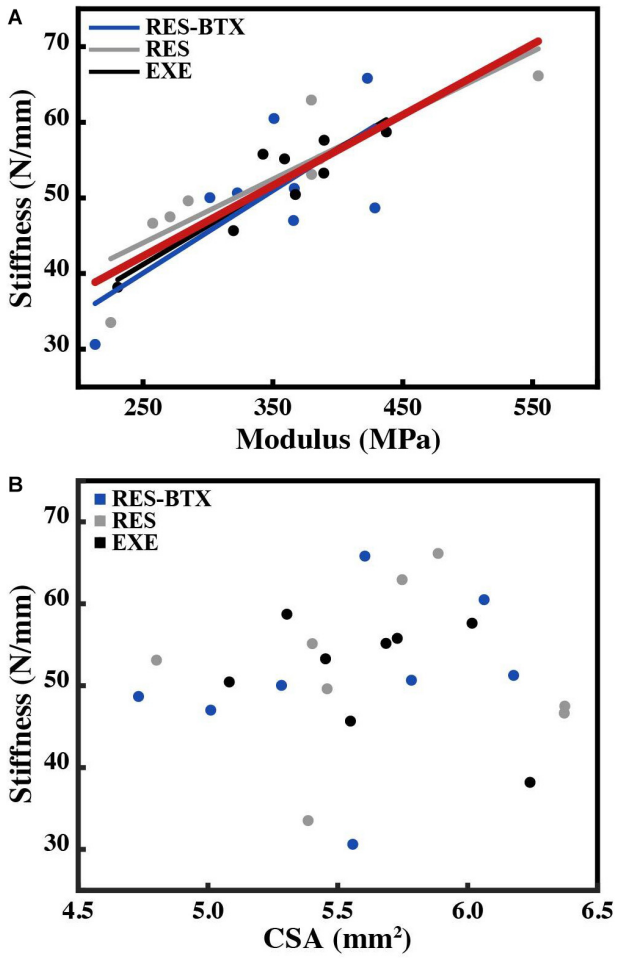

FIGURE 7 | Plot of **(A)** tendon stiffness vs. tendon modulus, with lines of best fit by group and for all animals (red) and **(B)** tendon stiffness vs. average tendon cross-sectional area (CSA, mm^2). Tendon stiffness across all animals correlates with modulus ($R^2 = 0.743$, $p < 0.01$), and not with average tendon cross-sectional area ($R^2 = 0.007$, $p = 0.698$).

TABLE 3 | Bone-tendon junction morphology and material properties.

	EXE	RES	RES-BTX
Strain at BTJ*	0.03 ± 0.03	0.03 ± 0.02	0.04 ± 0.02
Minimum Achilles tendon CSA (mm^2)*	2.48 ± 0.48	2.14 ± 0.38	2.55 ± 0.29
Stress at BTJ (N/mm^2)*	12.89 ± 3.38	16.13 ± 5.60	12.83 ± 4.74

*Values reported as group mean ± standard deviation. *Represents non-parametric Kruskal–Wallis testing and post-hoc Dunn testing where applicable.*

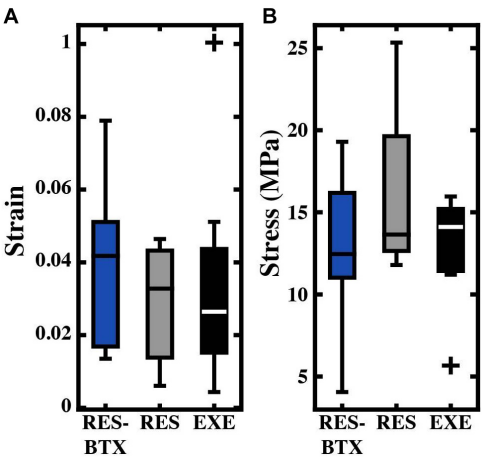

FIGURE 8 | Boxplots of **(A)** strain (mm/mm) and **(B)** stress (MPa) by condition for the bone-tendon junction region. Crosses (+) indicate values that are outside 1.5 times the interquartile range above the upper quartile and below the lower quartile. Values used were taken when the total tendon strain equaled 0.04. No significant differences were found between groups.

period in children (Waugh et al., 2014). Comparing our study to short-term exercise interventions is nevertheless difficult for several reasons. First, these studies are increasing as opposed to decreasing a baseline tendon load. Secondly, while they are conducted during development, these studies comprise a very small portion of the individuals' growth span, and therefore do not capture the prominent remodeling of tendon associated with growth (Curwin et al., 1994; Wren et al., 1997; Waugh et al., 2012; Mersmann et al., 2017b).

The lack of tendon plasticity in the RES-BTX group is also surprising considering muscle paralysis and tendon unloading is typically expected after botulinum toxin treatment (Longino et al., 2005; Schwartz et al., 2013). Unlike previous investigators, we administered BTX-A bilaterally, preventing single-leg unweighting known to occur in some quadrupedal rodent model studies (Longino et al., 2005; Fortuna et al., 2015). It is possible, therefore, that by maintaining their bipedal stance and gait the guinea fowl in this study maintained loading of their gastrocnemius muscles to some degree. Alternatively, passive muscle force might have been developed if the gastrocnemius muscles were maintained at longer lengths. Either of these scenarios may have mitigated the stress shielding we had expected from our BTX-A treatment. After BTX-A injections, we observed qualitatively a short-term (1–2 days) reduction in standing and an affected gait (especially in younger animals). However, posture and gait quickly returned to normal, consistent with the notion of a muted BTX-A effect. It is also important to note that other analyses of chronic BTX-A treatment in growing animals have also resulted in minimal changes to tendon properties (Eliasson et al., 2007). This may indicate a different BTX-A response in rapidly growing animals compared to mature animals or human children (e.g., cerebral palsy treatment) who have slower growth rates.

What Can Explain the Lack of Tendon Plasticity Across the EXE, RES, and RES-BTX Groups?

We suggest that the results of this study can best be explained if we reject the hypothesis that there is a constant load-dependent relationship between the external load level and tendon stiffness during growth. Instead, our results are consistent with the theory

that there are lower and upper thresholds of external load stimulus necessary to induce a plastic response (**Figure 9**). It has been suggested that a threshold of tendon connective tissue strain exists below which a catabolic response is initiated (Brown et al., 1998; Lavagnino and Arnoczky, 2005; Arampatzis et al., 2007). *In vitro* studies have shown that this lower homeostatic strain limit can be as little as 0.025 (Nirmalanandhan et al., 2008) or 0.01 if the appropriate strain frequency is applied (Lavagnino et al., 2003). Similarly, protection against tendon degradation due to immobilization, including a reduction in modulus, has been shown to occur *in vitro* if loads as low as 1 MPa are maintained (Hannafin et al., 1995; Arnoczky et al., 2003). In our study, all groups had an equal amount of low-intensity exercise, but standing and walking comprised the majority of the daily activity (**Table 1**). Surprisingly, even BTX-A administration did not alter the amount of time spent standing and walking, and for reasons explained above, BTX-A animals might have loaded their tendons during these activities. We posit this frequent low-intensity loading could surpass the relatively low stress and strain thresholds that have been proposed for inhibiting tendon degradation (low threshold in **Figure 9**). Although we do not have *in vivo* experimental values for tendon stress or strain, or the relative intensity of the muscle-tendon load, muscle data provided in Cox et al. (2019) allow for simple estimates of these parameters. Using the maximum isometric force (F_{max}) of the gastrocnemius muscles (scaled to body mass) and their pennation angles, we can predict a theoretical maximal force in the Achilles tendon. The level of activation (A, scaled from 0 to 100%) required to generate 1 MPa tendon stress can subsequently be predicted from a simple linear activation-force relationship and the tendon CSA_{avg} from the experimental animals:

$$A = \frac{1\text{MPa} \cdot CSA_{avg}}{F_{max}}$$

where the CSA_{avg} is taken as the average value from the three experimental groups. This prediction yields an activation level of 4% required by the gastrocnemius muscles to generate 1 Mpa stress in the Achilles tendon. This equation does not take into account force reductions due to dynamic force-length and force-velocity affects. If we assume these losses were as high as 50%, we predict an activation level of 8%. Even this upward adjustment in activation level is likely achieved in standing, and surpassed in walking, based on experimental muscle activity and blood flow measurements (Daley and Biewener, 2003; Marsh et al., 2004). Thus, if the lower threshold for tendon maintenance is low, as *in vitro* data indicate, the animals in this study may have readily met this threshold. In fact, an experimental *in vivo* activation level of 38% has been reported for walking guineafowl (Daley and Biewener, 2003). Furthermore, linking the *in vivo* forces measured during walking in this study with the reported tendon CSA yields a stress of 4.6 MPa in the lateral gastrocnemius tendon (Daley and Biewener, 2003). Thus, the stress in the Achilles tendon may have well exceeded 1 MPa during much of the daily activity in this study. It is also notable that a stress of 1 MPa in the tendons analyzed in this study will generate strains in excess of 0.01 (**Figure 4**).

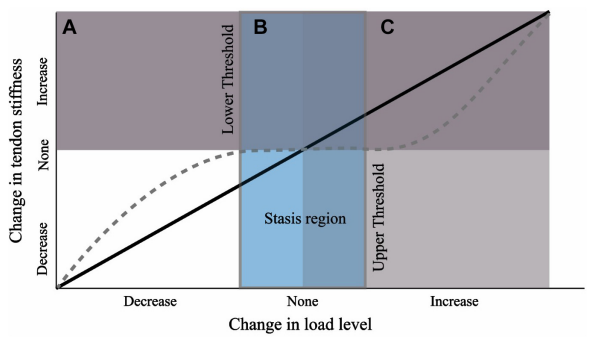

FIGURE 9 | Hypothesis for tendon response to a change in load level during growth from a nominal baseline value. Black line depicts a linear relationship. We propose the response curve may more closely resemble the dashed gray curve where a threshold of change in load must be crossed before triggering a plastic response. The wide stasis region may result due to a strong load-independent biological growth component (e.g., biological growth factors).

An unexpected conclusion arising from this study, therefore, is that tendon appears to continue to develop and is resilient to altered external load levels so long as a minimum threshold of tendon load is maintained. A similar view of load-resilient tendon growth was proposed by Eliasson et al. (2007) in their study of Achilles tendon response to chronic BTX-A treatment in growing rats. These authors likewise found no changes in Achilles stiffness and strength and proposed that during the growth period, tendon size and strength are under systemic control and that there is a lower-bound threshold of tendon loading that, if surpassed, permits tendon maintenance.

A baseline of low-intensity activity might also help explain the discrepancy between our results and those of Nakagaki et al. (2007), who reported a reduction in Achilles tendon stiffness in their activity-restricted domestic fowl. Guinea fowl are game birds that, unlike domestic fowl, exhibit high activity levels even when space is restricted. Similar to other wild species of fowl (e.g., junglefowl; Dawkins, 1989), the percentage of time spent resting was very low in all groups and they were recorded walking approximately 25% of the observed time (**Table 1**). A rough estimate of the daily distance walked in our study (based on time spent walking and estimated speed of 0.5 m/s) is approximately 5.9 km per bird. In comparison, the time spent at rest (sitting) is approximately 60–70% in domestic fowl, with as little as 3–10% of time spent walking (Hansen, 1994; Cornetto and Estevez, 2001; Bizeray et al., 2002). Even in free-range housing, domestic fowl spend approximately 50% of the time at rest (Rodriguez-Aurrekoetxea et al., 2015). If the caged birds from the study of Nakagaki et al. (2007) were (presumably) more sedentary than our animals, they may not have reached a lower tendon load threshold required for tendon maintenance. As Woo et al. (1982) observed, extreme disuse has the potential to initiate a rapid decline in tendon properties. From this perspective, their findings might demonstrate a disuse response as opposed to changes in the tendon induced by high loads.

A potentially strong contributing factor to our proposed "mechanical threshold" hypothesis is non-mechanical mediated

growth. The lack of tendon adaptation between EXE and the other groups may arise because the load-independent biological component of tendon development overwhelmed the mechanobiological component (mechanically stimulated development; Wren et al., 1997). Tendon development has been shown to be under the control of several cellular and extracellular matrix signal pathways and growth factors (for reviews see Birk and Zycband, 1994; Gaut and Duprez, 2016). These biological components play a part in the marked alteration in tendon properties across the growth period; for example, as has been pointed out previously, a 40,000-fold increase in elastic modulus occurs between chick fetal tendon and adult tendon (Gaut and Duprez, 2016), and a 30-fold increase in chick tendon tensile strength has been reported over only a 2 week post-natal development period (Silver et al., 2003). If the tendon has a strong load-independent biological growth component, this might outweigh the mechanobiological response arising from altered exercise loads. Furthermore, growth-mediated mechanotransduction arising from changes in body weight may likewise dominate any remodeling signal arising from variation in external load (e.g., movement). Together, these growth-mediated factors may explain why the lower and upper threshold of external exercise load required for tendon remodeling in a growing animal maybe difficult to penetrate, resulting in a wide "stasis region" (**Figure 9**). This interpretation is consistent with another study that implemented long-term exercise training in growing horses (Kasashima et al., 2008). In that study, a baseline level of low-intensity activity appears to have been retained across the experimental and control groups (i.e., lower threshold for tendon maintenance is met) and in which the tendons of interest did not exhibit stiffness adaptations (i.e., upper threshold for tendon remodeling is not met).

A second possible explanation for the lack of tendon response in the EXE group is if the mechanical characteristics of the altered tendon load required for tissue adaptation were not met by our treatment. It is generally understood that strain-mediated mechanotransduction regulates tendon homeostasis (Wren et al., 2000; Arnoczky et al., 2002; Arampatzis et al., 2007). However, the characteristics of the applied strain, including the strain magnitude, strain duration and repetitive strain rate influence tendon adaptation (Arnoczky et al., 2002; Yamamoto et al., 2005; Arampatzis et al., 2007; Bohm et al., 2014). Studies of increased loading on intact human Achilles tendon indicate that the most pronounced tendon remodeling occurs under both large strain magnitudes and long strains durations, with a lack of adaptation at low strains (Arampatzis et al., 2007, 2010). A similar reliance on strain magnitude for tendon adaptation has been observed in *in vitro* studies of both tendon load depravation and load augmentation (Arnoczky et al., 2002; Nirmalanandhan et al., 2008; Wang et al., 2013, 2015). The high-intensity activities undertaken by the EXE group, in particular jumping and landing, generate large Achilles forces and strains in guinea fowl and other ground birds (Henry et al., 2005; Konow et al., 2012; Arellano et al., 2019). The duration of the strain application is also long in these movements, allowing for tendon pre-stretch in jumping and energy damping during landing (Roberts and Azizi, 2011; Roberts, 2016). This suggests that the removal of these high-intensity activities in the RES and RES-BTX groups may have been well suited for inducing tendon adaptation (i.e., reduced cross-sectional area, stiffness, modulus or hysteresis). It is also plausible that it is only an increase in strain and strain duration that leads to tendon adaptation, whereas a large reduction in strain and strain duration from normal habitual movements (predicted in the RES and RES-BTX groups in this study) does not. Furthermore, data from human training studies indicate that repetitive loading may be required for Achilles tendon adaptation (Bohm et al., 2014). It remains possible that removal of repetitive loading, in particular, is also required to induce an unloading response in the tendon. The high-intensity activities in the EXE occurred intermittently, possibly minimizing the effectiveness of removing these loads in the RES and RES-BTX groups for generating an adaptive stimulus.

Functional Implications of Unaltered Tendon Mechanical Properties

The Achilles tendon is essential for elastic energy storage and return, as well as for amplifying power production in acceleration movements and assisting energy dissipation during landing (Roberts and Azizi, 2011; Roberts, 2016). Our data indicate that these functions are likely unaltered between our experimental groups, although how the tendon interacts with other possible modifications in other tissues, for example muscle, is not known. Our previous companion study on the same EXE and RES animals found that the allowance of high-intensity movements over the growth period resulted in greater maximum center of mass vertical jump velocity and peak jump force, work, and power once the animals reached adult age (Cox et al., 2020). Despite functional differences, the amount of extensor muscle mass, including that of the gastrocnemius muscles, was not different between groups. This led to the conclusion that neural factors, rather than muscle adaptation, might be more closely associated with the improved performance in the EXE group. Our data showing unaltered Achilles tendon properties between the EXE and RES group further supports this conclusion.

Unlike the studies of Eliasson et al. (2007) and Khayyeri et al. (2017), we did not observe any effect on tendon hysteresis. This finding implies that, not only is the capacity for tendon elastic energy storage likely unaltered (if tendon stiffness is unaltered), but that the amount of energy returned in cyclical loading is likely also unaffected by loading history during growth. These data help toward a mechanistic explanation for the similar energy cost of steady-state running between EXE and RES birds reported in Cox et al. (2020). Energy recycling in tendon, in particular the Achilles tendon, has been proposed as a major factor determining locomotor energetics, including in running birds and other animals (Biewener and Baudinette, 1995; Roberts et al., 1997; Lichtwark and Wilson, 2008; Roberts, 2016). It follows that if this property is unaffected during growth that adult running economy may also remain unchanged. It is, however, of note that the hysteresis values recorded in this study are relatively high compared to many other tendons reported in the literature [see for example Bennett et al. (1986) and the summary by Finni et al. (2012)]. High hysteresis values may exacerbate tendon hyperthermia (Wilson and Goodship, 1994). Other factors, such

as heat dissipation and cell heat tolerance (Birch et al., 1997) may also need to be considered to understand whether the high hysteresis affects tendon damage in guineafowl. Also, while the classic view is that tendon has a hysteresis of less than 10%, there are several examples of tendon having higher hysteresis values in both humans (Finni et al., 2012) and other species (Shadwick, 1990; Pollock and Shadwick, 1994 (see select species); Vereecke and Channon, 2013). Finally, we cannot rule out the possibility that our methodological approach resulted in a higher hysteresis than what occurs *in vivo*. For example, it is possible that if the entire tendon-aponeurosis complex was tested, or if a more realistic strain rate or loading duration was used, that we would observe lower hysteresis values.

Our results also suggest that tendon strength may have been unaltered across groups. The bone-tendon junction has previously been identified as the point of failure in other studies of tendon mechanics (Jack, 1950; Woo et al., 1983; Woo and Buckwalter, 1988; Jarvinen, 1992; Wren et al., 2001, 2003). Consistent with these studies, the region at the Achilles bone-tendon junction in the guinea fowl has the smallest cross-sectional area and is thus susceptible to the highest stress. The absence of changes to the material or geometric properties at the bone tendon junction suggests tendon strength may have been preserved across groups (experimental failure mechanics were not investigated in this study). The safety factor of the tendon may therefore be relatively higher in the RES and RES-BTX groups that do not engage in high-intensity movements. Interestingly, a lack of modulation in tendon safety factor indicates less economical use of tissue in the RES and RES-BTX groups (Alexander, 1981; Gosline, 1992), but supports the hypothesis that tendon growth is under systemic control (Eliasson et al., 2007).

Finally, our data have implications for both broader evolutionary aspects of musculoskeletal plasticity and for human musculoskeletal health. A tendon relatively insensitive to growth-period loading history may present a selective advantage, as sudden, unpredictable changes in environment will not change the tendon's mechanical and functional growth trajectory. This may be especially effective in fast growing species, such as birds. The evolutionary adaptive consequences of tendon plasticity are nevertheless complex and other non-adaptive scenarios may also be applicable. Our data could also be taken as a sign that maintaining a minimum load threshold could be an important goal for preserving proper tendon growth and health. For example, the lack of tendon adaptation seen here indicate a lower sensitivity to disuse compared to muscle, and may help guide studies addressing the relative responsiveness of these tissues to disuse and movement function (Mersmann et al., 2017b). However, we caution against making direct inferences to human development, and rather see our data as hypothesis-generative.

Limitations

The results of this study suggest that, contrary to the intention of our experimental design, Botulinum toxin may not have induced considerable further tendon unloading beyond that due to restricted movement alone. We observed qualitative changes in the animals' posture and time spent standing in the 2 days immediately post injection when animals were housed in cages for observation, but we did not record specific movement behavior or mechanics. These deficiencies, however, rapidly diminished and movement returned to normal when the animals were returned to pen housing as indicated by our movement scores. To test the efficacy of Botulinum toxin in adults of this species, we also performed BTX-A injections in a group of adult animals that were part of a separate study. In these animals we observed a marked reduction in movement ability, including a loss of jumping behavior. Detailed measurements of the physiological effect of BTX-A-induced paralysis were, nevertheless, not performed in the present study. For example, we do not have electromyography recordings, reflex tests or data on the amount of force reduction in the tendon post BTX-A injections that could validate the BTX-A treatment. As discussed previously, it therefore remains possible that over the course of the growth period the average tendon loading was not greatly reduced below that of the RES group.

This study measured the material properties of the free tendon, but this may not fully capture variations in elasticity in this muscle-tendon unit. These properties matched very closely the properties measured by Buchanan and Marsh (2001), despite their use of a different *in vivo* technique that incorporated the free tendon and aponeurosis. Nevertheless, aponeurosis strain has been shown to be an important component of tendon strain (Roberts et al., 1997; Arellano et al., 2019) and dynamic changes in aponeurosis strain has been shown to modulate overall tendon stiffness *in vivo* (Azizi and Roberts, 2009; Arellano et al., 2019). Further analyses incorporating material properties of the aponeurosis might reveal load-induced plasticity over the growth period different to those reported here. We also did not experimentally test tendons to failure. While our measurements of the bone-tendon junction provide indirect information relevant to tendon strength, experimental measurements of tendon failure might reveal differences not observed in the present study.

Findings from this study are based on linking average group movement and tendon material data. Our methods did not permit us to link an individual bird's movement data to its corresponding tendon material properties. It is likely that activity levels varied between animals, and that this contributed to variation in tendon properties that we could not account for. However, as our previous study (Cox et al., 2020) found, the marked restriction in high-intensity activities resulted in a reduction in jumping performance in the same animals as in this study, indicating that the treatment did alter locomotor function, but not the properties of the Achilles tendon as determined from our group average comparisons.

Finally, we caution against making direct comparisons to human tendon growth and plasticity. The guinea fowl provide a valuable model for tendon loading and growth. In particular, their bipedal gait result in limb loading characteristics that have many similarities to humans (Rubenson and Marsh, 2009; Rubenson et al., 2010). This overcomes some of the limitations of using quadrupedal rodent models in musculoskeletal research (Hu et al., 2017). There are other physiological characteristics of our fowl model that might affect comparisons to humans; in

particular, their very rapid growth might result in a different tendon response to altered load compared to that of the relatively slower postnatal development of humans.

Here we aimed to help resolve the effect of unloading on tendon by implementing a scope of altered tendon load across the entire growth span in an avian bipedal model. In conclusion, we found the growing Achilles tendon in guinea fowl insensitive to variations in disuse stimuli. A lack of change in stiffness or modulus suggest thresholds of load variation exists that must be surpassed to induce mechanical adaptation to the growing tendon.

DATA AVAILABILITY STATEMENT

The data are available from the Penn State University data repository site, ScholarSphere https://doi.org/10.26207/v5gr-7e21.

ETHICS STATEMENT

The animal study was reviewed and approved by The Pennsylvania State University Institutional Animal Care and Use Committee.

AUTHOR CONTRIBUTIONS

KK, SC, MS, TR, SP, and JR contributed to the conception and design of the study. KK, SC, MS, AD, MH, TN, and JR developed the methodologies and collected the data. KK, SC, MS, and JR analyzed the data and contributed to figure preparation. KK and JR drafted the initial manuscript. All authors contributed to the manuscript drafting and editing. All authors contributed critically to the data interpretation and approved the final manuscript.

FUNDING

This study was supported in part through a seed grant from the Center for Human Evolution and Diversity, The Pennsylvania State University, and through the National Institute of Arthritis and Musculoskeletal and Skin Diseases of the National Institutes of Health under grant number R21AR071588. The content is solely the responsibility of the authors of this paper, and does not necessarily represent the views of the National Institutes of Health.

ACKNOWLEDGMENTS

We would like to thank Justin Csaszar and the Animal Care Staff at The Pennsylvania State University Centralized Biological Laboratory. We would also like to thank Randy McCullough for his assistance in building the custom apparatus for testing tendon material properties, and Ian Dechene for his assistance in collecting data and creating figures.

REFERENCES

Alexander, R. M. (1981). Factors of safety in the structure of animals. *Sci. Prog.* 67, 109–130.

Arampatzis, A., Karamanidis, K., and Albracht, K. (2007). Adaptational responses of the human achilles tendon by modulation of the applied cyclic strain magnitude. *J. Exp. Biol.* 210, 2743–2753. doi: 10.1242/jeb.003814

Arampatzis, A., Peper, A., Bierbaum, S., and Albracht, K. (2010). Plasticity of human achilles tendon mechanical and morphological properties in response to cyclic strain. *J. Biomech.* 43, 3073–3079. doi: 10.1016/j.jbiomech.2010.08.014

Arellano, C. J., Konow, N., Gidmark, N. J., and Roberts, T. J. (2019). Evidence of a tunable biological spring: elastic energy storage in aponeuroses varies with transverse strain in vivo. *Proc. R. Soc. B Biol. Sci.* 286, 3–8. doi: 10.1098/rspb.2018.2764

Arnoczky, S. P., Tian, T., Lavagnino, M., and Gardner, K. (2003). Ex vivo static tensile loading inhibits MMP-1 expression in rat tail. *J. Orthop. Res.* 22, 328–333.

Arnoczky, S. P., Tian, T., Lavagnino, M., Gardner, K., Schuler, P., and Morse, P. (2002). Activation of stress-activated protein kinases (SAPK) in tendon cells following cyclic strain: the effects of strain frequency, strain magnitude, and cytosolic calcium. *J. Orthop. Res.* 20, 947–952. doi: 10.1016/S0736-0266(02)00038-34

Azizi, E., and Roberts, T. J. (2009). Biaxial strain and variable stiffness in aponeuroses. *J. Physiol.* 587, 4309–4318. doi: 10.1113/jphysiol.2009.173690

Bennett, M. B., Ker, R. F., Dimery, N. J., and Alexander, R. M. (1986). Mechanical properties of various mammalian tendons. *J. Zool.* 209, 537–548.

Biewener, A. A., and Baudinette, R. V. (1995). In vivo muscle force and elastic energy storage during steady-speed hopping of tammar wallabies (*Macropus eugenii*). *J. Exp. Biol.* 198, 1829–1841.

Birch, H. L., Wilson, A. M., and Goodship, A. E. (1997). The effect of exercise-induced localised hyperthermia on tendon cell survival. *J. Exp. Biol.* 200, 1703–1708.

Birk, D. E., and Zycband, E. (1994). Assembly of the tendon extracellular matrix during development. *J. Anat.* 184(Pt 3), 457–463.

Bizeray, D., Estevez, I., Leterrier, C., and Faure, J. M. (2002). Effects of increasing environmental complexity on the physical activity of broiler chickens. *Appl. Anim. Behav. Sci.* 79, 27–41. doi: 10.1016/S0168-1591(02)00083-87

Bohm, S., Mersmann, F., and Arampatzis, A. (2015). Human tendon adaptation in response to mechanical loading: a systematic review and meta-analysis of exercise intervention studies on healthy adults. *Sport. Med. - Open* 1:7. doi: 10.1186/s40798-015-0009-9

Bohm, S., Mersmann, F., Tettke, M., Kraft, M., and Arampatzis, A. (2014). Human Achilles tendon plasticity in response to cyclic strain: effect of rate and duration. *J. Exp. Biol.* 217, 4010–4017. doi: 10.1242/jeb.112268

Brown, R. A., Prajapati, R., McGrouther, D. A., Yannas, I. V., and Eastwood, M. (1998). Tensional homeostasis in dermal fibroblasts: mechanical responses to mechanical loading in three-dimensional substrates. *J. Cell. Physiol.* 175, 323–332.

Buchanan, C. I., and Marsh, R. L. (2001). Effects of long-term exercise on the biomechanical properties of the achilles tendon of guinea fowl. *J. Appl. Physiol.* 90, 164–171. doi: 10.1152/jappl.2001.90.1.164

Charcharis, G., Mersmann, F., Bohm, S., and Arampatzis, A. (2019). Morphological and mechanical properties of the quadriceps femoris muscle-tendon unit from adolescence to adulthood: effects of age and athletic training. *Front. Physiol.* 10:1–12. doi: 10.3389/fphys.2019.01082

Cornetto, T., and Estevez, I. (2001). Behavior of the domestic fowl in the presence of vertical panels. *Poult. Sci.* 80, 1455–1462. doi: 10.1093/ps/80.10.1455

Cox, S. M., Easton, K. L., Lear, M. C., Marsh, R. L., Delp, S. L., and Rubenson, J. (2019). The interaction of compliance and activation on the force-length operating range and force generating capacity of skeletal muscle: a computational study using a guinea fowl musculoskeletal model. *Integr. Org. Biol.* 1:obz022.

Cox, S. M., Salzano, M. Q., Piazza, S. J., and Rubenson, J. (2020). Eliminating high-intensity activity during growth reduces mechanical power capacity but

not submaximal metabolic cost in a bipedal animal model. *J. Appl. Physiol.* 128, 50–58. doi: 10.1152/japplphysiol.00679.2019

Curwin, S. L., Roy, R. R., and Vailas, A. C. (1994). Regional and age variations in growing tendon. *J. Morphol.* 221, 309–320. doi: 10.1002/jmor.1052210306

Curwin, S. L., Vailas, A. C., and Wood, J. (1988). Immature tendon adaptation to strenuous exercise. *J. Appl. Physiol.* 65, 2297–2301. doi: 10.1152/jappl.1988.65.5.2297

Daley, M. A., and Biewener, A. A. (2003). Muscle force-length dynamics during level versus incline locomotion: a comparison of in vivo performance of two guinea fowl ankle extensors. *J. Exp. Biol.* 206, 2941–2958. doi: 10.1242/jeb.00503

Dawkins, M. S. (1989). Time budgets in red junglefowl as a baseline for the assessment of welfare in domestic fowl. *Appl. Anim. Behav. Sci.* 24, 77–80.

Dunn, O. J. (1964). Multiple comparisons using rank sums. *Technometrics* 6, 241–252.

Eliasson, P., Fahlgren, A., Pasternak, B., and Aspenberg, P. (2007). Unloaded rat achilles tendons continue to grow, but lose viscoelasticity. *J. Appl. Physiol.* 103, 459–463. doi: 10.1152/japplphysiol.01333.2006

Finni, T., Peltonen, J., Stenroth, L., and Cronin, N. J. (2012). Viewpoint: on the hysteresis in the human achilles tendon. *J. Appl. Physiol.* 114, 515–517. doi: 10.1152/japplphysiol.01005.2012

Fortuna, R., Vaz, M. A., Sawatsky, A., Hart, D. A., and Herzog, W. (2015). A clinically relevant BTX-A injection protocol leads to persistent weakness, contractile material loss, and an altered mRNA expression phenotype in rabbit quadriceps muscles. *J. Biomech.* 48, 1700–1706. doi: 10.1016/j.jbiomech.2015.05.018

Gaut, L., and Duprez, D. (2016). Tendon development and diseases. *Wiley Interdiscip. Rev. Dev. Biol.* 5, 5–23. doi: 10.1002/wdev.201

Gosline, J. M. (1992). "Efficiency and other criteria for evaluating the quality of structural biomaterials," in *Efficiency and Economy in Animal Physiology*, ed. R. Blake (Cambridge: Cambridge University Press), 43–64. doi: 10.1017/CBO9780511565588

Guthold, R., Stevens, G. A., Riley, L. M., and Bull, F. C. (2020). Global trends in insufficient physical activity among adolescents: a pooled analysis of 298 population-based surveys with 1·6 million participants. *Lancet Child Adolesc. Heal.* 4, 23–35. doi: 10.1016/S2352-4642(19)30323-30322

Hannafin, J. A., Arnoczky, S. P., Hoonjan, A., and Torzilli, P. A. (1995). Effect of stress deprivation and cyclic tensile loading on the material and morphologic properties of canine flexor digitorum profundus tendon: an in vitro study. *J. Orthop. Res.* 13, 907–914. doi: 10.1002/jor.1100130615

Hansen, I. (1994). Behavioural expression of laying hens in aviaries and cages: frequencies, time budgets and facility utilisation. *Br. Poult. Sci.* 35, 491–508. doi: 10.1080/00071669408417715

Henry, H. T., Ellerby, D. J., and Marsh, R. L. (2005). Performance of guinea fowl *Numida meleagris* during jumping requires storage and release of elastic energy. *J. Exp. Biol.* 208, 3293–3302. doi: 10.1242/jeb.01764

Hu, X., Charles, J. P., Akay, T., Hutchinson, J. R., and Blemker, S. S. (2017). Are mice good models for human neuromuscular disease? comparing muscle excursions in walking between mice and humans. *Skelet. Muscle* 7:26. doi: 10.1186/s13395-017-0143-149

Jack, E. A. (1950). Experimental rupture of the medial collateral ligament of the knee. *J. Bone Joint Surg. Br.* 32 B, 396–402. doi: 10.1302/0301-620X.32B3.396

Jarvinen, M. (1992). Epidemiology of tendon injuries in sport. *Clin. Sport Med.* 11, 493–504.

Kalkman, B. M., Holmes, G., Bar-On, L., Maganaris, C. N., Barton, G. J., Bass, A., et al. (2019). Resistance training combined with stretching increases tendon stiffness and is more effective than stretching alone in children with cerebral palsy: a randomized controlled trial. *Front. Pediatr.* 7:333. doi: 10.3389/fped.2019.00333

Kasashima, Y., Takahashi, T., Birch, H. L., Smith, R. K. W., and Goodship, A. E. (2008). Can exercise modulate the maturation of functionally different immature tendons in the horse? *J. Appl. Physiol.* 104, 416–422. doi: 10.1152/japplphysiol.00379.2007

Khayyeri, H., Blomgran, P., Hammerman, M., Turunen, M. J., Löwgren, A., Guizar-Sicairos, M., et al. (2017). Achilles tendon compositional and structural properties are altered after unloading by botox. *Sci. Rep.* 7:13107. doi: 10.1038/s41598-017-13107-13107

Konow, N., Azizi, E., and Roberts, T. J. (2012). Muscle power attenuation by tendon during energy dissipation. *Proc. R. Soc. B Biol. Sci.* 279, 1108–1113. doi: 10.1098/rspb.2011.1435

Lavagnino, M., and Arnoczky, S. P. (2005). In vitro alterations in cytoskeletal tensional homeostasis control gene expression in tendon cells. *J. Orthop. Res.* 23, 1211–1218. doi: 10.1016/j.orthres.2005.04.001

Lavagnino, M., Arnoczky, S. P., Tian, T., and Vaupel, Z. (2003). Effect of amplitude and frequency of cyclic tensile strain on the inhibition of MMP-1 mRNA expression in tendon cells: an in vitro study. *Connect. Tissue Res.* 44, 181–187. doi: 10.1080/713713679

Lichtwark, G. A., and Wilson, A. M. (2008). Optimal muscle fascicle length and tendon stiffness for maximising gastrocnemius efficiency during human walking and running. *J. Theor. Biol.* 252, 662–673. doi: 10.1016/j.jtbi.2008.01.018

Longino, D., Frank, C., Leonard, T. R., Vaz, M. A., and Herzog, W. (2005). Proposed model of botulinum toxin-induced muscle weakness in the rabbit. *J. Orthop. Res.* 23, 1411–1418. doi: 10.1016/j.orthres.2005.02.016

Lüdecke, D. (2019). *sjstats: Statistical Functions for Regression Models*. http://doi.org/10 10.5281/ZENODO.1489175.

Magnusson, S. P., Narici, M. V., Maganaris, C. N., and Kjaer, M. (2008). Human tendon behaviour and adaptation, in vivo. *J. Physiol.* 586, 71–81. doi: 10.1113/jphysiol.2007.139105

Marsh, R. L., Ellerby, D. J., Carr, J. A., Henry, H. T., and Buchanan, C. I. (2004). Partitioning the energetics of walking and running: swinging the limbs is expensive. *Science* 303, 80–83. doi: 10.1126/science.1090704

Mersmann, F., Bohm, S., and Arampatzis, A. (2017a). Imbalances in the development of muscle and tendon as risk factor for tendinopathies in youth athletes: a review of current evidence and concepts of prevention. *Front. Physiol.* 8:987. doi: 10.3389/fphys.2017.00987

Mersmann, F., Bohm, S., Schroll, A., Boeth, H., Duda, G. N., and Arampatzis, A. (2017b). Muscle and tendon adaptation in adolescent athletes: a longitudinal study. *Scand. J. Med. Sci. Sport* 27, 75–82. doi: 10.1111/sms.12631

Mersmann, F., Bohm, S., Schroll, A., Marzilger, R., and Arampatzis, A. (2016). Athletic training affects the uniformity of muscle and tendon adaptation during adolescence. *J. Appl. Physiol.* 121, 893–899. doi: 10.1152/japplphysiol.00493.2016

Miller, K. S., Connizzo, B. K., Feeney, E., Tucker, J. J., and Soslowsky, L. J. (2012). Examining differences in local collagen fiber crimp frequency throughout mechanical testing in a developmental mouse supraspinatus tendon model. *J. Biomech. Eng.* 134:041004. doi: 10.1115/1.4006538

Nakagaki, W. R., Biancalana, A., Benevides, G. P., and Gomes, L. (2007). Biomechanical and biochemical properties of chicken calcaneal tendon under effect of age and nonforced active exercise. *Connect. Tissue Res.* 48, 219–228. doi: 10.1080/03008200701492136

Nirmalanandhan, V. S., Shearn, J. T., Juncosa-Melvin, N., Rao, M., Gooch, C., Jain, A., et al. (2008). Improving linear stiffness of the cell-seeded collagen sponge constructs by varying the components of the mechanical stimulus. *Tissue Eng. - Part A.* 14, 1883–1891. doi: 10.1089/ten.tea.2007.0125

Pentidis, N., Mersmann, F., Bohm, S., Giannakou, E., Aggelousis, N., and Arampatzis, A. (2019). Triceps surae muscle-tendon unit properties in preadolescent children: a comparison of artistic gymnastic athletes and non-athletes. *Front. Physiol.* 10:615. doi: 10.3389/fphys.2019.00615

Pollock, C. M., and Shadwick, R. E. (1994). Relationship between body mass and biomechanical properties of limb tendons in adult mammals. *Am. J. Physiol. - Regul. Integr. Comp. Physiol.* 266, R1016–R1021. doi: 10.1152/ajpregu.1994.266.3.r1016

Prinzinger, R., Prebmar, A., and Schleucher, E. (1991). Body temperature in birds. *Comp. Biochem. Physiol. Part A: Physiol.* 99, 499–506. doi: 10.1016/0300-9629(91)90122-S

R Core Team (2016). *R: A Language and Environment for Statistical Computing*. Vienna, Austria: R Foundation for Statistical Computing.

Roberts, T. J. (2016). Contribution of elastic tissues to the mechanics and energetics of muscle function during movement. *J. Exp. Biol.* 219, 266–275. doi: 10.1242/jeb.124446

Roberts, T. J., and Azizi, E. (2011). Flexible mechanisms: the diverse roles of biological springs in vertebrate movement. *J. Exp. Biol.* 214, 353–361. doi: 10.1242/jeb.038588

Roberts, T. J., Marsh, R. L., Weyand, P. G., and Taylor, C. R. (1997). Muscular force in running turkeys: the economy of minimizing work. *Science* 275, 1113–1115. doi: 10.1126/science.275.5303.1113

Rodriguez-Aurrekoetxea, A., Leone, E. H., and Estevez, I. (2015). Effects of panels and perches on the behaviour of commercial slow-growing free-range meat chickens. *Appl. Anim. Behav. Sci.* 165, 103–111. doi: 10.1016/j.applanim.2015.02.004

Rubenson, J., Lloyd, D. G., Heliams, D. B., Besier, T. F., and Fournier, P. A. (2010). Adaptations for economical bipedal running: the effect of limb structure on three-dimensional joint mechanics. *J. R. Soc. interface* 8, 740–755.

Rubenson, J., and Marsh, R. L. (2009). Mechanical efficiency of limb swing during walking and running in guinea fowl (*Numida meleagris*). *J. Appl. Physiol.* 106, 1618–1630. doi: 10.1152/japplphysiol.91115.2008

Schmidt, E. C., Chin, M., Aoyama, J. T., Ganley, T. J., Shea, K. G., and Hast, M. W. (2019). Mechanical and microstructural properties of pediatric anterior cruciate ligaments and autograft tendons used for reconstruction. *Orthop. J. Sport. Med.* 7: 2325967118821667. doi: 10.1177/2325967118821667

Schwartz, A. G., Lipner, J. H., Pasteris, J. D., Genin, G. M., and Thomopoulos, S. (2013). Muscle loading is necessary for the formation of a functional tendon enthesis. *Bone* 55, 44–51. doi: 10.1016/j.bone.2013.03.010

Shadwick, R. E. (1990). Elastic energy storage in tendons: mechanical differences related to function and age. *J. Appl. Physiol.* 68, 1033–1040. doi: 10.1152/jappl.1990.68.3.1033

Silver, F. H., Freeman, J. W., and Seehra, G. P., (2003). Collagen self-assembly and the development of tendon mechanical properties. *J. Biomech.* 36, 1529–1553. doi: 10.1016/S0021-9290(03)00135-0

Stanley, R. L., Edwards, L. J., Goodship, A. E., Firth, E. C., and Patterson-Kane, J. C. (2008). Effects of exercise on tenocyte cellularity and tenocyte nuclear morphology in immature and mature equine digital tendons. *Equine Vet. J.* 40, 141–146. doi: 10.2746/042516408X266097

Vereecke, E. E., and Channon, A. J. (2013). The role of hind limb tendons in gibbon locomotion: springs or strings? *J. Exp. Biol.* 216, 3971–3980. doi: 10.1242/jeb.083527

Walsh, S., Frank, C., Shrive, N., and Hart, D. (1993). Knee immobilization inhibits biomechanical maturation of the rabbit medial collateral ligament. *Clin. Orthop. Relat. Res.* doi: 10.1097/00003086-199312000-00042

Wang, J. H. C. (2006). Mechanobiology of tendon. *J. Biomech.* 39, 1563–1582. doi: 10.1016/j.jbiomech.2005.05.011

Wang, T., Lin, Z., Day, R. E., Gardiner, B., Landao-Bassonga, E., Rubenson, J., et al. (2013). Programmable mechanical stimulation influences tendon homeostasis in a bioreactor system. *Biotechnol. Bioeng.* 110, 1495–1507. doi: 10.1002/bit.24809

Wang, T., Lin, Z., Ni, M., Thien, C., Day, R. E., Gardiner, B., et al. (2015). Cyclic mechanical stimulation rescues achilles tendon from degeneration in a bioreactor system. *J. Orthop. Res.* 33, 1888–1896. doi: 10.1002/jor.22960

Waugh, C. M., Blazevich, A. J., Fath, F., and Korff, T. (2012). Age-related changes in mechanical properties of the achilles tendon. *J. Anat.* 220, 144–155. doi: 10.1111/j.1469-7580.2011.01461.x

Waugh, C. M., Korff, T., Fath, F., and Blazevich, A. J. (2014). Effects of resistance training on tendon mechanical properties and rapid force production in prepubertal children. *J. Appl. Physiol.* 117, 257–266. doi: 10.1152/japplphysiol.00325.2014

Wilson, A. M., and Goodship, A. E. (1994). Exercise-induced hyperthermia as a possible mechanism for tendon degeneration. *J. Biomech.* 27, 899–905. doi: 10.1016/0021-9290(94)90262-90263

Woo, S. L., Gomez, M. A., Woo, Y. K., and Akeson, W. H. (1982). Mechanical properties of tendons and ligaments. II. The relationships of immobilization and exercise on tissue remodeling. *Biorheology* 19, 397–408.

Woo, S. L., and Buckwalter, J. A. (1988). Injury and repair of the musculoskeletal soft tissues. *J. Orthop. Res.* 6, 907–931. doi: 10.2106/00004623-198870070-198870031

Woo, S. L., Gomez, M. A., Seguchi, Y., Endo, C. M., and Akeson, W. H. (1983). Measurement of mechanical properties of ligament substance from a bone-ligament-bone preparation. *J. Orthop. Res.* 1, 22–29. doi: 10.1002/jor.1100010104

Wren, T. A. L., Beaupré, G. S., and Carter, D. R. (1997). A model for loading-dependent growth, development, and adaptation of tendons and ligaments. *J. Biomech.* 31, 107–114. doi: 10.1016/S0021-9290(97)00120-126

Wren, T. A. L., Beaupré, G. S., and Carter, D. R. (2000). Tendon and ligament adaptation to exercise, immobilization, and remobilization. *J. Rehabil. Res. Dev.* 37, 217–224.

Wren, T. A. L., Lindsey, D. P., Beaupré, G. S., and Carter, D. R. (2003). Effects of creep and cyclic loading on the mechanical properties and failure of human achilles tendons. *Ann. Biomed. Eng.* 31, 710–717. doi: 10.1114/1.1569267

Wren, T. A. L., Yerby, S. A., Beaupre, G. S., and Carter, D. R. (2001). Mechanical properties of the human achilles tendon. *Clin. Biomech.* 26, 772–777. doi: 10.1016/j.clinbiomech.2011.02.011

Yamamoto, E., Kogawa, D., Tokura, S., and Hayashi, K. (2005). Effects of the frequency and duration of cyclic stress on the mechanical properties of cultured collagen fascicles from the rabbit patellar tendon. *J. Biomech. Eng.* 127, 1168–1175. doi: 10.1115/1.2073587

Conflict of Interest: The authors declare that the research was conducted in the absence of any commercial or financial relationships that could be construed as a potential conflict of interest.

frontiers in Bioengineering and Biotechnology

BRIEF RESEARCH REPORT
published: 05 February 2021
doi: 10.3389/fbioe.2021.539135

3D Models Reveal the Influence of Achilles Subtendon Twist on Strain and Energy Storage

*Katherine R. Knaus and Silvia S. Blemker**

Department of Biomedical Engineering, University of Virginia, Charlottesville, VA, United States

The Achilles tendon (AT) has complex function in walking, exchanging energy due to loading by the triceps surae muscles. AT structure comprises three subtendons which exhibit variable twist among themselves and between individuals. Our goal was to create 3D finite element (FE) models to explore AT structure-function relationships. By simulating subtendon loading in FE models with different twisted geometries, we investigated how anatomical variation in twisted tendon geometry impacts fascicle lengths, strains, and energy storage. Three tendon FE models, built with elliptical cross sections based on average cadaver measurements, were divided into subtendons with varied geometric twist (low, medium, and high) and equal proportions. Tendon was modeled as transversely isotropic with fascicle directions defined using Laplacian flow simulations, producing fascicle twist. Prescribed forces, representing AT loading during walking, were applied to proximal subtendon ends, with distal ends fixed, and tuned to produce equal tendon elongation in each case, consistent with ultrasound measurements. Subtendon fascicle lengths were greater than free tendon lengths in all models by 1–3.2 mm, and were longer with greater subtendon twist with differences of 1.2–1.9 mm from low to high twist. Subtendon along-fiber strains were lower with greater twist with differences of 1.4–2.6%, and all were less than free tendon longitudinal strain by 2–5.5%. Energy stored in the AT was also lower with greater twist with differences of 1.8–2.4 J. With greater subtendon twist, similar elongation of the AT results in lower tissue strains and forces, so that longitudinal stiffness of the AT is effectively decreased, demonstrating how tendon structure influences mechanical behavior.

Keywords: Achilles tendon, fascicle twist, tendon strain, tendon energy storage, subtendon morphology, finite element modeling, free tendon loading

OPEN ACCESS

Edited by:
Toni Arndt,
Swedish School of Sport and Health Sciences, Sweden

Reviewed by:
Georgios Maliaris,
International Hellenic University, Greece
Rod S. Barrett,
Griffith University, Australia

***Correspondence:**
Silvia S. Blemker
ssblemker@virginia.edu

Specialty section:
This article was submitted to Biomechanics, a section of the journal Frontiers in Bioengineering and Biotechnology

Received: *28 February 2020*
Accepted: *15 January 2021*
Published: *05 February 2021*

Citation:
Knaus KR and Blemker SS (2021) 3D Models Reveal the Influence of Achilles Subtendon Twist on Strain and Energy Storage. Front. Bioeng. Biotechnol. 9:539135. doi: 10.3389/fbioe.2021.539135

INTRODUCTION

The Achilles tendon (AT) plays an important but complex role in human movement. This unique tendon transmits forces from the three muscles of the triceps surae to the calcaneus during production of ankle plantarflexion torque. Due to muscle loading, the AT stores and returns energy as it stretches and recoils (Lichtwark and Wilson, 2005; Zelik and Franz, 2017). Each of the triceps surae muscles perform different functions in the generation of propulsion and vertical support during walking (Neptune et al., 2001; Anderson and Pandy, 2003; McGowan et al., 2008;

Francis et al., 2013), and each muscle has a unique architecture (Ward et al., 2009; Handsfield et al., 2014; Bolsterlee et al., 2019). Therefore, the three triceps surae muscles apply different forces to the AT (Arndt et al., 1998), which means that the AT functions as three combined tendons, leading to a more complex relationship between structure and function than in a tendon attached to a single muscle.

The evidence of complex loading conditions can be visualized using ultrasound imaging during walking. For example, non-uniform displacements have been observed in the *in vivo* free tendon; the deep portion of the tendon displaces more than the superficial portion between toe-off and mid-stance, indicating greater elongation of this region (Franz et al., 2015). These kinematic results likely occur due to the combination of complex loading and the complicated structure of the AT. The internal structure of the Achilles free tendon comprises three subtendons (Handsfield et al., 2016), which are distinguishable groups of fascicles that originate from individual muscles: the gastrocnemius lateral head, medial head, and the soleus. These subtendons have been observed in cadavers to twist around each other before inserting into the calcaneus (Cummins and Anson, 1946; Szaro et al., 2009; Edama et al., 2015). The twisted structure occurs in all ATs and the direction of twist is consistent across individuals. However, the amount of subtendon twist varies between individuals, such that previous authors have used that variation to classify tendons into three groups (Cummins and Anson, 1946; Edama et al., 2015; Pękala et al., 2017). These detailed anatomical studies present many questions about the functional consequences of AT internal structure and how mechanical behavior may vary with differences in anatomy. For example, would strain experienced by the tendon during a given elongation vary with differences in the twisted structure of its subtendons? Would differences in subtendon twist change the amount of energy stored during that same stretch?

Computational models enable exploration into the relationships between tendon structure and function. A finite element (FE) model of Achilles subtendons (Handsfield et al., 2017b) demonstrated how sliding and differential loading are possible mechanisms underlying observed non-uniform displacements (Slane and Thelen, 2015). Shim et al. (2018) developed subject-specific models of the Achilles free tendon in which they incorporated variations in fascicle twist. Their study confirmed that varying tendon twist does impact mechanical behavior. However, tendon geometry and material properties also varied in this study and have been shown to be highly variable between individuals and contribute to differences in mechanical behavior (Shim et al., 2014). It remains unclear to what extent observed fascicle twist within the subtendons may influence tendon mechanics, independent of these other variations in the AT.

Variation in subtendon twisted morphology could also affect *in vivo* measurements of tendon mechanical behavior. For example, strains in the AT are generally estimated by tracking the distance between the distal and proximal endpoints (Kubo et al., 2002; Lichtwark and Wilson, 2005; Onambele et al., 2006), assuming that strain is a linear measure between these two endpoints. Similar methods are employed in combination with force estimation to determine tendon work (Lichtwark and Wilson, 2005; Zelik and Franz, 2017). It is possible that tendon fibers twisted along the length of the tendon may affect the relationship between the tendon tissue strain and energy storage and the longitudinal estimates of strain and energy storage.

The goal of this work was to investigate how differences in subtendon internal twisted structure influences AT fascicle morphology, strains, and energy storage. Our secondary goal was to explore how subtendon twisting may affect quantification of AT strain and energy storage made with *in vivo* measurements. In order to quantify the effects of twist geometry, independent of differences in free tendon shape and material properties, we built a FE model of the AT with three different internal structures. The different versions of the model represented the average of the three classifications of Achilles subtendon fascicle twisting observed in unloaded cadaver tendons (Pękala et al., 2017) and simulations were performed in which the tendon models were loaded to represent tendon displacement in walking. We analyzed the simulations to (1) determine how functional tendon behavior varied with differences in subtendon twisted morphology, and (2) assess how varied morphology contributed to errors in quantification of strain and energy storage *in vivo*.

MATERIALS AND METHODS

Model Geometries

A three dimensional (3D) Achilles free tendon geometry was created in Autodesk Inventor (Autodesk Inc. San Rafael, CA, United States) based on measurements from Pękala et al. (2017). Two elliptical axial cross sections were defined a distance of 60 mm apart and a surface was lofted between them to create a 3D geometry with a volume of 5804.85 mm^3 (**Figure 1**). The proximal cross section (major axis = 17.83 mm, minor axis = 5.76 mm, area = 80.66 mm^2) represented the point on the tendon that is just distal to the soleus musculotendinous junction (MTJ). This location was chosen as the most proximal location that the free tendon can be assumed to be in series with all three triceps surae muscles (Epstein et al., 2006). The distal cross section (major axis = 22.04 mm, minor axis = 6.42 mm, area = 111.13 mm^2) represented the point on the tendon that is just proximal to the superior portion of the insertion into the calcaneus.

Using this 3D tendon geometry, three models were created with different internal structures characterized by the amount of subtendon twist. Surfaces divided each 3D model into three subtendons that corresponded with each of the triceps surae muscles: lateral gastrocnemius (LG), medial gastrocnemius (MG), and soleus (SOL). Subtendon divisions were defined such that the proximal cross sections were the same in each model while the distal cross sections varied, resulting in three unique undeformed models with differing sub-structure geometries: low twist, medium twist and high twist (**Figure 1**). The distribution of volume between the three subtendons was the same in all models (LG = 44%, MG = 27.5%, SOL = 28.5%). The three model geometries corresponded with the average of the classifications of AT torsion (Type I, Type II, and Type III) described by

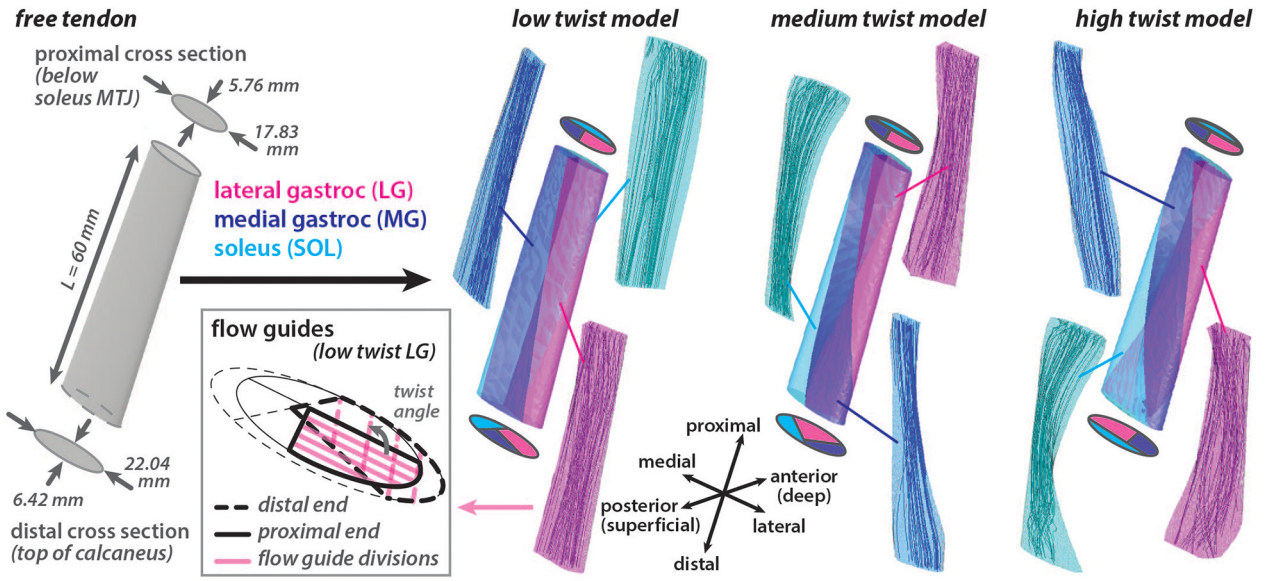

FIGURE 1 | Achilles free tendon geometry was developed with elliptical cross sections at the ends. Three unique models with differing amounts of subtendon twist in the undeformed configuration were created by subdividing the free tendon geometry using internal surfaces. These surfaces had the same proximal subtendon cross section divisions and differing distal cross section divisions. Flow guides were used to direct the amount of fascicle twist in each subtendon by creating surfaces that were parallel in the axial cross sections that divided the subtendon volume. Flow guide surfaces are shown in the axial plane for the proximal and distal ends of the lateral gastrocnemius (LG) subtendon in the low twist model. The angle between the flow guides at the ends defined the *twist angle* of the fascicles within the subtendon. Fascicle tracts in the undeformed models, reconstructed from the resulting fiber directions, are shown.

Pękala et al. (2017). These twisted model geometries were the undeformed or resting configuration of models where there was zero stress.

Model Fascicles

Each model was meshed automatically into 3D tetrahedral elements (AMPS Technologies, Pittsburgh, PA, United States). The low twist model contained 4,336 nodes and 16,595 elements, the medium twist model contained 4,147 nodes and 16,168 elements, and the high twist model contained 4,291 nodes and 16,355 elements. Each subtendon was meshed independently so that nodes on adjacent surfaces were not shared. An element convergence analysis was performed by repeating simulations of the low twist model with different mesh densities. The selected mesh was chosen such that the differences in the primary metrics of average *along-fiber strain* was less than 0.1% and in total *strain energy* was less than 3% when the number of elements increased by a factor of ten. Additionally, the maximum and minimum strain differed by 5 and 3%, respectively, and the first principle stress differed by less than 3%.

A local fiber direction (a_0) was defined for each element to represent the tendon fascicle structure, with a previously described method utilizing Laplacian simulations (Handsfield et al., 2017a). For each 3D subtendon, fibers were directed from the proximal cross section (inlet surface) to the distal cross section (outlet surface). When characterizing of three tendon twist types, Pękala et al. (2017) dissected the individual subtendons and quantified the average degree of twist of the fascicles in each unloaded subtendon. Based on these measurements, fascicle twist in each undeformed subtendon was enforced by implementing flow guides (Handsfield et al., 2017a) that were internal surfaces that divided the subtendons into four twisting portions. These surfaces were parallel in axial cross sections. The *twist angle* was defined as the angle in the axial plane between the proximal and distal edges of the flow guides (**Figure 1**). Unique flow guides resulted in different fascicle *twist angles* in each model (low twist model: LG = 107°, MG = 17°, SOL = 105°; medium twist model: LG = 157°, MG = 35°, SOL = 145°; high twist model: LG = 211°, MG = 68°, SOL = 200°).

To compute the lengths of the subtendon fascicles in the undeformed models, streamlines, generated at seed points on the proximal surface, were mapped through the field of local fiber direction vectors (a_0) in MATLAB (MathWorks Inc., Natick, MA, United States). These streamlines defined fascicle tracts, which were then truncated to not extend beyond the volume of the subtendon geometry or extrapolated to terminate on the distal surface using a method adapted from Bolsterlee et al. (2017). We defined *fascicle lengths* as the lengths of the adjusted fascicle tracts as they twisted from the proximal origin to distal insertion were calculated as previously described (Bolsterlee et al., 2017). At least 250 fascicle tracts were created for each model subtendon, representing the internal fascicle geometry in the undeformed condition with zero strain.

Constitutive Model

Subtendons were modeled as transversely isotropic, hyperelastic, quasi-incompressible material (Weiss et al., 1996; Criscione et al., 2001; Blemker et al., 2005). The constitutive model has been

described in detail by Blemker et al. (2005) and has the strain energy density function defined in Eq. 1:

$$\Phi(\boldsymbol{C}, \boldsymbol{a}_0) = W_1 + W_2 + W_3 + \Phi^{vol} \quad (1)$$

where $\boldsymbol{a}_0$ is the local fiber direction, $\boldsymbol{C}$ is the right Cauchy-Green deformation tensor. The dilatational portion of the strain energy ($\Phi^{vol} = \frac{K}{2}\ln(J^2)$) relates to the volume change where $J = \sqrt{\det(\boldsymbol{C})}$ and depends on a bulk modulus with a value set to K = 5e3 MPa. The strain energy associated with along-fiber shear ($W_1 = G_1(B_1(\bar{I}_4, \bar{I}_5))^2$) depends on a shear modulus set to G_1 = 3 MPa and the strain energy associated with cross-fiber shear ($W_2 = G_2(B_2(\bar{I}_1, \bar{I}_4, \bar{I}_5))^2$) depends on a shear modulus set to G_2 = 15 MPa (Fiorentino and Blemker, 2014). $\bar{I}_1, \bar{I}_4, \bar{I}_5$ are deviatoric invariants of C. The function for the strain energy associated with along-fiber stretch (W_3) characterizes the relationship between Cauchy stress in the tendon (σ) and the fiber stretch ($\lambda = \sqrt{\bar{I}_4}$) and is defined to be consistent with a piece-wise tendon stress-strain relationship in Eq. 2:

$$\lambda\frac{\partial W_3}{\partial \lambda} = \begin{cases} \sigma(\lambda) = P_1\left(e^{P_2(\lambda-1)} - 1\right) & 1 < \lambda < \lambda^* \\ \sigma(\lambda) = P_3\lambda + P_4 & \lambda \geq \lambda^* \end{cases} \quad (2)$$

where λ^* represents the fiber stretch at which σ becomes linear and was set to λ^* = 1.03. In the piece-wise equation, P_3 and P_4 were defined so σ is C^0 and C^1 continuous at $\lambda = \lambda^*$ P_1 and P_2 were set to values of 1.75 MPa and 48.3, respectively, so that the slope in the linear region was 360 MPa (Onambele et al., 2006).

The constitutive model was implemented in the multi-physics FE analysis program, AMPSol (AMPS Technologies, Pittsburgh, PA, United States), by creating a user-defined hyperelastic material with explicit strain energy function specification.

Model Boundary Conditions

Frictionless sliding contact was assigned between the surfaces of adjacent subtendons in each model. The mechanics of the inter-subtendon matrix in the human AT are unknown and the interfascicular matrix has been shown to allow relative sliding of tendon fascicles in comparative studies (Thorpe et al., 2015), so this approach has been used previously to model Achilles subtendon interaction (Handsfield et al., 2017b). The distal end of each sub tendon was fixed, and the proximal end was constrained to move only in the proximal-distal direction.

To simulate uniaxial loading applied to the AT during walking, pressure boundaries were applied to the proximal surface of each subtendon. The applied pressure on each subtendon was tuned so that in each model the displacement of the proximal surfaces of the MG and LG subtendon were 7.6 mm and the displacement of the proximal SOL subtendon surface was 5.9 mm. These displacements were determined based on measurements of the maximum elongations measured in the superficial and deep portions of the AT during walking (Franz et al., 2015). These *in vivo* subtendon elongations were estimated from the change in distance between average nodal positions of tendon tissue measured with ultrasound speckle tracking and calcaneus marker positions from motion capture of healthy young adults walking at a speed of 1.25 m/s.

Calculating Strain and Energy Storage

We determined subtendon strain in the longitudinal direction, which we called *longitudinal strain*, by dividing the change in length by the original length of the subtendon measured in the proximal-distal direction, consistent with *in vivo* methods of measuring AT strain (Kubo et al., 2002; Lichtwark and Wilson, 2005; Onambele et al., 2006). *Longitudinal strain* was equivalent to the proximal surface displacement divided by the initial distance between the distal and proximal cross sections (60 mm). We determined strain the fiber direction at the tissue-level, which we called *along-fiber strain*, by calculating the average along-fiber stretch (λ) in each subtendon and subtracting 1.

We calculated the energy stored in the tendon during loading by integrating the average tendon work relationship for the full AT (force in all subtendons versus the average subtendon length change), which we called *full tendon stored energy*. This approach was chosen to be consistent with *in vivo* methods of calculating AT negative work (Lichtwark and Wilson, 2005; Zelik and Franz, 2017). We alternatively calculated the energy stored in the tendon during loading by integrating the average tendon work relationship for the individual subtendons (force in individual subtendon versus that subtendon's length change) then summing the work done by each subtendon; we called this value *summed-subtendon stored energy*. We also determined the total *strain energy* in the AT by integrating the strain energy density (Φ) across all the elements in the subtendon; the strain energy density is directly calculated using the tendon constitutive model.

Kruskal–Wallis tests were used to determine whether differences in *fascicle lengths* and *along-fiber strain* occurred between subtendons of the three models. *Post hoc* Wilcoxon rank sum tests were used to test for differences in subtendon *fascicle lengths* and *along-fiber strains* between each pair of models. The Holm–Bonferroni method was used to correct for family wise error rate for tests repeated over the three subtendons. Significance was set at $p = 0.05$.

RESULTS

Undeformed Subtendon Fascicle Lengths Are Increasingly Longer Than Free Tendon Length at Greater Twist Angles

All subtendon *fascicle lengths* were longer than the free tendon length of 60mm in the undeformed configuration (**Figure 2**). For the low twist model, subtendon *fascicle lengths* were: LG = 61.09 ± 0.19 mm, MG = 61.03 ± 0.12 mm, and SOL = 61.33 ± 0.30 mm. For the medium twist model, subtendon *fascicle lengths* were: LG = 61.53 ± 0.28 mm, MG = 62.02 ± 0.27 mm, and SOL = 61.85 ± 0.52 mm. For the high twist model, subtendon *fascicle lengths* were: LG = 62.39 ± 1.13 mm, MG = 62.24 ± 0.39 mm, and SOL = 63.18 ± 0.78 mm. The MG subtendon had the shortest

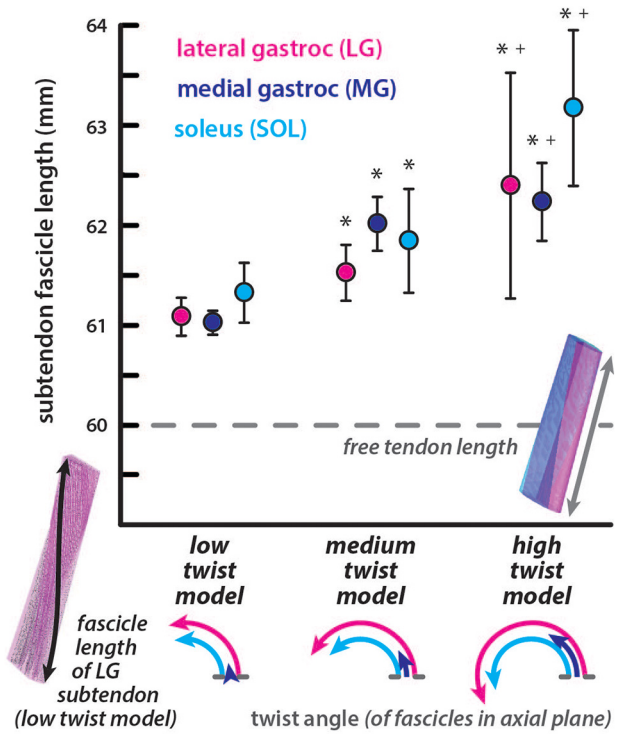

FIGURE 2 | Subtendon *fascicle lengths* in the undeformed models are longer than resting free tendon length. *Fascicle lengths* are longer in subtendons of models with more twisted geometry. The average length of fascicle tracts in each subtendon are plotted with error bars indicating standard deviations. Significant differences ($p < 0.00001$) in lengths were found in subtendons compared to the low twist (*) and medium twist (+) models. The dotted line indicates the length of the free tendon, which would be consistent with *fascicle lengths* if no twisting among or within the subtendons occurred. The *twist angle* of the fascicles within each subtendon are illustrated in the axial plane for each model.

fascicles and the SOL subtendon had the longest fascicles in low and high twist models. *Fascicle lengths* were more variable in subtendons with higher *twist angles*. For all subtendons, resting *fascicle lengths* were significantly shorter ($p < 0.00001$) in the low compared to the medium twist model, in the low compared to the high twist model, and in the medium compared to the high twist model. The percent differences in average *fascicle lengths* compared to the free tendon length were relatively small (low twist: LG = 1.80%, MG = 1.71%, and SOL = 2.19%; medium twist: LG = 2.52%, MG = 3.32%, and SOL = 3.04%; high twist: LG = 3.90%, MG = 3.66%, and SOL = 5.16%).

Subtendon Along-Fiber Strains Are Lower Than Longitudinal Strain During Elongation and Are Lower With Greater Subtendon Twist

The *longitudinal strain* was the same in all models with higher strain in the LG and MG subtendon (12.7%) than the SOL subtendon (9.8%) (**Figures 3A,B**), corresponding with differential displacement between the deep and superficial portions of the AT (Franz et al., 2015). Average *along-fiber strains* were lower than *longitudinal strains* in all models with values for each subtendon decreasing from the low twist model (LG = 9.9 ± 0.8%, MG = 10.5 ± 0.6%, and SOL = 7.9 ± 0.7%) to the medium twist model (LG = 9.2 ± 1.0%, MG = 9.0 ± 1.4%, and SOL = 7.1 ± 0.9%) to the high twist model (LG = 7.2 ± 1.2%, MG = 8.8 ± 0.9%, and SOL = 6.4 ± 1.2%), with significant differences ($p < 0.002$) in the LG of the low and medium twist models compared to high twist The MG subtendon had the highest average *along-fiber strain* in the low and high twist models and the SOL subtendon had the lowest average *along-fiber strain* in all three models (**Figure 3A**). *Along-fiber strains* were non-uniform throughout all subtendons in all of the models (**Figure 3C**). The percent differences in average *along-fiber strains* compared to the *longitudinal strains* ranged from 20-55% (low twist: LG = −25.7%, MG = −19.5%, and SOL = −22.5%; medium twist: LG = −33.0%, MG = −37.0%, and SOL = -32.3%; high twist: LG = −55.0%, MG = −38.6%, and SOL = −41.8%).

Energy Stored in the Tendon for Similar Elongations Is Lower With Greater Subtendon Twist

The average subtendon length change was the same in all models but the tendon force required to achieve the same displacement was lower in models with greater twist (low twist = 2.49 kN, medium twist = 2.18 kN, and high twist = 1.90 kN). Therefore, the *full tendon stored energy* was also lower in models with greater twist (low twist = 7.91 J, medium twist = 6.92 J, high twist = 6.04 J) (**Figure 4**). Similarly, the *summed-subtendon stored energy* was lower in models with greater twist (low twist = 8.10 J, medium twist = 7.09 J, and high twist = 6.22 J), though values were slightly higher than the *full tendon stored energy*. Total *strain energy* showed a similar trend as tendon stored energy and was lower in models with greater twist (low twist = 6.73 J, medium twist = 5.63 J, and high twist = 4.34 J), though *strain energy* in all models was less than the energy determined with both longitudinal methods. The strain energy density was non-uniform throughout all subtendons in all of the models, with areas of high energy corresponding with areas of high strain (**Figure 3C**). The percent differences in total *strain energy* from the *full tendon stored energy* increased with greater twist (low twist = −16.2%, medium twist = −20.5%, and high twist = −32.7%), while percent differences in total *strain energy* from the *summed-subtendon stored energy* displayed a similar trend and were slightly larger (low twist = −18.5%, medium twist = −23.0%, and high twist = −35.7%).

DISCUSSION

The primary goal of this study was to use models of the Achilles free tendon to explore how mechanical behavior varies with morphology differences in subtendon and fascicle twist. Models predicted that, with more twisted resting geometry, the AT had longer *fascicle lengths* when undeformed and exhibited reduced *along-fiber strain* and lower energies stored during elongation, thus altering the free tendon's response to loading.

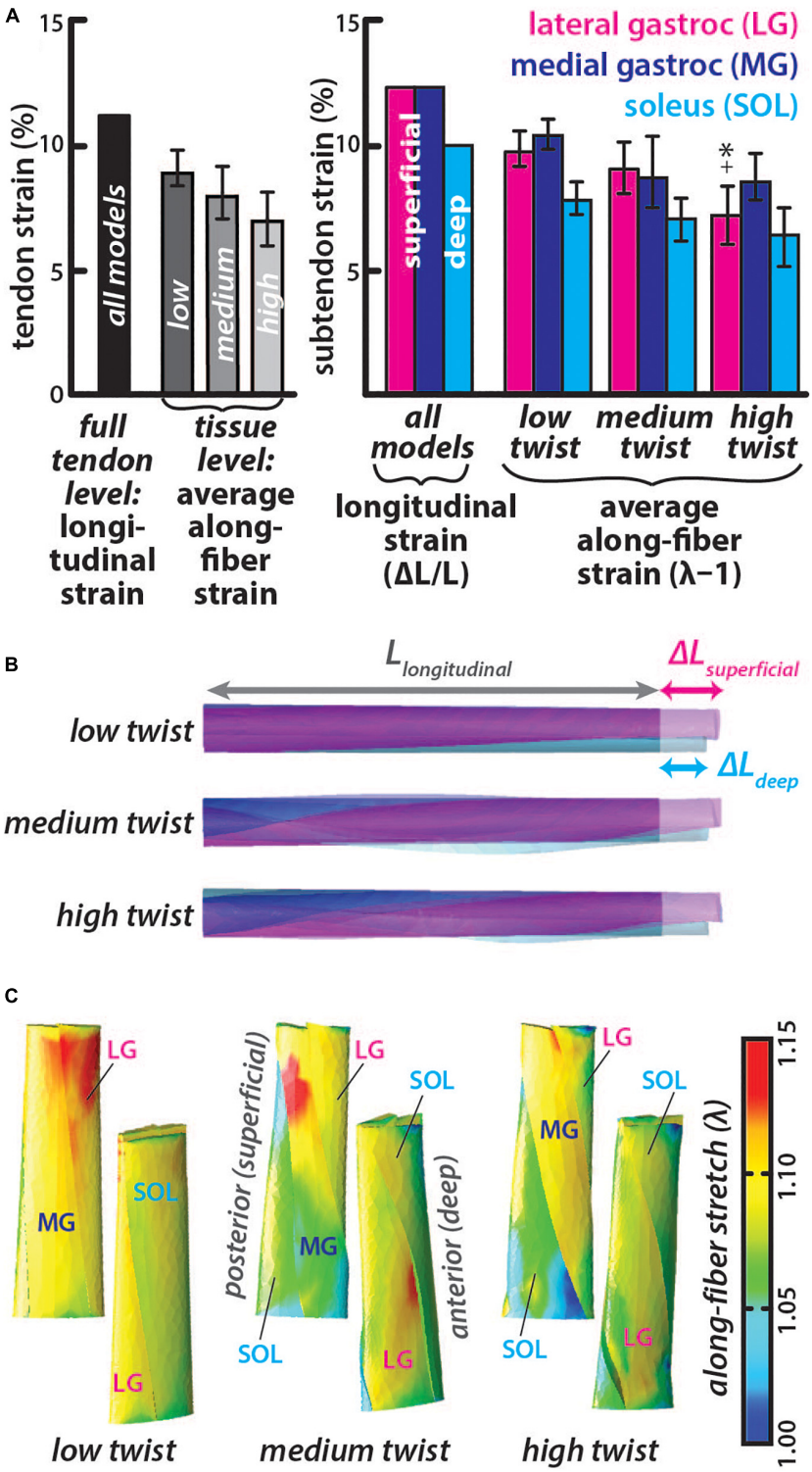

FIGURE 3 | Subtendon *along-fiber strains* are lower than *longitudinal strain* and was lower in subtendons of models with greater twist. **(A)** The *longitudinal strain* was the same in all models and measured as the change in length in the proximal-distal direction divided by the initial length. The average *along-fiber strain* was determined in each full tendon model as well as in the individual subtendons, with error bars indicating standard deviations. Significant differences ($p < 0.002$) in *along-fiber strain* were found in high twist LG subtendon compared to the low twist (*) and medium twist (+) models. **(B)** All twist models experienced the same elongation in the proximal-distal direction, with greater displacement in the superficial (at the proximal end) subtendons (LG and MG) than the deep subtendon (SOL). **(C)** Posterior and anterior view of each model show the along-fiber stretch (λ) from each simulation, where a stretch value of one is the zero-strain or undeformed condition.

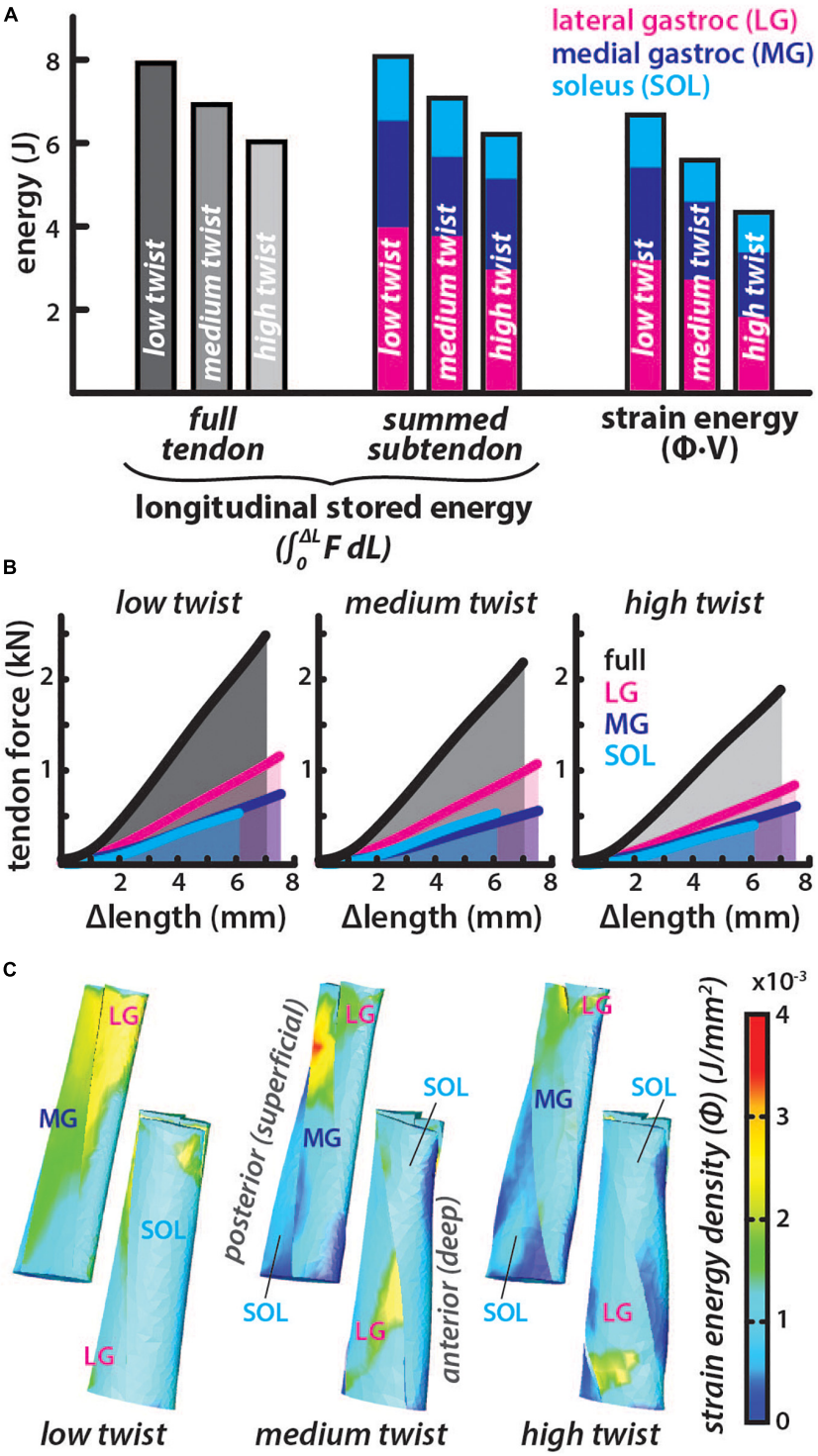

FIGURE 4 | Energy stored in the tendon for similar elongations is lower in models with greater subtendon twist. **(A)** The total energy stored in each twist type was calculated longitudinally using two methods. *Full tendon stored energy* was calculated by integrating the force (F) from all subtendons over the average length change (ΔL) of the all subtendons. *Summed-subtendon stored energy* was calculated by integrating the force (F) from each subtendon over the average length change (ΔL) of that subtendon then summing the results. Total *strain energy* was also computed using the strain energy density (Φ) and volume (V) of each element. Colored bars show the proportion of energy stored in each subtendon. **(B)** The average tendon length change is plotted with the total force in black and the area under the curve was calculated to find *full tendon stored energy*. Subtendon length changes and forces are plotted with colored lines and area under each curve was summed to compute the *summed subtendon stored energy*. **(C)** Posterior and anterior view of each model show the strain energy density (Φ) from each simulation, which was multiplied with element volumes and summed to calculate total strain energy.

Models predicted that increasing the amount of twist of the Achilles subtendon resting morphology effectively lowered stiffness in the free tendon even though the tissue level material properties were held constant. In the models, the tissue-level strain varied with twist while the elongation was the same. The average *along-fiber strain* was lower in models with greater twist (**Figure 3A**), leading to larger differences in the strain at the tissue-level compared to the tendon-level strain. The distribution of strains within the tissue differed as well (**Figure 3C**). Similar to our results, AT FE models with twisted geometry developed by Shim et al. (2018) predicted that greater geometric twist redistributed internal stresses during loading allowing larger loads to be applied in simulations before stress in the tissue reached a given rupture limit. Tendon twisted geometry could be a mechanism to reduce the tendon tissue strains experienced during a given muscle-tendon-unit (MTU) excursion. A more twisted morphology may therefore aid in avoiding rupture as failure strain of tendon has been shown to be highly conserved between different tendons in different species (LaCroix et al., 2013).

In our simulations where tendon elongation was the same, greater twist corresponded with lower stored energy at both the tendon level (longitudinal stored energy) and at the tissue level (strain energy) (**Figure 4A**). Longitudinal energy differences can be attributed to the varied forces applied in each model for the same elongation (**Figure 4B**), while the *strain energy* differences were also influenced by variation in tissue-level strain (**Figure 3A**). Twisting may actually improve the efficiency of energy return by the tendon, as tendon-level strain and energy storage requires less tissue deformation that could lead to conformational changes at the collagen level that would result in energy loss. In fact, equine energy storing tendons with helical substructures have been shown to experience less hysteresis loss than postural tendons with less fascicle rotation (Thorpe et al., 2013). Furthermore, the lower forces required in higher twist tendon models to elongate as much as the low twist model (**Figure 4B**), suggest that the amount of twist would impact series-elasticity of the musculotendon unit. A more compliant AT may enable greater force control by the triceps surae muscles (Alexander, 2002) and has the potential to alter the efficiency of these muscles (Lichtwark and Wilson, 2007; Uchida et al., 2016).

It is unknown if the variation in morphologic twist between individuals is an adaptation to mechanical stimuli or simply a product of anatomical variability. However, the amount of twist seems to provide tradeoffs in injury prevention and energetic efficiency. The twist of the subtendons and the *twist angle* of their fascicles may be an important consideration in the repair of AT ruptures. As the amount of twist does not vary much between the right and left sides (Pękala et al., 2017), twist in the contralateral tendon could serve as a reference in reconstructing the ruptured tendon. Alternatively, twist could be applied before suturing in an effort to preserve compliance as elasticity decreases (Karatekin et al., 2018) or to protect the repaired tendon from further injury. This approach to improving AT reconstruction is an exciting opportunity for further studies.

Each of the three subtendons had different twist angle in all undeformed models, resulting in different average *fascicle lengths* (**Figure 2**). The MG subtendon had lower *twist angles* and generally shorter fascicles compared to the LG subtendon, and therefore experienced higher *along-fiber strains* even though *longitudinal strains* were the same in both subtendons (**Figure 3**). These results suggest that the MG subtendon is more vulnerable to injury due to its lower twist angle, which may help explain how failure of a single subtendon occurs, resulting in a partial tear in the Achilles (Smigielski, 2008). Further studies could work to determine if tears occur more often in the less twisted MG subtendon. The SOL subtendon had the greatest *twist angle* in all models and generally had longer fascicles. Subtendon twist within the free tendon influenced *fascicle lengths* in addition to the fascicle *twist angle*, so in the case of the medium twist model, the MG subtendon had longer fascicles despite its lower *twist angle*. The difference in *twist angles* between these subtendons could be associated with the diversity in morphology of the muscles they attach to. Dean et al. (2007) demonstrated that a twisted tendon in the jaw of a spotted ratfish facilitated more uniform strains in the fibers of a muscle with a broad attachment, so that these fibers could operate at similar lengths on the force-length curve. The triceps surae muscles also have broad attachments though the attachment morphology of each muscle is different (Dalmau-Pastor et al., 2014), possibly necessitating different subtendon twist angles to achieve the same equalizing effect on fiber operating lengths.

Our secondary goal was to assess how morphological complexity of the AT impacts how *in vivo* measurements of tendon behavior should be interpreted. We hypothesized that varying lengths and geometry resulting from twisted morphology may lead to errors during *in vivo* calculations of strain and energy. We found that resting *fascicle lengths* were only slightly underestimated by 1.5-5.5% by using measurements of tendon length. However, strains and energy storage measured at the fascicle level were both overestimated by 20–55 and 15–35%, respectively when using longitudinal methods that are consistent with *in vivo* measurements. The amount of error increases with twist. Unfortunately, definitively calculating measurement errors due to subtendon twist is not possible as methods of determining the amount of twist *in vivo* have not been developed, to our knowledge. Hopefully the future development of imaging techniques will allow for correction of such measurement errors in the future. Additionally, the high twist group accounts for less than 6% of the population studied in Pękala et al. (2017) so most tendons will likely have a low (48% of population) or medium (46% of population) amount of twist. Therefore, the extent of error associated with the low (strain = 19–26%, energy = 16–19%) and medium (strain = 32–37%, energy = 20–23%) twist models will represent most of the population included in *in vivo* studies.

There are several limitations to this study that should be noted. Our goal was to characterize the mechanical consequences of varying subtendon twist, independent of variation in tendon geometry or material properties. To this end we developed a model with a generic geometry so that we could create variations in internal structure and examine the effects on tendon behavior when loaded uniaxially. Future work to develop more detailed models is needed to fully investigate how subtendon twist influences *in vivo* AT behavior. Methods enabling *in vivo*

quantification of subtendon twist would improve subject-specific models. Twist could be incorporated with other model inputs, like geometry and material properties, that tendon behavior is sensitive to Shim et al. (2014). Furthermore, validation with *in vivo* data is required to better understand the predictions made in this study. We chose to use the measurements of subtendon structure reported by Pękala et al. (2017) because of the extent of quantitative anatomical data provided. We are aware that the subtendon proportions and cross section in that study (Pękala et al., 2017), deviate somewhat from those reported by previous authors (Szaro et al., 2009; Edama et al., 2015). Since measurements in these studies were performed *ex vivo* in dissected tendons, a major assumption of our model was that subtendon twist was a morphological characteristic that could exist independent of loading. Therefore, we implemented twist in the geometry of the undeformed models, as opposed to applying a torsional loading condition to achieve twist. AT rotation has been observed in response to *in vivo* loading (Obst et al., 2014), and model twist likely changes during simulated loading. All model *twist angles* are reported for the undeformed configuration.

All tendon measurements used to create model geometries were made in fresh frozen cadavers (Pękala et al., 2017), though simulation conditions were chosen to represent *in vivo* tendon loading (Franz et al., 2015). Displacements of subtendon proximal ends were controlled to match elongations estimated with speckle tracking in the free tendon. In the *in vivo* experiments, elongation was calculated from the proximal end to the calcaneal marker. The distal end of the models was located at the superior edge of the calcaneus, which resulted in shorter model tendons and therefore higher strains than in the *in vivo* study. Although AT strains of this magnitude have been reported during one-legged hopping (Lichtwark and Wilson, 2005), model predicted strains are likely larger than what occurs during walking. However, all models experienced the same *longitudinal strains*, allowing for comparison of tissue level strains due to differences in subtendon twist. Further, conclusions about strain in each subtendon are difficult to interpret from these results as the free tendon modeled here does not capture full external portion of proximal tendon associated with lateral or MG head. Simulations were performed quasi-statically and only included tendon loading. Further work is needed to incorporate more detailed viscoelastic behavior of AT in order to accurately simulate full tendon work loops. We assumed the tendon was unloaded prior to simulated elongation and, thus, we applied no initial stretch to the models. Estimates of *in vivo* AT loading show that the tendon is not stress-free at the beginning of the gait cycle (Keuler et al., 2019). As the start of our simulations correspond to this time point, it may be appropriate to apply a pre-stretch to the subtendons, which would affect when the tendon would transition from the toe region to the linear portion of the stress-strain curve, leading to higher stresses at the strains enforced in this study. While estimates of stress in the full tendon exist, it is unclear how loading may be distributed between the subtendons. Evidence of differences in slack angles of the triceps surae muscles (Hirata et al., 2015) suggests that the initial stretch at a given joint angle would vary between the subtendons, though current methods are unable to estimate what these loads should be. An exciting direction for future work would be to investigate how inhomogeneous subtendon loading in addition to variation in subtendon morphology influence the behavior of the AT.

In conclusion, the models developed in this paper of the AT with varied subtendon twisted geometry help us understand how this morphological characteristic can result in different amounts of tissue strain and energy storage within the tendon in response to similar loading. High *twist angles* in tendon fascicles can contribute to errors in quantifying these mechanical behaviors when methods that rely on 2D measurements at the endpoints are employed. The knowledge of this effect will aid in the interpretation of future studies of AT behavior and inspire future work to design methods that enable measurements of *in vivo* subtendon structure.

DATA AVAILABILITY STATEMENT

The datasets generated for this study are available on request to the corresponding author.

AUTHOR CONTRIBUTIONS

KK and SB: conceptualization, writing – review, and editing. KK: model development and analysis and writing – original draft preparation. SB: funding acquisition. Both authors contributed to the article and approved the submitted version.

FUNDING

Funding for the completion of this study was provided by the National Institutes of Health grant R01AG051748 and grant U01AR069393.

ACKNOWLEDGMENTS

The authors would like to acknowledge Geoffrey Handsfield, Darryl Thelen, Jason Franz, and all other Tendonados for their assistance and insight related to this project.

REFERENCES

Alexander, R. M. (2002). Tendon elasticity and muscle function. *Comp. Biochem. Physiol. A Mol. Integr. Physiol.* 133, 1001–1011. doi: 10.1016/S1095-6433(02)00143-5

Anderson, F. C., and Pandy, M. G. (2003). Individual muscle contributions to support in normal walking. *Gait Posture* 17, 159–169. doi: 10.1016/S0966-6362(02)00073-5

Arndt, A. N., Komi, P. V., Brüggemann, G. P., and Lukkariniemi, J. (1998). Individual muscle contributions to the in vivo achilles tendon force. *Clin. Biomech.* 13, 532–541. doi: 10.1016/S0268-0033(98)00032-1

Blemker, S. S., Pinsky, P. M., and Delp, S. L. (2005). A 3D model of muscle reveals the causes of nonuniform strains in the Biceps Brachii. *J. Biomech.* 38, 657–665. doi: 10.1016/j.jbiomech.2004.04.009

Bolsterlee, B., D'Souza, A., Gandevia, S. C., and Herbert, R. D. (2017). How does passive lengthening change the architecture of the human medial gastrocnemius

muscle? *J. Appl. Physiol.* 122, 727–738. doi: 10.1152/japplphysiol.00976.2016

Bolsterlee, B., D'Souza, A., and Herbert, R. D. (2019). Reliability and robustness of muscle architecture measurements obtained using diffusion tensor imaging with anatomically constrained tractography. *J. Biomech.* 86, 71–78. doi: 10.1016/J.JBIOMECH.2019.01.043

Criscione, J. C., Douglas, A. S., and Hunter, W. C. (2001). Physically based strain invariant set for materials exhibiting transversely isotropic behavior. *J. Mech. Phys. Solids* 49, 871–897. doi: 10.1016/S0022-5096(00)00047-8

Cummins, E. J., and Anson, B. J. (1946). The structure of the calcaneal tendon (of Achilles) in relation to orthopedic surgery, with additional observations on the plantaris muscle. *Surg. Gynecol. Obstet.* 83, 107–116.

Dalmau-Pastor, M., Fargues-Polo, B., Casanova-Martínez, D., Vega, J., and Golanó, P. (2014). Anatomy of the triceps surae. *Foot Ankle Clin.* 19, 603–635. doi: 10.1016/j.fcl.2014.08.002

Dean, M. N., Azizi, E., and Summers, A. P. (2007). Uniform strain in broad muscles: active and passive effects of the twisted tendon of the spotted ratfish hydrolagus colliei. *J. Exp. Biol.* 210, 3395–3406. doi: 10.1242/jeb.007062

Edama, M., Kubo, M., Onishi, H., Takabayashi, T., Inai, T., Yokoyama, E., et al. (2015). The twisted structure of the human achilles tendon. *Scand. J. Med. Sci. Sports* 25, e497–e503. doi: 10.1111/sms.12342

Epstein, M., Wong, M., and Herzog, W. (2006). Should tendon and aponeurosis be considered in series? *J. Biomech.* 39, 2020–2025. doi: 10.1016/j.jbiomech.2005.06.011

Fiorentino, N. M., and Blemker, S. S. (2014). Musculotendon variability influences tissue strains experienced by the biceps femoris long head muscle during high-speed running. *J. Biomech.* 47, 3325–3333. doi: 10.1016/j.jbiomech.2014.08.010

Francis, C. A., Lenz, A. L., Lenhart, R. L., and Thelen, D. G. (2013). The modulation of forward propulsion, vertical support, and center of pressure by the plantarflexors during human walking. *Gait Posture* 38, 993–997. doi: 10.1016/j.gaitpost.2013.05.009

Franz, J. R., Slane, L. C., Rasske, K., and Thelen, D. G. (2015). Non-uniform in vivo deformations of the human achilles tendon during walking. *Gait Posture* 41, 192–197. doi: 10.1016/j.gaitpost.2014.10.001

Handsfield, G. G., Bolsterlee, B., Inouye, J. M., Herbert, R. D., Besier, T. F., and Fernandez, J. W. (2017a). Determining skeletal muscle architecture with laplacian simulations: a comparison with diffusion tensor imaging. *Biomech. Model. Mechanobiol.* 16, 1845–1855. doi: 10.1007/s10237-017-0923-5

Handsfield, G. G., Inouye, J. M., Slane, L. C., Thelen, D. G., Miller, G. W., and Blemker, S. S. (2017b). A 3D model of the achilles tendon to determine the mechanisms underlying nonuniform tendon displacements. *J. Biomech.* 51, 17–25. doi: 10.1016/j.jbiomech.2016.11.062

Handsfield, G. G., Meyer, C. H., Hart, J. M., Abel, M. F., and Blemker, S. S. (2014). Relationships of 35 lower limb muscles to height and body mass quantified using MRI. *J. Biomech.* 47, 631–638. doi: 10.1016/j.jbiomech.2013.12.002

Handsfield, G. G., Slane, L. C., and Screen, H. R. C. (2016). Nomenclature of the tendon hierarchy: an overview of inconsistent terminology and a proposed size-based naming scheme with terminology for multi-muscle tendons. *J. Biomech.* 49, 3122–3124. doi: 10.1016/j.jbiomech.2016.06.028

Hirata, K., Kanehisa, H., Miyamoto-Mikami, E., and Miyamoto, N. (2015). Evidence for intermuscle difference in slack angle in human triceps surae. *J. Biomech.* 48, 1210–1213. doi: 10.1016/j.jbiomech.2015.01.039

Karatekin, Y. S., Karaismailoglu, B., Kaynak, G., Ogut, T., Dikici, A. S., Esmerer, E. U., et al. (2018). Does elasticity of achilles tendon change after suture applications? Evaluation of repair area by acoustic radiation force impulse elastography. *J. Orthop. Surg. Res.* 13:45. doi: 10.1186/s13018-018-0751-z

Keuler, E. M., Loegering, I. F., Martin, J. A., Roth, J. D., and Thelen, D. G. (2019). Shear wave predictions of achilles tendon loading during human walking. *Sci. Rep.* 9:13419. doi: 10.1038/s41598-019-49063-7

Kubo, K., Kawakami, Y., Kanehisa, H., and Fukunaga, T. (2002). Measurement of viscoelastic properties of tendon structures in vivo. *Scand. J. Med. Sci. Sports* 12, 3–8. doi: 10.1034/j.1600-0838.2002.120102.x

LaCroix, A. S., Duenwald-Kuehl, S. E., Lakes, R. S., and Vanderby, R. (2013). Relationship between tendon stiffness and failure: a metaanalysis. *J. Appl. Physiol.* 115, 43–51. doi: 10.1152/japplphysiol.01449.2012

Lichtwark, G. A., and Wilson, A. M. (2005). In vivo mechanical properties of the human achilles tendon during one-legged hopping. *J. Exp. Biol.* 208, 4715–4725. doi: 10.1242/jeb.01950

Lichtwark, G. A., and Wilson, A. M. (2007). Is achilles tendon compliance optimised for maximum muscle efficiency during locomotion? *J. Biomech.* 40, 1768–1775. doi: 10.1016/j.jbiomech.2006.07.025

McGowan, C. P., Neptune, R. R., and Kram, R. (2008). Independent effects of weight and mass on plantar flexor activity during walking: implications for their contributions to body support and forward propulsion. *J. Appl. Physiol.* 105, 486–494. doi: 10.1152/japplphysiol.90448.2008

Neptune, R. R., Kautz, S. A., and Zajac, F. E. (2001). Contributions of the individual ankle plantar flexors to support, forward progression and swing initiation during walking. *J. Biomech.* 34, 1387–1398. doi: 10.1016/S0021-9290(01)00105-1

Obst, S. J., Renault, J.-B., Newsham-West, R., and Barrett, R. S. (2014). Three-dimensional deformation and transverse rotation of the human free achilles tendon in vivo during isometric plantarflexion contraction. *J. Appl. Physiol.* 116, 376–384. doi: 10.1152/japplphysiol.01249.2013

Onambele, G. L., Narici, M. V., and Maganaris, C. N. (2006). Calf muscle-tendon properties and postural balance in old age. *J. Appl. Physiol.* 100, 2048–2056. doi: 10.1152/japplphysiol.01442.2005

Pękala, P. A., Henry, B. M., Ochała, A., Kopacz, P., Tatoń, G., Młyniec, A., et al. (2017). The twisted structure of the achilles tendon unraveled: a detailed quantitative and qualitative anatomical investigation. *Scand. J. Med. Sci. Sports* 27, 1705–1715. doi: 10.1111/sms.12835

Shim, V. B., Fernandez, J. W., Gamage, P. B., Regnery, C., Smith, D. W., Gardiner, B. S., et al. (2014). Subject-specific finite element analysis to characterize the influence of geometry and material properties in achilles tendon rupture. *J. Biomech.* 47, 3598–3604. doi: 10.1016/j.jbiomech.2014.10.001

Shim, V. B., Handsfield, G. G., Fernandez, J. W., Lloyd, D. G., and Besier, T. F. (2018). Combining in silico and in vitro experiments to characterize the role of fascicle twist in the achilles tendon. *Sci. Rep.* 8:13856. doi: 10.1038/s41598-018-31587-z

Slane, L. C., and Thelen, D. G. (2015). Achilles tendon displacement patterns during passive stretch and eccentric loading are altered in middle-aged adults. *Med. Eng. Phys.* 37, 712–716. doi: 10.1016/j.medengphy.2015.04.004

Smigielski, R. (2008). Management of partial tears of the gastro-soleus complex. *Clin. Sports Med.* 27, 219–229. doi: 10.1016/j.csm.2007.10.005

Szaro, P., Witkowski, G., Śmigielski, R., Krajewski, P., and Ciszek, B. (2009). Fascicles of the adult human achilles tendon – an anatomical study. *Ann. Anat.* 191, 586–593. doi: 10.1016/j.aanat.2009.07.006

Thorpe, C. T., Godinho, M. S. C., Riley, G. P., Birch, H. L., Clegg, P. D., and Screen, H. R. C. (2015). The interfascicular matrix enables fascicle sliding and recovery in tendon, and behaves more elastically in energy storing tendons. *J. Mech. Behav. Biomed. Mater.* 52, 85–94. doi: 10.1016/j.jmbbm.2015.04.009

Thorpe, C. T., Klemt, C., Riley, G. P., Birch, H. L., Clegg, P. D., and Screen, H. R. C. (2013). Helical sub-structures in energy-storing tendons provide a possible mechanism for efficient energy storage and return. *Acta Biomater.* 9, 7948–7956. doi: 10.1016/j.actbio.2013.05.004

Uchida, T. K., Hicks, J. L., Dembia, C. L., and Delp, S. L. (2016). Stretching your energetic budget: how tendon compliance affects the metabolic cost of running. *PLoS One* 11:e0150378. doi: 10.1371/journal.pone.0150378

Ward, S. R., Eng, C. M., Smallwood, L. H., and Lieber, R. L. (2009). Are current measurements of lower extremity muscle architecture accurate? *Clin. Orthop. Relat. Res.* 467, 1074–1082. doi: 10.1007/s11999-008-0594-8

Weiss, J. A., Maker, B. N., and Govindjee, S. (1996). Finite element implementation of incompressible, transversely isotropic hyperelasticity. *Comput. Methods Appl. Mech. Eng.* 135, 107–128. doi: 10.1016/0045-7825(96)01035-3

Zelik, K. E., and Franz, J. R. (2017). It's positive to be negative: achilles tendon work loops during human locomotion. *PLoS One* 12:e0179976. doi: 10.1371/journal.pone.0179976

Conflict of Interest: The authors declare that the research was conducted in the absence of any commercial or financial relationships that could be construed as a potential conflict of interest.

Advantages of publishing in Frontiers

OPEN ACCESS
Articles are free to read for greatest visibility and readership

FAST PUBLICATION
Around 90 days from submission to decision

HIGH QUALITY PEER-REVIEW
Rigorous, collaborative, and constructive peer-review

TRANSPARENT PEER-REVIEW
Editors and reviewers acknowledged by name on published articles

Frontiers
Avenue du Tribunal-Fédéral 34
1005 Lausanne | Switzerland

Visit us: www.frontiersin.org
Contact us: frontiersin.org/about/contact

REPRODUCIBILITY OF RESEARCH
Support open data and methods to enhance research reproducibility

DIGITAL PUBLISHING
Articles designed for optimal readership across devices

FOLLOW US
@frontiersin

IMPACT METRICS
Advanced article metrics track visibility across digital media

EXTENSIVE PROMOTION
Marketing and promotion of impactful research

LOOP RESEARCH NETWORK
Our network increases your article's readership